March 2022

COMPUTATIONAL STUDY OF INTERNAL FLOW, NEAR NOZZLE AND EXTERNAL SPRAY OF A GDI INJECTOR UNDER FLASH-BOILING CONDITIONS

Chinmoy krushna Mohapatra
University of Massachusetts Amherst

Recommended Citation

Mohapatra, Chinmoy krushna, "COMPUTATIONAL STUDY OF INTERNAL FLOW, NEAR NOZZLE AND EXTERNAL SPRAY OF A GDI INJECTOR UNDER FLASH-BOILING CONDITIONS" (2022). *Doctoral Dissertations*. 2425.
https://doi.org/10.7275/27766634 https://scholarworks.umass.edu/dissertations_2/2425

COMPUTATIONAL STUDY OF INTERNAL FLOW, NEAR NOZZLE AND EXTERNAL SPRAY OF A GDI INJECTOR UNDER FLASH-BOILING CONDITIONS

A Dissertation Presented

by

CHINMOY K. MOHAPATRA

Submitted to the Graduate School of the
University of Massachusetts Amherst in partial fulfillment
of the requirements for the degree of

DOCTOR OF PHILOSOPHY

February 2022

Mechanical and Industrial Engineering

COMPUTATIONAL STUDY OF INTERNAL FLOW, NEAR NOZZLE AND EXTERNAL SPRAY OF A GDI INJECTOR UNDER FLASH-BOILING CONDITIONS

A Dissertation Presented

by

CHINMOY K. MOHAPATRA

Approved as to style and content by:

David P. Schmidt, Chair

Stephen de Bruyn Kops, Member

Omar A. Abdelrahman, Member

Sundar Krishnamurty, Department Head
Mechanical and Industrial Engineering

DEDICATION

This dissertation is dedicated to my beloved parents.

ACKNOWLEDGMENTS

I would like to acknowledge my Ph.D. advisor, Prof. David P. Schmidt, for his immense support, patience, wisdom and phenomenal contributions in shaping me as an independent researcher. Prof. Schmidt, you are an inspiring character. Your passion for teaching and research while maintaining a healthy environment around you will be the guiding blocks for my future endeavors. I will fondly look at all the memories of our collaboration while working under your supervision. Prof. Schmidt, I would be forever thankful to you for giving me the opportunity to learn from you.

I would like to acknowledge the support I received from my doctoral committee, Prof. Stephen de Bruyn Kops, and Prof. Omar AbdelRahman, in the successful completion of my doctoral degree. Thank you very much for your probing questions and thorough guidance in building a higher quality dissertation. It has been a great learning experience for me.

During the course of my Ph.D., I have been fortunate enough to collaborate with some of the leading scientists from Argonne National Lab, Sandia National Lab and other institutions. I would like to acknowledge some of them during this time. Thank you, Dr. Lyle Pickett (Sandia) for valuable insights and taking the initiatives for the Engine Combustion Network (ECN). I deem myself lucky to be able to contribute to the ECN workshops and monthly web meetings. ECN shows us the power of open-source science, where none of the contributors get paid directly for their effort. However, they come together annually to discuss the interesting physics behind the fuel injection systems both computationally and experimentally. Auto industries have greatly benefited from the discoveries of ECN. I would like to thank Dr. Chris Powell (Argonne), Dr. Brandon Sforzo (Argonne), Dr. Katie Matusik (former Argonne), Prof. Daniel Duke (former Argonne), Prof. Kaushik Saha (former Argonne), Dr. Gina Magnotti (Argonne), Dr. Lorenzo Nocivelli (Argonne), Dr. Joshua Lacey (former University of Melbourne), and Dr. Joonsik Hwang (former Sandia) for their valuable insights in to the physics of spray atomization. I have personally learned a lot by having numerous discussions with you all at various platforms.

I would also like to acknowledge the support of colleagues and friends from the Multi-phase flow simulation laboratory including Sampath, Hannah, Peetak, Brandon and Gabe.

A special mention to my M.S. advisor Prof. Milind A. Jog from the University of Cincinnati,OH. His timely guidance helped me to choose the research career path.

Additionally, the work of this dissertation would not have been possible without the generous financial support from various industrial partners. I am thankful to the General Motors Research Centre for funding the early part of Ph.D. research. A special mention to Dr. Ronald Grover Jr. for his technical acumen which helped me in formulating the early problem statements of my Ph.D. work. I am sincerely grateful to the TOYOTA motors North America -R&D division for their financial support to the major part of my Ph.D. research. I will cherish the endless technical discussions with Dr. Oana Nitulescu and Dr. Tom Shieh. Those discussions helped me immensely in developing the core of my Ph.D. research. I would like to thank the partners from the Spray Combustion Consortium (SCC) for extending the financial support to the exploratory study of my doctoral research. The support of NSF-funded XSEDE computing resources and the Leadership Computing Facility at Argonne, for running CFD simulations, is greatly appreciated.

Last, but not the least, I would like to acknowledge the sacrifice and support of my family and friends from India in getting me here. Firstly, I am thankful to my partner Archana, especially for her continuous support during the final journey of my doctoral studies. My cousin, Dr. GuruKrushna, for always showing me the way and for his constant encouragements throughout. Finally, I acknowledge the unparalleled sacrifices of my parents and uncle (Ashrambapa). Their teaching of never give-up attitude and staying humble in success helped me a lot in navigating the troubled waters during my doctoral studies.

I truly could not have achieved this success without each and every one of you and I am eternally grateful to you all.

ABSTRACT

COMPUTATIONAL STUDY OF INTERNAL FLOW, NEAR NOZZLE AND EXTERNAL SPRAY OF A GDI INJECTOR UNDER FLASH-BOILING CONDITIONS

FEBRUARY 2022

CHINMOY K. MOHAPATRA
B. Tech., NATIONAL INSTITUTE OF TECHNOLOGY,ROURKELA
M. S., UNIVERSITY OF CINCINNATI
Ph.D., UNIVERSITY OF MASSACHUSETTS AMHERST
Directed by: Professor David P. Schmidt

The early and late portions of transient fuel injection have proven to be a rich area of research, especially since the end of injection can cause a disproportionate amount of emissions in direct injection internal combustion engines. While simulating the internal flow of fuel injectors, valve opening and closing events are the perennial challenges. A typical adaptive-mesh CFD simulation is extremely computationally expensive, as the small gap between the needle valve and the seat requires very small cells to be resolved properly. Capturing complete closure usually involves a topological change in the computational domain. Furthermore, Internal Combustion Engines(ICE) operating with Gasoline Direct Injection(GDI) principle are susceptible to flash boiling due to the volatile nature of the fuel.

The presented work simulates a gasoline direct injector operating under cavitating conditions by employing a more gradual and easily implemented model of closure that avoids spurious water-hammer effects. The results show cavitation at low valve lift for both flash boiling and non-flash boiling conditions. Further, this study reveals post-closure dynamics that result in dribble, which is expected to contribute to unburnt hydrocarbon emissions. Flashing versus non-flashing conditions are shown to cause different sac and nozzle behavior after needle closure. In particular, a slowly boiling sac causes spurious injection behavior.

Furthermore, a qualitative analysis of the injector tip-wetting phenomena under both flash-boiling and non-flashing conditions are conducted and different wetting mechanisms are identified. The jet expansion mechanism is observed to dominate the wetting process during the main injection period, whereas the sac conditions drive the post-closure wetting phenomena. Additionally, the effect of flash-boiling conditions on the near-nozzle spray during the quasi-steady period of the injection cycle is explored. The exploration captured hole-to-hole variations in the rate of injection (ROI), rate of momentum (ROM) and hydraulic coefficients of injection. Moreover, it also indicates influences of the in-nozzle variations on the near-nozzle spray behaviors.

Finally, a novel plume-based coupling approach is developed to couple the Eulerian near nozzle simulations with the Lagrangian spray simulations under both non-flashing and flash-boiling conditions. Predictions from the novel coupling approach are validated with the experimental observations. This coupling approach requires running an Eulerian primary atomization model, i.e., the $\Sigma - Y$ model, to initialize the Lagrangian parcels for the secondary atomization process. Hence, this coupling approach does not depend upon the linearized instability models to simulate the dense spray region.

TABLE OF CONTENTS

LIST OF TABLES

LIST OF FIGURES

CHAPTER 1

INTRODUCTION

Since the age of the industrial revolution, the internal combustion engine(ICE) has been one of the greatest inventions. Numerous engineers and researchers have contributed to its continuous improvement with their growing knowledge of thermodynamics and combustion. ICEs have seen a wide range of applications in utility devices (pumps, mowers, generators, etc.), as well as all types of means of transportation (tractors, propeller aircraft, ships, passenger cars, and other on/off road vehicles). ICEs have revolutionized the transportation sector due to their high thermal efficiency and high power output to volume ratio.

The wide use of ICEs can be linked to the economic growth and the industrialization of the modern world. In the early days, people were not concerned about the size and efficiency of the engines. However, the situation has changed drastically in the last decades. Nowadays ICEs are fighting with electrical motors to coexist in the automotive world.

We live in a world where the fossil fuel supply is finite and the population grows every day resulting in a higher energy demand. According to a study by Exxon [3] the global energy demand is expected to grow by 25% in the year 2040. One-third of this requirement is expected to be met by fossil fuels. Increasing usage of fossil fuel has given rise to a growing concern over pollution and climate change, which has compelled engineers to develop cleaner and more efficient means of power generation.

Although ICEs have undergone a series of development, there is still a lot of room for improvement. Under ideal conditions, modern gasoline engines have an efficiency of 30%, which gets lower in real-world conditions. Furthermore, combustion of fossil fuel in direct injection engines (DI) produces nitrogen oxides (NOx), unburnt hydrocarbons (UHC), carbon monoxide(CO), and other greenhouse gases. As the global emission and fuel economy regulations continue to tighten, automakers are working diligently to develop cleaner and more efficient engines.

Design of a better and cleaner combustion system is essential for the development of cleaner and efficient vehicles. An important step in this designing process is to optimize the fuel injection systems. They are active area of research, as they determine the characteristics and distribution of the air-fuel mixture through the combustion cycles. The current work addresses some of the most pertinent questions of the fuel injection and spray atomization research, especially in the context of gasoline direct injection(GDI) systems.

1.1 Gasoline Direct Injection

Gasoline Direct Injection is considered to be a more advanced version of the conventional multi-port fuel injection(MPFI) system, where the fuel is directly injected into the combustion chamber instead of the intake ports. In recent years, global auto manufacturers have preferred GDI systems over the MPFI systems due to improved combustion efficiencies, reduced emissions and increased fuel economy in ICEs applications [75], [244]. The injection pressure of GDI systems is higher as compared to that of the MPFI systems. Consequently, it leads to better atomization of the fuel entering into the combustion chambers, thus yielding a higher rate of vaporization.

Usually, a spontaneous phase change process known as flash-boiling is observed in gasoline injection systems due to the volatile nature of the gasoline fuel, i.e., relatively high vapor pressure at low temperature. Flash-boiling is encountered when a superheated liquid is subjected to sudden depressurization. This phase change process is governed by a finite rate of heat transfer. Flash-boiling phenomena are usually encountered in the gasoline engines under low and part load conditions. Although flash-boiling phenomena have been widely witnessed in several chemical engineering and nuclear engineering applications, their use as an effective atomization mechanism in ICEs is relatively new. Hence, the effects of flash-boiling phenoemna on the gasoline spray are not completely understood and constitute the essence of this dissertation work.

1.2 Overview of the current research

The current report for my doctoral dissertation consists of a detailed literature survey in the flash-boiling atomization field and descriptions of my research observations.

- In Chapter 2 of this dissertation, the underlying physics of the flash-boiling process will be discussed. Additionally, different modeling approaches for the flash-boiling process and their results will be reviewed. This chapter will also include some of the prominent experimental observations of flash-boiling phenomena in the spray applications.
- Chapter 3 will review the different atomization modeling approaches and their advantages and shortcomings.
- Chapter 4 will include a detailed description of the governing equations for the in-house developed CFD code for internal flow modeling. Additionally, the novel sealing algorithm and the primary atomization model will be discussed.
- In Chapter 5 of this dissertation, observations for a first of kind multiple injection cycle simulation for the GDI injector have been presented.
- In Chapter 6 of this dissertation, the sealing algorithm will be applied to study the end of injection (EOI) behaviors of the GDI injector.

- In chapter 7 of this dissertation, a qualitative analysis will be performed to understand the tip-wetting behaviors under both non-flashing and flashing conditions.

- Hole-to-hole variations in the mass flow rate and the momentum rate predictions will be discussed in Chapter 8. The chapter will also include some of the quasi-steady state analysis of the near-nozzle predictions.

- In chapter 9, a novel plume-based coupling approach will be developed. Predictions from this approach will be validated with the available experimental data for both flashing and non-flashing conditions.

- In chapter 10, a pilot study to include the surface tension based models in the in-house HRMFoam solver will be performed. The chapter will also summarize the current findings of this dissertation.

- Based on the summary and the current findings of this dissertation, a few future research recommendations will be proposed in chapter 11.

CHAPTER 2

FLASH BOILING: A REVIEW

The atomization process involves disintegration of bulk liquid mass into small droplets in a gaseous environment. It has wide industrial applications ranging from internal combustion engines, gas turbine engines, industrial furnaces, drug delivery spray, spray coating of surface materials to food processing industries. Among these applications, ICEs demand effective combustion of tiny droplets produced by the atomization processes. Furthermore, effective combustion is driven by the evaporation rate of droplets with less effective surface area. These droplets are produced by the successful break up of liquid jets or annular liquid sheets during atomization processes.

Hence, liquid jet and sheet break up has been the soul of the atomization research over the past century. All conventional atomizers (centrifugal, rotary, pressure swirl, ultrasonic, piezoelectric atomizers, etc.) use mechanical energy to disintegrate the continuous bulk liquid phase into a dispersed phase. However, some atomizers ensure the disintegration of the bulk liquid by forcing a biphasic flow, i.e., bubbly mixture through orifices. In effervescent atomizers, the bubbly mixture is ensured by introducing external atomizing gases into the liquid. However, researchers have faced difficulties in controlling the spray parameters of effervescent atomizers. The other way of ensuring the biphasic flow is by super heating either the bulk liquid or a specific liquid component of the mixture. The following discussions will explore the flash-boiling atomization methods.

The liquid is said to be super heated when it is at a temperature above the saturation condition corresponding to its pressure. As shown in the Figure 2.1, liquid can gain its super heat in two different ways, i.e., either being heated (from O to A) at a constant pressure or by depressurization (from O to B). Vaporization caused by rapid depressurization can be classified as either cavitation or flash boiling based upon the ambient pressure or injection temperature level.

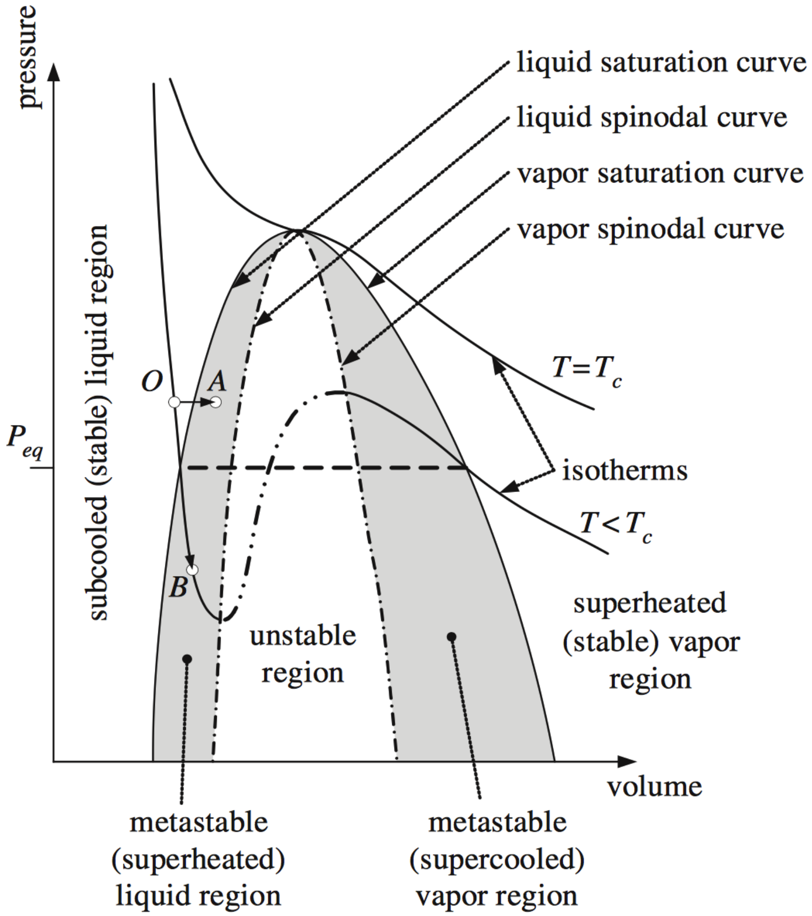

Figure 2.1: Pressure vs. volume curve, showing the thermodynamics of flashing boiling. Image from [201].

Cavitation is usually encountered in the regions of low temperature or low pressure. In these regions, vapor density is low and a small amount of super heat is sufficient enough to initiate the vaporization process. The cavitating bubble are short lived, as they collapse within micro-seconds. On the contrary, flash-boiling is a highly thermal non-equilibrium process and is witnessed in the regions with high temperature and pressure conditions. Flash-boiling is usually encountered when the downstream pressure is lesser than the liquid vapor pressure. Thus, the vapor bubbles generated locally in the upstream regions do not collapse; rather, they stay intact and expand in the downstream.

In flowing systems, depressurization might occur due to changes in the channel flow area, for example, the diverging sections of converging diverging nozzles. Sudden pressure release due to the valve opening/closing or some crack development in liquid containers can also lead to the depressurization process. The phase change phenomena can also occur because of the hydro static pressure drop in vertical flow paths.

Flash-boiling has a decisive presence in many industrial or technical applications. For instance, desalination of sea water using multi-stage flash distillation [211], impulse drying of grapes to improve wine quality [196], and paper pulp production [234]. In many chemical and industrial applications, accidental release of a liquefied hazardous chemical or contaminant can potentially lead to fatal injuries and serious environmental pollution. Under such conditions, the nature of the release i.e., either sub-cooled or super-heated is the key to quantify the hazard due to the leakage [43]. In the nuclear industry, the depressurization problem is associated with the hypothetical Loss of Coolant Accident(LOCA) of pressurized water. When uncontrolled, such scenarios can be hazardous for human lives and the environment. Hence, a thorough understanding of the flash-boiling process is also essential in addressing such issues.

The ability to produce rapid phase change has motivated the use of flash-boiling sprays in the cooling of hot space shuttle parts [6], [7]. Flash-boiling of geothermal fluids have been in use for the power generation in water-based geothermal power plants [54], [205]. Lately, flash atomization has also witnessed applications in printing industries and pharmaceutical sprays because of its ability to produce fine spray. In pharmaceutical sprays, large droplets can lead to oral thrush, cough and bronchospasm [227].

With growing concerns of global warming and climate change and the subsequent tightening of the emission norms, design of efficient spray combustion systems has become essential in automotive and aerospace industries. Sprays formed by flash-boiling processes are usually accompanied by droplets of smaller mean diameter, higher homogeneity, wider cone angles and shorter penetration depth compared to the sprays formed by the mechanical means for the same range of operating pressure. Flash-boiling sprays have the ability to provide the desired sprays for combustion systems at low injection pressure ranges. Besides, flashing is also known to occur in the engine start-up stages in the case of liquid propellant based rocket engines [99] and also during the idle and low-speed conditions in gasoline engines [12], [240]. Irrespective of being subjected to a great deal of scrutiny both experimentally and theoretically, the application of flash-boiling as a primary atomization mechanism is still not understood completely.

In the following sections, some prominent experiments, modeling procedures, and CFD-studies especially in the context of the application of flash-boiling as an atomization mechanism in automotive fuel injectors are reviewed.

2.1 Physics of flash-boiling and theoretical modeling

From a physical point of view, the two-phase flow with mass and heat transfer, i.e, the boiling flow, is more complicated compared to the single phase flow. One of the many challenges is to understand the mechanism of bubble formation in pure liquid and to describe the rapid transition from the pure liquid state to the vapor-liquid mixture.

Hence, understanding the complete physics involved in the flash-boiling process is exacting. The inception of flashing in an initially sub-cooled liquid occurs when its super-heat limit is reached. The maximum degree of attainable liquid super-heat or pressure undershoot determines the intensity of the subsequent boiling process. The isothermal pressure drop, shown by the line OB in Fig. 2.1, corresponds to a superheated condition of the liquid. It implies that at a given temperature, the liquid has a pressure that is lower than its saturation pressure. Whereas, line OA in Fig. 2.1 refers to a scenario where the liquid temperature is more than its boiling temperature at a given pressure. The minima of the isotherms in the P-V diagram is given by $\dfrac{\partial P}{\partial V} = 0$, which equivalently means that the isothermal compressibility ,$K_T \rightarrow \infty$. The locus of such points is called the liquid spinodal curve. The condition of stability of pure fluids require the isothermal compressibility to be a positive number. Thus, the spinodal curve determines the theoretical thermodynamics extent to which the liquid can be brought without any vaporization. Beyond this threshold, the pure liquid ceases to exist and will undergo spontaneous phase change as a reaction to any significant perturbation, for example, rapid pressure drop. The region bounded by the liquid saturation curve and the liquid spinodal curve is known as the metastable liquid region.

Furthermore, the spinodal curve represents a fictional limit which can never be verified experimentally, because the liquid always starts to flash-boil in experiments before it reaches this limit. Therefore, it is often replaced by the empirical kinetic homogeneous nucleation limit, which can be observed experimentally. Lienhard and Karimi [**?**] have observed this limit to lie close to the spinodal curve. However, the experiments for achieving the homogeneous nucleation limit must be performed in carefully controlled laboratory conditions, free from impurities. That includes the liquid is free from any impurities and the experimental vessel is perfectly clean to avoid any wall effects. Otherwise, the meta-stable liquid undergoes phase change before reaching the homogeneous nucleation limit. The limit of such nucleation process is defined by the heterogeneous nucleation limit curve, which lies between the liquid saturation curve and the homogeneous nucleation limit curve. In Fig. 2.2, the blue dashed line represents the homogeneous nucleation limit, whereas the red dashed line represents the heterogeneous nucleation limit. This process of rapid/spontaneous phase change in a super-heated liquid is termed as flash-boiling and is divided into three stages namely, nucleation, bubble growth and atomization. Each of these processes are described below.

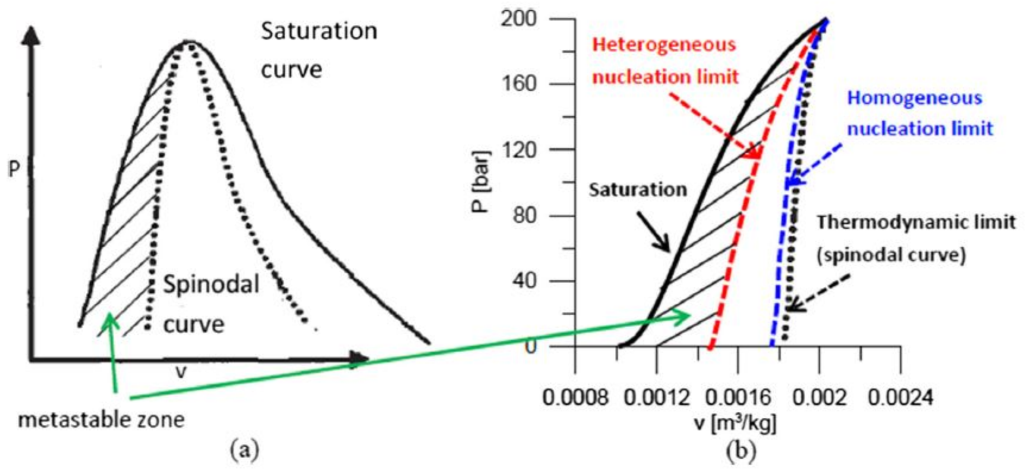

Figure 2.2: Spinodal Curve and attainable super-heat limit of water. Image from [110].

2.1.1 Nucleation

The nucleation process involves formation of bubbles either from the bulk liquid or from other sources such as dissolved gases, suspended particles and/or the imperfections of the orifice walls. Based upon the source of bubble formation, the nucleation process can be broadly classified into homogeneous nucleation and heterogeneous nucleation. Before describing the modeling of different nucleation processes, it is important to understand the equilibrium of dispersed phase and the critical work required to form a stable embryo during the nucleation process, which will be explained in the following section.

2.1.1.1 Equilibrium and stability of a dispersed phase

In the current study, the liquid phase has been referred to as the continuous phase, whereas the gaseous phase as the dispersed phase. The equilibrium condition between the dispersed phase, i.e., the vapor bubbles and the the liquid phase can be examined based upon the thermodynamic and mechanical point of views. Both the equilibrium conditions are well represented by the Clausius-Clapeyron Equation and the Laplace-Kelvin Equation, respectively.

1. The Clausius-Clapeyron Equation:

   The Clausius-Clapeyron equation assumes thermodynamic equilibrium at the vapor-liquid interface. Therefore, the vapor pressure is considered to be saturated. As a result, the correlation shown in the Eqn. 2.1 is dependent upon temperatures.

   $$\left(\frac{dp}{dT}\right)_{sat} = \frac{h_{LG}}{T_{sat}\left(v_{G,sat} - v_{L,sat}\right)} \tag{2.1}$$

   The Eqn. 2.1 is further simiplified into a linearized form, as shown in the Eqn. 2.2.

   $$P_G - P_L = \left(\frac{T_G - T_{sat}}{T_{sat}}\right)\frac{h_{LG}}{\left(v_{G,sat} - v_{L,sat}\right)} \tag{2.2}$$

   In Eqn. 2.1 and 2.2, T_G and T_{sat} are the vapor temperature and saturated liquid temperature, respectively, i.e. $T_G = T_{sat}(P_G), T_{sat} = T_{sat}(P_L)$. Additionally, $v_{G,sat}$ and $v_{L,sat}$ represents the specific volume of the vapor and the liquid, respectively. The heat of vaporization is presented by h_{LG}. Furthermore, P_L and P_G represents the pressure in the liquid and the vapor phase.

   The Clausius-Clapeyron equation assumes a fairly flat interface between phases, hence neglects the surface force. In such cases, thermodynamic equilibrium can exist between the phases , if the two phases are of equal temperature, pressure and chemical potential.

2. The Laplace-Kelvin Equation:

   For a dispersed phase, where the interface shape is significant, a mechanical equilibrium needs to be considered in addition to the thermodynamic equilibrium. The pressure difference between the two phases that are in thermodynamic equilibrium is given by the Laplace's equation, represented in Eqn. 2.3.

$$P_G - P_L = \frac{2\sigma}{R_l} \tag{2.3}$$

   In the Eqn. 2.3, σ and R_l represents the surface tension and the radius of curvature, respectively. Under equilibrium conditions, the chemical potential of the two phases must be equal. Using this condition and the linearized Clausius-Clapeyron Equation, Cole et al. [45] developed the following formulation.

$$P_G - P_L = (P_{sat} - P_L)\left(1 - \frac{v_{L,sat}}{v_{G,sat}}\right) \tag{2.4}$$

   The set of Eqns. 2.3 and 2.4 are known as the Laplace-Kelvin equation. It states that a vapor embryo grows only after reaching a critical bubble radius (R_{cr}). The work needed to create the vapor embryo of the critical radius is defined as the critical work (W_{cr}), which is further expressed in the Eqn. 2.5

$$W_{cr} = \frac{4}{3}\pi\sigma R_{cr}^2 = \frac{16\pi\sigma^3}{3(P_{sat} - P_L)^2(1 - \frac{v_L}{v_G})^2} \tag{2.5}$$

   In the Eqn. 2.5, P_{sat} represents the saturation pressure of the liquid. The critical work can further be expressed based on the Gibbs number(Gb), Boltzmann's constant (k) and the liquid temperature (T), as shown in the Eqn. 2.6

$$Gb = \frac{W_{cr}}{kT} \tag{2.6}$$

2.1.1.2 Modeling

As discussed earlier, the nucleation process can be subdivided into homogeneous nucleation and heterogeneous nucleation.

- Homogeneous nucleation: The homogeneous nucleation, also referred to as bulk nucleation, is usually encountered at high degrees of superheat and at random locations in the bulk liquid. Fluctuations of the bulk liquid density at the molecular level are usually the primary reasons behind the bulk nucleation phenomena. Blander and Katz [32] observed bubble nucleation to occur when the degree of superheat is as high as 90% of the liquid's critical temperature. Furthermore, the kinetic theory of homogeneous nucleation is based on the assumption that at a given time, the number of nuclei growing to a visible size is proportional to the number of nuclei formed. Using this theory, Skripov [206] formulated the set of Eqns. 2.7 and 2.8 to predict the number of bubbles generated per unit volume per unit time(J_{CNT}).

  $$J_{CNT} = J_0 exp\left(- \frac{W_{cr}}{kT} \right) \tag{2.7}$$

  $$J_0 = N_M B' \tag{2.8}$$

  Where, N_M is the number density of the liquid molecules and is calculated based upon the molecular weight of the liquid. He also suggested that the molecular interactions per second (B') to be a constant i.e. 10^{12}. On the contrary, Blander and Katz [32] have suggested a widely accepted formulation for J_0, mentioned in the Eqn. 2.9.

  $$J_0 = N_M \sqrt{\frac{2\sigma}{\pi m_M B}} \tag{2.9}$$

  In the Eqn. 2.9, $B = 1$ for cavitating conditions, otherwise $B = 2/3$ [32]. However, the above expression ignores the correlation between successive events which impacts the number of vapor embryos present in a cluster at a particular instant [89]. Hence, a number of modifications to the classical nucleation theory have been suggested [114], [169], and [90].

- Heterogeneous nucleation:

  In real world scenarios, neither the bulk liquid is ever free of impurities, nor the nozzle walls of the nozzles are perfectly smooth. Hence, bubble generation in the bulk liquid is observed at a much lower degree of superheat compared to the homogeneous nucleation. This nucleation process is known as heterogeneous nucleation. The heterogeneous nucleation process is characterized by lower bubble radius compared to the homogeneous nucleation [201]. Unlike the homogeneous nucleation, the heterogeneous nucleation limit curve is observed to be farther from the spinodal curve and closer to the saturation curve. This is observed because the depressurization during the heterogeneous nucleation stops well before reaching the spinodal curve [161]. During the heterogeneous nucleation (flashing process), rapid nucleation and bubble growth are encountered at relatively low superheat and tend to increase the pressure due to the expansion of vapor bubbles, resulting in a halt in the depressurization process.

  Heterogeneous nucleation necessitates a nucleation mechanism due to thermodynamic fluctuations, however, at a much lower value of activation energy. To bridge the gap of activation energy, Alamgir and Lienhard [107] and Skripov[206] introduced a heterogeneity factor ϕ and modified the critical work needed for nucleation. According to them, the nucleation flux($J_{HET,B}$) can be computed based upon the classical homogeneous nucleation theory, as shown below.

$$J_{HET,B} = J_0 exp\left(- \frac{W_{cr}\phi}{kT} \right) \tag{2.10}$$

Numerous studies have been conducted on bubble nucleation during surface boiling. Among them, Bankoff [20] studied the theoretical thermodynamic aspects of nucleation processes and found the energy required to initiate the bubble nucleation is highly dependent upon the shape of the geometrical surface, i.e., whether the surface has a cavity, a flat plane, or a protruding point. Blander and Katz have proposed a model for heterogeneous nucleation flux ($J_{HET,smoothwall}$) for a smooth surface mentioned in Eqn. 2.11 . They introduced an extra geometrical factor η, which is a function of solid-liquid contact angle.

$$J_{HET,smoothwall} = N_M^{2/3}.\eta.\sqrt{\frac{2\sigma}{\pi m_M B\phi}}.exp\bigg(-\frac{W_{cr}\phi}{k_B T_l}\bigg) \tag{2.11}$$

Subsequently, several other models have been developed to account for the surface roughness and cavity of the wall.

2.1.2 Bubble growth

Once bubbles which meet all the stability criteria are created, their growth period initiates. One of the early and most popular theories which explains the bubble growth process, is the mono-layer theory. Based on this theory, a bubble that is submerged in a superheat thermal boundary layer removes that layer locally. Consequently, the instantaneous superheat degree is diminished [56]. The vapor growth phenomena are nonlinear problems, as they involve moving boundaries and a strong coupling between the liquid momentum and the heat transfer through the interface. Hence, it is difficult to get analytical expressions for the same without sufficient assumptions.

2.1.2.1 Modeling

The bubble growth period can be subdivided into three sub regimes [16]. The initial bubble growth regime is known as the surface tension regime, where the forces acting on bubbles are in equilibrium. Hence, the bubble growth rate is slow. Although the initial period is very short, disregarding it leads to overpredictions of the bubble growth rate for subsequent phases [21].

As the bubble grows, the effect of surface tension diminishes and the growth rate is limited by the momentum transfer, i.e., how fast the bubble can push the surrounding liquid. This growth regime is known as the inertia regime. During this regime, the bubble attains its maximum velocity. Rayleigh [168] first came up with a model stated in the Eqn. 2.12 to calculate the bubble growth rate for a spherical bubble without accounting for the surface tension and viscosity.

$$R\ddot{R} + \frac{3}{2}\dot{R}^2 = \frac{\mathrm{P}_v - \mathrm{P}_{amb.}}{\rho_l}. \tag{2.12}$$

In Eqn. 2.12, R, $\dot{R}$, and $\ddot{R}$ represent the bubble radius , its first and second derivatives with respect to time, respectively. Further, P_v, P_{amb}, and ρ_l represent the pressure inside the vapor bubble, ambient pressure, and the liquid density, respectively. Eqn. 2.12 has since been generalized by including the effects of surface tension and viscosity by Plasset and Zwick [162] and the resulting relation is often called the Rayleigh-Plesset equation [37], given by

$$R\ddot{R} + \frac{3}{2}\dot{R}^2 = \frac{1}{\rho_l}\Big(\mathrm{P}_v - \mathrm{P}_{amb.} + \frac{2\sigma}{R} - \frac{4\mu}{R}\dot{R}\Big). \tag{2.13}$$

The final stage of the bubble growth happens to be the slowest of all stages and is dominated and restricted by the thermal diffusion through the bubble-liquid interface. Mikic et al. [125] were the first to develop a correlation by successfully coupling the effects of inertia and heat transfer by neglecting the effect of the bubble growth acceleration term ($\ddot{R}$). Their correlation suffers from the assumption of the linearized Clausius-Clapeyron equation that describes the relationship between the vapor pressure, temperature and the constant vapor density. This assumption of the linearized relation between the vapor pressure and the constant vapor density is difficult to justify in the case of thermal non-equilibrium. Hence, disagreements between experiments and model predictions are observed for conditions with large initial super-heat, or conditions where the variations in the vapor density are significant. This anomaly was addressed by Miyatake et al. [126] who improved on the works of Theofanous and Patel [220] by incorporating the $\ddot{R}$ term and also by accounting for the nonlinear relation between the vapor pressure and the temperature. They also incorporated the growth rate during the surface tension regime. Furthermore, Riznic et al. [179] observed the bubble growth rate to be higher in flowing systems compared to static systems due to the relative velocity between the phases. Their correlation based upon the relative velocity between phases (v_r) is mentioned below.

$$\left(\dot{R}\right)_{v_r \neq 0} = \left(\dot{R}\right)_{v_r = 0} \sqrt{1 + \frac{2}{3}\frac{v_r t}{R}} \tag{2.14}$$

2.2 Modeling of flashing flows

Since the middle of the last century, a significant amount of research has been dedicated to the modeling of two-phase flow mixtures produced by flashing flows. Owing to the biphasic nature of flow, thermodynamic and hydrodynamic nonequilibrium pose the biggest challenge to the accurate modeling of the underlying physics while representing practical scenarios. Modeling the velocity slip and heat transfer between phases, vapor generation, and their interactions add complexity to the posed problem. Based upon the interactions between phases, the flow regime can be divided into bubbly flow, churn flow, and slug flow. In many industrial applications, there exist no distinct boundaries between the different flow regimes, which is again an extra disadvantage in the modelling of flash-boiling process. Hence, many researchers have assumed different flow regimes as per their convenience to develop their models, which hinders the universality of these models. The early flash-boiling models were focused to estimate the mass flow rate and discharge coefficient without revealing much details about the physics of the flow.

Based upon the hydrodynamic aspects, the flash-boiling models can be classified into homogeneous flow model, separated flow model, and two fluid models, which will be explained below [201], [178], [46].

1. Homogeneous flow model: The model assumes hydrodynamic equilibrium between phases, that implies both the phases are assumed to have equal velocity and pressure. These assumptions also satisfy the conditions of rapid momentum and mass exchange. Consequently, the resulting governing equations resemble those for a single fluid. The fluid properties such as density, viscosity, thermal conductivity etc. for the mixture are obtained as a result of either mass or volume averaging. The homogeneous flow model is preferred for the cases where one phase is finely dispersed in the other. However, the model runs into accuracy issues when applied to scenarios with high pressure fluctuations or rapid acceleration.

2. Separated flow model: This model is applied to the cases with high density ratio between the phases or low pressure systems, as the assumption of equal velocities between the phases become erroneous. Hence, the velocities of the phases are relaxed primarily by introducing a slip ratio (ratio of velocities). This is accomplished by solving different momentum equations for both the phases. It also accounts for the drag at the interface due to the relative velocity between the phases, which is often calculated by empirically correlating the interfacial shear stress and the slip ratio or the velocity difference. The drift flux model [84] is a special case of such model, because it predicts void fractions based upon given velocity differences.

3. Two fluid model: The two-fluid model is considered to be a sub-category of multi-fluid models, also known as the 6-equation model. The governing equations consist of two sets of separate equations for continuity, momentum, and

energy. Additional constitutive relations are solved to model the equilibrium and interactions between the phases. Approaches similar to that of the separated flow models are used to model the differences in the velocities of the phases, whereas the differences in the temperatures are solved through an energy balance equation. The differences in temperatures arise due to the time lag between the phase change process and the flow inertia. The interfacial phenomena, such as mass flux exchange due to evaporation or condensation, changes in interfacial energy because of the surface tension dependency on temperature, and interfacial deformations due to rapid depressurization in the nozzles, give rise to the pressure non-equilibrium. Due to the above complexities, pressure non-equilibrium is often ignored while modeling the two-phase flows. However, the non-equilibrium becomes significant when the velocity either approaches or exceeds the two-phase speed of sound. The model also suffers from empiricism problems for complex flow situations where heat, mass, and momentum exchange exist simultaneously [178]. To capture more underlying physics of flash-boiling through this class of model, one needs to add more constitutive relations. These constitutive relations are often non-trivial and modeling them properly is the biggest challenge one faces.

In the majority of industrial applications, the vapor phase is finely dispersed in the liquid phase in the case of flash-boiling flows. Thus, they are modeled as homogeneous flows hydro-dynamically with an appropriate thermal nonequilibrium model acting as a constitutive relation to close governing equations [201]. Hence, the primary objective of a flash-boiling model is to account for the thermal nonequilibrium between the phases by estimating nucleation and vapor generation. Based upon the vapor generation model, the existing models can further be classified into three categories, i.e., bubble dynamics-based models, thermodynamic rate-based models, and interfacial exchange model.

2.2.1 Bubble dynamic based model

Bubble dynamics based models for vapor generation include submodels for nucleation, bubble growth rate, and bubble number density. Models for the first two parts have already been explained in the earlier sections 2.1.1.2 and 2.1.2.1, respectively.

The bubble number density, denoted as N_B, affects the interfacial area per unit volume in bubbly flow. Different correlations for N_B have been developed by Lienhard et al.[107], Riznic and Ishii [179], and by Shin and Jones [204]. However, these models include several empirical constants.

The model developed by Kishii et al.[94] moved away from the empiricism of calculating the local number density by solving a conservation equation in a control volume approach , and is represented in the Eqn. 2.15.

$$\frac{\partial N_B}{\partial t} + \frac{\partial (N_B U)}{\partial x} = \Psi, \tag{2.15}$$

In the Eqn. 2.15, U is the velocity, and Ψ is the source term which is evaluated by accounting for the change in the bubble number density due to different nucleation processes and bubble interactions. Another approach, worthy of mention, corresponds to the work of Elias and Chambre [64, 65] who solved an equation similar to the Eqn. 2.15 for the concentration function N_{R_B}. It is a distribution function for the bubble number density lying between an interval of bubble radius. The temporal growth of the concentration function of Elias and Chambre [64, 65], is governed by the bubble growth, given by:

$$-\frac{\partial N_{R_B}}{\partial t} = \frac{\partial}{\partial R}\Big(N_{R_B}\frac{DR}{Dt}\Big) \tag{2.16}$$

Furthermore, the vapor void fraction α is determined by using the bubble radius (R) predicted by the bubble growth model and the bubble number density as shown in the Eqn. 2.17.

$$\alpha = \frac{4\pi}{3} R^3 N_B. \tag{2.17}$$

Bubble dynamics based models suffer from several levels of empiricism, lack of general validity, and are often tuned to replicate the available experimental data. In the past, these models have assumed thermal equilibrium while being applied to one-dimensional homogeneous flows. However, recently these models have been applied to multidimensional CFD codes as submodels to describe the flash-boiling processes [120], [87] and [109].

The assumption of thermal equilibrium can only be applied to processes with very fast heat transfer rate and driven by the fluid temperature. In the case of a cold fluid undergoing the phase change due to depressurization, the vapor density in the bubble is insignificant when compared to the liquid density. Therefore, the activation energy of vaporization is insignificant. This is usually encountered in the case of cavitating flows [93]. However, the vapor density is much higher in the case of superheated bubbles, thus limiting the rate of heat transfer. Hence, it renders the assumption of thermal equilibrium imprecise for flash-boiling flows. Therefore, thermal nonequilibrium becomes an important characteristic of flash-boiling models to achieve better accuracy. A few notable nonequilibrium models based on the bubble dynamics approach include the ones by Blinkov et al. [33], Elias et al. [64] and Ritcher [178]. However, these models are limited only to one-dimensional flows, to date.

2.2.2 Thermodynamic rate based models

From the above discussions, it is evident that the majority of the bubble dynamics-based models are semianalytic in nature and have a large degree of empiricism. Determining the void fraction (α) in such conditions is a cumbersome process. The accuracy of these models also depends upon the reliable analytical derivation of the bubble growth rate. To avoid these complexities, another class of models, which are also empirical in nature, are often used to determine the vapor generation rate. These models are termed as relaxation models, since they account for the transition of the system from a state of thermodynamic nonequilibrium to equilibrium on the basis of the vapor mass fraction.

Homogeneous Equilibrium Model (HEM), developed by Wallis et al. [228], models one extreme of this relaxation process, where the phase change is instantaneous due to an extremely fast heat transfer rate. HEM predicts the critical mass flow rate accurately in the case of long pipes where the fluid has enough time to approach the state of equilibrium. However, this model fails when applied to the flow in short pipes or orifices or processes with very slow heat transfer rate. Flow through such a system is so fast that the time required for the phase change process to reach an equilibrium state is insufficient. On the contrary, the Homogeneous Frozen Model(HFM) proposed by Henry and Fauske [76] is an empirical nonequilibrium model which is appropriate for short channel flows. Whereas, the Homogeneous Relaxation Model (HRM) models the scenarios which lie in between the two extremes modeled by the HEM and HFM.

HRM was originally developed by Bilicki et al. [30] for one-dimensional two-phase flows to model the complex process of relaxation by determining the total derivative of the quality (x), represented in the Eqn. 2.18.

$$\frac{Dx}{Dt} = \frac{\bar{x} - x}{\Theta} \tag{2.18}$$

In the Eqn. 2.18, $\bar{x}$ refers to the equilibrium vapor mass fraction and is a function of the local and saturation enthalpies of the liquid. It is again determined by using the Eqn. 2.20. Furthermore, x is the instantaneous mass fraction of the vapor, and is a function of the void fraction (α), vapor density (ρ_v) and the mixture density (ρ), as shown in the Eqn. 2.19. Finally, Θ is the relaxation time.

$$x = \frac{\alpha \rho_v}{\rho} \tag{2.19}$$

$$\bar{x} = \frac{h - h_l}{h_v - h_l} \tag{2.20}$$

In the Eqn. 2.20, h, h_l, h_v are the local enthalpies of the mixture, liquid, and vapor, respectively. The void fraction in turn depends upon the local density of the mixture (ρ), vapor (ρ_v) and liquid (ρ_l) and is given by Eqn. 2.21.

$$\alpha = \frac{\rho_l - \rho}{\rho_l - \rho_v} \tag{2.21}$$

Downar-Zaploski et al. [58] developed a correlation for the relaxation time (Θ) by performing an empirical fit of their experimental observations of flashing water flows in long pipes as shown in the Eqn. 2.22.

$$\Theta = \Theta_0 \alpha^a \psi^b \tag{2.22}$$

In the Eqn. 2.22, ψ is the non dimensional pressure, where $\Theta_0, a, and\ b$ are constants which have different values for high pressure and low pressure applications as represented in the Eqn. 2.23 and 2.24 .

For lower pressure, i.e., $P \leq 10\ bar$, the recommended coefficients are:

$$\Theta_0 = 6.51 \times 10^{-4} s, a = -0.257, b = -2.24, \psi = \frac{P_{sat} - P}{P_{sat}} \tag{2.23}$$

For higher pressure, i.e. $P \geq 10\ bar$, the recommended coefficients are:

$$\Theta_0 = 3.87 \times 10^{-7} s, a = -0.54, b = -1.76, \psi = \frac{P_{sat} - P}{P_{cr} - P_{sat}} \tag{2.24}$$

HRM overcomes the need for intricate multistep modeling dictated by bubble dynamics based methods to determine the vapor generation. In HRM, α determines the initial vapor generation due to phase change, whereas the non-dimensional pressure term ψ is indicative of the amount of energy available for additional vapor generation due to superheat. The dependence of α on Θ corroborates the fact that the initial vapor generation rate in the domain provides surface area for additional vapor formation [135].

The one-dimensional HRM is appropriate for flow through pipes with large length-to diameter ratios. In these pipes, the axial variation of the flow parameters determine the thermal-hydraulic behavior of the jet, but the effects of cross-sectional parameters are insignificant. However, the cross-sectional parameters become significant when the length and diameters of the nozzles are of the same order. Such conditions necessitate the need for multidimensional vapor generation models.

Schmidt et al. [191], [189] were the first one to extend the one-dimensional HRM to two-dimensional forms and later to the multi-dimensional form in an Eulerian frame of reference. As shown in the Eqn. 2.25, they used the chain rule to express the total derivative of the density instead of the conventional equation of state. This expression allows the pressure to respond to the compressibility of the individual phases and the phase change phenomena.

$$\frac{D\rho}{Dt} = \left.\frac{\partial\rho}{\partial p}\right|_{x,h}\frac{Dp}{Dt} + \left.\frac{\partial\rho}{\partial x}\right|_{p,h}\frac{Dx}{Dt} + \left.\frac{\partial\rho}{\partial h}\right|_{p,x}\frac{Dh}{Dt}. \tag{2.25}$$

2.2.3 Interfacial exchange based model

One of the popular approaches is to postulate that the phase change process is induced by the interphase heat transfer. The vapor generation rate (Γ_g) during the evaporation process is related to the heat flux through the interface ($\dot{q}$) via Eqn. 2.26.

$$\Gamma_g = A_i\frac{\dot{q}}{L} \tag{2.26}$$

In the Eqn. 2.26, A_i represents the interfacial area density, which requires further modeling according to the flow regime .

Estimating the heat transfer coefficient on the liquid side is the biggest challenge one faces while evaluating the vapor generation rate using the two-fluid approach. Hence, the applicability of these sophisticated methods is restrained largely by the reliability of closure models which represent interactions between the phases.

2.3 Experimental studies

The process of flash-boiling atomization has been studied experimentally for several decades now. The current section reviews some of the early experimental investigations to classify the flash-boiling process. It also discusses some of the experimental studies performed to gain insight into the effects of flash boiling on the performance parameters of plain/straight nozzles and fuel injectors.

2.3.1 Flash-boiling mechanism

Brown and York [38] were the first to report flash-boiling atomization while performing experiments with water and Freon-11 in straight nozzles of different length to diameter ratios. They also concluded that flash boiling is an effective mode of atomization without the need of high pressure and high velocities.

Wildgen and Straub [232] studied flashing water jets and identified two modes of flashing, i.e., particle boiling and surface boiling. During particle boiling, the bubbles in the water jets are formed due to the presence of suspended particles. However, surface boiling is a wall phenomenon which is observed in the absence of suspended particles. According to them, the surface boiling or wall boiling occurs only in longer nozzles.

Oza et al. [146][147] observed different regimes of flash boiling while performing experiments in an electromagnetic (poppet) injector with fluids of different volatility, i.e. propane, methanol and indolene. They classified the regimes into internal flashing, when flashing is initiated within the injector, and external flashing, which is external to the nozzle with an intact liquid core surrounded by droplets.

However, Reitz et al. [171] refuted the claims of Oza et al. [146][147] about the internal flashing. He conducted photographical studies to gain further insight into the flash-boiling mechanism in a single-hole cylindrical nozzle. He used water as the working fluid at a constant pressure gradient but at different liquid temperatures. He also observed an intact liquid core upto certain distance from the exit of the nozzle. The length of the liquid core reduced with the increasing inlet temperature. His study was also able to elucidate a decrease in the drop size and mass flow rate with the increase in inlet fluid temperature. Eventually, they observed a vapor-locked phenomenon when the inlet fluid temperature approached its boiling temperature.

Park and Lee [151] also used transparent cylindrical nozzles to investigate the flash-boiling mechanism with water as the test fluid. As they increased the superheat defined by the Eqn. 2.27, they observed different internal flow regimes ranging from bubbly flow, slug flow, to annular flow.

$$\Delta T = T_{inj.} - T_{sat.}(P_{\infty}), \tag{2.27}$$

In the Eqn. 2.27, $T_{inj.}$ is the injection/inlet temperature of the liquid and $T_{sat.}(P_{\infty})$ is the saturation temperature of the fluid corresponding to the chamber pressure. As the degree of superheat increased, the bubbles created near the nozzle wall during the bubbly flow regime started to interact with each other forming slugs of vapor in the liquid core. This regime was classified as the slug flow regime, which later translated into the annular flow regime with an increase in the superheat. In the annular flow regime, a distinct vapor core surrounded by an annular liquid film near the wall is observed. According to Park and Lee [151], slug and/or annular flow regimes can be witnessed in long nozzles at low injection pressure and higher injection temperature compared to that of the bubbly flow. Long nozzles provide longer residence time for the bubbles to grow and coalesce compared to that of short nozzles. Consequently, bubbly flow is observed in short nozzles. Furthermore, slug and annular flow regimes are characterized by larger spray angles and finer droplets in comparison to the bubbly flow. In bubbly flow, small droplets are observed around an intact liquid core. Peter et al. [157] also observed similar effects in the shattering of liquid jets due to different flow regimes.

Kitamura et al. [92] studied the break-up of flashing water and ethanol jets through long straight nozzles. According to their hypothesis, bubble nucleation has negligible effects on the jet break-up process at low superheat and the break-up is dominated by mechanical (aerodynamic) effects. However, the contrary was true for the jet break-up process under high superheats. Furthermore, they were able to arrive at a correlation to determine this transition from a mechanical force-dominated jet break-up to a bubble nucleation dominated jet break-up on the basis of the nondimensional superheat. The nondimensional superheat is expressed by the Jakob number (Ja), as shown in the Eqn. 2.28

$$Ja = \frac{\text{Available sensible heat energy}}{\text{Available latent heat energy}} = \frac{\rho_l C_p \Delta T}{\rho_v h_{fg}} \tag{2.28}$$

Based on the superheat level, Cleary et al. [43] classified the jet break-up regimes into subcooled, transitional, and flare-flashing regimes. In the subcooled regime, the water jet shattered far from the nozzle due to mechanical forces, as shown in the Fig. 2.3A. However, an intact liquid core for a short distance from the exit of the nozzle was observed in the transition regime, as seen in the Fig. 2.3B. This liquid core further shattered into tiny droplets forming an wide spray angle. In the third regime, i.e., in the Fig. 2.3C, Cleary et al. [43] observed violent break-up of the liquid jet immediately after the nozzle exit because of bubble interactions and explosion. This condition was termed as the flare-flashing regime where thermal effects dominated the jet break-up process.

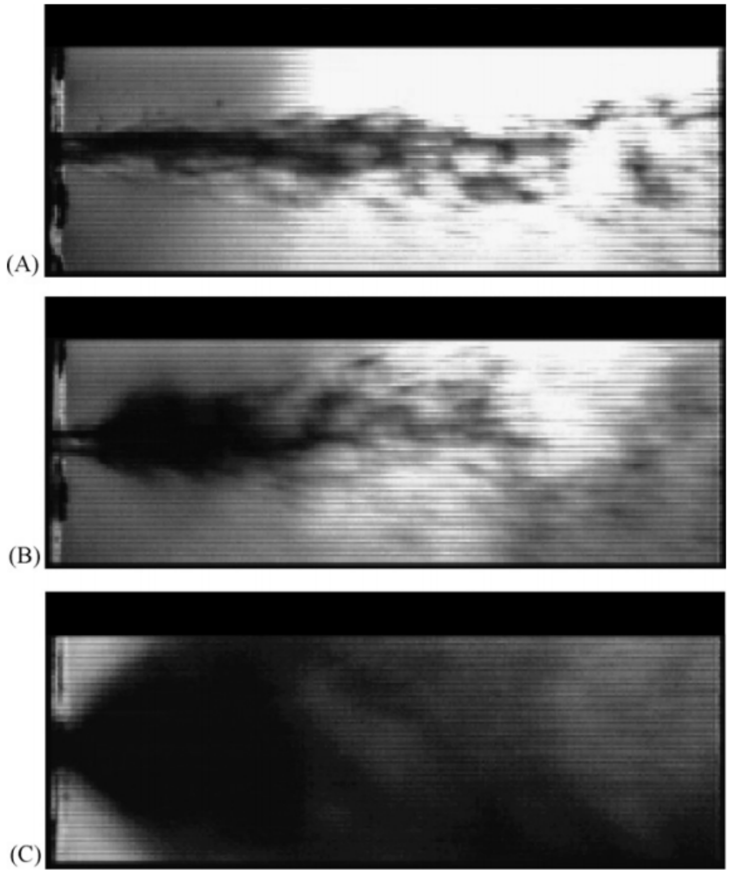

Figure 2.3: Jet transition from mechanical breakup to flare flashing, as identified by Cleary et al. [43]. Image adopted from [43].

Furthermore, from a thermodynamical point of view, Lamanna et al. [100] refuted the earlier definitions of liquid superheat and suggested a new formulation involving pressure ratio. They defined the pressure ratio as the ratio of the saturation pressure of the fuel at the injection temperature to the ambient pressure.

2.3.2 Flash-boiling and fuel injectors

Many of the experiments described in the Sec. 2.3.1 were conducted on plain/straight orifices with water as the test fluid and were successful in identifying the different modes of flash-boiling sprays. However, they convey a little about the spray performance parameters generated by fuel injectors in flash-boiling conditions. Vanderwege et al. [226], and Schmitz et al. [195] conducted experiments in pressure swirl atomizers with gasoline as the test fluid. Their observations threw light on the effects of fuel volatility and nozzle geometry on the spray structures. They concluded that the higher volatile component of the liquid fuel is more susceptible to flash boiling causing disintegration of the liquid jet, resulting in smaller droplets. Further studies by Allen et al. [9] corroborated their observations and concluded that gasoline is more susceptible to early inception of vapor generation than diesel primarily due to its high volatility.

Since then, the focus of flash-boiling studies in the GDI systems has shifted to the valve-covered orifice (VCO) and sac-type injectors. These injectors have been the subject of an immense amount of scrutiny in the past, because of their continued application in diesel injection systems [188]. Flow asymmetry is one of the important features of these injectors. The rotational behavior of this asymmetric flow results in strong vortex cores between the inlet, nozzle and sac area. The low-pressure region in the vortex core results in the string-shaped cavitation. This kind of flow field was initially identified by Arcoumanis et al. [15] in diesel injection and was also observed by Gilles-Birth et al. [71] in their study using gasoline injection through VCO nozzles. However, these studies do not provide any explanation on the coupling or the influence of string-shaped cavitation on flash boiling.

Aleiferis et al. [8, 40, 198] used different hydrocarbon fuels (gasoline, iso-octane, n-pentane, ethanol, and butanol) in an optical injector to study the in-nozzle cavitation and its effects on flash boiling and subsequent spray formation. They identified the higher vapor pressures because of the elevated fuel temperatures to be the culprit behind the intense in-nozzle cavitation. Subsequently, the rigorous expansion and interactions of bubbles led to rigorous flashing in low-pressure environments.

This coupling of cavitation and flash boiling with the effects of the injector geometry resulted in an asymmetric flow with large spray angles. They also elucidated the significant role that the ambient/gas pressure played while deciding the degree of spray superheating. According to them, the cavitation increased the spray angle, but had insignificant effects on improving the spray quality, which was more influenced by the superheating of the fuel. Aleiferis and co-workers further suggested that the saturation pressure of the most volatile component of the mixture should be considered while determining the degree of superheat, a claim that was later refuted by Araneo et al. [13, 14], who suggested that the saturation pressure of the multicomponent fuel is influenced by the saturation pressure of individual fuel components.

Due to the limitations in spray diagnostic techniques, many experimental studies [129, 237, 240, 241] often report the quantitative aspects of the spray, such as the drop size, spray angle, and penetration at several distances from the nozzle exit, where the spray is either thin or dilute. However, the application of these information in spray modeling is a futile exercise, since the effects of flash boiling begin to wane out as we proceed downstream. Zeng et al. [240] were the first to report the effects of flash boiling on the spray plume angle, which increases with the increase in superheat level during the transition regime, but starts decreasing in hard flash-boiling conditions. This difference in trend can be attributed to the improper measurement of the spray width without considering the transition distance from nozzle exit [13]. Recent experimental study by Araneo et al. [13] shows that the spray angle expands in the near field region and starts contracting in the far field for multihole injectors under flash-boiling conditions. Therefore, they have suggested to be careful while considering the transition region, which is a function of the superheat. This also supports some of the past ambiguities observed by Lamanna et al. [100], Wu et al. [235] and Montanaro et al. [130]. Wu et al. [235] have also reported a wider near-nozzle spray for the 2 hole GDI injector compared to the single hole injector. A similar trend for the 3-hole and 6-hole injectors were also observed by Kramer et al. [96]. Khan et al. [91] have reported an adverse effect of the injector opening velocity on the near-nozzle spray width in flashing conditions.

Similarly, there exist ambiguities in the literature of spray penetration measurements. Montanaro et al. [130] found a lesser spray penetration in the flash-boiling condition compared to that in the non-flashing condition. Chen et al. [41] have obtained a similar trend in their novel study of heated tip GDI injectors. Khan et al. [91] found an insignificant effect of the injector opening velocity on the spray penetration under hard flashing conditions. However, Zeng et al. [240] observed favorable effects of the superheating of the fuel on the spray penetration under hard flashing conditions.

Furthermore, experimentalists have observed the spray collapse event for multihole injectors under flashing conditions. It should be noted that the spray collapse event is detrimental to the combustion process. Collapsing sprays are often characterized by narrowing spray width, which prohibits proper air-fuel mixing, resulting in improper combustion and increased emissions. During spray collapse events, multiple spray jets interact with each other to form a single jet of spray. Consequently, the axial spray penetration increases, which could potentially lead to the film formation on the piston head. However, the process of spray collapse and its inception is less understood among the communities and the researchers are of different opinion for the reason of spray collapse inception. Some of these reasons include, but are not limited to, the possibility of a low pressure region in the injector center-line [242], smaller droplets experiencing lesser resistance from the aerodynamic forces [226, 195], nozzle hole configuration [129, 11], and jet-to-jet interactions [96]. Furthermore, Guo et al. [74] suggested jet-to-jet interactions during the flashing condition might induce a local low-pressure region at the injector tip, resulting in the bending of spray plumes towards the center-line of the injector axis. They also suggested that the condensation process inside the spray plumes can also play a significant role in inducing the spray collapse, which needs further validation. Recently, Lacey et al. [97] have found that the nozzle diameter, drill angle, and specific volume of the fuel play an important role in inducing jet-to-jet interaction in multihole injectors, which results in spray collapse.

2.4 CFD study of flash-boiling

The previous section 2.3.2 shows that the majority of experimental studies talk about the effects of flash boiling on external spray characteristics, but the studies on the internal flow behaviors of nozzles and near nozzle characteristics are pretty limited because of the experimental constraints. The near nozzle flow physics are important driving parameters for the external flow characteristics. Hence, many CFD studies try to simulate the near-nozzle behaviors coupled with the internal flow. A few of the prominent CFD studies with a concentration on flash boiling have been discussed in the current section.

Janet et al. [87] applied a bubble dynamics-based two-fluid model to simulate the flow through a converging diverging nozzle in flash-boiling conditions. They also incorporated a heterogeneous wall nucleation model and an interfacial heat transfer model to account for the vapor generation. Their observations of the wall nucleation and axial pressure distribution were in good agreement with the experimental investigations. However, their simulations under predicted the radial distribution of the vapor phase owing to the low bulk interphase mass transfer rate.

Similarly, Liao et al. [109] applied a bubble dynamics-based two-fluid model with a constant bubble number density to simulate the flashing flow through a converging diverging nozzle. They were able to capture the flashing inception with a good agreement with the experiments but predicted a lower pressure undershoot and uniform radial distribution of the vapor phase because of the assumption of constant number density.

The computationally expensive nature of the bubble dynamics models limits their applications in complex fuel injectors. Recently, Shen et al. [200] applied a bubble dynamics-based model to study the flash-boiling spray of a multihole injector without simulating the complete geometry. They were able to predict a low-pressure region near the injector tip resulting in spray collapse.

Schmidt et al. [189] have successfully validated the two-dimensional Homogeneous Relaxation Model against the experiments conducted by Reitz [171] and were able to accurately predict the choking flow and vapor lock phenomena. Since its multidimensional extension, HRM has been successfully applied to the study of flash boiling in pressure swirl atomizers [135], and super-heated jet fuel [105]. Since then, many researchers have successfully simulated the cavitating flow through single-hole and multi-hole diesel injectors [238, 245, 24, 22, 23]. Subsequently, the original capability of HRM code has been improved to simulate the effect of ambient gas on near nozzle flow characteristics by solving an extra transport equation for the mass fraction of the non-condensible gas (NCG) as the third phase. The improved model has been successfully validated against the phase-contrast X-Ray imaging (PCI) of the internal nozzle flow [60] in both the flashing and non-flashing conditions.

Moulai et al. [132], Strek et al. [213], Saha et al. [183, 185] and Baldwin et al. [19] have simulated the flashing and non-flashing sprays through a multihole GDI nozzle for the Spray G target conditions put forward by the Engine Combustion Network(ECN) [1] using the HRM model. Moulai et al. [132] showed the influence of the counterbore and the differences in the gas ingestion process between flashing and non-flashing conditions. Strek et al. [213] compared the hole-to-hole variations in the mass flow rate and density with the X-Ray tomography data. Saha et al. [183] studied the effect of needle lift on the internal flow pattern in both flashing and non-flashing conditions using static grids of different needle elevations. They observed that the flashing flow pattern is more affected by the low needle lift compared to the non-flashing one. Baldwin et al. [19] applied the HRM model to the ECN prescribed GDI injector with a transient needle motion and predicted the string flash boiling and swirling spray with a nonequilibrium thermal core.

2.5 Inferences

The following inferences can be drawn from the review of the various experimental investigations of flash-boiling sprays:

- Flash-boiling significantly reduces the drop size while improving the spray quality.
- Internal flash boiling is primarily observed in long nozzles subjected to higher degrees of superheat.
- The occurrence of cavitation increases the degree of flashing and near nozzle spray width.
- In flash boiling conditions, the near nozzle spray width has a different trend compared to the far nozzle spray width.
- In multihole injectors, an increase in superheat although helpful in reducing the drop size, but is often characterized by spray collapse because of the higher jet-to-jet interactions. Collapsing spray may result in increased spray penetration and may lead to spray impingement on the piston head.

The following can be summarized from the discussion of the modeling aspects of flash-boiling and two-phase flows in general:

- The bubble dynamics-based models suffer from severe empiricism and are often restricted to one-dimensional flow. Mostly, two-fluid models lack the desired accuracy because of the unavailability of proper closure models. These models are computationally expensive and are often considered for simpler geometries.

- Multidimensional modeling is necessary for fuel injectors, primarily to study the influence of the cross-sectional flow parameters.
- Thermodynamic rate-based models can be applied to a range of thermodynamic behaviors, i.e., ranging from equilibrium to frozen flows. These models have been observed to perform better compared to the bubble-dynamics-based models under flash-boiling conditions in automotive spray applications [39].
- Multidimensional nature, a wide range of applicability, and validity of the homogeneous relaxation model (HRM) can be stated as the reasons for claiming that a level of maturity has been achieved in modeling internal nozzles both in diesel and gasoline direct injection systems.

CHAPTER 3

ATOMIZATION MODELS: A REVIEW

The spray and atomization process is a multiphase flow phenomenon, which includes the gas phase as the continuum, whereas the liquid phase is in the form of discrete droplets and ligaments. The kinetic energy of the spray represents the main source for the production of turbulence which governs the microscale air-fuel mixing. The disintegration of the continuous liquid phase occurs when the external disruptive forces such as aerodynamic force, surface shear force, and centrifugal force acting on the liquid surface exceed the surface tension force. This initial breakup process is often termed as primary break-up or primary atomization. Liquid ligaments and large droplets produced during the primary atomization event are unstable and undergo further break-up to form smaller stable droplets. This process is identified as the secondary breakup or secondary atomization.

In traditional fluid mechanics, the spray behaviors are conveniently characterized with several nondimensional parameters, such as: the Liquid Reynolds Number (Re_l), Liquid Weber Number (We_l), Aerodynamic Weber Number (We_g), and the Ohnesorge Number (Oh), as mentioned below.

$$Re_l = \frac{\rho_l u_l d_l}{\mu_l}, We_l = \frac{\rho_l u_l^2 d_l}{\sigma}, We_g = \frac{\rho_g U_{rel}^2 d_l}{\sigma}, Oh = \sqrt{\frac{We_l}{Re_l}} = \frac{\mu_l}{\sqrt{\rho_l \sigma d_l}} \tag{3.1}$$

In Eqn. 3.1, ρ, u, and d represent the density, velocity, and diameter of each phase, respectively. Whereas, the subscripts $_l$ and $_g$ represent the liquid and gaseous phases. Furthermore, U_{rel} represents the relative velocity between the phases.

The primary break-up process can be classified into different regimes based on the previously mentioned nondimensional numbers, as discussed below.

- Rayleigh regime: This regime is usually witnessed for flows with low Reynolds number, where identical droplets are produced. In this regime, the jet disintegration is driven by the surface tension force.

- Aerodynamic regime: At intermediate Reynolds number, the drop formation is influenced by the aerodynamic forces. These forces result in symmetric (first wind-induced mode) and asymmetric (second wind-induced mode) wave growth on the gas-liquid interface leading to jet disintegration.

- Atomization regime: This regime is generally encountered for flows with very high Reynolds number, where the jets get disintegrated immediately after the nozzle exit. The sizes of the resulting droplets are much smaller than the nozzle diameter. All practical automotive sprays fall in this regime, thus, the current thesis explores models for the atomization regime.

Images of the different breakup regimes can be seen in Fig. 3.1.

The atomization regime can be described by two regions, i.e., the dense spray region and the dilute spray region, as shown in Fig. 3.2. The dense spray region is observed close to the nozzle exit, where a mixing layer surrounds the distinct liquid core. The mixing layer consists of liquid ligaments and big unstable droplets, which undergo further break-up processes. As we proceed farther from the exit of the nozzle, the droplets formed from the primary and secondary atomization processes undergo further break-up to form stable droplets. Consequently, the spray region gets wider and sparse. This region is known as the dilute spray region. Droplet evaporation becomes dominant in this region. Computational scientists have put a lot of effort to model these different regions of atomization. A few of the famous approaches are discussed below.

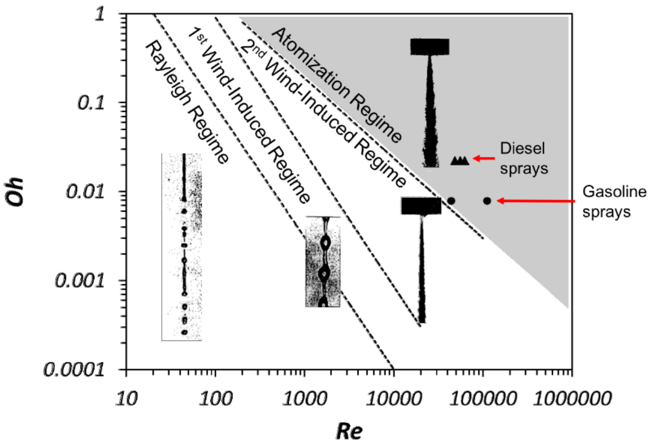

Figure 3.1: Four main regimes of round jet breakup, namely the Rayleigh regime, the first wind-induced regime, the second wind-induced regime, and the atomization regime characterized by the *Oh* number and *Re* number [118]

3.1 Lagrangian-Eulerian methods

As the name suggests, the Lagrangian-Eulerian (LE) approach treats the discrete liquid phase as the Lagrangian particle, whereas the continuous gas phase is treated as the Eulerian phase. Since its inception, the LE approach has become an industrial standard to model the spray dynamics, owing to the simplicity of implementation and high computational efficiency. The LE spray models usually focus on tracing the trajectories of individual droplets or parcels alongside the continuum. However, the suitability of the LE method to the dense spray region is a topic of debate, as these models are droplet oriented [18]. Hence, the formulations for these model don't consider the interactions between neighboring droplets.

3.1.1 Statistical description of the spray equation

Williams [233] was the first one to introduce a statistical description for the stochastic behavior of sprays. The Williams spray equation includes formulations for

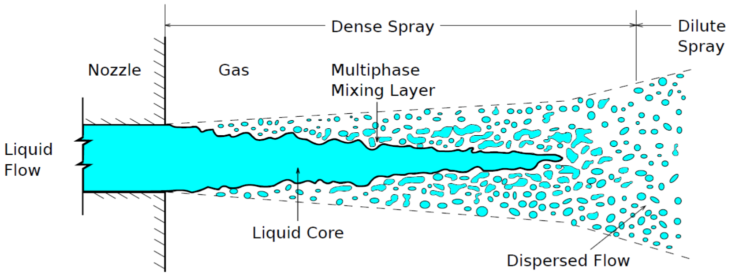

Figure 3.2: The spray regions of an atomizing jet. Image adopted from [66].

the formation of new droplets, their growth rate, collision between droplets, and the aerodynamic forces acting on them. He used a probability density approach to model the spray droplets, represented by the PDF, $f(t, x, y, z)$. Here, f is the probable number of droplets per unit volume in time and space, described by its location ($\mathbf{x}$), velocity ($\mathbf{v}$), radius ($\mathbf{r}$), the temperature (T_d), the deformation parameter (y), and the rate of deformation ($\dot{y}$). The Williams spray equation is mentioned below.

$$\frac{\partial f}{\partial t} + \nabla_x . (f\mathbf{v}) + \nabla_v . (f\dot{\mathbf{v}}) + \frac{\partial (f\dot{\mathbf{r}})}{\partial \mathbf{r}} + \frac{\partial \left(f\dot{T}_d\right)}{\partial T_d} + \frac{\partial (f\dot{y})}{\partial y} + \frac{\partial (f\ddot{y})}{\partial \dot{y}} = \dot{S}_{coll} + \dot{S}_{bu} \quad (3.2)$$

In Eqn. 3.2, $\dot{\mathbf{r}}, \dot{\mathbf{v}}$, and $\dot{T}_d$ are the time rate of change of the droplet radius, droplet velocity and the droplet temperature, respectively. The droplet acceleration ($\dot{\mathbf{v}}$) is further calculated by determining the drag force exerted on the liquid droplets by the continuum. Two notable drag models, i.e., the spherical drag model or the droplet drag model are usually used in engineering applications to calculate the drag force. These models compute the drag force by determining the relative velocities between the droplets and their drag coefficients. Further, $\dot{\mathbf{r}}$ is evaluated by applying the principles of convective heat and mass transfer to the phenomena of evaporation or condensation. Additionally, the fundamentals of energy balance help in determining the $\dot{T_d}$, where the energy supplied to the droplet either raises the droplet temperature or complements the latent heat of vaporization. Drop distortion parameters ($y, \dot{y}$, and $\ddot{y}$) are modeled by the Taylor's drop oscillator model (TAB) [145]. It describes the distortion of the droplets by a forced, damped harmonic oscillator. Here, the liquid viscosity and surface tension act as the damping and restoring forces, respectively, whereas the aerodynamic drag force acts as the forcing term.

The right hand side of the Williams spray equation includes two source terms, i.e., $\dot{S_{coll}}$, and $\dot{S_{bu}}$. The first term, $\dot{S_{coll}}$, accounts for the collision of droplets and the second term, $\dot{S_{bu}}$, considers the droplet break-up process. Two different approaches have been suggested by O'Rourke et al. [145] and Schmidt et al. [193] for modeling the $\dot{S_{coll}}$. The former approach calculates the probability of parcels colliding with other parcels based upon the size, velocity, and number of droplets present inside them [145]. However, the latter approach is based upon the No Time Counter (NTC) method inspired by the gas dynamics fundamentals used in the direct simulations Monte Carlo techniques (DSMC) [31].

The source term, $\dot{S_{bu}}$, accounts for breakups due to both primary and secondary atomization. Several modeling approaches have been proposed to model these breakup phenomena. A few of the popular breakup models are listed below.

- Linearized instability models: This class of models are based on the linear stability theory [170], [25], which assumes the breakup of a liquid jet is dominated by the growth of the most unstable surface waves. Following this assumption, Reitz and Diwakar [172] performed a first order linear analysis of a Kelvin-Helmotz (KH) instability growing on the surface of cylindrical liquid jet penetrating into a quiescent incompressible gaseous environment. Subsequently, they postulated the KH breakup model for the primary atomization regime. This breakup model is also known as the blob injection model as the initial liquid structures are modeled as spherical blobs which have the same size as the diameter of the nozzle.

For the secondary breakup, Patterson and Reitz [154] proposed the Rayleigh-Taylor(RT) breakup model inspired by the theoretical work of Taylor [219], who studied the stability of a liquid-gas interface when subjected to acceleration/deacceleration in the normal direction. According to them [154], the RT instabilities grows when the fluid acceleration is in the opposite direction of the density gradient. Subsequently, Baele and Reitz [25] proposed a hybrid KH-RT model for engine applications, where both the KH and RT breakup model are implemented in a competing manner.

Although, these models are popular among the industry users owing to their simplicity, they don't account for the in-nozzle turbulence or cavitation. Additionally, these models are based on linear theory which has excellent success in predicting the most unstable modes in various canonical two-phase flows, such as liquid sheets, cylindrical jets, annular jets, liquid films, and liquid threads [203], [111], which are often laminar in nature. However, application of these break up models in automotive sprays, which are often characterized by high Reynolds number and very small nozzle diameters is questionable [4].

- Turbulence and cavitation models: Based on the blob injection models, Huh and Gosman [80] proposed a turbulence induced breakup model. According to them, the initial surface perturbations are driven by the turbulent forces within the liquid. Subsequently, Nishimura and Assanis [139] extended the work of Huh and Gosman [80] and postulated a cavitation and turbulence-induced primary breakup model for the diesel spray applications. To account for the cavitation, they introduced parcels containing bubbles to the spray chamber simulations. Furthermore, Som and Aggarwal [207] introduced the KH-Aerodynamic Cavitation Turbulence (KH-ACT) model for the primary atomization regime. However, all these models are still based on the linear stability theory at their core. Additionally, performances of these models are driven by the heavy tuning of the model constants for automotive spray applications. Models tuned for one test condition often fail to accurately predict the spray behaviors in other conditions without tuning of model constants. Hence, these models are not truly predictive in nature and lacks general applicabilities.

- Taylor-Analogy Breakup model (TAB model): This model was first postulated by O'Rourke and Amsden [145] based on the the analogy between and oscillating and distorting droplet and a damped spring mass system. According to this analogy, the external aerodynamic drag forces and the surface tension forces acting on a droplet are equivalent to the external force and the restoring force of a spring mass system, respectively. Whereas, the viscous force of the liquid droplet acts as a damping force. Based on this analogy, the amplitude of oscillations are evaluated for the forced-harmonic oscillator system. Breakup of a parent droplet is only considered when the amplitude of this oscillation exceeds the droplet radius. Post-breakup droplet radius is evaluated by accounting for the energy conservation. Subsequently, Tanner [217] showed under-predictions of droplet diameters for full cone sprays by the TAB model and proposed an enhanced version known as the ETAB model. This model reflects a cascade of droplet breakups where droplet size is reduced in a continuous manner until the child droplets attain stability.

3.2 Direct Numerical Simulation

The Direct Numerical Simulation (DNS) involves solving the governing equations for both phases, with the objective to resolve all necessary length and time scales associated with the flow field. For high pressure injection systems, the flow velocity can approach the speed of sound. Hence, the DNS approach requires to solve the compressible formulation of the Navier-Stokes equation, as shown in the following Eqs. 3.3 and 3.4

$$\nabla.\left(\rho\mathbf{U}\right)=0 \tag{3.3}$$

$$\frac{\partial\rho\mathbf{U}}{\partial t}+\nabla.\left(\rho\mathbf{U}\otimes\mathbf{U}\right)=-\nabla p+\nabla.\left(\mu\left(\nabla\mathbf{U}+\nabla^{T}\mathbf{U}\right)\right)+\rho g+T_{\sigma} \tag{3.4}$$

In the above equation, T_σ is the surface tension force, which is nonzero only on the interface. Hence, it poses a further challenge of tracking the interface in the high-fidelity modeling of the multiphase flow. Furthermore, in spray modeling, the fluid interface might be discontinuous, as it constantly moves, deforms, and breaks apart. Thus, it becomes cumbersome to directly resolve the smallest length scale associated with the droplets and the ligament breakup process. Therefore, two different approaches are generally used to describe the motion and the location of the interface. One of these approaches involves modeling and tracking of the interface with marker particles in a Lagrangian framework. This approach is known as the interface tracking method [177]. However, these marker particles require constant rearranging to ensure their conformity to the interface. As a result, the interface tracking method suffers from mass conservation and faces difficulties in handling topological changes [187]. The other approach involves capturing the interface either by the volume of fluid method (VOF) [223] or the level-set method [143].

The VOF methods [78], [142], [187] define an indicator function (α) for the volume fraction, which carries a value ranging from 0 to 1. In a pure phase, i.e., in gas or liquid, α carries a value of 0 or 1, whereas any decimal value between 0 and 1 represents the interface. Furthermore, the VOF methods solve an advection equation for α to track the interface. However, due to the step behavior of the indicator function, a geometric or algebraic reconstruction of the interface is applied. It prevents the smearing of the interface due to numerical diffusion [239], [153], [173], [176], [182].

In level-set methods, a scalar field ϕ is defined in the domain. At the interface, ϕ is assigned a fixed value of ϕ_0, and in the pure phase ϕ is either greater than ϕ_0 or lesser than ϕ_0. Away from the interface, smoothing functions for ϕ are used to avoid numerical diffusion. However, level-set methods are not volume conserved in nature. To avoid these drawbacks, a fine grid resolution or coupling level-set method with the VOF method has been proposed [77], [216].

Despite the advantages of capturing the spray physics accurately using sharp interface approaches, these methods are still not popular in engineering applications because of the following reasons.

- It is expensive to fully resolve the interface for the flow with high Reynolds number. Automotive sprays such as diesel and gasoline sprays operate in the high Reynolds number and Weber number regime. hence, these flows are highly turbulent in nature. DNS simulations of turbulent flows are expensive and numerically challenging [73].
- Very small bubbles can be present in the spray under flash-boiling conditions, which render further complexity in the tracking and modeling interface.
- In the near nozzle regions of the diesel and gasoline sprays, a distinct sharp interface is not physically present [49, 48].
- During atomization, the interface undergoes severe deformations such that the length scale reduces to zero, e.g., pinching of droplets or breakup of ligaments.

Because of the above mentioned difficulties associated with the atomization process, 3-D DNS are not preferred for primary atomization. Rather, many of the studies pertaining to the primary atomization process are Large Eddy Simulations (LES) for the single phase region coupled with the VOF methods for the two-phase region. These approaches are similar to the under-resolved DNS method, hence known as the Quasi-DNS approach. The Quasi-DNS approaches have appropriately captured the in-nozzle turbulence and their effects on the primary atomization process [28], [29], [50]. However, the Quasi-DNS approach is still expensive for engineering applications.

3.3 Eulerian methods

One of the famous Eulerian methods is the Eulerian Liquid Eulerian Gas (ELEG) [85] or the two-fluid approach, where both phases are treated as the continuum throughout the domain. The ELEG method considers additional source terms for the lift, drag, and virtual mass forces in the momentum equation. The literature shows a good agreement of the near field spray predictions by the ELEG approach with the experimental observations, but the accuracy drops significantly in the sparse regions of the spray. The ELEG approach is also computationally expensive compared to other approaches. To avoid these limitations, Subramaniam and O'Rourke [215] suggested to use the EE approach in the near-field region and the LE approach in the dispersed spray region [148]. However, coupling the Eulerian liquid phase with the Lagrangian liquid phase is perplexing, as it requires knowledge about the relationships between the two representations. Recently, Pai et al. [148] sampled the Eulerian liquid phase data by probability distribution functions to achieve the coupling between the Eulerian and Lagrangian liquid phases. They have also provided consistency relationships which must be satisfied for a proper EE-LE transition.

Another well-known Eulerian approach, the $\Sigma - Y$ approach, models the primary atomization using the diffused interface method. The $\Sigma - Y$ model was first postulated by Vallet and Borghi [225]. It solves a density-averaged flow field while incorporating models for interfacial effects. The $\Sigma - Y$ model revolves around four basic assumptions as mentioned below.

1. At very high Reynolds number, as seen in automotive sprays, large-scale features are independent of the surface tension and viscous forces. These forces are predominant at smaller length scales, where a large velocity gradient occurs or the curvature of the interface is large.

2. The mean velocity of the RANS turbulence closure model ($k - \epsilon$) can be used to study the velocity field of the flow.

3. The dispersion of the liquid phase in the gaseous phase is mixing dominated and can be computed by solving a transport equation for the liquid mass fraction. The closure of the liquid mass fraction transport equation can be modeled by the turbulent diffusion liquid flux term.

4. The average droplet size for the dispersed liquid phase can be predicted by solving a transport equation for the mean surface area of the liquid/gas interface per unit volume (Σ).

Based on the first two assumptions, the mean flow for both phases can be treated as a mixture with variable density which shares a single velocity field. As a result, the mass and momentum conservation equation for the mixture can be represented in the following forms.

$$\begin{aligned} \frac{\partial \bar{\rho}}{\partial t} + \frac{\partial \bar{\rho}\tilde{u}_i}{\partial x_i} &= 0 & (3.5) \\ \frac{\partial \bar{\rho}\tilde{u}_j}{\partial t} + \frac{\partial \bar{\rho}\tilde{u}_i\tilde{u}_j}{\partial x_i} &= -\frac{\partial \bar{p}}{\partial x_j} - \frac{\partial \bar{\rho}\widetilde{u_i'u_j'}}{\partial x_i} & (3.6) \end{aligned}$$

In Eqn. 3.5 and 3.6, $\tilde{}$ indicates Favre/density averaging, $\bar{}$ indicates time averaging, and $'$ indicates turbulent fluctuations. The Reynolds stress term ($\widetilde{u_i'u_j'}$) in the Eqn. 3.6 can be closed using the Boussinesq eddy viscosity model following the second assumption.

Using the third assumption, the transport equation for the mean liquid mass fraction ($\tilde{Y} = \dfrac{\bar{\rho Y}}{\bar{\rho}}$) can be represented as seen in the Eqn. 3.7.

$$\frac{\partial \bar{\rho}\tilde{Y}}{\partial t} + \frac{\partial \bar{\rho}\tilde{u}_i\tilde{Y}}{\partial x_i} = -\frac{\partial \bar{\rho}\widetilde{u_i'Y}}{\partial x_i} \tag{3.7}$$

The closure of the turbulent mixing term ($\widetilde{u_i'Y}$) in the Eqn. 3.7, is modeled by the Fick's diffusion law given by Eqn. 3.8, where, Sc is the turbulent Schmidt number.

$$\bar{\rho}\widetilde{u_i'Y} = \frac{\mu_t}{Sc}\frac{\partial \tilde{Y}}{\partial x_i} \tag{3.8}$$

Following the fourth assumption, a transport equation for Σ is solved and represented in the Eq. 3.9.

$$\frac{\partial \bar{\Sigma}}{\partial t} + \frac{\partial \tilde{u}_j\bar{\Sigma}}{\partial x_j} = \frac{\partial}{\partial x_j}\left(D_\Sigma \frac{\partial \bar{\Sigma}}{\partial x_j}\right) + (A+a)\bar{\Sigma} - V_s\bar{\Sigma}^2, \tag{3.9}$$

The first term on the right hand side of the Eqn.3.9 represents the diffusion term, where the second term represents the production of the interface. The interface production term considers the contributions from the collisions of droplets and the stretching of the interface due to the gradient of the mean velocity. The third term on the right hand side of the equation models the destruction of the interface due to coalescence. Since its conceptualization, the $\Sigma - Y$ equation has been successfully applied to model the primary atomization in diesel spray and gasoline sprays. However, there is still a lot of scope left to improve the model.

3.4 Inferences

- The LE approaches are popular among the industry users, as they offer solutions with reasonable accuracy while incurring low computational cost for engineering applications.

- The LE models struggle with accuracy in the dense spray region.
- It is cumbersome to initialize the LE model due to the lack of available experimental data in the near nozzle region.
- The LE models also suffer from numerical stability problems and mesh dependency issues.
- True DNS are costly in highly atomizing conditions due to the wide range of scales involved in the process.
- Quasi-DNS methods can be used to validate the engineering level models in regions where experimental results are unattainable.
- Quasi-DNS methods are computationally exorbitant, because of the stringent requirements on the grid resolution.
- The $\Sigma - Y$ model overcomes the restrictions posed by the quasi-DNS approach.

CHAPTER 4

GOVERNING EQUATIONS

4.1 CFD Solver

This chapter includes a detailed description of the governing equations of the in-house Eulerian CFD solver, HRMFoam. The solver is implemented using the libraries of the foam-extend [2] branch of the OpenFOAM CFD framework. HRMFoam solver was initially developed by Schmidt et al. [189], later extended by Gopalakrishnan et al. [72] and Nerooorkar et al. [136], [137], [138]. Several past publications [194], [19], [132], [213], and [44] have successfully validated the HRMFoam code for different flow applications such as channel flow, condensing two-phase injector flow, cavitating diesel flow, and flash-boiling GDI flow.

The HRMFoam solver implements a diffuse interface based approach to ensure mixing between the individual phases, i.e., pure liquid phase, pure non-condensible gas (NCG) phase and the vapor phase. To ensure mixing, the solver defines a mixture density (ρ) which is formulated based on the density of fuel (ρ_f), density of the non-condensible gas (ρ_g) and the NCG mass fraction (y), as shown in Eqn. 4.1. The fuel density is further determined by accounting for the liquid fuel density (ρ_l), vapor density (ρ_v) and the vapor mass fraction (x), as seen in Eqn. 4.2.

$$\rho = \Big(\frac{1-y}{\rho_f} + \frac{y}{\rho_g}\Big)^{-1} \tag{4.1}$$

$$\rho_f = \Big(\frac{1-x}{\rho_l} + \frac{x}{\rho_v}\Big)^{-1} \tag{4.2}$$

From the above discussion, it is evident that the mixture density (ρ) is determined by the fuel quality (x), NCG mass fraction, and the density of individual phases. Furthermore, the densities of the phases depend upon the pressure and enthalpy values. Hence, the mixture density can be denoted by $\rho\left(x, y, p, h\right)$. The diffuse interface approach assumes mechanical equilibrium between the phases which means all the phases experience same velocity and pressure fields. The governing equations for mass and momentum conservation are represented in Eqns. 4.3, and 4.4, respectively. The transported variables in these equations are Favre averaged as the formulation accounts for turbulence and variable density.

$$\begin{aligned} \frac{\partial \rho}{\partial t} + \nabla \cdot \left(\Phi\right) &= 0 && (4.3) \\ \frac{\partial \rho \overrightarrow{U}}{\partial t} + \nabla \cdot \left(\Phi \overrightarrow{U}\right) &= -\nabla p + \nabla \overrightarrow{\overrightarrow{\tau}} && (4.4) \end{aligned}$$

In the preceding equations, Φ represents the face centered mass flux, and $\overrightarrow{\overrightarrow{\tau}}$ corresponds to the stress tensor, which includes both the viscous and turbulent stresses. To account for the mixing of ambient air and fuel, a transport equation for the mean non-condensible mass fraction, y, is solved, as shown in Eqn. 4.5.

$$\begin{aligned} \frac{\partial \rho y}{\partial t} + \nabla \cdot \left(\Phi y\right) &= \nabla \cdot \left(\rho \widetilde{u' Y'}\right) && (4.5) \\ \rho \widetilde{u' Y'} &= \frac{\mu_t}{Sc_r} \nabla y && (4.6) \end{aligned}$$

In Eqn. 4.5, the turbulent diffusion gas flux term, $\widetilde{u' Y'}$, accounts for the mixing effect of the relative velocity between the two phases. This term is closed using Fick's law of diffusion [53], as seen in Eqn. 4.6, where μ_t and Sc_r are the turbulent viscosity and realizable Schmidt number fields.

The HRMFoam solver uses the homogeneous relaxation model (HRM) to define the amount of vapor generation. In HRM, "Homogeneous" refers to the assumption of homogeneous mixing of the two phases within any computational cell. Whereas, "Relaxation" refers to the process that local flows develop towards thermal equilibrium. This model was proposed by Billicki and Kestin [30] based on the modification to the homogeneous equilibrium model to incorporate the one-dimensional variability of the vapor generation and condensation rates. This model governs the local rate of change of the dryness fraction (x), which tends towards its equilibrium value ($\bar{x}$) over a specific time scale (Θ), as shown in Eqn. 4.7. The local enthalpy and pressure are inputs for a lookup table generated by the REFPROP database [108] that governs the equilibrium quality.

$$\frac{Dx}{Dt} = \frac{\bar{x} - x}{\Theta} \tag{4.7}$$

Based upon Reocreux's "Moby Dick" experiments [174], Downar-Zapolski et al. [58] proposed the time scale for phase change to be a function of the fuel void fraction (α) and a non-dimensional pressure (ψ). Expressions to calculate these quantities are included in Eqs. 4.8 and 4.9.

$$\alpha = \frac{x\rho_l}{\rho_v + x(\rho_l - \rho_v)} \tag{4.8}$$

$$\psi = \left|\frac{p_{sat} - p}{p_{crit} - p_{sat}}\right| \tag{4.9}$$

In Eqn. 4.9, p_{sat} is the saturation pressure and p_{crit} is the critical pressure of the fuel. Here, p refers to the local total pressure instead of partial pressure. They also proposed the following correlations for the time scale for operating pressures exceeding 10 bar, Eqn. 4.10.

$$\Theta = \Theta_0 \alpha^{-0.54} \psi^{-1.76} \tag{4.10}$$

$$\Theta_0 = 3.84 \times 10^{-7} s \tag{4.11}$$

To ensure energy conservation, a transport equation for the enthalpy (h)is included in the HRMFoam solver, refer Eqn. 4.12.

$$\frac{\partial \rho h}{\partial t} + \nabla.(\Phi h) = \frac{Dp}{Dt} + \nabla.\mathbf{J} + D \tag{4.12}$$

In Eqn. 4.12, $\mathbf{J}$ accounts for the diffusion of the enthalpy and D represents the conversion of kinetic energy to sensible enthalpy due to viscosity and turbulence.

4.1.1 PISO algorithm

The coupling between the momentum and the mass balance equations is ensured by a modified Pressure Implicit Splitting Operator(PISO) algorithm. The discretized form of the momentum equation 4.4 in a quasi-linear formulation is mentioned in Eqn. 4.13.

$$a_p \mathbf{u}_p + \sum_N a_N \mathbf{u}_N = -\nabla p \tag{4.13}$$

In Eqn. 4.13, the subscript p is used to represent the current computational cell, while N represents the neighboring cells. The term a accounts for the coefficient of velocity ($\mathbf{u}$) which appears in the linearized momentum equation due to the discretization of the advection, diffusion and the source terms. Furthermore, the term accounting for the neighboring cells is replaced by another operator ($\mathbf{H}(\mathbf{u})$), Eqn. 4.14.

$$a_p \mathbf{u}_p = \mathbf{H}(\mathbf{u}) - \nabla p \tag{4.14}$$

To allow for the pressure to respond to compressibility, fluctuations of density due to phase change, and density change from turbulent mixing with the NCG, HRM is extended to the three dimensions(3-D). The 3-D formulation is achieved by connecting the predicted phase change with the conservation of mass and momentum through a simple chain rule, as shown in Eqn. 4.15

$$\frac{D\rho}{Dt} = \left.\frac{\partial\rho}{\partial p}\right|_{x,y,h}\frac{Dp}{Dt} + \left.\frac{\partial\rho}{\partial h}\right|_{x,y,p}\frac{Dh}{Dt} + \left.\frac{\partial\rho}{\partial x}\right|_{y,p,h}\frac{Dx}{Dt} + \left.\frac{\partial\rho}{\partial y}\right|_{x,p,h}\frac{Dy}{Dt} \tag{4.15}$$

An assumption of adiabatic condition leads to $dh = 0$. Using this assumption and the mass conservation formulation for the term $\frac{D\rho}{Dt}$, Eqn. 4.15 reduces to the following form. The formulation ensures response of the pressure field to the divergence of the velocity.

$$-\rho\nabla.\mathbf{u} = \left.\frac{\partial\rho}{\partial p}\right|_{x,y,h}\frac{Dp}{Dt} + \left.\frac{\partial\rho}{\partial x}\right|_{y,p,h}\frac{Dx}{Dt} + \left.\frac{\partial\rho}{\partial y}\right|_{x,p,h}\frac{Dy}{Dt} \tag{4.16}$$

Furthermore, substituting Eqn. 4.14 results in Eqn. 4.17.

$$-\rho\nabla.\frac{\mathbf{H}(\mathbf{u})}{a_p} + \rho\nabla.\left(\frac{1}{a_p}\nabla p\right) = \left.\frac{\partial\rho}{\partial p}\right|_{x,y,h}\frac{Dp}{Dt} + \left.\frac{\partial\rho}{\partial x}\right|_{y,p,h}\frac{Dx}{Dt} + \left.\frac{\partial\rho}{\partial y}\right|_{x,p,h}\frac{Dy}{Dt} \tag{4.17}$$

In Eqn. 4.17, the terms $\frac{Dy}{Dt}$ and $\frac{Dx}{Dt}$ are closed using the formulations presented in Eqns. 4.5, and 4.7, respectively. Furthermore, the term $\frac{Dp}{Dt}$ in Eqn. 4.17 is expanded resulting in Eqn. 4.18.

$$\begin{split}\frac{1}{\rho}\left.\frac{\partial\rho}{\partial p}\right|_{x,y,h}\left(\frac{\partial p}{\partial t} + \nabla.(p\mathbf{u}) - p\nabla.\mathbf{u}\right) + \nabla.\frac{\mathbf{H}(\mathbf{u})}{a_p} - \frac{1}{a_p}\nabla^2 p + \\ \frac{1}{\rho}\left.\frac{\partial\rho}{\partial x}\right|_{y,p,h}\frac{Dx}{Dt} + \frac{1}{\rho}\left.\frac{\partial\rho}{\partial y}\right|_{x,p,h}\frac{Dy}{Dt} = 0\end{split} \tag{4.18}$$

The partial derivatives of ρ with respect to p, x and y are further written in the following forms.

$$\left.\frac{\partial\rho}{\partial p}\right|_{x,y,h} = \rho^2\left(\frac{1-y}{\rho_v a_v^2} + \frac{(1-y)(1-x)}{\rho_l a_l^2} + \frac{y}{\rho_v a_g^2}\right), \tag{4.19}$$

$$\left.\frac{\partial\rho}{\partial x}\right|_{y,p,h} = (y-1)\rho^2\left(\frac{1}{\rho_v} - \frac{1}{\rho_l}\right), \tag{4.20}$$

$$\left.\frac{\partial\rho}{\partial y}\right|_{x,p,h} = -\rho^2\left(\frac{1}{\rho_g} - \frac{1-x}{\rho_l} - \frac{x}{\rho_l}\right) \tag{4.21}$$

In Eqn. 4.19, a_v, a_l and a_g are the speed of sound in fuel vapor, liquid fuel, and ambient gas, respectively. Based upon Brennen's analysis [37], the partial derivative $\left.\frac{\partial\rho}{\partial p}\right|_{x,y,h}$ is assumed to be related to the enthalpic sonic speed of the two-phase mixture and is given by Eqn. 4.22

$$\left.\frac{\partial\rho}{\partial p}\right|_{x,y,h} = \frac{1}{a^2} \tag{4.22}$$

However, the expression for compressibility in Eqn. 4.19 is found to be numerically unstable due to the very abrupt changes in two-phase regions. Consequently, a smoother mass-weighted expression for compressibility is adopted in the present work and is respresented in Eqn. 4.23:

$$\left.\frac{\partial\rho}{\partial p}\right|_{x,y,h} = \rho\left(\frac{(1-y)x}{\rho_v a_v^2} + \frac{(1-y)(1-x)}{\rho_l a_l^2} + \frac{y}{p}\right) \tag{4.23}$$

After implicitly solving the pressure by the help of Eqn. 4.18, the flow velocity $\mathbf{u}$ is updated using Eqn. 4.14.

4.2 Needle Closure Model

The challenge of modeling sealing is how to effectively cut off the communication between two parts of the domain at the needle seat. While the obvious approach is to topologically sever the domain, this approach would encounter a few disadvantages. The first is the abruptness of such an operation would create massive disturbances in the flow, triggering strong waves that could result in spurious waterhammer effects. While such effects are expected in rapid valve closure, an instantaneous severance would be unnaturally violent. Secondly, it is unclear what a linear solver that is designed for solving a single domain problem would do when confronted with two disjoint problems stored in a single linear system.

Instead, we propose to model what cannot be directly resolved in the simulation. When the needle is nearly closed to the seat, the drag force produced by the walls begins to dominate the flow. The closure model will employ a gradual increase in drag that halts the flow through the narrow gap. To avoid degenerate cells, this sealing model will active at low, but finite, needle valve lift. To model this event, a volumetric source term $\left(\bar{f}\right)$ is added to the right hand side of the momentum equation, Eqn. 4.4. The modified momentum equation is mentioned below.

$$\begin{aligned} \frac{\partial \rho \mathbf{u}}{\partial t} + \nabla.(\Phi \mathbf{u}) &= -\nabla p + \nabla \bar{\bar{\tau}} + \bar{f} \qquad (4.24) \\ \bar{f} &= \rho \mathbf{u} \frac{S_f}{S_d} \qquad (4.25) \end{aligned}$$

Eqn. 4.25 describes the artificial drag force, with S_f and S_d declared as the sealing factor and drag constant, respectively. The drag constant represents how vigorously the imposed force opposes the motion of the fluid. A very small value of the order 10^{-8}s or 10^{-9}s is generally assigned to S_d. The value must be sufficiently high to bring the velocity of the fluid down to near-zero values in the sealing region.

Furthermore, the drag force is applied gradually to avoid an unrealistically violent closure or opening. This is accomplished by modeling S_f as a continuous function of time and seal constant S_∞, as shown in Eqn. 4.26. The discrete S_∞ is unity only when the needle-seat sealing is being applied.

$$S_f = S_\infty \left(1 - e^{-\left(\frac{t}{\tau}\right)}\right) \qquad (4.26)$$

In Eqn. 4.26, τ represents the time relaxation factor. Changing τ changes the rate at which the sealing is applied or removed. The expression in Eqn. 4.25 creates an exponential decay of velocity dependent on the strength of the drag constant, S_d. The drag is turned on or off at a rate governed by τ. This gradual switching is controlled by S_f, which represents a relaxation towards the state indicated by S_∞. In the seat region, which is designated by an user input of a bounding box, the value of S_∞ is switched between zero and unity to represent opening or closing, respectively. For rest of the domain, the value is always zero so that the artificial drag force is zero at all times.

Because of the form of Eqn. 4.25, when treated implicitly, the source term appears on the diagonal of the matrix in the linear system of equations for velocity, the a_p term of Eqn. 4.13. This formulation intrinsically benefits stability by increasing the diagonal dominance of the matrix. If the drag term and temporal term dominate the equation, then the decay of velocity should, at least for momentum, unconditionally stable. Considering the coupling with the other transport equations, one cannot *a priori* know the stability of the system as a whole.

4.3 Primary atomization model

Rachakonda et al. [166], [165] expanded the capabilities of the in-house HRM solver to model the primary atomization by including a modified vesrion of the $\Sigma - Y$ solver discussed in Sec. 3.3. The formulation includes a transport equation for the variable Ω, mass based liquid-gas interface density, defined in the Equation 4.27. The formulation is numerically more stable compared to other formulations proposed by several researchers [69] , [225], [10], [51], and [42] due to its volume conserving nature. However, unphysical droplet diameters are predicted by the formulation in the primary atomization regime. Hence, the current research uses an improved formulation, which will be discussed in the latter part of this section.

$$\Omega = \frac{\Sigma}{\rho} \tag{4.27}$$

In Eqn. 4.27, Σ is the interfacial area density which has a unit of m^{-1}. Further, Σ and the liquid volume fraction $(\overline{Y})$ can be used to predict the Sauter mean diameter(SMD) in the primary atomization regime, as seen in Eqn. 4.28 . The formulation applies the assumption that the liquid phase in a computational cell can be modeled with spherical droplets to determine SMD in the transition region from the dense spray to sparse spray region, as shown in Eqn. 4.28.

$$SMD = \frac{6\overline{Y}}{\Sigma} \tag{4.28}$$

Recently, several revisions of the initial $\Sigma - Y$ formulation [225] have been proposed [26], [104], [63], [79] to expand the modeling paradigm into the secondary atomization regime. The notable formulation proposed by Lebas et al. [104] is mentioned in Eqn. 4.29. The equation includes an indicator function (Ψ) that acts as a switch between the terms for secondary atomization, i.e., $\left(\dot{\Omega}_{breakup}, \dot{\Omega}_{coal/coll}\right)$ and the primary atomization terms $\left(\dot{\Omega}_{mixture}, \dot{\Omega}_{stress}\right)$. The term Ω_{vap} accounts for the production/destruction of the interface due to vaporization.

$$\begin{aligned}\frac{\partial \rho\Omega}{\partial t} + \nabla.\left(\rho u \Omega\right) = \nabla.\left(\frac{\mu_t}{Sc_\Sigma}\nabla\Omega\right) + \rho\Psi\left(\dot{\Omega}_{mixture} + \dot{\Omega}_{stress}\right)\\ + \rho\dot{\Omega}_{vap} + \rho\left(1-\Psi\right)\left(\dot{\Omega}_{breakup} + \dot{\Omega}_{coal/coll}\right)\end{aligned} \tag{4.29}$$

However, including models for secondary atomization in an Eulerian primary atomization model is computationally expensive. Moreover, the secondary break up processes can be modeled by droplet oriented approaches. Hence, a simplified version of the $\Sigma - Y$ formulation, proposed by Lebas et al. [104] is used in the current research. The formulation only accounts for the primary atomization regime in the GDI applications, as seen in Eqn. 4.30.

$$\frac{\partial \rho\Omega}{\partial t} + \nabla.\left(\rho u \Omega\right) = \nabla.\left(\frac{\mu_t}{Sc_\Sigma}\nabla\Omega\right) + \rho\left(\dot{\Omega}_{mixture} + \dot{\Omega}_{stress}\right) \tag{4.30}$$

In Eqn. 4.30, $\dot{\Omega}_{mixture}$ ensures production of the liquid/gas interface due to mixing of phases. This term further enables the initialization of the mean interface surface density. Nevertheless, it is of importance only in the vicinity of the nozzles. The mixture term is modeled based on the assumption that the initial length scale of the produced liquid blob should be proportional to the turbulent length scale (l_t) [104], [63]. The expression for the mixture term is included in Eqn. 4.31, and it depends upon the gradient of liquid mass fraction ($\tilde{Y}$). Liquid mass fraction is further determined by Eqn. 4.32.

$$\dot{\Omega}_{mixture} = \frac{12\nu_t \rho^2}{Sc_\Sigma \rho_l \rho_g l_t} \left(\nabla \tilde{Y}\right) . \left(\nabla \tilde{Y}\right) \tag{4.31}$$

$$\tilde{Y} = \frac{m_l}{m_t} = \left(\frac{m_l}{m_f}\right)\left(\frac{m_f}{m_t}\right) = \left(1 - \frac{m_v}{m_f}\right)\left(1 - \frac{m_g}{m_t}\right) = (1-x)(1-y) \tag{4.32}$$

In Eqn. 4.30, $\dot{\Omega}_{stress}$ represents the source term that accounts for the production/destruction of interface due to the turbulent stretching. It also considers the effects of collision and coalescence in the dense spray region [104]. The stress term attempts to attain an equilibrium interfacial surface density $\left(\Omega^*_{eq}\right)$ in a duration proportional to the turbulent time scale (τ_t). Further, the equilibrium interfacial surface density corresponds to the quantity of surface that would be obtained by keeping the liquid volume fraction $\left(\bar{Y}\right)$, and the mixture turbulent kinetic energy (k) constant at a critical Weber number (We_{cr}). We hypothesize that the droplets in the primary atomization regime attain the largest expected radius based on the critical Weber numbers in the range of $1-6$, as observed by Pilch and Erdman for a wide range of Ohnesorge number [160]. The terms, $\dot{\Omega}_{stress}$ and $\dot{\Omega}^*_{eq}$ are calculated based on Eqns. 4.34, and 4.35. In these equations, k and σ correspond to the turbulent kinetic energy and the surface tension force.

$$\dot{\Omega}_{stress} = \frac{\Omega}{\tau_t}\left(1 - \frac{\Omega}{\Omega^*_{eq}}\right) \tag{4.33}$$

$$\Omega^*_{eq} = \frac{\bar{Y}k}{\sigma We_{cr}} \tag{4.34}$$

$$We_{cr} = 1 : 6 \tag{4.35}$$

These auxiliary transport equations for the interfacial surface density do not feedback into the momentum or energy equations. Hence, to reduce computational cost, these equations can be turned off when modeling primary atomization is not the prime goal of the computation. The future chapter about the plume-based coupling approach uses this $\Sigma - Y$ formulation to model primary atomization proicess.

CHAPTER 5

CASE STUDIES: MULTIPLE INJECTIONS IN GDI SYSTEMS

The early and late portions of transient fuel injection have proven to be a rich area of research, especially since the end of injection can create a disproportionate amount of emissions in direct injection internal combustion engines. A perennial challenge in simulating the internal flow of fuel injectors is the valve opening and closure event. In a typical adaptive mesh CFD simulation, the small gap between the needle valve and the seat must be resolved to very small cells, resulting in costly computations. Capturing a complete closure usually involves a topological change in the computational domain. In this chapter, we have applied the needle closure algorithm, discussed in the previous section 4.2, to a gasoline direct injection system operating under cavitating conditions. The closure algorithm is designed to avoid spurious water-hammer effects.

Traditionally, multiple fuel injection pulses have been employed in diesel engines to improve emissions and heat release rate [134], and [221]. Similarly, in GDI applications, multiple injection strategies have shown benefits in dramatically improving combustion stability and spark authority when compared to a single injection event [180]. The current chapter demonstrates the first of a kind single simulation of a multiple gasoline injection event known to the authors.

SIMULATION SETUP

Geometric details

The ECN Spray G nozzle consists of a multihole nozzle with eight counterbore orifices. Its geometric details are listed in Table 5.1. For the current simulations, the specified nominal values are used to build the computational domain (named Generation 1 geometry), shown in Figure 5.1 and Figure 5.2. The spherical shape of the needle is also built from the nominal manufacturing dimensions. A semispherical volume of 9 mm diameter is added as the discharge plenum to simulate the first millimeters of the spray development.

Table 5.1: ECN Spray G nominal nozzle geometry parameters.

Nozzle type	valve covered orifice (VCO)
Bend angle	0°
Number of holes	8
Orifice shape	circular
Hole shape	straight
Nozzle shape	step hole
L/D ratio	1.4
Orifice diameter	0.165 mm
Orifice length	$0.16 - 0.18$ mm
Step diameter	0.388 mm
Orifice drill angle	37° relative to nozzle axis
Full outer spray angle	80°

Mesh

A primarily hexahedral mesh for the nominal geometry with a cell count of 1.44 million has been created using the GridPro meshing tool. The grid spacing is roughly 7μm in the sac region, as opposed to the spacing of around 10μm in the nozzle region. To avoid higher cell counts, an anisotropic refinement in the narrow region between the needle and the nozzle was performed. The mesh in the seat region can be seen in Fig. 5.3. The mesh is created at an initial displacement of $5\mu m$. A prior work investigated mesh independence [132] and in the present work the cell count is

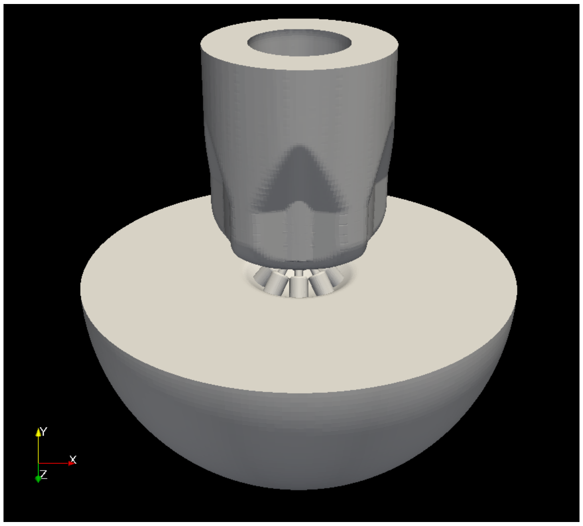

Figure 5.1: ECN spray G computational domain with the outlet plenum of 9mm diameter.

Figure 5.2: ECN spray G nominal geometry showing distribution of the 8 nozzle holes and 5 dimples.

comparable to or higher than that of other diffuse interface simulations reported by Moulai et al. [132] and Saha et al. [183],[185]. In the study by Moulai et al.[132], these spacings were 10μm and 40μm, respectively. For Saha et al., they were 15μm and 30μm [183], and [185].

Needle motion

Needle motion in the simulation is controlled by a profile of a typical double injection for these conditions. This profile is generated using the experimental data. The profile is adjusted to account for the initial lift of the mesh, as shown in Fig. 5.4. The layer addition and removal algorithm is used to accomplish the prescribed mesh motion.

In this simulation, the sealing algorithm is activated whenever the needle lift is less then $1\mu m$ from its initial position. The mesh is built with the needle lifted $5\mu m$ from the seat, so the algorithm is effectively disengaged at $6\mu m$ of lift. When engaged, the algorithm brings the fluid within the needle-seat region to rest by applying the large artificial drag force previously described.

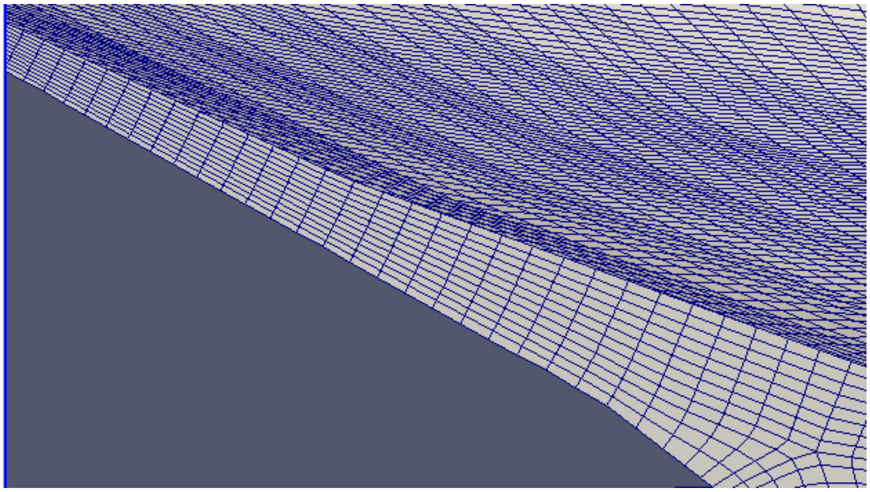

Figure 5.3: Cut plane of the CFD mesh in the needle seat area prior to the needle lift

Table 5.2: Non-flashing (spray G) operating condition defined by the ECN

Spray G operating condition	
Fuel	Iso-octane
Upstream pressure	20 MPa
Fuel temperature	90 ^{0}C
Ambient temperature	300 ^{0}C
Ambient density	3.5 kg/m^3
Back pressure	600 kPa

Initial and boundary condition

The computational study is based upon the Engine Combustion Network (ECN) Spray G operating conditions, mentioned in Table 5.2.Under these conditions, the elevated back pressure leads to a non-flashing flow.

Zero-gradient boundary conditions are used for velocity at both the inlet and the outlet. For the pressure at the inlet, a total pressure boundary condition is chosen. At the outlet, a transonic total pressure boundary condition is applied. This boundary

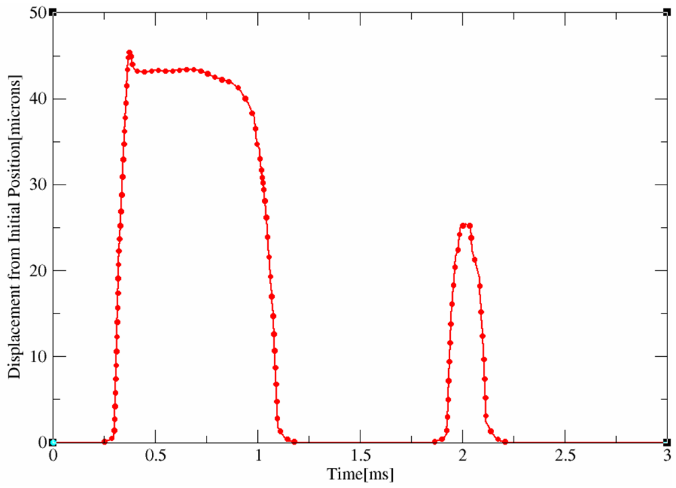

Figure 5.4: Needle lift profile used in the CFD simulations

condition switches between the zero-gradient and total pressure boundary conditions based upon the Mach number at the exit.

During the initial condition, the needle is closed and the fluid is stationary, so all pressure drop should occur at the needle seat. To avoid the formation of spurious pressure waves in the flow domain during the start of the simulation, a hyperbolic tangent drop of pressure across the needle seat area is applied, as shown in the Figure 5.6. The interface between the fuel and the non-condensible gas is placed at the lower bound of the sealing region, as seen in Fig. 5.7. This leaves the sac initially filled with the non-condensible gas. The initial values of the sealing constant (S_∞) and the sealing factor (S_f) are both unity in the seat region and zero elsewhere. The sealing field at the start of the simulation can be seen in the Fig. 5.5.

Turbulence closure and model assumptions

To model turbulence, the SST $k - \omega$ RANS model in conjunction with the log-layer wall function is used. This model is well known for resolving separating flows with adverse pressure gradients. In the present simulation, iso-octane is used as the fuel. To account for the compressibility effects, the current work assumes the

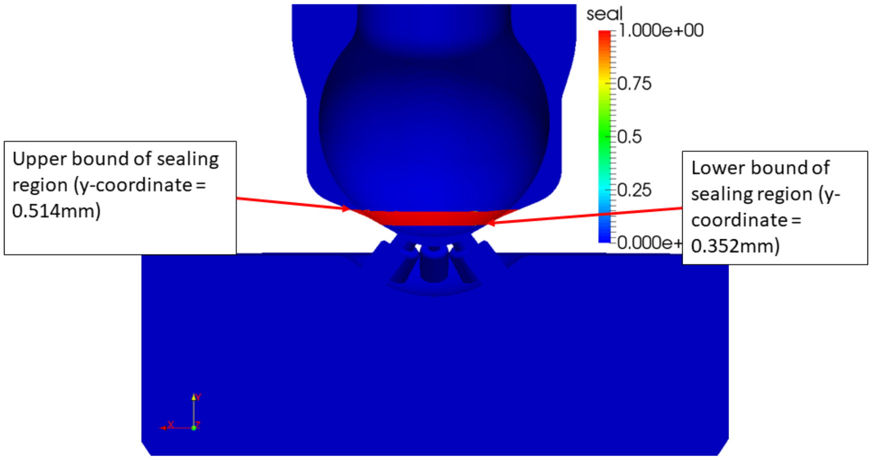

Figure 5.5: Initialization of the sealing field at the start of simulation

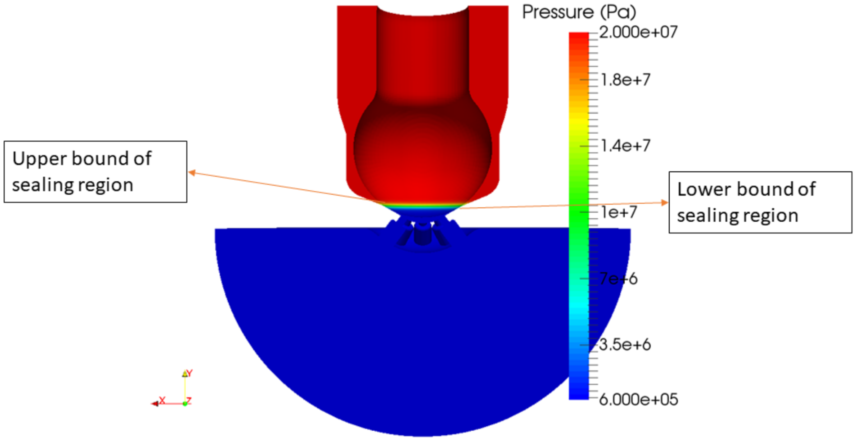

Figure 5.6: Initialization of the pressure field at the start of simulation

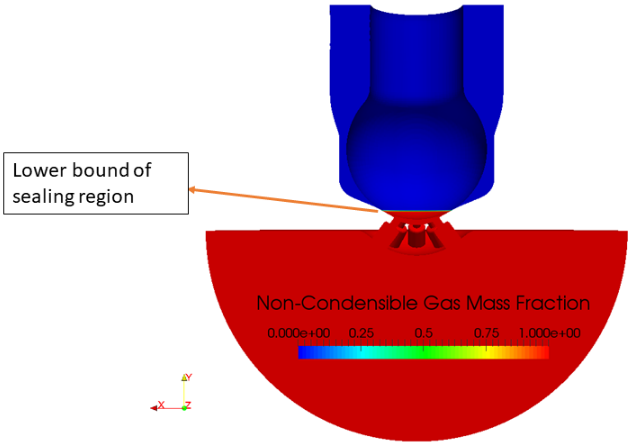

Figure 5.7: Initialization of the non-condensible gas field at the start of simulation

liquid fuel to be compressible. Furthermore, the walls are assumed to be adiabatic, which is consistent with the assumptions by Gavaises et al. [70] in the case of diesel injection systems. For further simplification of the posed problem, no heat transfer is considered between the non-condensible gas and the liquid fuel. To model these phenomena, a careful evaluation of the interfacial heat transfer coefficient over the complete injection cycle is required, which is beyond the scope of the current research.

5.1 Results and discussion

5.1.1 Sealing

As discussed in the previous chapter, the sealing algorithm switches the value of S_∞ to unity in the seat region whenever the gap between the needle wall and the injector wall is less than 6 μm. The value of S_f plummets to zero everywhere, shortly after the needle lift exceeds the needle displacement limit, i.e., $1 \mu m$. As intended, once the needle is closed after the main injection event, the value of S_∞ switches to unity and the value of S_f quickly follows. The right-bottom image in Fig. 5.8 shows the value of S_f during the dwell period between the individual injection cycles.

The effect of the sealing field on the flow domain is as intended. In Fig. 5.8, velocity contours in the sealing region are presented for the different instances of the dwell phase. Careful inspection shows that the velocity in the sealing region diminishes to negligible values while the downstream jets persist for a short period.

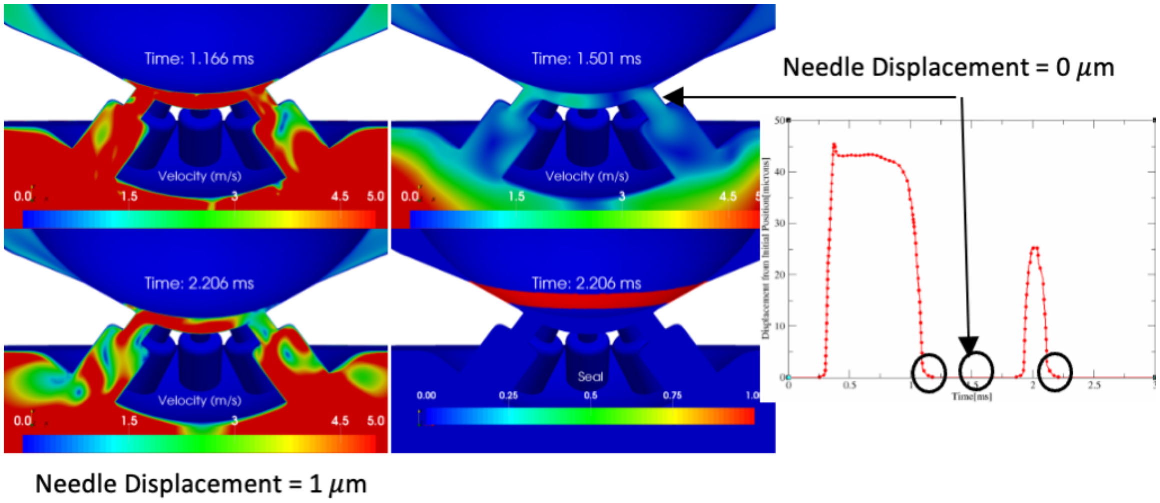

Figure 5.8: Sealing Region and corresponding velocity contour at different time stamps during needle closure event.

5.1.2 Rate of Injection (ROI)

The Rate of Injection (ROI) for the multiple injection event is measured at the nozzle exit, as shown in Fig. 5.9 . The ROI is found to follow the needle displacement curve. However, an interesting phenomenon during the second injection is observed. Although the maximum needle displacement during the second injection is half of that of the first injection cycle, the maximum predicted ROI for the injection cycles are found to be of similar order.

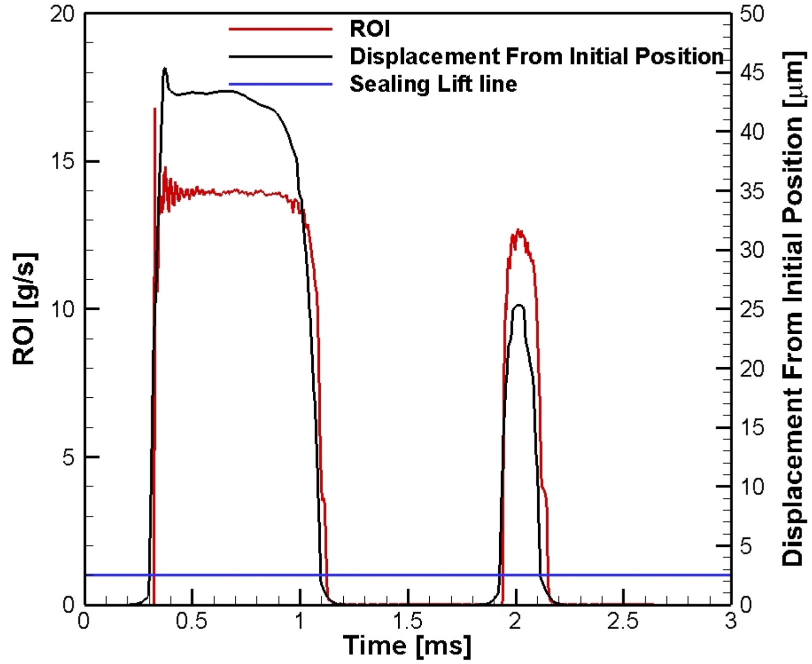

Figure 5.9: Rate of Injection curve for a multiple injection event

5.1.3 Cavitation

The simulation captures cavitation during the low lift period of the needle's transient motion(during both needle opening and closing phases). The cavitation bubbles created at the end of both the first and second injection cycles are found to linger until the start of the dwell period. This cavitation can be a major contributor to the injector failure in the needle-seat region [186]. Fig. 5.10 presents the fuel vapor volume fraction and the corresponding local low pressure regions during the needle opening phase indicating the cavitation event. Similarly, cavitation is also demonstrated during the needle closure event for both injection shots, as seen in Fig. 5.11. After completion of the 2^{nd} injection, fuel vapor has been observed in the sac in addition to the seat region. A detailed analysis of the seat and sac bubbles during the needle closure events will be included in the future chapters.

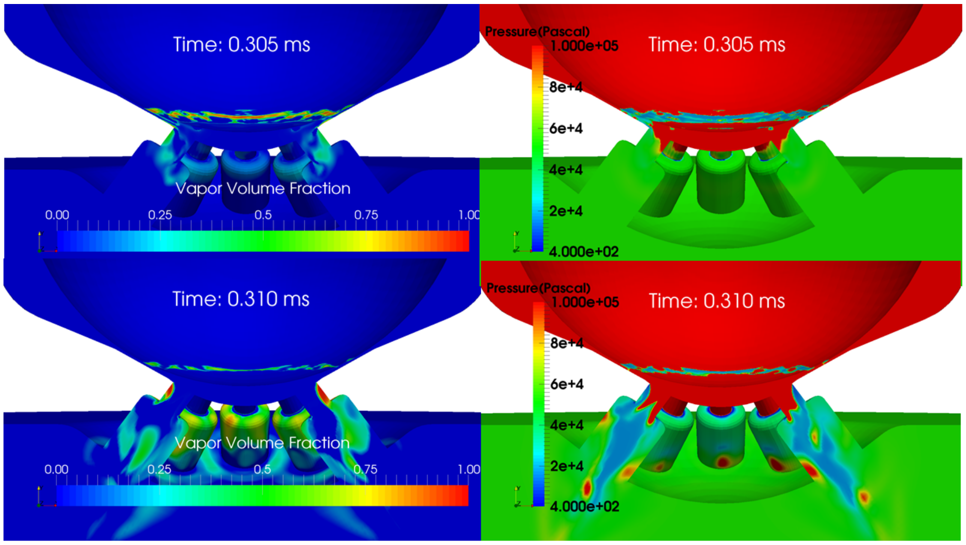

Figure 5.10: Vapor volume fraction and low pressure region showing cavitation during needle opening phase of the 1st injection cycle.

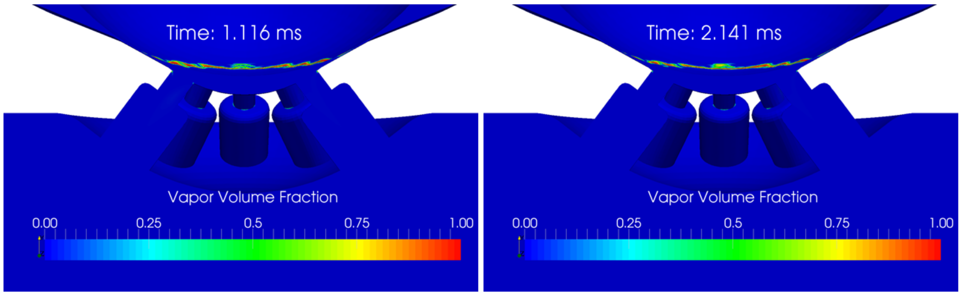

Figure 5.11: Vapor volume fraction showing cavitation during needle closing phase of the both 1st and second injection cycle.

5.1.4 Residual fuel

Just after needle closure, the velocity at the sealing region decreases to zero and the pressure inside the sac is reduced. However, residual fuel exists in the nozzle holes. Although the inertia of this residual fuel causes it to exit the hole, it decelerates because of the low pressure gradient present. As a result, the spray plume coming out of the exit plane starts to oscillate leading to eventual jet disintegration. This slow moving liquid fuel jet is unlikely to atomize well. Hence, it is most likely to contribute to the hydrocarbon emissions during combustion. Figure 5.12 indicates possible liquid fuel dribbling events during the EOI of both the first and second injection pulses.

5.2 Conclusions

A sealing algorithm has been developed and successfully applied to a non-flashing Spray G injection with a double injection cycle. The primary results are summarized below:

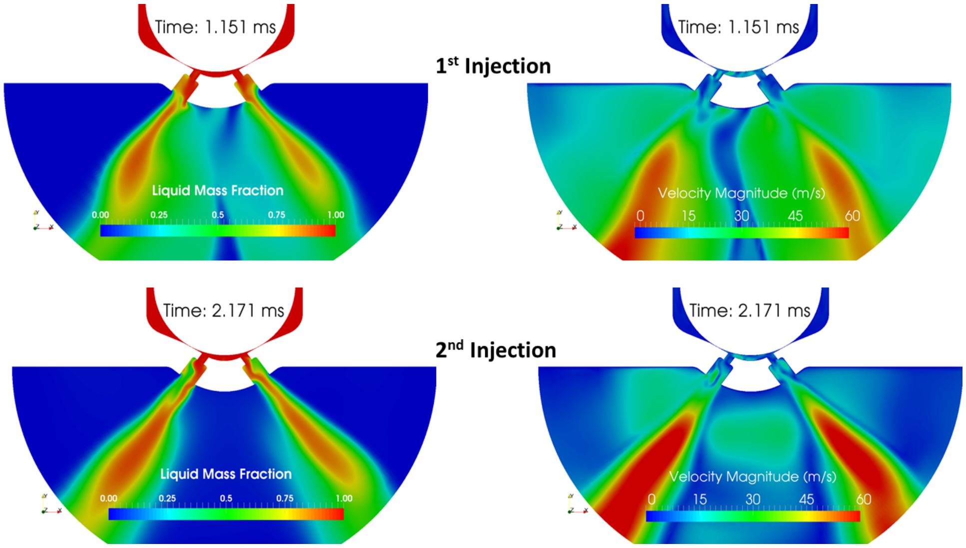

Figure 5.12: Liquid fuel mass fraction and velocity contour at 1.151 ms (EOI of the first injection),2.171 ms (EOI of the second injection) showing dribble and jet disintegration

- Results demonstrate the ability of the sealing algorithm to completely block the needle-seat area at low needle lifts, resulting in zero flow velocity within the sealing region.

- At low needle lift and during both SOI and EOI, fuel vapor generation is observed as the liquid fuel passes through the narrow region between the needle and seat.

- Towards the end of the second injection, fuel vapors are captured within the sac region.

- After the end of injection, the possible liquid fuel dribble leading to eventual jet disintegration has been demonstrated.

CHAPTER 6

EFFECT OF FLASH-BOILING ON THE NEEDLE CLOSURE EVENT

Gasoline Direct Injection (GDI) engines offer the potential of dense and efficient power generation, but incur difficulties with emissions. GDI engines have made significant progress since their inception, but more study is required to understand the impact of the injector's internal flow physics on the overall durability and performance of the engine. The Start of Injection(SOI) and End of Injection(EOI) are two crucial phases of the needle's transient motion. Both of these injection phases generate pressure waves and flow turbulence attributable to the opening and closing of the valve. Cavitation, a critical concern for the health of the needle seat, is often encountered at both the SOI and EOI [186]. Liquid fuel dribble, a major contributor to unburned hydrocarbon emissions, is encountered at the EOI phase. Hot gas ingestion occurs in the counterbore and nozzle regions during the needle's dwell time between injections. This ingestion of gas can have adverse effects on the next cycle's SOI, as it both delays the liquid injection and leads to more liquid vaporization[47, 159].

The computational research on SOI and EOI phases for the GDI injector is limited comapred to the diesel injection system. Ishii et al.[83] studied the flow inside a multihole GDI injector with transient needle motion under non-flashing conditions using a VOF model with the particle/grid hybrid method. They captured the liquid fuel dribble and film formation at the EOI, but also showed a leakage velocity through the seat area during this injection phase. Their model was computationally expensive, as very fine grids were required to properly simulate the particles. Cavitation and turbulence, which are quite common during the EOI for GDI injectors, were not modeled. The EOI event of a GDI injector has also been simulated by [133] while using a VOF approach. They implemented the 1-D Sauer and Schnerr model in conjunction with the Continuum Surface Model (CSM) to capture the sac and tip conditions post-needle closure. However, the simulated ambient conditions were limited to non-flashing conditions, and their simulations only included the needle lift curve for the needle closing phase due to the computationally expensive nature of the VOF approach. Recently, Hwang et al. [82] employed the diffuse interface approach to predict the boil-off characteristics of a single axial-hole transparent nozzle under non-flashing, mildly flashing, and flare-flashing conditions. They were able to get good agreement for the boil-off time under non-flashing and flare-flashing conditions with the experimental observations. Yet, they overpredicted the boil-off time for mildly flashing conditions. The needle valve opening and closing represents a general challenge in computational fluid dynamics. The valve closure represents an abrupt change in domain topology, and the flash boiling process in highly turbulent flow involves sudden vapor generation and collapse that is difficult to model.

In the present chapter, the needle closure model in tandem with the homogeneous relaxation model has been applied to a single injection cycle of GDI injector operating in different ambient conditions. This allows for a novel study of the EOI for the multihole GDI injector under flash boiling conditions. The details about the model implementation are discussed in the previous chapters. Moreover, the current study includes the different sac conditions present, post-needle closure, for different ambient conditions, and the mechanism driving these sac conditions. The studies about the tip-wetting phenomena for both flash-boiling and non-flashing conditions are also included. The study indicates dribbling in the non-flashing condition. Additionally, the CFD predictions are compared with the existing experimental observations.

6.1 Simulation setup

The current simulations use the same geometry and mesh described in Ch. 5. However, the needle displacement curve is different, as shown in Fig. 6.1. The needle displacement curve is adjusted to account for the initial mesh lift. The maximum lift for the single injection event is $55\mu m$. The simulations are performed for ECN prescribed non-flashing(G) and flash-boiling (G2) conditions. The operating conditions are mentioned in the Table 6.1. Both conditions have the same injection pressure and fuel temperature ($20MPa$ and 90^0C respectively), but the ambient density and back pressure are different. The back pressure and ambient density are $600kPa$ and $3.5kg/m^3$ for the non-flashing case, whereas they are $53kPa$ and $0.5kg/m^3$ for the flashing condition.

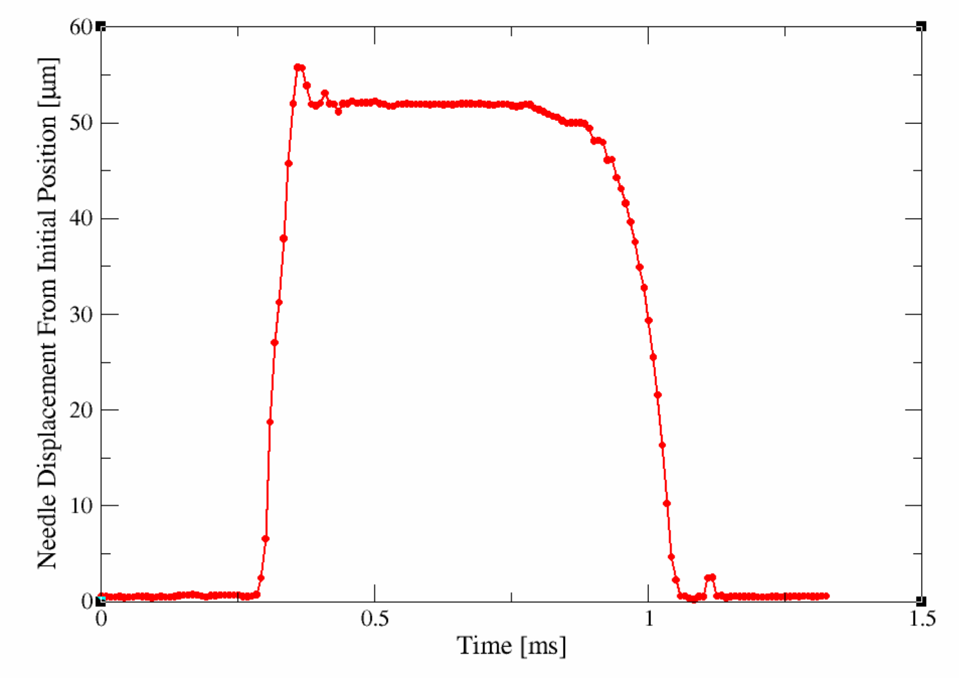

Figure 6.1: Ensemble-averaged needle displacement profile generated by X-ray measurement [59]

In the current simulations, the sac is initialized with non-condensible gas at the start of injection. The sealing algorithm is activated whenever the needle is displaced

Table 6.1: Operating condition for G (Non-Flashing) and G2 (Flashing) condition.

Parameter	G-Standard	G2-Flash boiling
Fuel	Iso-Octane	Iso-Octane
Fuel temperature	90 °C	90 °C
Ambient temperature	573 K	333 K
Fuel pressure	20 MPa	20 MPa
Ambient density	$3.5\,\mathrm{kg\,m^{-3}}$	$0.5\,\mathrm{kg\,m^{-3}}$
Ambient Pressure	600 kPa.	53 kPa

less then $1\mu m$ from its initial position. The lalplacian mesh motion library of FOAM extend is used to lift the needle according to the experimentally measured needle displacement curve. The same model assumptions discussed in the previous chapter 5 are used for the current simulations.

6.2 Results and discussion

6.2.1 Rate of Injection

For validation, Rate of Injection (ROI) data from the flashing and non-flashing cases are compared with the experimentally measured ROI profile provided by the ECN. These measurements were obtained by Duke et al. [59] through the Bosch long tube method. The simulated maximum rate of injection and the ROI profile both match well with the experimental observations, as seen Fig. 6.2. The percentage difference between the experimental observations and the computational predictions for the maximum ROI and the ROI during the steady injection phase are 3% and 4%, respectively. In the current simulation, the needle is assumed to be closed until it reaches a displacement of 6μm from the seat. This assumption leads to a difference in the observed needle opening duration between the experiment and the simulations, i.e., the simulations assumed the needle opening duration to be 735μs versus the observed needle opening duration of 760μs. Consequently, the simulated ROI is observed to diminish to a zero value faster compared to the experimental ROI.

The differences in the injection duration can also be attributed to the fact that the simulations assumed the sac to be empty at the start of the simulation, whereas the long tube method starts with a liquid-filled tube. The simulations predict a total injected mass of 10.01 mg for both the flashing and non-flashing conditions. The Spray G target condition specifies a total injected mass of 10 mg, and experiments have observed 10.1 mg being injected. Furthermore, the ROI predicted by the non-flashing condition is similar to the ROI predicted by the flashing condition. It implies that the different downstream pressures have no effects on the mass flow rate. This corroborates the fact that these nozzles are operating in choking conditions [132].

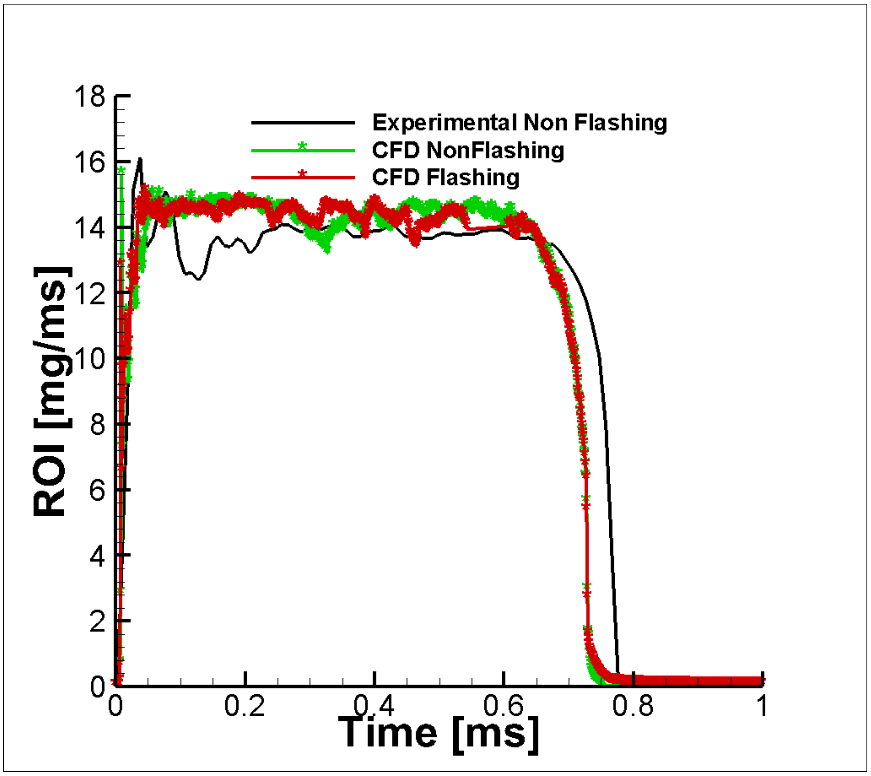

Figure 6.2: Simulated and experimental ROI vs time. Experimental ROI obtained through the long-tube method [59]and simulated ROI taken at the nozzle exit

6.2.2 EOI sac condition

Post injection sac and nozzle conditions can be detrimental to the emissions behavior of GDI engines. Traces of liquid or vapor fuel in the sac will alter the behavior of a second injection compared to the empty sac condition, and can also affect the hydraulic injection duration.

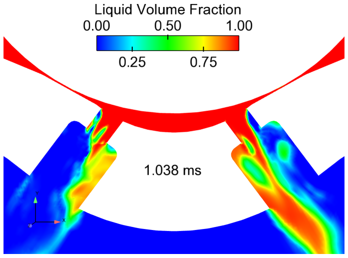

Figure 6.3: Liquid volume fraction just before needle closing, i.e., $t = 1.038$ ms for non-flashing conditions.

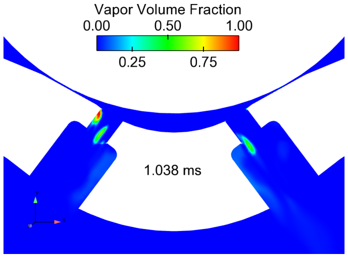

Figure 6.4: Vapor volume fraction before needle closing, i.e., $t = 1.038$ ms for non-flashing conditions showing cavitation due to the nozzle inlet corner.

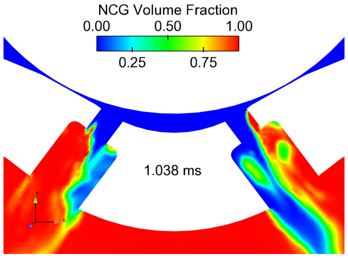

Figure 6.5: NCG volume fraction before needle closing i.e. $t = 1.038$ ms for non-flashing conditions showing gas entrainment in the counter bore.

For reference, we define a pressure ratio as the ratio of local static pressure, i.e, the pressure at the cell center to the saturation pressure of the fuel at its injected temperature. For the non-flashing case, the ambient pressure ratio is around 7.7. Figures 6.3, 6.4, and 6.5 captures the gas ingestion during the phase of injection where the needle is open. As described by Fig. 6.4, 6.5, 6.12 a local low pressure region is also created in the counterbore and at the nozzle inlet corner, resulting in vapor generation. When the needle begins to close, the low pressure waves created in the seat region and at the nozzle exit start to move into the sac, resulting in low pressure spots inside the sac. This water hammer type transient phenomenon is clearly visible in a simple pressure contour, as shown in figures 6.12, 6.13, and 6.14. These low pressure spots dip below the prevailing saturation pressure, resulting in the cavitation seen in figures 6.6 and 6.7, but these bubbles are very short lived as the back pressure is greater than the saturation pressure. Post needle closure, i.e., during the dwell phase, the sac reaches the ambient pressure and entrains ambient gas. This leads to a mixture of liquid fuel and ambient gas for the initial condition of the next injection (see Fig. 6.9, 6.10, 6.11). Similar observations have been made by Moon et al. [131] experimentally. However, they injected n-heptane from a 3-hole GDI injector under non-flashing conditions.

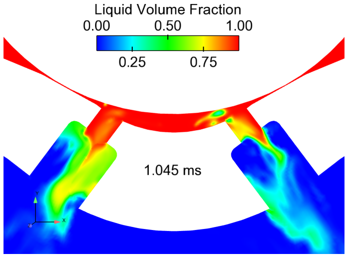

Figure 6.6: Liquid volume fraction just after needle closing i.e. $t = 1.045$ ms for non-flashing conditions showing cavitation.

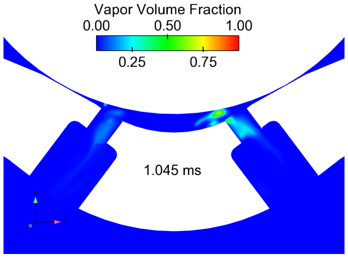

Figure 6.7: Vapor volume fraction just after needle closing i.e. $t = 1.045$ ms for non-flashing conditions showing cavitation.

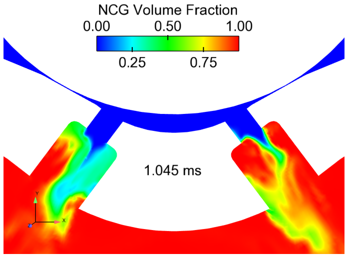

Figure 6.8: NCG volume fraction just after needle closing i.e. $t = 1.045$ ms for non-flashing conditions showing no presence of gas in the sac.

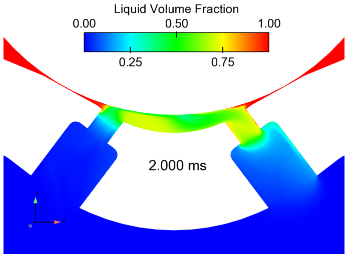

Figure 6.9: Liquid volume fraction long after needle closing i.e. $t = 2.000$ ms for non-flashing conditions.

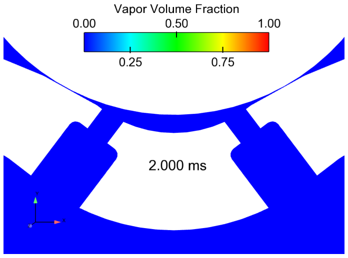

Figure 6.10: Vapor volume fraction long after needle closing i.e. $t = 2.000$ ms for non-flashing condition showing no traces of vapor inside the sac.

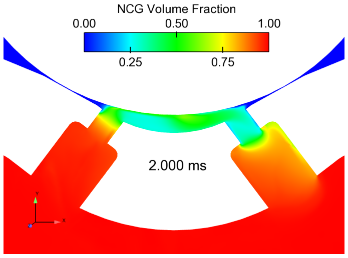

Figure 6.11: NCG volume fraction long after needle closing i.e. $t = 2.000$ ms for non-flashing condition showing presence of gas inside the sac.

Drastically different sac and nozzle conditions are observed for the flash boiling case, where the ambient pressure ratio is 0.68. The simulation captures low pres-

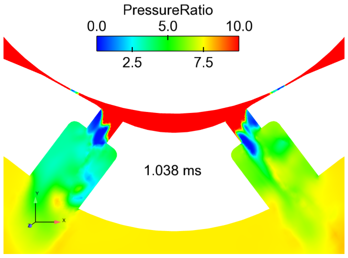

Figure 6.12: Pressure ratio just before needle closing i.e. $t = 1.038$ ms for non-flashing conditions.

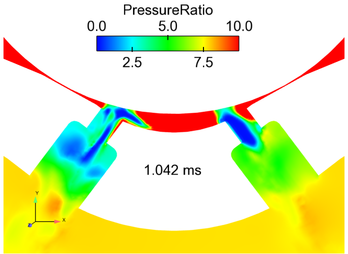

Figure 6.13: Pressure ratio just after needle closing i.e. $t = 1.042$ ms for non-flashing conditions.

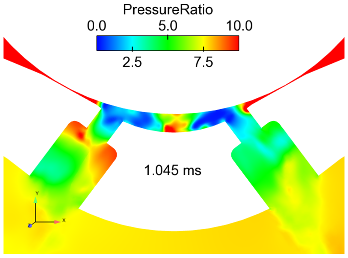

Figure 6.14: Pressure ratio after needle closing i.e. $t = 1.045$ ms for non-flashing conditions showing receding low pressure waves.

sure regions inside the counter bore region. These regions further increase vapor generation and create a vapor core in the jet emanating from the nozzle, as seen in Fig. 6.15, 6.16, 6.18, 6.19, 6.24, and 6.25. Post needle closure, a local low pressure region is observed inside the sac leading to the vapor generation seen in figures 6.19 and 6.25. Further investigation shows similar reflecting pressure waves compared to the non-flash boiling case. However, the vapors generated during the flash boiling case are much longer lived than the non-flashing case due to lower ambient pressure waves. The pressure in the sac region reaches the ambient pressure gradually during the needle's closed dwell phase as before. Nevertheless, the residual fuel inside the sac starts boiling off slowly as the ambient pressure is now below the saturation pressure. The resultant expanding fuel vapor inside the sac and nozzle does not allow the ambient gas to be entrained into the nozzle and sac. The post-injection boiling sac phenomena can be viewed in figures 6.21, 6.22, 6.23, and 6.26, taken at EOI. A similar boiling sac phenomenon was witnessed by [82] in a single axial-hole transparent nozzle with n-pentane as the test fluid under flashing conditions.

For further comparison between the flash boiling and non-flashing cases, the total volume of liquid and vapor fuel and non-condensible gas present in the sac and nozzle are calculated separately for each time step using the empty volume of the sac for

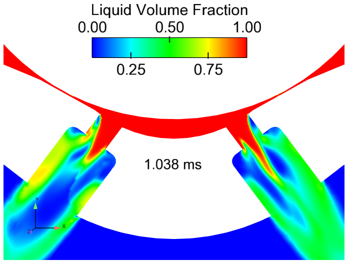

Figure 6.15: Liquid volume fraction before needle closing i.e. $t = 1.038$ ms for flash-boiling conditions.

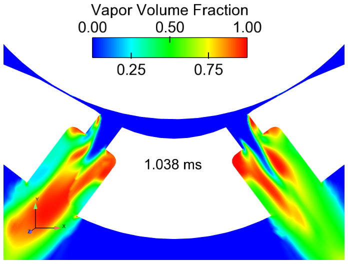

Figure 6.16: Vapor volume fraction before needle closing i.e. $t = 1.038$ ms for flash-boiling conditions.

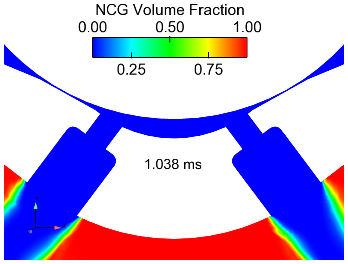

Figure 6.17: NCG volume fraction before needle closing i.e. $t = 1.038$ ms for flash-boiling conditions.

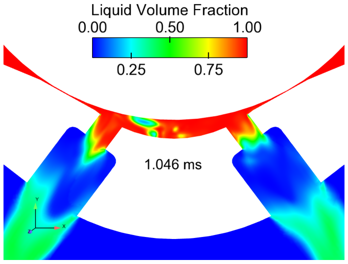

Figure 6.18: Liquid volume fraction just after needle closing i.e. $t = 1.046$ ms for flash-boiling conditions.

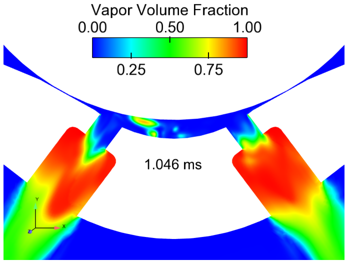

Figure 6.19: Vapor volume fraction long after needle closing i.e. $t = 1.046$ ms for flash-boiling conditions.

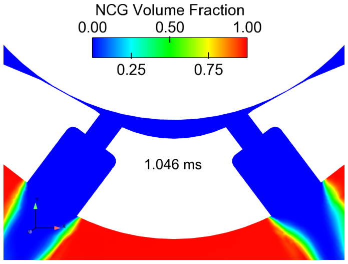

Figure 6.20: NCG volume fraction just after needle closing i.e. $t = 1.046$ ms for flash-boiling conditions.

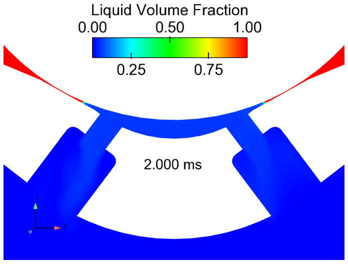

Figure 6.21: Liquid volume fraction long after needle closing i.e. $t = 2.000$ ms for flash-boiling conditions.

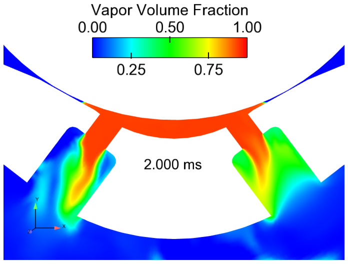

Figure 6.22: Vapor volume fraction long after needle closing i.e. $t = 2.000$ ms for flash-boiling conditions.

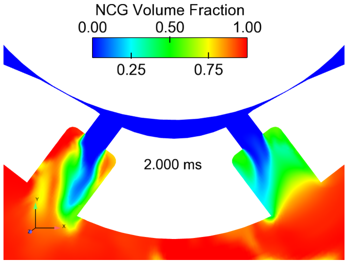

Figure 6.23: NCG volume fraction long after needle closing i.e. $t = 2.000$ ms for flash-boiling conditions.

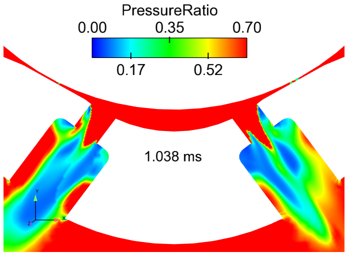

Figure 6.24: Pressure ratio just before needle closing, i.e., $t = 1.038$ ms for flash-boiling conditions.

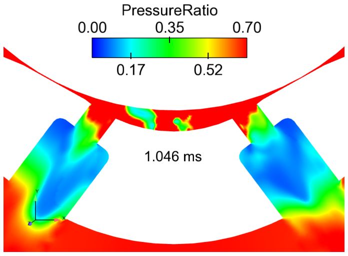

Figure 6.25: Pressure ratio just after needle closing, i.e., $t = 1.046$ ms for flash-boiling conditions.

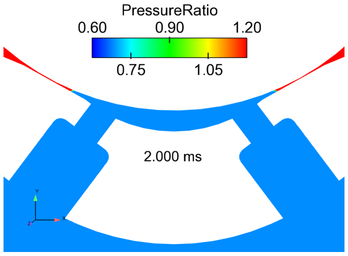

Figure 6.26: Pressure ratio long after needle closing, i.e., $t = 2.000$ ms for flash-boiling conditions.

reference. Fig. 6.27 and 6.28 represent the liquid volume fraction, vapor volume fraction, and NCG volume fraction for the complete injection cycle under the non-flashing and flashing conditions, respectively. From these figures, it can be concluded that the sac and nozzle reach a non-flashing postinjection condition where almost 50% of the space is occupied by the liquid fuel, while the other 50% is occupied by the non-condensible gas. Alternatively, for the flashing condition, 90% of the liquid fuel present in the sac and nozzle vaporizes to fill the sac and keep the non-condensible gas away from the nozzles. The total volume of the sac and nozzle for the 8-hole GDI injector is 0.09 mm^3. Hwang et al. [82] observed a boil-off time of 1 ms for the sac volume of 0.07 mm^3 with the pressure ratio of 0.69. From Fig. 6.28, it can be observed that the sac takes roughly 0.96 ms to get filled with 90% fuel vapor under flash-boiling condition. The boiling time is of similar order compared to the experimentally observed sac boil-off time. Even so, it should be noted that the experiments were performed with a different fuel and nozzle configuration.

6.2.3 The λ_2-criterion

The ensuing spray from the multihole GDI injector is highly turbulent. Thus, there exist many vortical coherent structures in the internal nozzle region. Furthermore, these vortices interact among themselves while either extending between

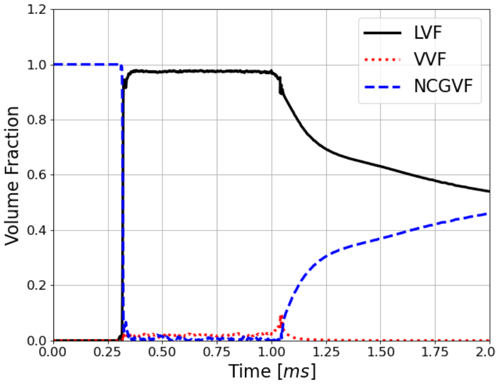

Figure 6.27: Liquid Volume Fraction, Vapor Volume Fraction and NCG Volume Fraction for a non flashing condition for the sac and nozzle region

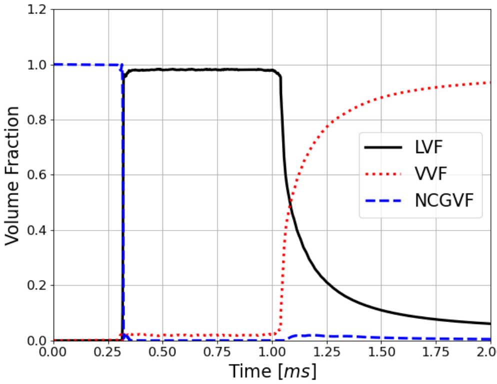

Figure 6.28: Liquid Volume Fraction, Vapor Volume Fraction and NCG Volume Fraction for a flash boiling condition for the sac and nozzle region

neighboring holes, or just ending in a single nozzle hole. In this section, we intend to capture the vortices which are present during the needle closing phase and impact the sac boil-off process. The λ_2-criterion defines a vortex as a connected fluid region with two eigen values of the velocity gradient tensor. It looks for a pressure minimum but removes the effects of unsteady straining and viscosity by discarding them. The definitions for the Q-criterion and the λ_2-criterion tend to be similar, however, their vortex predictions differ significantly for the regions where vortex stretching or compression are dominant. The λ_2-criterion is the median of the three eigen vectors $(\lambda_1, \lambda_2, \lambda_3)$ of $S^2 + \Omega^2$. Here, $S, and\ \Omega$ represent the symmetric and antisymmetric components of the velocity gradient. Nonetheless, the Q-criterion is evaluated as, $Q = -\frac{1}{2}(\lambda_1 + \lambda_2 + \lambda_3)$. For vortices in the variable density flows, Jeong et al. [88] observed better identification with the λ_2-criterion compared to the Q-criterion. According to them, the vortices can be visualized as iso-surfaces for different negative values of λ_2.

Fig. 6.29, and 6.30 include the iso-surfaces of the λ_2 criteria colored by the pressure ratio and the vapor volume fraction for the non-flashing condition at $t = 1.042ms$, respectively. The time stamp corresponds to the needle closure phase. The figures capture vortices extending from the sac region into the nozzle holes. Furthermore, the pressure in the vortex core falls below the saturation pressure, resulting in the formation of vapor bubbles inside the sac. This observation of sac cavitation corroborates our previous observations in Fig. 6.7.

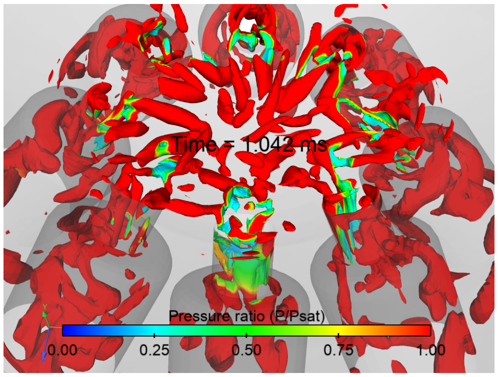

Figure 6.29: Iso-surface for $\lambda_2 = -8e + 11$ colored by the pressure ratio for the non-flashing condition at $t = 1.042ms$, i.e., after the needle closure.

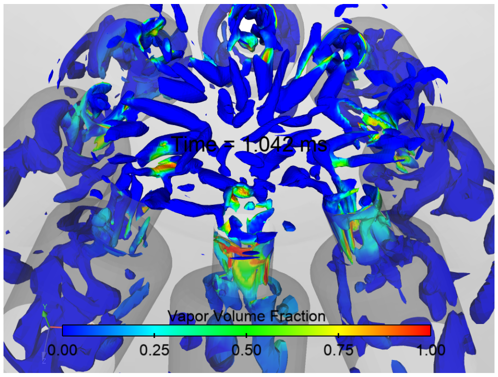

Figure 6.30: Iso-surface for $\lambda_2 = -8e + 11$ colored by the VVF for the non-flashing condition at $t = 1.042ms$, i.e., after the needle closure.

Similarly, vortices extending between the sac and the nozzle holes are also identified for the flash-boiling condition through the λ_2 criteria, as shown in Fig. 6.31 and 6.32. Nonetheless, the strengths of vortices are found to be lower compared to the non-flashing condition. Subsequently, these vortices tend to terminate early in the flash-boiling condition. These contrasting observations can be explained by the hypothesis that the flash-boiling condition has a lower angular velocity due to a higher moment of inertia compared to the non-flashing condition. The presented graph in Fig. 6.33 further supports our hypothesis. Fig. 6.33 represents the variations of the volume-averaged vorticity magnitude multiplied with the mixture density over the EOI phase. During the steady injection phase, i.e., when the needle is at the maximum lift, the ambient pressure does not impact the pressure inside the sac. However, post injection, the sac region experiences a lower pressure front for the flashing condition compared to the non-flashing case. Subsequently, the residual fuel inside the sac region vaporizes and expands, resulting in a higher moment of inertia for the flash-boiling condition. Hence, Fig. 6.33 indicates a lower magnitude of Enstrophy for the flashing condition. The evaluation procedures for Enstrophy in a rotating flow are mentioned below.

$$Enstrophy = \rho \int (||\Omega||^2_{tr})\, d\forall \tag{6.1}$$

$$Enstrophy = \rho \int (|\overrightarrow{\Omega}|^2)\, d\forall \tag{6.2}$$

$$\overrightarrow{\Omega} = [\Omega_i, \Omega_j, \Omega_k] \tag{6.3}$$

$$Enstrophy = \rho \int \left(\Omega_i^2 + \Omega_j^2 + \Omega_k^2\right)\, d\forall \tag{6.4}$$

$$\Omega = \frac{1}{2}\left(\nabla \mathbf{U} - (\nabla \mathbf{U})^T\right) \tag{6.5}$$

$$\Omega = \begin{bmatrix} 0 & \mathbf{U}_{j,i} - \mathbf{U}_{i,j} & \mathbf{U}_{k,i} - \mathbf{U}_{i,k} \\ \mathbf{U}_{i,j} - \mathbf{U}_{j,i} & 0 & \mathbf{U}_{k,j} - \mathbf{U}_{j,k} \\ \mathbf{U}_{i,k} - \mathbf{U}_{k,i} & \mathbf{U}_{j,k} - \mathbf{U}_{k,j} & 0 \end{bmatrix} \tag{6.6}$$

$$\Omega = \begin{bmatrix} 0 & \Omega_k & -\Omega_j \\ -\Omega_k & 0 & \Omega_i \\ \Omega_j & -\Omega_i & 0 \end{bmatrix} \tag{6.7}$$

In Eqns. 6.1, and 6.2, $||\Omega||$ and $\overrightarrow{\Omega}$ correspond to the spin tensor and the vorticity vector, respectively. The calculation procedures for the spin tensor are mentioned in Eqs. 6.5, 6.6.

6.2.4 Tip wetting

In an ideal scenario, the sac should be free of any trace of liquid fuel and should be filled with the non-condensible gas post-needle closure. If not, this liquid leads to tip wetting post-injection. Eventually, the unatomized liquid film on the injector

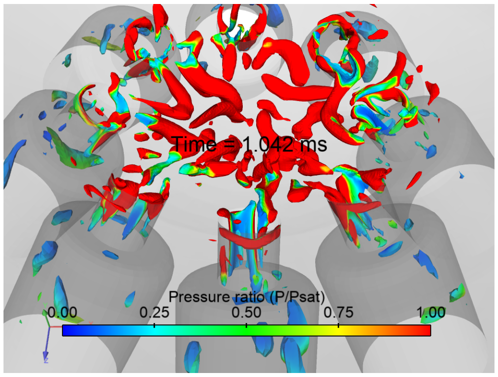

Figure 6.31: Iso-surface for $\lambda_2 = -8e + 11$ colored by the pressure ratio for the flashing condition at $t = 1.042ms$, i.e., after the needle closure.

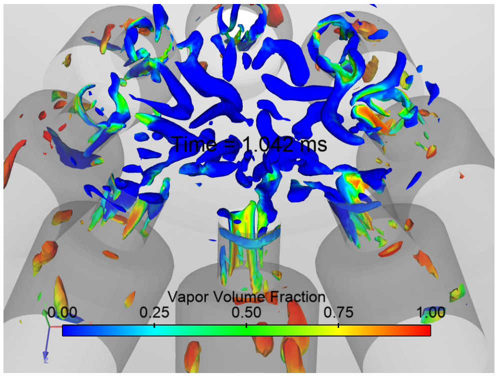

Figure 6.32: Iso-surface for $\lambda_2 = -8e + 11$ colored by the vapor volume fraction for the flashing condition at $t = 1.042ms$ i.e. after the needle closure.

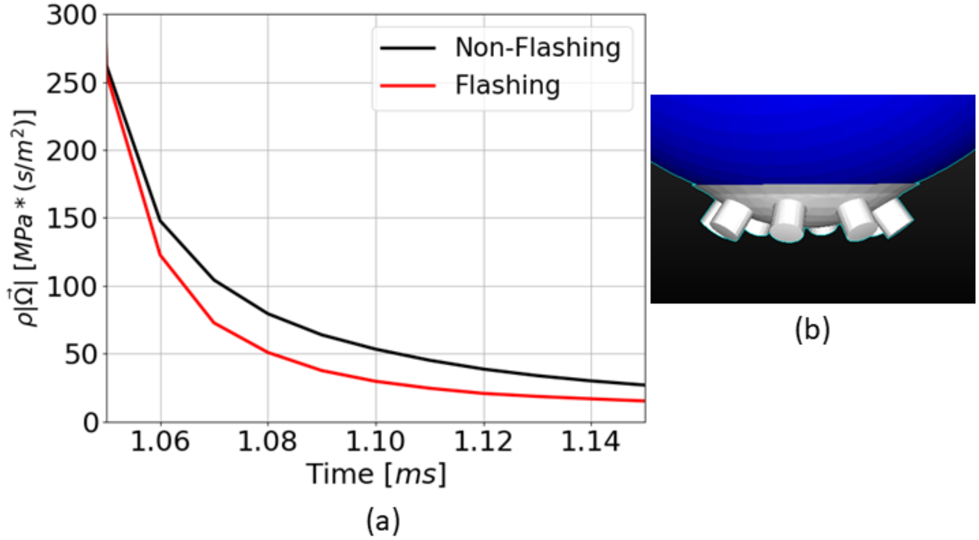

(a)

(b)

Figure 6.33: (a) Volume averaged density (ρ) multiplied with the vorticity magnitude $\left(|\vec{\Omega}|\right)$ vs time for the both non-flashing and flashing conditions. (b) The gray colored area showing the sac and nozzle regions which are used for the volume averaging.

tip leads to tip coking and soot formation [95]. Adverse effects of coked injectors on further spray and combustion cycles have also been reported [17], and [202]. In this section, we have identified the different tip-wetting phenomena for the non-flashing and flash-boiling conditions.

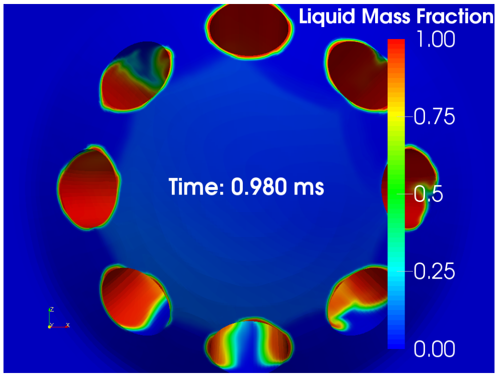

Figure 6.34: The injector tip colored by the liquid mass fraction for the non-flashing condition at $t = 0.98ms$.

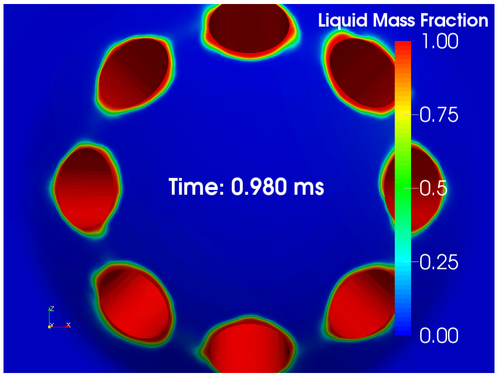

Figure 6.35: The injector tip colored by the liquid mass fraction for the flash-boiling condition at $t = 0.98ms$.

Contours of liquid mass fraction on the injector tip for both the non-flashing and flashing conditions during the needle closing phase, i.e., at $t = 0.98ms$ are included in Fig. 6.34 and 6.35, respectively. Clearly, for the flash-boiling condition, the injector tip near the counterbore is more wetted during the needle closing phase compared to the non-flashing condition. This phenomenon can be explained by the underexpanded jet theory, postulated by Lacey et al. [98] for flash-boiling spray. Based on this theory, when the underexpanded jet exits the counterbore region, it expands in the nozzle vicinity. However, for the non-flash boiling condition, the ambient gas entrains into the counterbore area creating buffer regions. These buffer regions inhibit the ensuing liquid jet to wet the tip regions around the counter bore exit which are away from the injector axis. Differences in jet behavior including the gas entrainment phenomena for both conditions can further be observed via the mid-plane clips in Fig. 6.36, and 6.37.

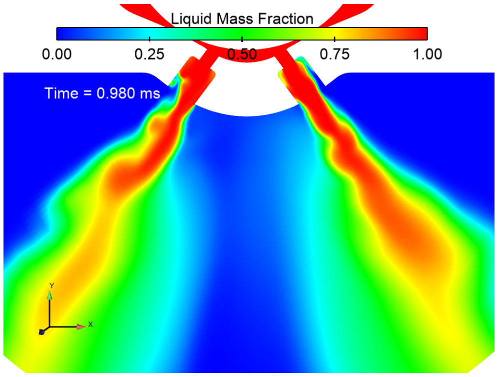

Figure 6.36: Mid plane clip colored by the liquid mass fraction for the non-flashing condition at $t = 0.98ms$ showing NCG entrainment and the liquid jet bending.

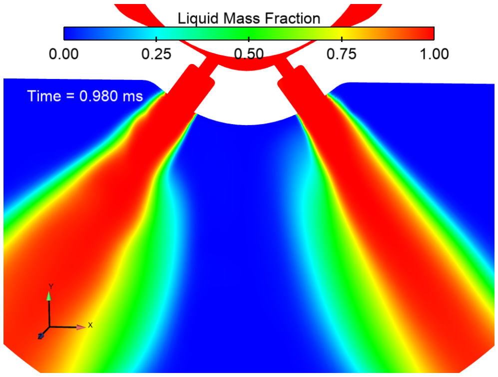

Figure 6.37: Mid plane clip colored by the liquid mass fraction for the flash-boiling condition at $t = 0.98ms$ showing no NCG entrainment.

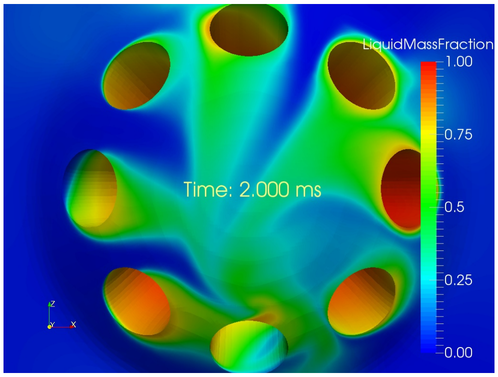

Figure 6.38: The injector tip colored by the liquid mass fraction for the non-flashing condition at $t = 2.0ms$.

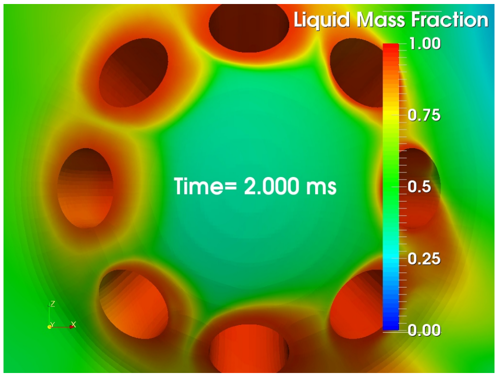

Figure 6.39: The injector tip colored by the liquid mass fraction for the flash-boiling condition at $t = 2.0ms$.

Furthermore, the tip-wetting behaviors are compared at $t = 2.0ms$, i.e., long after the needle closure. Again, more tip wetting is witnessed for the flash-boiling condition compared to the non-flashing condition, as seen in Fig. 6.38, and 6.39. These results complement the findings by Leick et al. [106]. Fig. 6.39 also captures the boiling film on the injector tip for the flash-boiling condition. Our current model formulations do not include surface tension terms. Hence, it is impossible to quantify the amount of fuel that sticks to the injector tip wall. Nonetheless, more studies are needed to fully understand the tip-wetting phenomena.

6.2.5 Dribble

Dribble is another EOI phenomenon which is undesirable, as it involves large droplets and unatomized ligaments. These unatomized fluid structures can be one of the major sources of soot emission in the GDI engines. The diffused interface approach coupled with the RANS turbulence model is not adequate to capture these detailed dribbling structures. Even so, an indication of dribble can be obtained by analyzing the ROI post injection [82]. Oscillations in the ROI can be observed in Fig. 6.40.

To obtain further indications of the dribble in the non-flash-boiling condition, the contours for the liquid mass fraction and the velocity magnitude are compared on a mid-plane clip, as seen in Fig. 6.41, and 6.42. In Fig 6.41, the left plume contains regions with high liquid mass fraction ($Liquid\ Mass\ Fraction \approx 0.75$) away from the injector indicating liquid fuel. Fig. 6.42 shows high velocity magnitude in these regions. Furthermore, the local maxima of the liquid mass fraction along the plume are separated by local minima. Velocities corresponding to these local minima of the liquid mass fraction are also found to be low, as shown in Fig 6.42. These intermittencies in the velocity magnitude and the liquid mass fraction profile along the liquid plume ensuing from the injector represent the disintegration of the

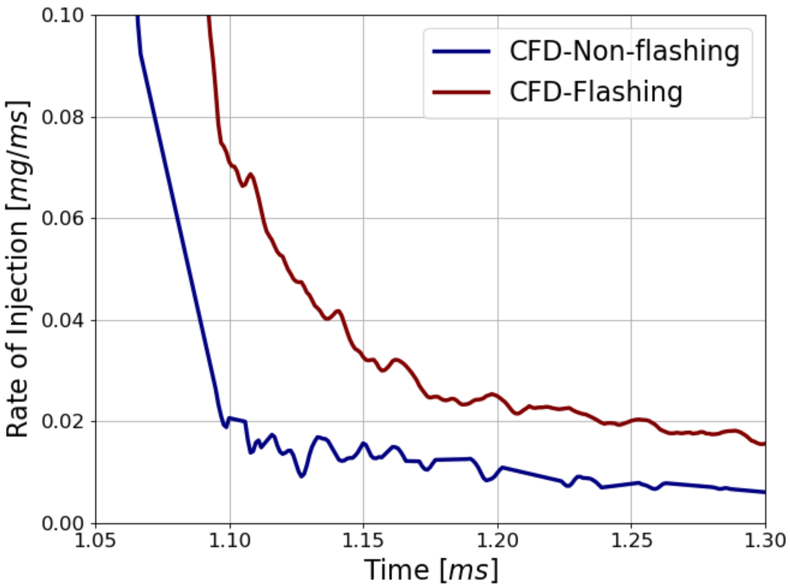

Figure 6.40: Simulated ROI vs time. Truncated ROI to indicate the oscillations post needle closure.

liquid plume. The current modeling approach does not track the interface, hence, cannot capture the jet break-up phenomena. Nonetheless, the above dispersion can be treated as indications for the dribbling phenomena. However, our current simulations in flashing conditions do not capture similar indications for the dribbling phenomena. A pilot study to include the surface tension models in the in-house HRMFoam solver will be expolred in the future chapter

6.3 Summary and conclusions

The current work includes the study of internal nozzle flow dynamics in the EOI phase for a multihole GDI injector operating at both non-flash boiling and flash-boiling conditions. Furthermore, the numerical predictions for the rate of injection are validated with the experimental observations. The main findings of this study are summarized as follows:

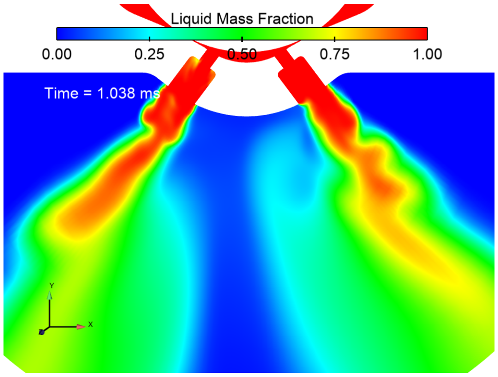

Figure 6.41: Mid plane clip colored by the Liquid Mass Fraction indicating dribble at $t = 1.038ms$ for the non-flashing condition.

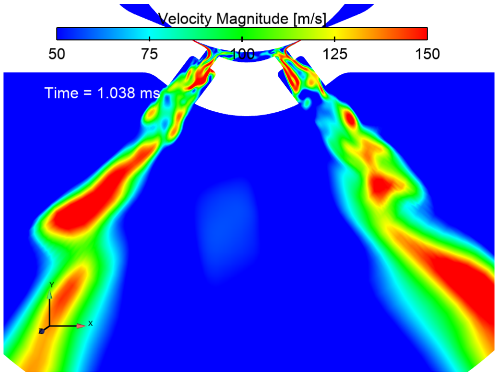

Figure 6.42: Mid plane clip colored by the velocity magnitude indicating different velocities in the ensuing liquid jet at $t = 1.038ms$ for the non-flashing condition.

- The ratio of ambient pressure to the saturation pressure has minimal effect on the rate of injection, corroborating the fact that these nozzles operate in choked conditions. The numerically observed spray injection duration is smaller compared to the experimental observation because of the difference in the assumed injector opening duration. These limitations can be avoided either by modifying the experimentally measured needle displacement curve or by changing the sealing constant. The modified curve should account for the sealing algorithm and the limitation of the initial mesh lift. However, we choose not to modify the experimentally observed boundary condition, i.e., the needle lift curve.

- Post need closure, the downstream low pressure waves are observed propagating into the nozzles. Additionally, the ambient gas travels into the sac for the non-flash boiling condition. Hence, a mixed sac condition is observed, where liquid fuel and ambient gas coexist. This observation supports the experimental findings in literature.

- For the flash-boiling condition, a boiling sac condition is observed at the EOI. Similar observations have been made by the experimentalists with different fuel and a different injector. Furthermore, the expanding vapors do not allow the ambient gas to enter into the sac region.

- During the needle closing phase, cavitating bubbles are found in the needle seat area due to the water-hammer effect. Additionally, just after needle closure, cavitating bubbles get generated in the sac due to the interactive sac vortices. These observations are confirmed with the analysis of λ_2 criterion. These bubbles can be detrimental to the injector's needle seat and sac.

- Furthermore, the amount of gas and vapor present in the sac and nozzle post-needle closure are also quantified. Under non-flashing conditions, the nozzle and sac are found to have almost equal amounts of liquid fuel and non-condensible gas long after needle closure. Yet, almost 90% fuel vapor is found in the flash-boiling condition. These results need further confirmation by experiments.

- Different tip-wetting characteristics are also observed in the flash-boiling condition compared to the non-flash boiling condition. During the needle closing phase, the tip area surrounding the nozzle outlet is found to be more wetted in the flash boiling condition compared to the non-flashing condition. This difference in observation can be attributed to the expansion characteristics of the underexpanded flashing jets. Furthermore, long after completion of the injection, the injector tip is found to be covered by liquid fuel and its vapor in the flash-boiling condition. This wetted tip can lead to tip coking during the combustion cycle. Nonetheless, our current simulations lack the ability to quantify the thickness of this liquid film.

- Indications of dribbling during non-flashing conditions are also captured.

The investigation of the EOI in the microsac GDI injector for a single injection event under both flashing and non-flashing conditions is a novel and interesting result.

The current investigation captures the nuances of EOI in different ambient conditions. The tip wetting and dribbling phenomena need further exploration and validation in different ambient conditions. In the future chapter, the current modeling capabilities of the diffused interface approach will be expanded to include formulations to model interfacial phenomena.

CHAPTER 7

A QUALITATIVE ANALYSIS OF THE TIP-WETTING PHENOMENA UNDER FLASH-BOILING CONDITIONS

The efficiency of an engine, as well as the composition of the exhaust emission are driven by the in-cylinder combustion process. Effective combustion further depends upon the preceding air-fuel mixing process [167]. The macroscopic characteristics of the the fuel spray, i.e., the shape of jet, entrainment of hot gas, and behaviors of individual liquid structures drive the mixing process [218]. Since the introduction of the direct injection strategy, there have been clear advantages and disadvantages. The direct injection strategy has improved the fuel economy while avoiding abnormal knocking [244], [75]. Hence, GDI engines emit less green house gases (CO_2) while achieving a specific power output in the lower engine speeds [224], [117]. Nonetheless, gasoline engines equipped with GDI injectors are associated with higher particulate emissions compared to the port injected engines [102].

In general, wetted walls such as spray impinged combustion chamber, wetted piston crown and wetted injector tip are considered to be the major sources of particulate matter (PM) and particulate number (PN) emissions [208]. These wetted areas gives rise to pool fires [243], [115]. Furthermore, in endurance tests, PN emissions are found to increase with the operation time, although the tests are started with clean injectors [208], [202]. This increase in PN values is accredited to the thin layer of carbon deposit on the injector tip [208]. Injectors with a coked tip, i.e., fouled injectors are observed to have different macroscopic spray characteristics compared to clean injectors [112].

The fuel film, developed on the injector tip can not fully evaporate before the onset of combustion. Eventually, the film encounters the flame front which leads to higher PN emissions and tip coking due to lack of oxygen and high in-cylinder temperature [212]. Additionally, this porous coking structure aids accumulation of more liquid fuel on the tip which further slows down the evaporation process, thus facilitating the growth of carbon deposits [212]. Consequently, researchers [158] have found direct relationships between the engine soot emissions and the wetting degree of the injector tip.

However, the physics of tip-wetting phenomena under different ambient conditions is poorly understood. Recently, a few experimentalists have made efforts to understand the complex wall wetting phenomena. Leick et al. [106] from their experiments with the Laser-induced Fluorescence (LIF) technique concluded that the injection pressure and the flash-boiling conditions are the biggest factors in influencing the tip-wetting phenomena. Park et al. [152] and Song et al. [208] indicate more tip-wetting in the flash-boiling conditions. However, they don't explain the mechanism of the tip-wetting process. Based on the hypothesis proposed by Medina et al. [123], the tip-wetting mechanism includes several distinct wetting processes such as wide plume wetting, voretx tip wetting due to recirculation/air entrainment, and fuel dribble wetting. According to them, wide plume wetting is encountered when the liquid fuel reaches the outlet corner edge. Consequently, a film around the outlet is formed due to surface roughness, wide plume and adhesive forces. Furthermore, they theorize that the droplets stripping off the spray plume move towards the tip due to the air entrainment vortices leading to the vortex tip-wetting phenomena. Similarly, during the end of injection, they postulate the dribbling fuel to attach itself to the injector tip because of large size and low axial momentum. However, their engine experiments do not reveal the macroscopic/microscopic fluid dynamics behaviors to support their hypothesis due to the lack of physical and optical access to the injector tip. They also fail to explain the effects of different ambient conditions on the proposed hypothesis. Recent LIF and long microscopic experiments by Xiao et al. [236] support the theory of expansion wetting and the dribble wetting proposed by Medina et al. [123]. Furthermore, they also indicate that higher fuel temperatures negates the effects of flash-boiling on the tip-wetting phenomena. However, their experiments are performed in a two-hole GDI injector, where plume-to-plume interactions are insignificant. They also do not capture the internal flow dynamics of the injector which would impact the wetting process because of optical inaccessibility.

Therefore, computational studies are required to understand the complex wetting phenomena. Recently, Mouvanal et al. [133] simulated the EOI phase of a three hole GDI injector using the commercial CFD tool, ANSYS Fluent. Nonetheless, they only indicate certain wetted tip area around the counter-bore exit for the non-flashing condition. Other computational efforts include the work by Fischer et al. [67] who employ a Lagrangian framework coupled with the wall film model to visualize the wetting behavior. Their modeling framework is informed by the in-nozzle Eulerian simulations. However, they generate the Lagrangian parcels inside the counter-bore regions where the dense spray exists. Validity of the Lagrangian models in the near-nozzle regions will be reviewed in the future chapters. Furthermore, Mohapatra et al. [127] indicate different wetting behaviors under flashing and non-flashing conditions while simulating the internal flow by a diffuse interface based approach. The tip-wetting analysis of the current chapter will be premised on the suggestions by Mohapatra et al. [127]. The chapter includes a detailed qualitative analysis of the wetting behaviors under different ambient conditions. Besides, the simulation setups of the single injection event described in the previous Sec. 6.1 are used for the current analysis. The current modeling capabilities of the in-house code, discussed in the previous chapter 4 do not include the surface tension model. These models are essential in low Weber number flows, hence are not preferred for the spray modeling paradigm which involves high

Reynolds number and Weber number. Hence, the current modeling methods can not fully resolve the slow moving tip-wetting flow. Nevertheless, in the current chapter, indications of the tip-wetting flow are obtained by projecting the liquid fuel mixture of the boundary cells on to the tip-wall.

7.1 Results and discussion

To study the detailed mechanisms involved in the tip-wetting phenomena under different ambient conditions, the total simulation duration is subdivided into four distinct subphases based on the needle motion transients. The first subphase corresponds to the needle opening and quasi-steady state transients, whereas, the second phase captures the mechanisms involved during the quasi steady state in addition to the needle downward motion period. Subsequently, the third and fourth phases include the pre and post needle closure tip-wetting phenomena, respectively. The four distinct phases are marked on the needle displacement curve in Fig. 7.1. The different wetting mechanisms involved during these phases are discussed in the following subsections.

7.1.1 Phase One: Needle opening phase

In the current simulations, phase one includes the transients between 0.34 ms to 0.69 ms of the simulation period. Hence, during this phase, the needle moves from the seated condition and attains the maximum steady needle lift. In the flashing condition, indications of wetted tip around the counterbore exit is captured, as seen in Fig. 7.2. However, the wetting is not prominent in the non-flashing condition. This difference in observation is explained by the plume-wetting mechanism postulated by Medina et al. [123], and further supported by Fig. 7.3. Fig. 7.3 captures the jet expansion phenomena for the flashing condition. In contrast, the ambient air enters into the nozzles for the non-flashing condition resulting in buffer layers. These buffer

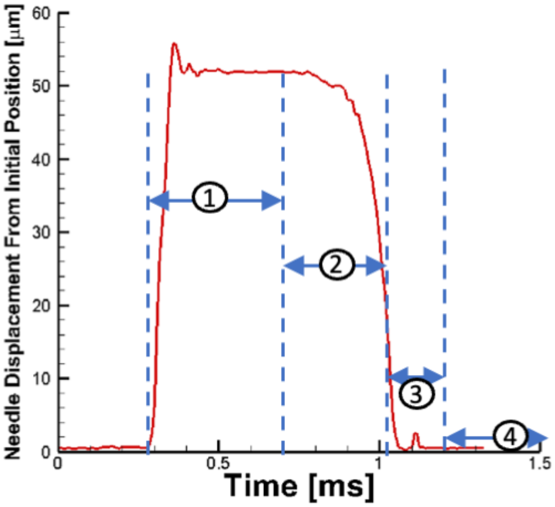

Figure 7.1: Different phases of tip-wetting phenomena marked on the needle displacement curve.

layers do not let the non-flashing jets to expand in the near nozzle regions resulting in different tip conditions.

7.1.2 Phase Two: Downward moving needle phase

The downward moving needle phase corresponds to the interval of 0.7 ms to 1.05ms. This phase also includes 0.1 ms of the quasi-steady state. Fig. 7.2 indicates the tip-wetting behaviors under both non-flashing (left) and flashing (right) conditions. The figure exhibits traces of fuel mass on the tip around the injector axis for the non-flashing condition. For non-flashing, the plumes are observed to be dispersive in nature due to the buffer layers present in the counterbore regions. Moreover, vortices created around the plumes impart an upward motion to the ambient gas. This upward moving gas carries the dispersed fuel mass towards the injector tip, refer Fig. 7.5.The described wetting mechanism is similar to the vortex tip wetting theory proposed by Medina et al. [123]. However, similar wetting process is not observed for the flash-boiling condition. The expansion jet wetting mechanism still dominates the tip-wetting process in flashing.

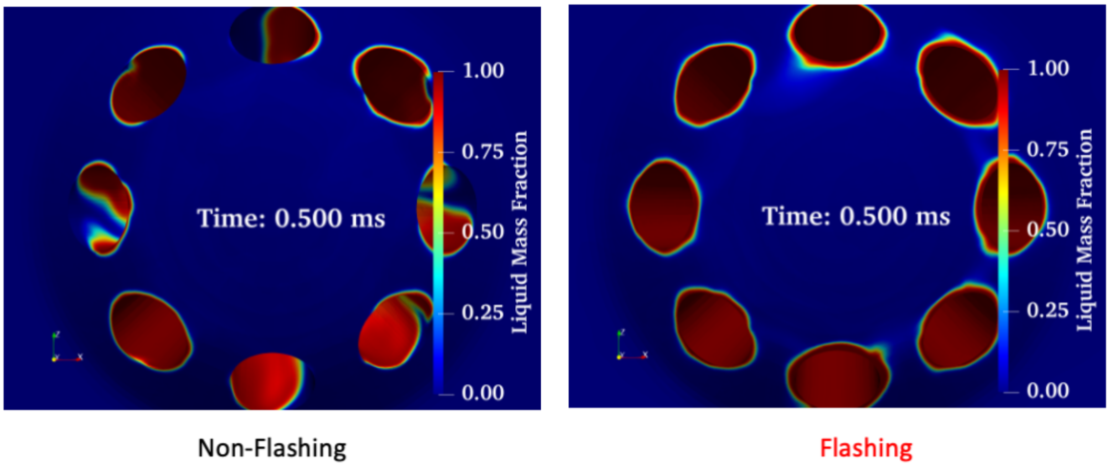

Figure 7.2: Tips colored by the liquid mass fraction (LMF) indicating different wetting phenomena for the non-flashing(left) and flashing (right) conditions.

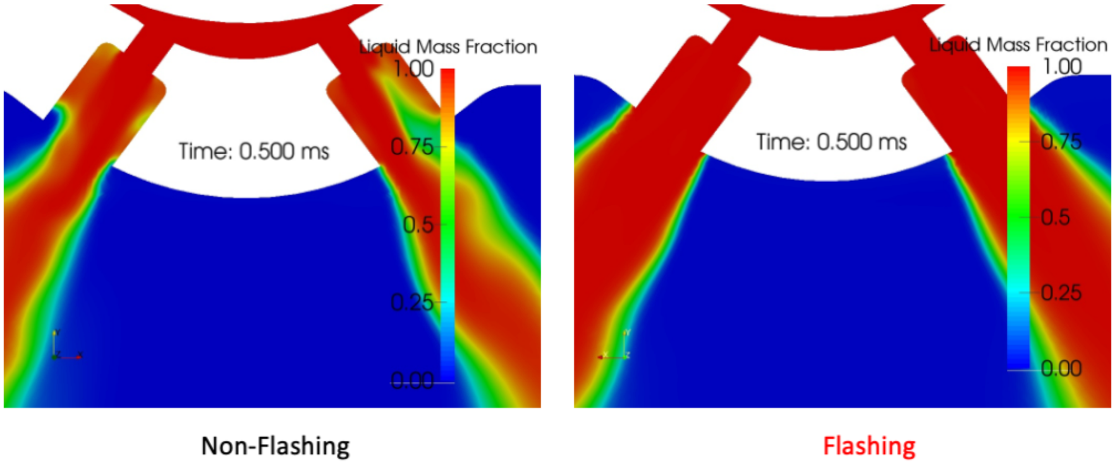

Figure 7.3: Mid-plane clip colored by the liquid mass fraction (LMF) indicating different jet behaviors for the non-flashing(left) and flashing (right) conditions.

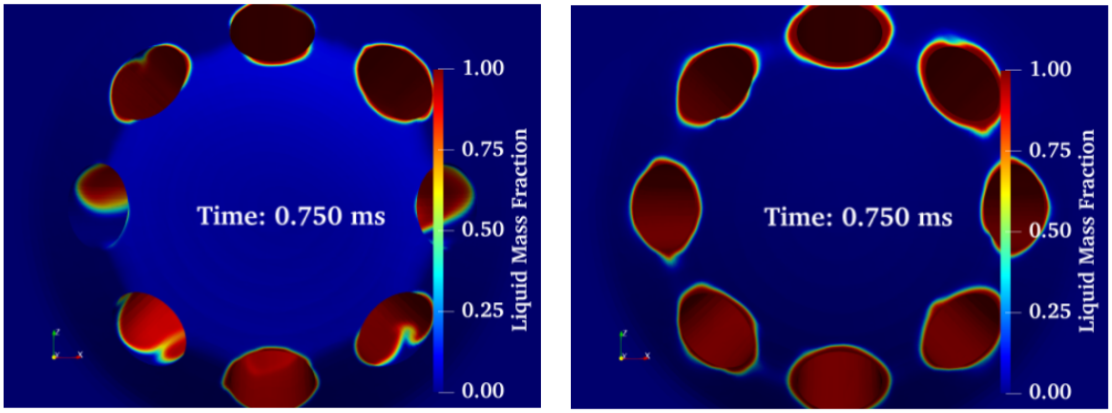

Non-Flashing

Flashing

Figure 7.4: Tips colored by the liquid mass fraction (LMF) indicating different wetting phenomena for the non-flashing(left) and flashing (right) conditions.

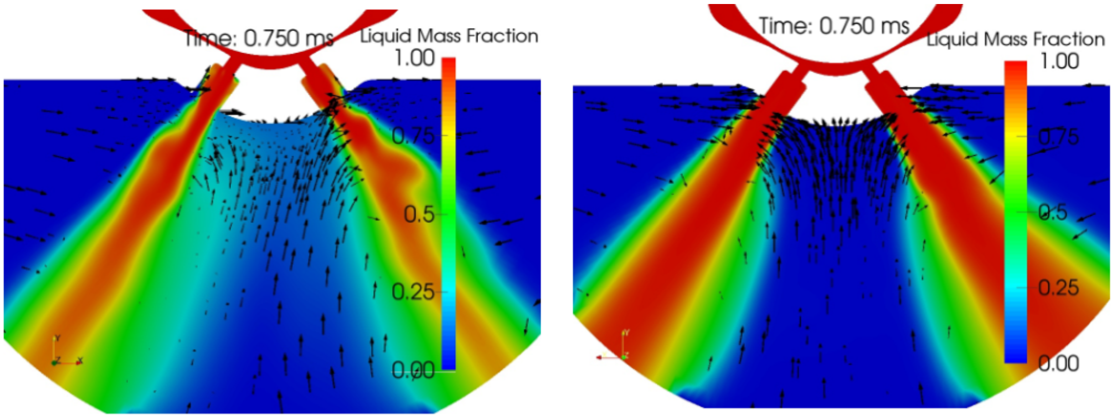

Non-Flashing

Flashing

Figure 7.5: Mid-plane clip colored by the liquid mass fraction (LMF) with glyph vectors scaled by the velocity magnitude indicating different mechanism driving the wetting phenomena for the non-flashing(left) and flashing (right) conditions.

7.1.3 Phase Three: Needle closing phase

As discussed in previous Ch. 6, this phase corresponds to the duration when the gap between the needle and the seat region is small enough to trigger the sealing algorithm, i.e., $1.06ms - 1.2ms$. Eventually the needle closes, disconnecting the upstream flow domain from the sac region. As a result, the momentum of the spray plumes starts to decrease creating dribbling like pheonmena, refer Sec. 6.2.5. However, the ambient gas still maintains the motion towards the injector holes. Thus, vortices get formed in the ambient, as shown in Fig. 7.6. These vortical structures carry the slow moving fuel mass towards the injector. Hence, a significant amount of tip-wetting is predicted immediately after the needle closure for both non-flashing and flashing conditions, refer Fig. 7.7. This tip-wetting mechanism further supports the fuel dribble wetting hypothesis of Medina et al. [123].

7.1.4 Phase Four: Post-needle closure phase

Fig. 7.8 includes the injector tip colored by the liquid fuel mass fraction for the time stamps of 1.25 ms, 1.5 ms, and 2.00ms for different ambient conditions. At this point, the needle has already been closed. The sealing algorithm discussed in the Sec. 4.2 ensures no flow from the upstream of the seat to the sac-nozzle regions. The figure suggests a gradual increment of fuel mass on the tip. Even so, for the non-flashing condition, footprints of the fuel mass are found to decrease on the injector tip. The previous discussion in Ch. 6 shows that the sac region attains the pressure equilibrium with respect to the ambient condition. The discussion further indicates mixed sac and boiling sac conditions for the non-flashing and flashing conditions, respectively. Hence, it would be safe to conclude that post needle closure, the tip-wetting phenomena is driven by the sac conditions. This conclusion is consistent with the hypothesis by Medina et al. [123]. Thus, in flashing, the post needle closure tip wetting is driven by the vapor dribbling phenomena.

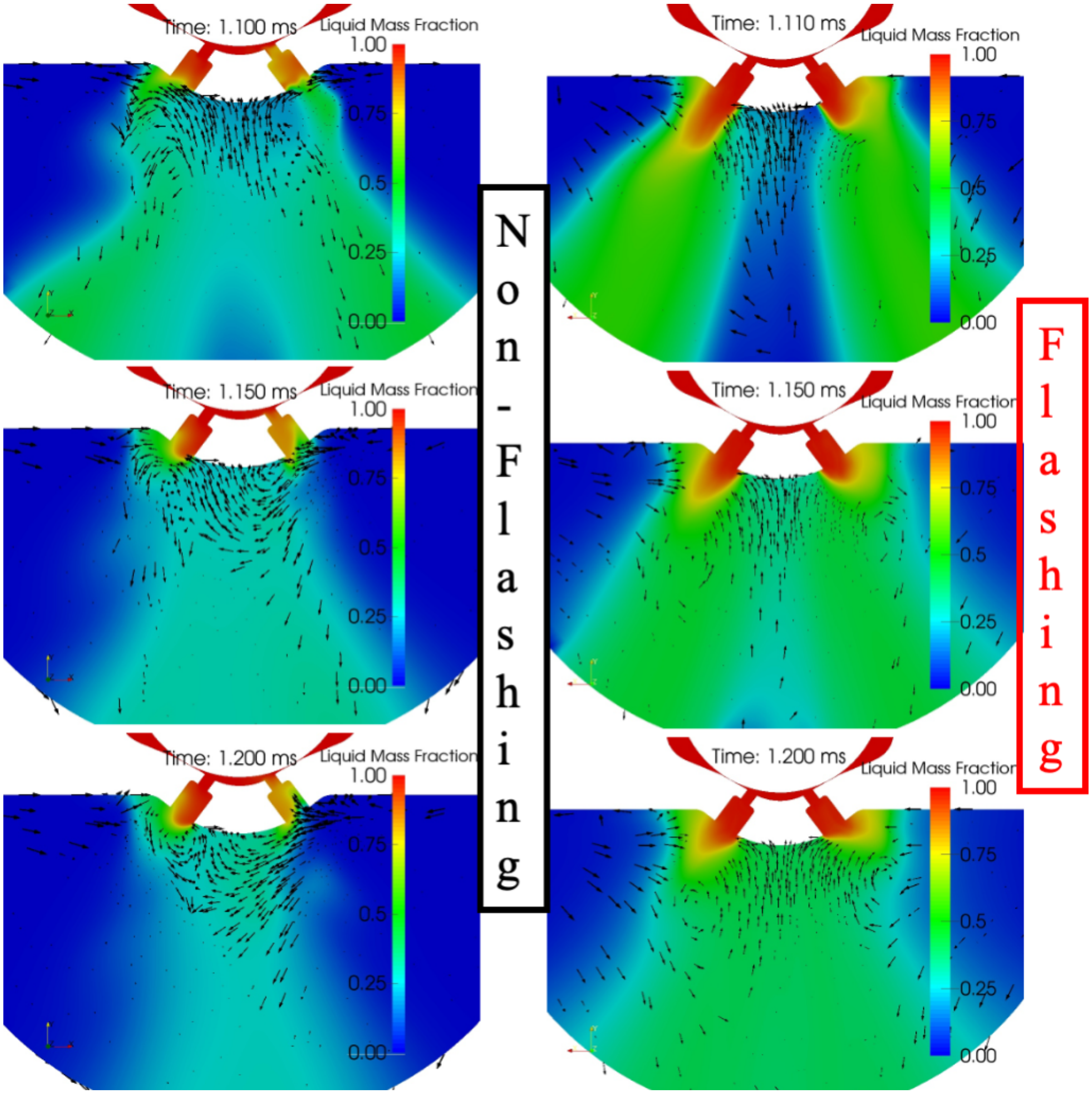

Figure 7.6: Mid-plane clip colored by the liquid mass fraction (LMF) with glyph vectors scaled by the velocity magnitude indicating the mechanism behind the wetting phenomena for the non-flashing(left) and flashing (right) conditions during needle closure.

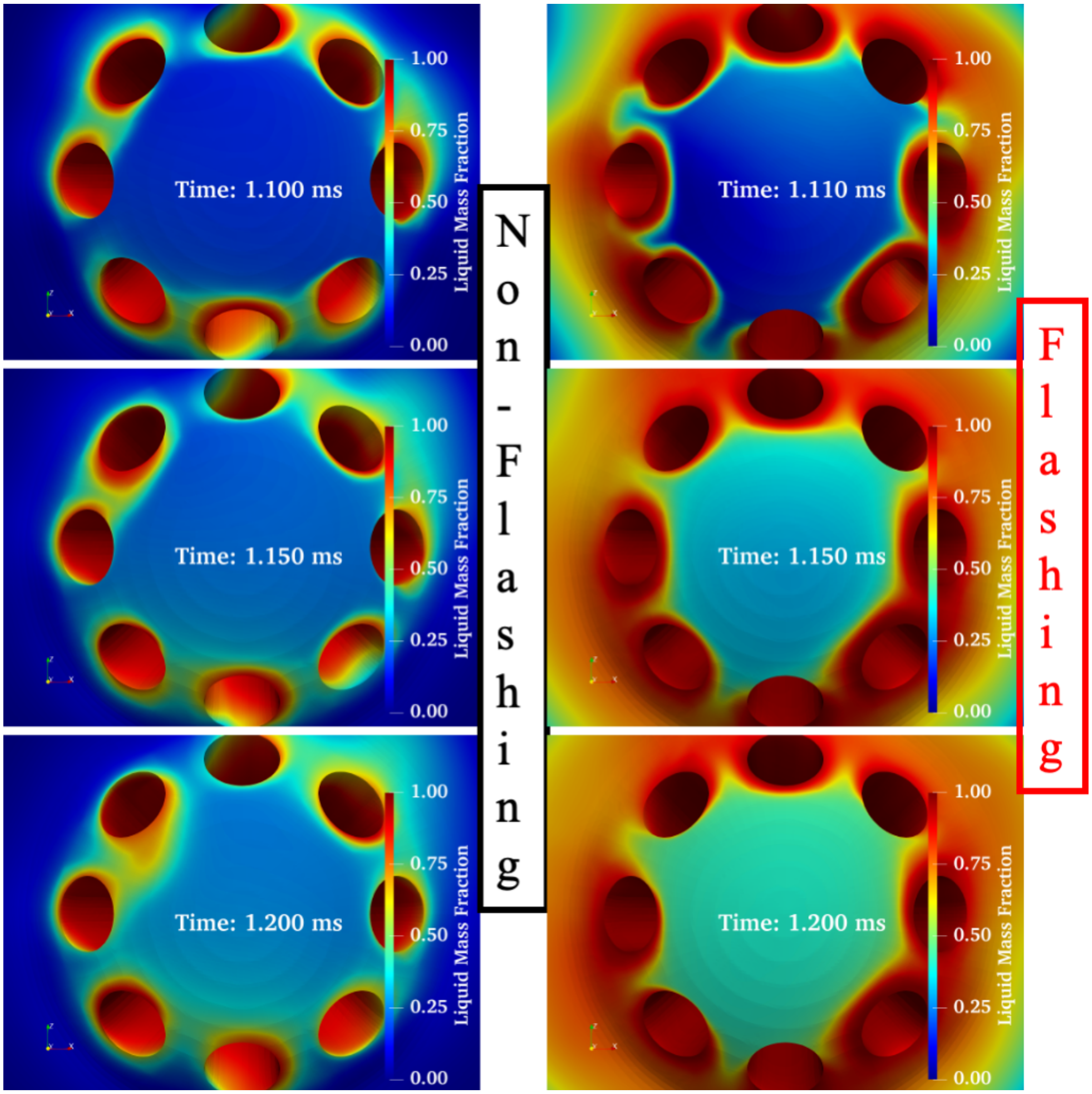

Figure 7.7: Tips colored by the liquid mass fraction (LMF) indicating different wetting phenomena for the non-flashing(left) and flashing (right) conditions during needle closure.

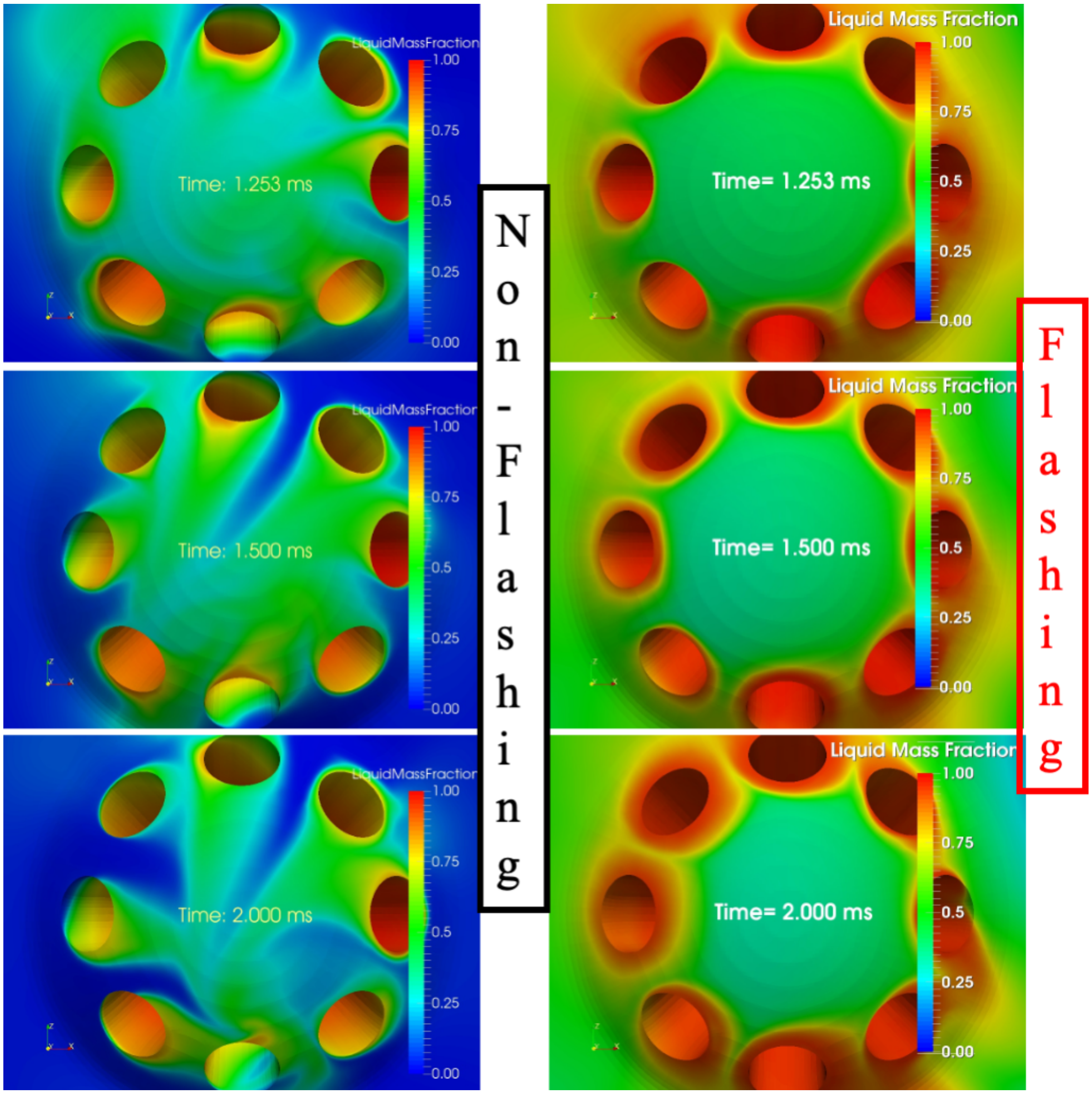

Figure 7.8: Tips colored by the liquid mass fraction (LMF) indicating different wetting phenomena for the non-flashing(left) and flashing (right) conditions post-needle closure.

7.2 Conclusions

In the current chapter, the in-house solver HRMFoam in conjunction with the sealing model is applied to simulate the tip-wetting phenomena. The current solver does not include surface tension models which are essential to simulate the low Weber number wall bounded flows. Hence, the solver can not fully resolve and quantify the fuel mass sticking to the injector wall. However, a qualitative study of the tip-wetting behaviors under different ambient conditions is performed by projecting the mixture mass of the boundary cells onto the injector wall. This study is able to corroborate the hypothesis put forward by experimentalists to explain the complex wall wetting phenomena. Major findings of this study are summarized below.

- The complete injection duration is subdivided into multiple subphases to explain the distinct wetting mechanisms which are prevalent in different ambient conditions.

- The flashing spray plume expansion drives the wall wetting behaviors around the counterbore exit. However, in the non-flashing condition, wetting is inhibited by the buffer regions between the spray plumes and the non-condensible gas.

- During the downward motion of the needle, traces of fuel mass are observed on the injector tip for the non-flashing condition. Upward moving ambient gas carrying the dispersed fuel is accounted for such tip wetting.

- A significant amount of tip-wetting is observed during needle closure phase for both flashing and non-flashing conditions. During this period, wetting is dominated by the dribbling fuel and upward moving ambient gas.

- Post needle closure, tip wetting is driven by the sac conditions. Hence, fuel mass on the injector tip tend to decrease because of mixed sac conditions. However, in the flash-boiling condition, boiling sac results in vapor dribbling which drives the increasing tip-wetting behaviors.

CHAPTER 8

QUASI STEADY STATE ANALYSIS OF MOVING NEEDLE GDI SIMULATIONS

Gasoline direct injection (GDI) offers the opportunity to carefully tailor the delivery of fuel. A designer could hypothetically control where and when the fuel arrives in the cylinder. However, to take advantage of this opportunity, we must have the capability of predicting how a specific injector will deliver fuel and how this fuel will atomize and mix with the surrounding air. This predictive ability depends on our understanding of the internal flow intricacies. The internal details of fuel injectors have a profound impact on the emissions from gasoline direct injection (GDI) engines [229]. However, the impact of injector design features is not completely understood due to the difficulty in observing and modeling internal injector flows. GDI flows involve moving geometry, flash boiling, and high levels of turbulent two-phase mixing.

To understand the effects of the internal flow field of the GDI injector on the near nozzle behavior, quasi-steady state analysis of the moving mesh simulations are included in this chapter. In moving needle simulations, quasi-steady state corresponds to the period when the needle is at the maximum lift. Hence, the flow field variables are time averaged over the same duration, i.e., 0.4-0.9 ms in the current simulations to eliminate the transient variability. This allows for a better understanding of the effects of different ambient conditions (non-flashing and flashing) on the internal and near nozzle spray behaviors during the steady injection phase. The simulation setups described in the previous section 6.1 are used for the current analysis.

8.1 Results and discussion

8.1.1 Time averaged hydraulic coefficients

Mass flux measurements in addition to the momentum flux measurements, have proven to be essential to characterize the hydraulic behavior of injection systems [155], and [156]. Payri et al. [155], and [156] defined dimensionless coefficients such as discharge coefficient (C_d), momentum coefficient (C_M), velocity coefficient (C_v), and area coefficient (C_a) to describe the internal flow behaviors based on these measurements.

- **Discharge coefficient:** This coefficient is defined as the ratio of real or measured mass flux ($\dot{m}$) to the maximum theoretical mass flux ($\dot{m}_{th}$). Additionally, the theoretical mass flux is calculated by considering the maximum Bernoulli velocity (U_{th}) crossing the total nozzle cross-sectional area (A_0). The correlations for the computationally and theoretically predicted mass flow rates are represented in Eqn. 8.1, and 8.2.

$$\dot{m} = \int_{A_0} \rho \; U \, dA \tag{8.1}$$

$$\dot{m}_{th} = A_0 \rho_f \sqrt{\frac{2\Delta P}{\rho_f}} \tag{8.2}$$

$$C_d = \frac{\dot{m}}{\dot{m}_{th}} \tag{8.3}$$

In Eq. 8.1, and 8.2, $\rho,\ \rho_f,\ U,\ and\ \Delta P$ represent the mixture density, density of the liquid fuel, velocity at the nozzle exit, and the pressure drop, respectively.

- **Momentum coefficient:** Similarly, the momentum coefficient is defined as the ratio of the measured momentum flux $\left(\dot{M}\right)$ to the maximum theoretical momentum flux $\left(\dot{M}_{th}\right)$, Eqn. 8.4. Again, the theoretical momentum flux is evaluated based on the Bernoulli assumption, as shown in Eqns. 8.5 and 8.6.

$$C_M = \frac{\dot{M}}{\dot{M}_{th}} \tag{8.4}$$

$$\dot{M}_{th} = 2A_0\Delta P \tag{8.5}$$

$$\dot{M} = \int_{A_0} \rho\, U^2\, dA \tag{8.6}$$

- **Velocity coefficient** This coefficient correlates the effective velocity (U_{ef}) to the maximum theoretical Bernoulli velocity. It is calculated with the following equation,

$$C_v = \frac{U_{ef}}{U_{th}} = \frac{U_{ef}}{\sqrt{2\Delta P/\rho_f}} \tag{8.7}$$

- **Area coefficient**. This coefficient is used for evaluating the reduction of the effective area (A_{ef}) with respect to the geometric one, and it is calculated as

$$C_a = \frac{A_{ef}}{A_o} \tag{8.8}$$

Based on these definitions, Mohapatra et al. [128] show alternative approaches to evaluate the coefficient of velocity and the coefficient of area, as shown in Eq. 8.9, and 8.10. These coefficients help in identifying the head loss at the nozzle outlets that would otherwise be obscured by the coefficient of discharge. Furthermore, Lagrangian models described in section 3.1 use these dimensionless coefficients to initialize parcels in engine simulations.

$$C_v = \frac{C_M}{C_d} \tag{8.9}$$

$$C_a = \frac{C_d}{C_v} \tag{8.10}$$

In the current section, the transient flow field variables such as density and velocity are averaged over the quasi-steady phase and the corresponding rate of injection

(ROI), rate of momentum (ROM), and dimensionless hydraulic coefficients are evaluated for both the flashing and non-flashing conditions. Furthermore, the overall computational predictions for the non-flashing conditions are validated against the available experimental data [155], as shown in Table 8.1. The percentage difference between the experimentally measured ROI and the computational prediction for the non-flashing condition is one percent; as a result the corresponding difference between the coefficient of discharge is also less than one percent. However, a higher percentage of difference is observed for the ROM, which translates into higher differences (around 10 %) in other dimensionless coefficients (C_M, C_v, C_a). These observed differences can be attributed to two factors. The first factor is the experimental uncertainities in spray momentum measurements, as indicated by Payri et al. [155]. The experiments are performed while mounting the spray G injector in a frontal configuration, i.e., the injector axis aligns with the axis of the piezoelectric sensor. Hence, the spray impact angle has to be considered for the momentum measurements. For the non-flashing condition, the spray impact angle is different from the injector drill angle and is highly transient [132]. Payri et al. [155] also observed an uncertainty of six percent in the momentum measurement due to an error of 5^0 in the spray impact angle measurement. The second factor is the modeling errors, as indicated by Mohapatra et al. [128]. According to them, the CFD models over-predict the downstream fuel density. Moreover, they suggest to revisit the mixing model of non-condensible gas with the liquid fuel. A detailed comparison of the experimentally observed fuel density and the CFD predictions will be included in the subsequent subsection.

Furthermore, Table 8.1 captures the differences in the hydraulic coefficients for different ambient conditions. In comparison to the flashing condition, higher coefficients for the momentum and velocity are observed under the non-flashing condition. The percentage of difference is around four percent. The Table 8.1 further indicates the hole-to-hole variations in all computationally predicted hydraulic coefficients. For the

-		C_d	C_M	C_v	C_a	ROI (g/s)	ROM (N)
Experiment	Non-flashing	0.52	0.40	0.77	0.67	13.82	2.63
CFD All hole	Non-flashing	0.52	0.44	0.85	0.61	13.63	2.89
	Flashing	0.51	0.42	0.82	0.62	13.60	2.86
H1	Non-flashing	0.53	0.44	0.83	0.64	1.74	0.36
	Flashing	0.51	0.44	0.86	0.59	1.70	0.37
H2	Non-flashing	0.54	0.46	0.85	0.63	1.76	0.37
	Flashing	0.52	0.44	0.85	0.61	1.72	0.37
H3	Non-flashing	0.50	0.42	0.84	0.60	1.63	0.34
	Flashing	0.51	0.41	0.80	0.64	1.69	0.34
H4	Non-flashing	0.52	0.44	0.85	0.61	1.70	0.36
	Flashing	0.51	0.43	0.84	0.61	1.70	0.36
H5	Non-flashing	0.51	0.43	0.84	0.61	1.68	0.35
	Flashing	0.50	0.42	0.84	0.60	1.66	0.35
H6	Non-flashing	0.53	0.46	0.87	0.61	1.75	0.38
	Flashing	0.52	0.41	0.79	0.66	1.72	0.35
H7	Non-flashing	0.52	0.45	0.86	0.60	1.70	0.37
	Flashing	0.50	0.41	0.82	0.61	1.68	0.34
H8	Non-flashing	0.51	0.43	0.84	0.61	1.66	0.35
	Flashing	0.51	0.44	0.86	0.59	1.72	0.37

Table 8.1: Time averaged hydraulic coefficients (C_d, C_M, C_v, $and\, C_a$), ROI, and ROM for all holes combined and the individual holes under both flash-boiling and non-flashing conditions.

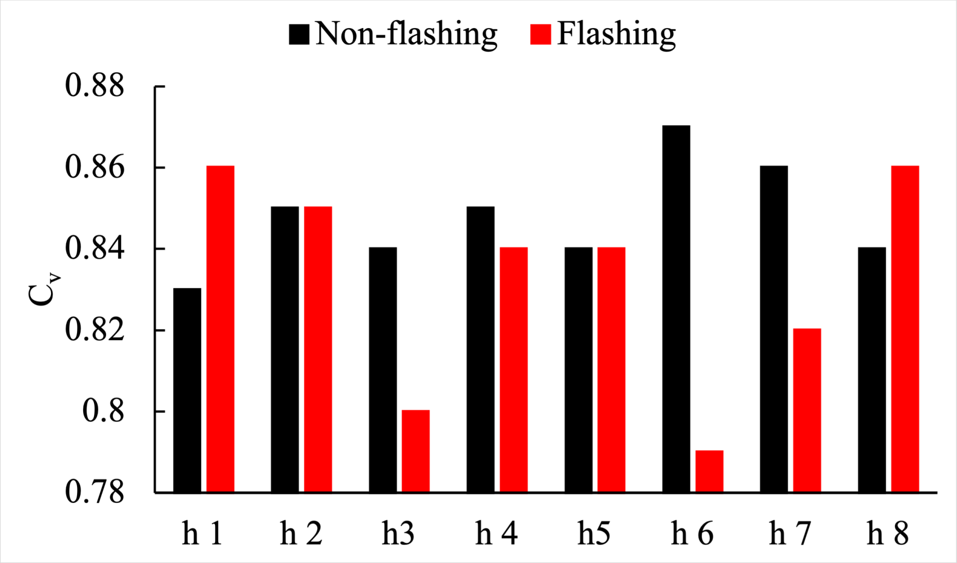

Figure 8.1: Bar chart showing the hole-to-hole variations in the coefficient of velocity under non-flashing and flashing conditions

flash-boiling condition, holes numbered one and six have the highest and the lowest coefficient of velocity, respectively. Whereas, the same holes have the lowest and the highest C_v under the non-flashing condition, as seen in Fig. 8.1. Similarly, the hole numbered one has the highest coefficient of area in the non-flashing condition, but the lowest in the flashing condition, refer Fig. 8.2. Under flashing, the hole numbered six has the highest coefficient of area.

8.1.2 Hole-to-hole variations in ROI and ROM

Hole-to-hole variations in the predicted ROI and ROM are observed during both the flashing and non-flashing conditions. To quantify these variations, the relative standard deviations (RSD) in the ROI across all 8 holes are calculated using the formulation represented in Eqn. 8.11.

$$RSD = \frac{100}{\overline{\dot{m}}} * \sqrt{\frac{\sum_{i=1}^{8}\left(\dot{m}_i - \overline{\dot{m}}\right)}{7}} \tag{8.11}$$

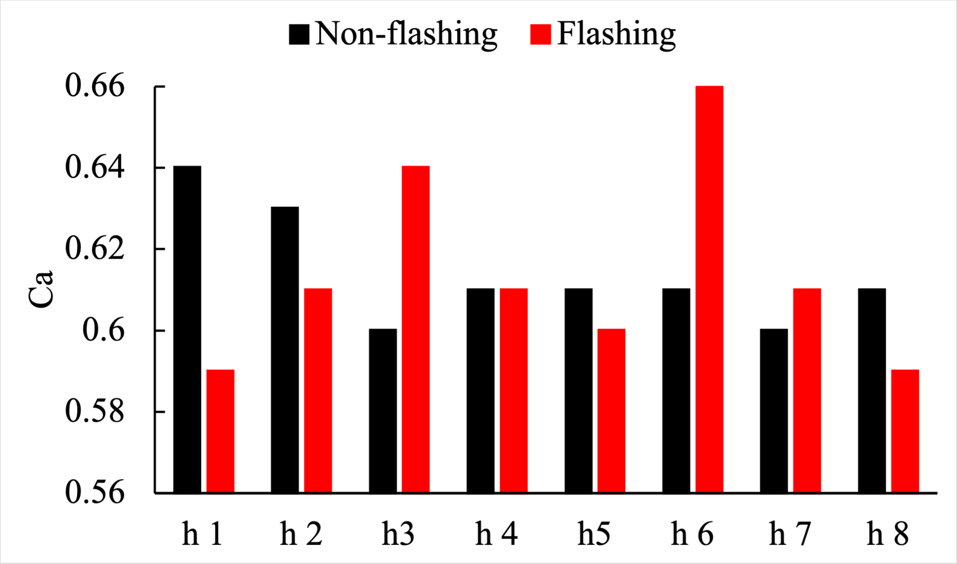

Figure 8.2: Bar chart showing the hole-to-hole variations in the coefficient of area under non-flashing and flashing conditions

In Eqn. 8.11, $\overline{\dot{m}}$ and $\dot{m}_i$ refer to the instantaneous mass flow rate averaged over all eight holes and the instantaneous mass flow rate through the hole numbered i, respectively. The hole-to-hole variations in the ROI in terms of the RSD can be seen in Fig. 8.3

A similar analysis for the momentum rate prediction is also performed. Momentum rate is a good indicator of the discharge through individual holes. The RSD of the ROI and ROM are transient in nature and have higher values during the quasi-steady state in comparison to the needle opening/closing transients. These hole-to-hole variations under non-flashing conditions corroborate the findings by Baldwin et al. [19]. They attribute the variations to transient interactive sac vortices, extending between multiple nozzle holes. Similar transient interacting vortex structures are also captured under flash boiling conditions, as shown in Fig. 8.5.

Fig. 8.5 consists of the total pressure (14 MPa) isosurface colored by the static pressure, indicating the string flash boiling phenomenon. Furthermore, it has a mid-plane clip colored by the mixture density. The density contour indicates the

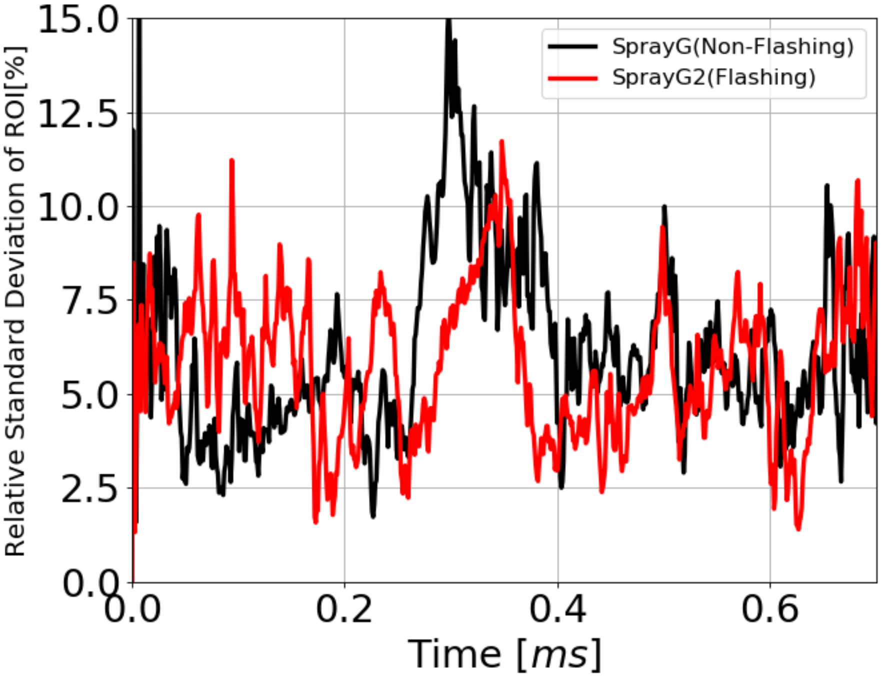

Figure 8.3: Relative standard deviation of the rate of injection across all the holes for both the flashing and non-flashing conditions

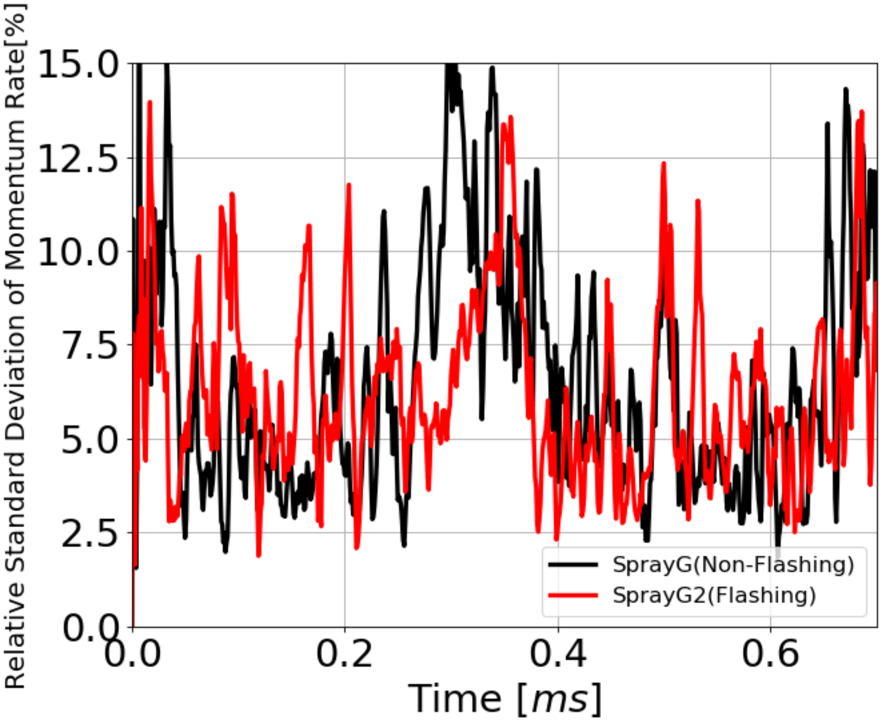

Figure 8.4: Relative standard deviation of the momentum rate across all the holes for both the flashing and non-flashing conditions

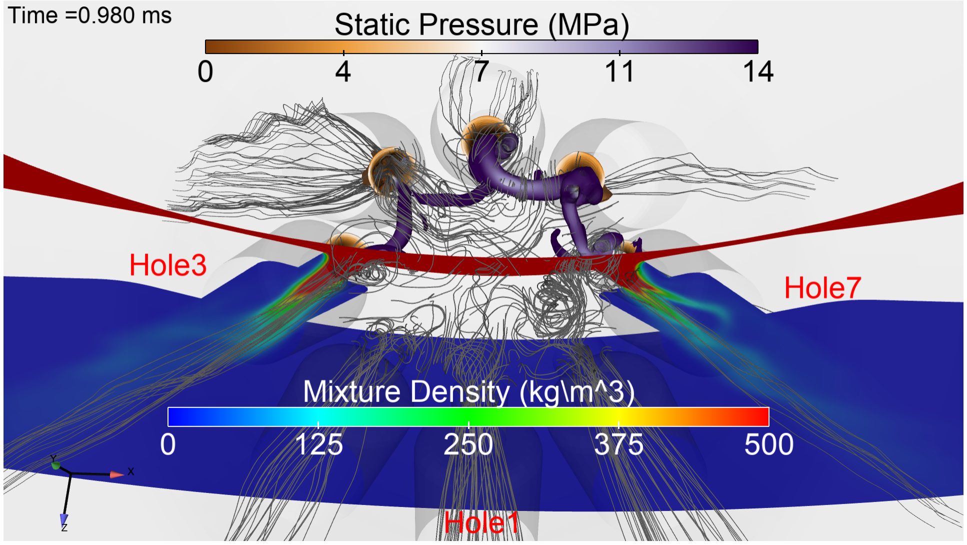

Figure 8.5: String flash-boiling in a transient moving mesh GDI simulation under flashing condition

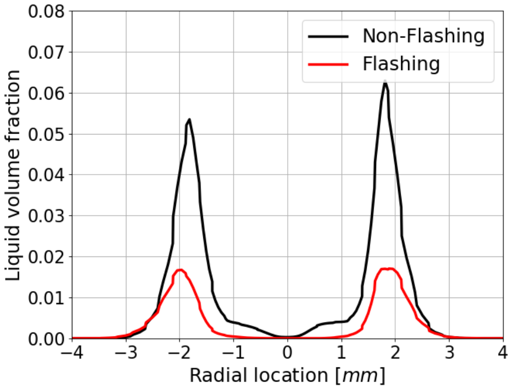

Figure 8.6: Line plots showing the time averaged liquid volume fraction for the hole1(left) and hole5(right) at 2mm downstream of the injector tip for both non-flashing (black color) and flashing (red color) conditions.

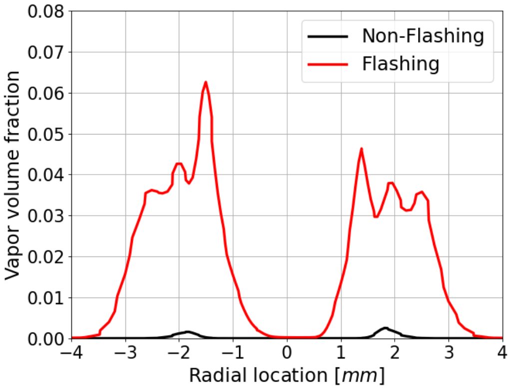

Figure 8.7: Line plots showing the time averaged vapor volume fraction for the hole1(left) and hole5(right) at 2mm downstream of the injector tip for both non-flashing (black color) and flashing (red color) conditions.

hollow-cone spray due to string flash boiling. The figure includes velocity streamlines representing the vortex generation in individual holes. It also captures the vortex interactions between the neighboring holes. These transient vortices are the primary reason behind the hole-to-hole variations in the eight-hole GDI injector.

8.1.3 Time averaged analysis of the near nozzle (2mm away from the injector tip) behaviors

For a better understanding of these in-nozzle transients and their effects on the near-nozzle spray behavior, a cut plane is chosen at the 2mm downstream location away from the injector tip. The chosen cut plane is perpendicular to the injector axis. The concerned flow variables (LVF, VVF, and axial velocity) are interpolated to the chosen 2-D cut plane and averaged over the quasi-steady state phase.

Figures 8.6, 8.8, 8.10, and 8.12 represent the predicted liquid volume fraction at the downstream location for each nozzle, whereas figures 8.7, 8.9, 8.11, and 8.13 represent the vapor volume fraction prediction at the same locations. As expected, the

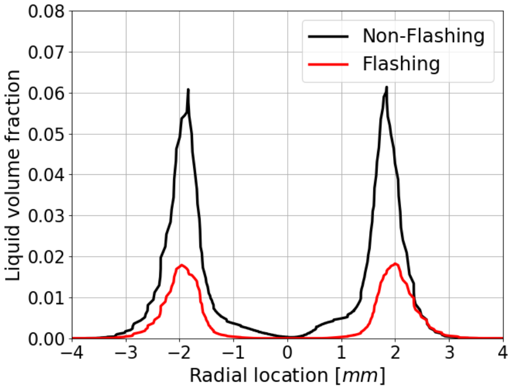

Figure 8.8: Line plots showing the time averaged liquid volume fraction for the hole2 (left) and hole6 (right) at 2mm downstream of the injector tip for both non-flashing (black color) and flashing (red color) conditions.

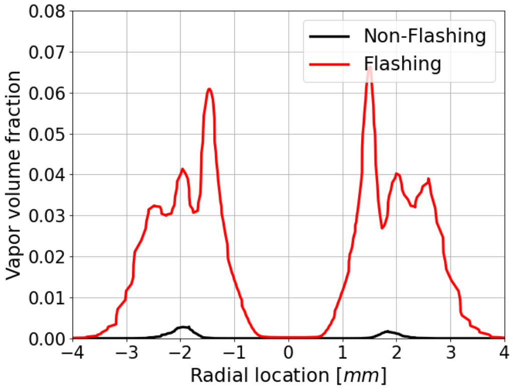

Figure 8.9: Line plots showing the time averaged vapor volume fraction for the hole2 (left) and hole6 (right) at 2mm downstream of the injector tip for both non-flashing (black color) and flashing (red color) conditions.

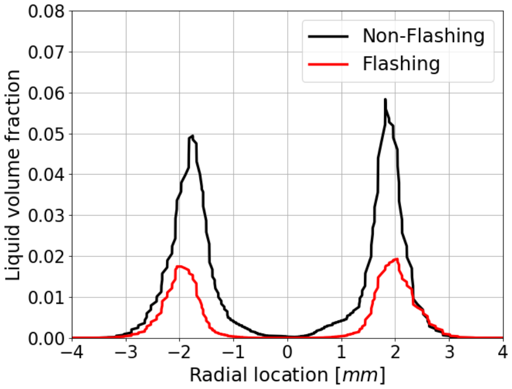

Figure 8.10: Line plots showing the time averaged liquid volume fraction for the hole3 (left) and hole7 (right) at 2mm downstream of the injector tip for both non-flashing (black color) and flashing (red color) conditions.

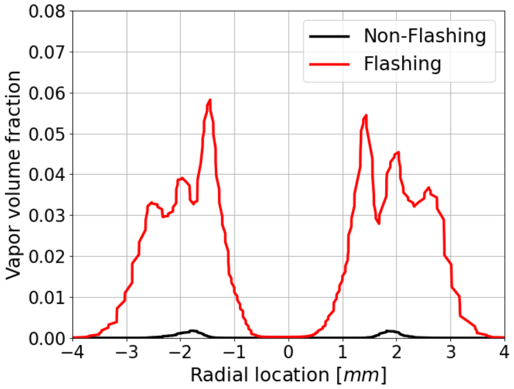

Figure 8.11: Line plots showing the time averaged vapor volume fraction for the hole3 (left) and hole7 (right) at 2mm downstream of the injector tip for both non-flashing (black color) and flashing (red color) conditions.

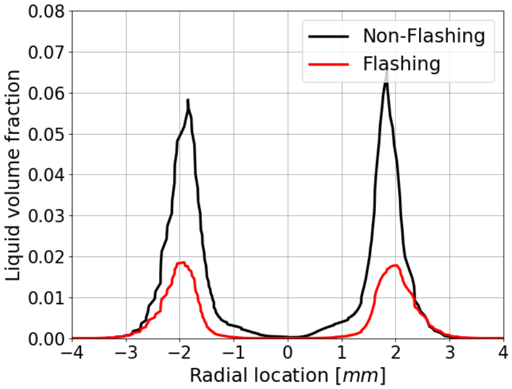

Figure 8.12: Line plots showing the time averaged liquid volume fraction for the hole4 (left) and hole8 (right) at 2mm downstream of the injector tip for both non-flashing (black color) and flashing (red color) conditions.

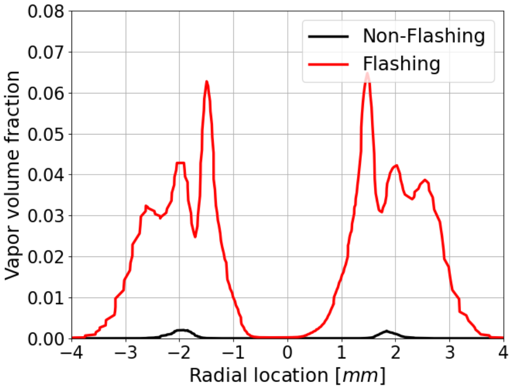

Figure 8.13: Line plots showing the time averaged vapor volume fraction for the hole4 (left) and hole8 (right) at 2mm downstream of the injector tip for both non-flashing (black color) and flashing (red color) conditions.

non-flashing condition predicts more liquid fuel at the downstream location compared to the flashing condition. Furthermore, different slopes of these line plots ascertain different spray angles for flashing compared to non-flashing conditions. Similarly, higher vapor volume fraction distributions are predicted for the flashing conditions. It should be noted that, although both flashing and non-flashing conditions predict similar ROIs because of the choked state, contrasting downstream flow behaviors and spray jet compositions are observed due to the dissimilar thermodynamic states.

Additionally, the axial velocity predictions for the individual plumes emanating from the 8-hole injector are compared for different ambient conditions. Figures 8.14 and 8.15 represent the downstream axial velocity predictions for the non-flashing and flash-boiling conditions, respectively. The negative velocities indicate the plume going away from the injector, whereas the positive velocities indicate the entrained chamber gas going towards the injector tip. For the flash-boiling conditions, the plume velocities are predicted to be higher compared to the non-flashing conditions.

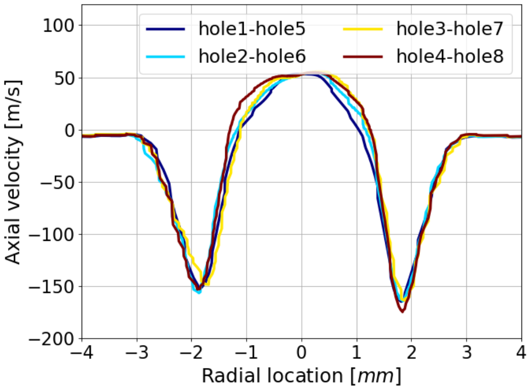

Figure 8.14: Axial velocity predictions at 2 mm downstream from the injector tip for all nozzle holes under the non-flashing condition

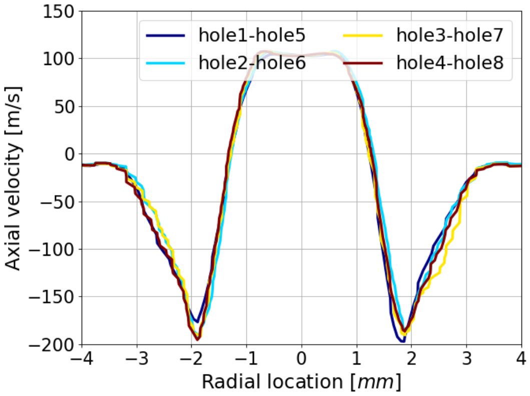

Figure 8.15: Axial velocity prediction at 2 mm downstream from the injector tip for all nozzle holes under flash-boiling condition

Similarly, higher velocities are observed for the entrained chamber gas in the flashing scenario.

Argonne measures the projected mass density at a distance of 2mm downstream away from the injector tip using an X-ray measurement techniques [122]. The measured quantity is time averaged over the quasi-steady state phase, which is similar to the time-averaged fuel density simulated by the CFD models. For the non-flashing condition, the projected fuel mass density [122] is compared to the mixture density at 2mm downstream location, as shown in Fig. 8.16. The CFD predictions of plume shapes qualitatively match the X-ray tomography measurements for the non-flashing condition, though the magnitude of the predicted mixture density is higher. Similar evidences are captured when the density is averaged over all eight holes, as shown in Fig. 8.17. In a similar fashion, the predictions for the flash-boiling condition for the hole one and five are also compared and higher differences between the density predictions are observed, refer Fig. 8.18.

These figures clearly show the predicted plumes have a very high concentration of fuel as consequence of the difference in the momentum predictions, though the mass

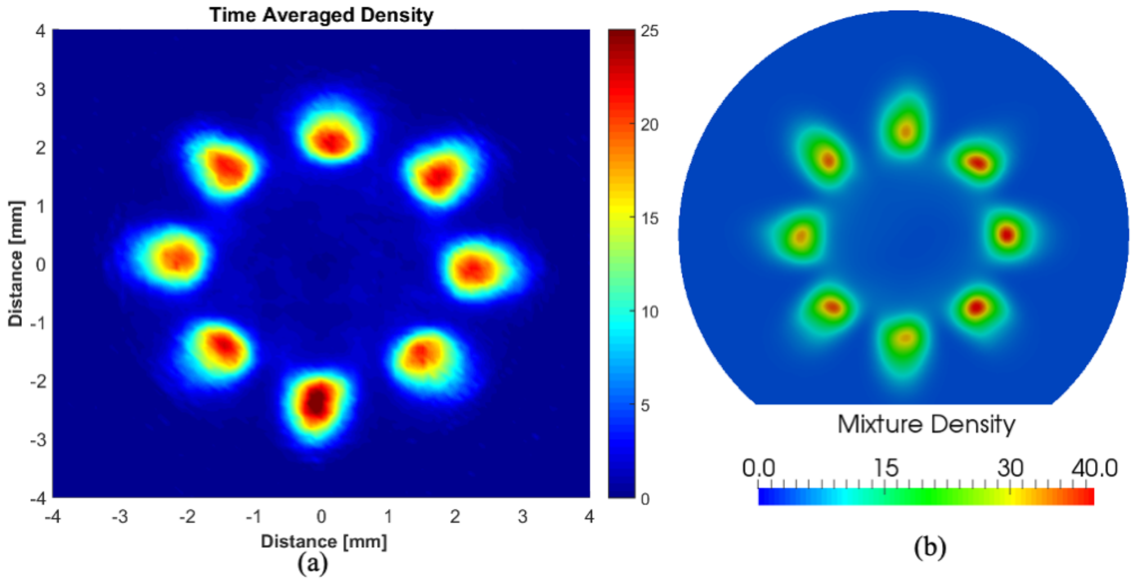

(a) (b)

Figure 8.16: Cut planes colored by the mixture density. (a) Density measured by X-Ray for the non-flashing condition. (b) Mixture density predicted by HRMFoam for the non-flashing condition.

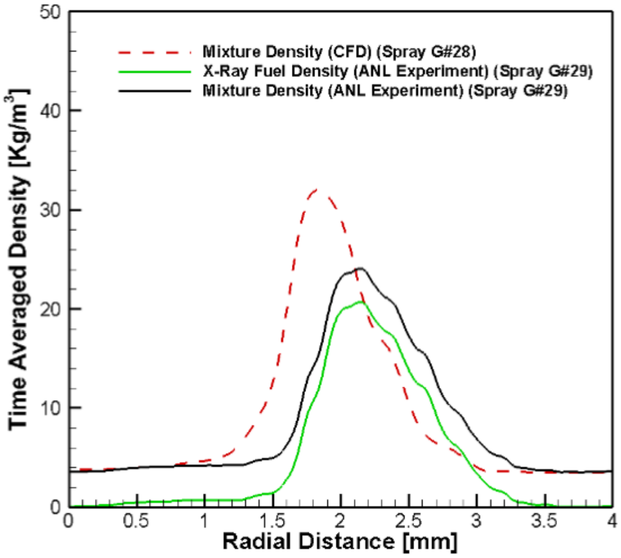

Figure 8.17: 2-D line plot showing the comparison between the X-Ray measured mixture density and the CFD predictions for the non-flashing condition. The mixture density is averaged over all the 8 holes for the quasi-steady phase.

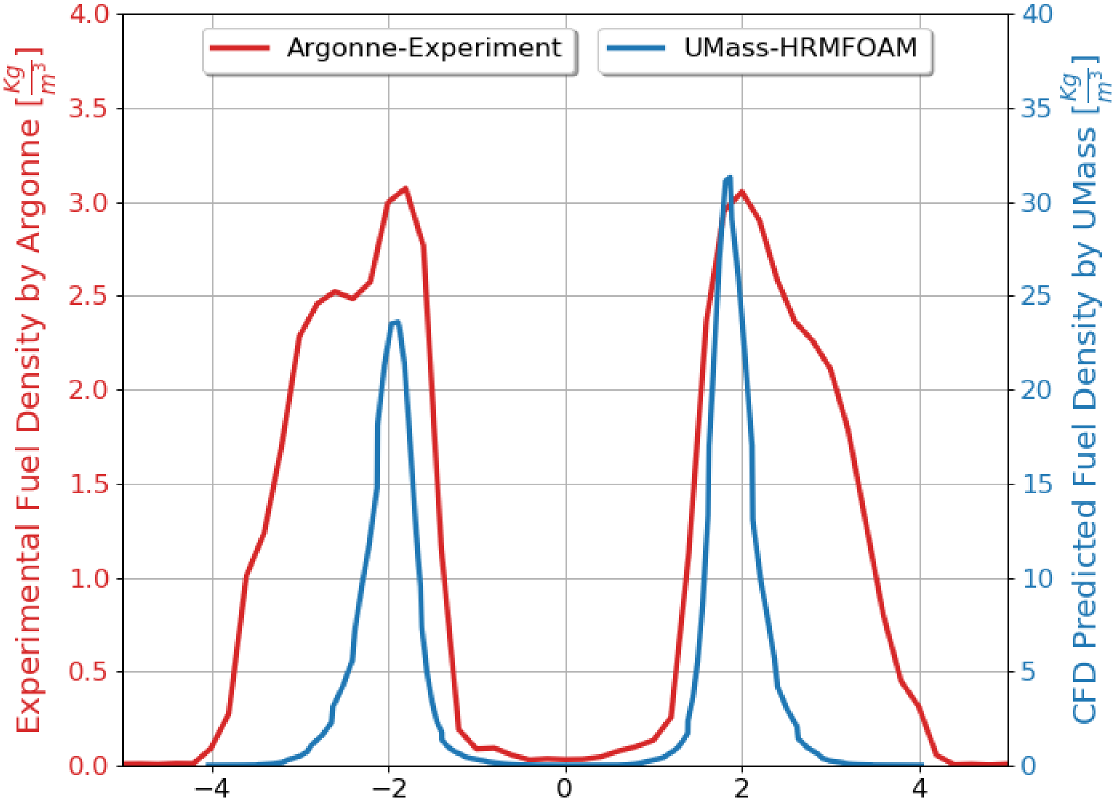

Figure 8.18: 2-D line plot showing the comparison between X-Ray measured mixture density and the CFD predictions for the hole one (left) and hole 5(right) under flash-boiling condition. The mixture density is time averaged over the quasi-steady phase.

flow rate matches with the experiments for both flash-boiling and non-flash-boiling conditions. The mass flow rate corresponds to the product of fuel density multiplied a velocity, integrated over an area. The fact that the mass flow rates are well predicted by both CFD simulations indicates a good level of accuracy of these quantities within the nozzle, which is the choke point of the flow. If a quasi-stable flow is assumed, the the CFD code should presumably be predicting the correct mass flow rate at the 2 mm observation plane.

The mass flow rate constrains the product of density and velocity. Thus, the downstream over-prediction in density is indicative that the predicted velocity is far too low. This discrepancy in density predictions requires a revisit of the mixing model of the non-condensible gas with the liquid fuel and the subsequent evaporation due to heat transfer. The current solver uses the simple Fickian diffusion law to account for the mixing of non-condensible gas and the liquid fuel. This law might not be applicable to the highly vaporizing and turbulent sprays as observed in the GDI injectors. Furthermore, the experimental predictions have shoulders at the peak density predictions, as shown in Fig. 8.18. However, the bi-modal curves predicted by the computation are found to be smooth in nature. This discrepancy indicates that the experiments capture the plume-to-plume interactions which are not observed in the computations.

Additionally, the current simulations use the $k - \omega\ SST$ to model the turbulence closure. In general, conventional two-equation models such as the $k - \omega\ SST$ model perform poorly for flows which are not in near-equilibrium state [27]. This class of turbulence models are based on single time-scale schemes [124]. However, the GDI flows involve multiple time-scales for both flashing and non-flashing conditions. A detailed time-scale analysis for both thermodynamic conditions will be included in the following sub-section.

Time scales	Non-flash-boiling	Flash-boiling
Bernoulli time scale	$6.94 \times 10^{-7}s$	$6.84 \times 10^{-7}s$
Vaporization time scale	$3.84 \times 10^{-7}s$	$3.84 \times 10^{-7}s$
Sealing model time scale	$2 \times 10^{-6}s$	$2 \times 10^{-6}s$
Time scale of needle opening phase	$4 \times 10^{-5}s$	$4 \times 10^{-5}s$
Time scale of quasi steady phase	$5.4 \times 10^{-4}s$	$5.4 \times 10^{-4}s$
Time scale of pre-needle closure phase	$1.6 \times 10^{-4}s$	$1.6 \times 10^{-4}s$
Time scale of needle closure phase	$2.0 \times 10^{-5}s$	$2.0 \times 10^{-5}s$
Time scale of post-needle closure phase	$1.5 \times 10^{-4}s$	$1.5 \times 10^{-4}s$
Turbulent time scale for needle opening	$5.41 \times 10^{-7}s$	$1.83 \times 10^{-7}s$
Turbulent time scale for quasi-steady phase	$1.33 \times 10^{-7}s$	$1.43 \times 10^{-7}s$
Turbulent time scale for pre-needle closure	$1.09 \times 10^{-7}s$	$1.09 \times 10^{-7}s$
Turbulent time scale for needle closure	$1.29 \times 10^{-7}s$	$3.65 \times 10^{-7}s$
Turbulent time scale for post-needle closure	$1.45 \times 10^{-6}s$	1.76×10^{-6}

Table 8.2: Different time-scales for both flash-boiling and non-flash-boiling conditions

8.1.4 Time-scale analysis

The complex GDI flows involve multiple time-scales due to the phase-change process, turbulence modeling, needle closure models and the needle motion. It is difficult to comment on the interactive nature of these time scales. Hence, Table 8.2 includes a comparison of the order of magnitude of these time-scales for both non-flashing and flashing conditions.

In tab. 8.2, the Bernoulli time scale refers to the theoretical time taken by the fluid to cross the defined length of the nozzle (L_{noz}) for a prescribed pressure gradient (L_{noz}) under both non-flash-boiling and flash-boiling conditions, as shown in Eqn. 8.12.

$$T_{Bern.} = L_{noz}\sqrt{\frac{\rho}{2\Delta p}} \tag{8.12}$$

In Eqn. 8.12, ρ corresponds to the saturated liquid fuel density at the inlet temperature and pressure.

The time scale of vaporization is assumed to be the same order as the time constant of the HRM model, as the other parameters such as volume fraction and the nondimensional pressure are of unity order. Hence, flashing and non-flashing conditions have the same time-scale for vaporization.

The complete injection duration is subdivided into distinct phases based on their impact on the flow field. These individual phases are classified as the needle opening phase, quasi-steady phase, pre-needle closure phase, needle closure phase and the post-needle closure phase. Furthermore, the turbulent time scale corresponds to the time-scale of dissipation of the turbulent kinetic energy (k) at a dissipation rate of ϵ. This time scale is also known as the eddy life time. As the turbulent time-scale is formulated based on the over all energy and its dissipation, it is a scale of the larger and more energetic eddies[62]. From the comparison presented in Table 8.2, it is evident that the turbulent time scales during the injection phase are of similar order as the vaporization time scales and the Bernoulli time scales. However, post-needle closure the turbulent time scales are found to be larger and of the order of the sealing model time scale. Furthermore, during needle opening phase, the eddy life time are found to be lager in the non-flashing condition compared to the flashing condition. In contrast, the trend reverses during the needle closure phase. This time scale also supports our hypothesis that the fluid in the sac and nozzle regions are less rotational in the flashing compared to the non-flashing condition. Hole-to-hole variations in the turbulent time scales for different thermodynamic conditions are also captured. These variations are tabulated in Table 8.3.

8.2 Inferences

The current work includes the study of internal nozzle flow dynamics in the quasi-steady phase for a multi-hole GDI injector operating at both non-flash boiling and flash-boiling conditions. The numerical predictions for the time-averaged rate of injection, rate of momentum, and dimensionless hydraulic coefficients are validated

		Opening	Quasi-steady	Pre-closure	Closure	Post-closure
H1	G1	$5.37 \times 10^{-7}s$	$1.29 \times 10^{-7}s$	$1.01 \times 10^{-7}s$	$1.31 \times 10^{-7}s$	$1.44 \times 10^{-6}s$
	G2	$1.81 \times 10^{-7}s$	$1.47 \times 10^{-7}s$	$1.25 \times 10^{-7}s$	$3.66 \times 10^{-7}s$	$1.67 \times 10^{-6}s$
H2	G1	$5.35 \times 10^{-7}s$	$1.19 \times 10^{-7}s$	$1.13 \times 10^{-7}s$	$1.30 \times 10^{-7}s$	$1.45 \times 10^{-6}s$
	G2	$1.86 \times 10^{-7}s$	$1.23 \times 10^{-7}s$	$1.01 \times 10^{-7}s$	$3.16 \times 10^{-7}s$	$1.95 \times 10^{-6}s$
H3	G1	$5.41 \times 10^{-7}s$	$1.38 \times 10^{-7}s$	$1.13 \times 10^{-7}s$	$1.35 \times 10^{-7}s$	$1.68 \times 10^{-6}s$
	G2	$1.85 \times 10^{-7}s$	$1.48 \times 10^{-7}s$	$0.89 \times 10^{-7}s$	$3.29 \times 10^{-7}s$	$1.83 \times 10^{-6}s$
H4	G1	$5.43 \times 10^{-7}s$	$1.47 \times 10^{-7}s$	$1.09 \times 10^{-7}s$	$1.22 \times 10^{-7}s$	$1.40 \times 10^{-6}s$
	G2	$1.88 \times 10^{-7}s$	$1.79 \times 10^{-7}s$	$1.05 \times 10^{-7}s$	$4.57 \times 10^{-7}s$	$2.04 \times 10^{-6}s$
H5	G1	$5.41 \times 10^{-7}s$	$1.21 \times 10^{-7}s$	$0.97 \times 10^{-7}s$	$1.37 \times 10^{-7}s$	$1.66 \times 10^{-6}s$
	G2	$1.80 \times 10^{-7}s$	$1.39 \times 10^{-7}s$	$1.08 \times 10^{-7}s$	$3.81 \times 10^{-7}s$	$1.76 \times 10^{-6}s$
H6	G1	$5.44 \times 10^{-7}s$	$1.38 \times 10^{-7}s$	$1.12 \times 10^{-7}s$	$1.39 \times 10^{-7}s$	$1.56 \times 10^{-6}s$
	G2	$1.78 \times 10^{-7}s$	$1.37 \times 10^{-7}s$	$1.22 \times 10^{-7}s$	$4.08 \times 10^{-7}s$	$1.85 \times 10^{-6}s$
H7	G1	$5.47 \times 10^{-7}s$	$1.34 \times 10^{-7}s$	$1.14 \times 10^{-7}s$	$1.38 \times 10^{-7}s$	$1.33 \times 10^{-6}s$
	G2	$1.89 \times 10^{-7}s$	$1.37 \times 10^{-7}s$	$1.13 \times 10^{-7}s$	$3.17 \times 10^{-7}s$	$1.56 \times 10^{-6}s$
H8	G1	$5.41 \times 10^{-7}s$	$1.38 \times 10^{-7}s$	$1.13 \times 10^{-7}s$	$0.97 \times 10^{-7}s$	$1.11 \times 10^{-6}s$
	G2	$1.76 \times 10^{-7}s$	$1.33 \times 10^{-7}s$	$1.15 \times 10^{-7}s$	$3.55 \times 10^{-7}s$	$1.45 \times 10^{-6}s$

Table 8.3: Turbulent time scales for individual holes during different phases of the needle motion.

with the experimental observations for the non-flashing condition. The main findings of this study are summarized as follows:

- For different ambient conditions, the percentage differences in the predicted ROI, ROM, C_d, C_M, C_v, and C_a are around four percent. However, when the ambient condition changes, the holes which have the highest and the lowest dimensionless coefficients also change.

- Distinct hole-to-hole variations are observed in the predicted ROI and ROM. A maximum relative standard deviation of fifteen percent is observed in the predicted ROI for the non-flashing condition. These hole-to-hole variations are driven by the transient sac vortices. These interactive vortices extend between multiple nozzle holes.

- The hole-to-hole variations in the internal nozzle flow influence the downstream flow behavior. Downstream flow behaviors are further impacted by the different ambient conditions. Consequently, hollow cone sprays with the vapor core at the centre are observed during the flash-boiling condition. Moreover, the flashing jets are observed to have higher axial velocities compared to the non-flashing jets. These high jet velocities additionally result in higher entrained chamber gas velocities.

- Discrepancies between the momentum measurements and the CFD predictions for both flash-boiling and non-flashing conditions can majorly be attributed to the modeling errors the CFD solver. The large error in the predicted and measured fuel concentration downstream of the injector likely indicates an issue with the fuel dispersion model. The Eulerian model of the fuel/air mixing typically rely on the simplest possible closure, Fickian diffusion. This closure presumes that turbulent mixing is entirely responsible for the fuel-air mixing. Further, the fuel dispersion models are not cognizant of the large density ratio between phases.

CHAPTER 9

PLUME BASED COUPLING APPROACH FOR GDI SPRAY

Modeling the complex air-fuel mixing process of GDI engines is a perennial challenge for computational fluid dynamics (CFD) simulations, as it involves predicting the complete evaluation of the fuel spray from the liquid phase to the vapor phase with adequate accuracy. Furthermore, complex phenomena such as break up and coalescence occur during the spray injection process. When the liquid fuel exits the nozzle and penetrates into the ambient air, it goes through the primary atomization process. During this process, the liquid jet disintegrates into ligaments and large droplets which represent the dense spray core regions. These large liquid structures undergo further breakup and coalescence processes to form stable droplets which are present in the dilute spray regions. Recently, several attempts have been made to model these complicated processes together. Among these approaches, the Lagrangian-Eulerian (LE) methods such as the Discrete Droplet Model (DDM) [25] have dominated the spray modeling in CFD. Efficient samplings of the actual drops have been enabled by the stochastic nature of the Lagrangian-Eulerian model [190] while avoiding the annoyance of numerical diffusion [61].

The LE approaches employ parcels (stochastic representation of a group of droplets) to represent the Lagrangian liquid fuel drops. The accuracy of the predictions by the DDM depends upon several submodels such as the droplet break-up model, drag model, collision model, evaporation model, and turbulent dispersion model [233]. However, the spray models are droplet oriented and take little account of the neighboring drops in the dense spray region [18]. It is very difficult to obtain the desired predictions without adjusting the numerous model parameters of the LE models [57]. Hence, it can be concluded that these models are not truly predictive as the model parameters are not known *a priori*, but require continuous manipulation. A recent published work by Agrawal et al. [5] questioned the validity of the linear stability theory, which is the central assumption of the KH-RT model, in the primary atomization region, i.e., the dense spray region. Besides, these models require careful definitions for droplet diameter, droplet temperature, droplet velocity, coefficient of discharge, spray cone angle, and turbulent intensity to initialize the parcels. Defining these physical parameters in GDI applications is a cumbersome process considering the fact that the ensuing spray is highly transient in the near-nozzle region and features hole-to-hole variations due to interactive vortices, as shown in Sec. 8.1. Furthermore, Secs. 8.1.1, and 5.1 have shown that the GDI injectors operating at different ambient conditions predict nearly similar mass flow rate and coefficient of discharge, although they exhibit completely different internal and near-nozzle flow behaviors. Most of the LE spray calculations are grossly under-resolved, as a higher number of cell counts [197] and parcel counts [190] compared to the existing practices are required to achieve converged results. Recently, researchers [209] [199] have applied the LE approach to GDI applications and are able to match the experimental predictions after heavy tuning of the model parameters, spray cone angle, and the turbulence model constants. Moreover, their simulation setups lack general applicabilities, as the setups tuned for one ambient condition require further tuning for better predictions in different ambient conditions. Paredi et al. [150] have observed good agreement between the experimental observations and the LE predictions with minimal tuning of the model constants for different ambient conditions. However, they vary the spray cone angles and use the Pope turbulence correction [163] to fine tune the computational predictions. Additionally, they have observed differences between the experimentally generated PLV (Projected Liquid Volume) maps and the computationally predicted

PLV maps, although the predicted 1-D spray analysis such as liquid length, vapor penetration, and axial velocity are close to the experimental measurements.

The second approach involves treating both the liquid and gaseous phases as the Eulerian phase for numerical calculations. The two-fluid approach treats both phases as a continuum throughout the domain, hence, requiring interface treatment. Therefore, the Eulerian-Eulerian (EE) approaches which use sharp interface methods are computationally expensive. To avoid these difficulties, Eulerian paradigms [238], [34], [69] that model the interface instead of resolving the interface have gained prominence. Other advantages include a lesser mesh dependency compared to the LE approach [238] and no requirements of initial parcels' definition. Furthermore, the Eulerian models are volume conserved as they account for the volume occupied by the spray, which is generally ignored by the LE simulations [149].

The literature [34], [86], [116], [103], and [53] shows good agreement between the experimental observations and the computational predictions by the EE approach in the dense spray region, but the accuracy of these models drops significantly in the sparse regions of the spray. Additionally, coupling of the internal injector flow with in-cylinder simulations is essential for predictive CFD for engine development. Practical experience has shown that small details in the injector flow can make a large difference in the engine emissions. Simultaneously, the internal injector flow evolves over small time and length scales compared to the in-cylinder flow. In consequence, the EE calculation will be prohibitively expensive, if applied to a complete engine simulation.

To address the above limitations, Subramanian at al. [214] have suggested to use the EE approach in the near-field region and the LE approach in the dispersed spray region. However, coupling the Eulerian liquid phase with the Lagrangian liquid phase is perplexing, as it requires knowledge about the overlap of the mesh and physical quantities between the two representations. Furthermore, Saha et al. [184] have used a diffused interface-based Eulerian approach to capture the flow field at the nozzle exit of a 8-hole GDI injector and used those data to initialize the parcels for further LE calculations. Nonetheless, the simulated discharge coefficient and the prescribed nozzle diameter are used to determine the initial droplet diameters. Additionally, they have used models based on the linear stability theory for primary atomization. Recently, Nocivelli et al. [141] [140] have considered the Sauter mean diameter (SMD) predicted by Ultra-Small-Angle X-ray Scattering (USAXS) measurements to define the distribution of droplet diameters during the primary atomization process. Parcels initialized with these droplets are considered for subsequent atomization. The USAXS measurements are taken at 1 mm downstream of the injector tip, yet the parcels are generated at the counter-bore exit which represent the dense spray region. Sphicas et al. [209] have used similar locations to inject parcels while initializing the droplet diameters by the predictions from the Eulerian-Lagrangian spray atomization (ELSA) approach. Even so, these one-way coupling approaches [209] [184] [141] [140] heavily depend upon the tuning of spray cone angles for better predictions in engine simulations.

In the current chapter, a new plume-based coupling approach inspired by the one-way coupling approach [184] is proposed. The one-way coupling approach applies the droplet oriented LE models in the dense spray region, where they struggle the most. However, the plume-based coupling approach runs the EE primary atomization model in the dense spray region. Followed by the suggestions by Subramaniam and O'Rourke [215], the plume-based coupling approach employs the LE models in the sparse spray region, where they work the best because of their inherent formulations. Because of the unique formulation of the plume-based coupling approach, it captures the nuances of the in-nozzle and near nozzle behaviors and drives the LE simulations accordingly. Thus, this approach does not depend upon the primary atomization models which are based upon the linear stability theory. The plume-based coupling approach is applied to the 8-hole GDI injector [1] operating under both flash-boiling and non-flashing conditions. Predictions from the novel approach are also validated against the existing experimental observations for different ambient conditions.

9.1 Model description

The current simulation approach includes two modeling frameworks. The first modeling framework simulates the internal and near nozzle flow behaviors including the primary atomization process using an Eulerian mixture model approach, that is based upon the Homogeneous Relaxation Model (HRM), described in secs. 4.1, 4.2, and 4.3. The second modeling framework incorporates the Lagrangian modeling approach implemented in the commercial 3D CFD solver, Converge 2.4 [175], to simulate the dilute spray regions. Furthermore, transition criteria are applied to couple both modeling frameworks.

9.1.1 Lagrangian model

Our current approach includes the discrete droplet models [61] of CONVERGE 2.4 [175] to simulate the sparse spray region. This method couples the liquid spray parcels to the Eulerian gas phase, which is discretized based on the finite volume approach. The $k - \epsilon$ turbulence model is used to model the gas phase turbulence. Subsequently, fluctuations in the parcel properties are modeled by the O'Rourke turbulent dispersion model [144]. Besides, the dynamic droplet drag model, Taylor analogy breakup (TAB) model [145], No Time Counter (NTC) droplet collision model [193], and the Frossling evaporation model [68] are employed to model the secondary break-up processes.

9.1.2 Plume-based coupling approach

It is computationally exorbitant to simulate the internal nozzle flow simulation coupled with the in-cylinder engine simulations in a single attempt, because the internal injector flow evolves over small time and length scales compared to the in-cylinder flow. Thus, our current approach involves running and tabulating the internal injector flow simulation *apriori*. Then, the approach uses a plume-based one-way coupling to inform the subsequent Lagrangian calculations. The first step of the coupling approach is to define a transition criteria, and the current transition criteria is based on the inter-droplet spacing. A specific inter-droplet spacing can be translated in to a unique liquid volume fraction (LVF) with the assumption of uniform cubic lattice arrangement of droplets in a three-dimensional space with a uniform droplet diameter. Direct numerical simulation (DNS) by Quan et al. [164] reveals strong droplet-droplet interactions for separation distances of less than four droplet diameters, which translates into a LVF of 0.01. However, we establish the plume boundaries, i.e., the transition surface, as the isosurface of LVF=0.04, which roughly correlates with the inter-droplet spacing of three droplet diameters. This isosurface is tessellated with triangles and exported as a polygon file format (.PLY) in the current workflow. While choosing a specific LVF to define the plume surfaces, special attention need to be given to ensure that the Eulerian plumes are closed at the tip. Closed tip plumes inherently ensure finite volume conservation while coupling the Eulerian-Eulerian simulations with the Lagrangian-Eulerian simulations. A lower value LVF, i.e., less than 0.04, demands a bigger Eulerian domain in comparison to the current internal flow simulations. A bigger computational domain for the internal flow simulations significantly increases the present computational cost, hence, it justifies the current choice of the inter-droplet spacing.

The next step of the coupling approach involves interpolating the flow field variables such as the temperature and velocity to the locations of the plume faces using the post-processing methods. The current work uses the commercial post-processing software Ensight to perform the flow field interpolation. Due to the inherently transient nature of the injection process, the plume data are written to the disk frequently.

Each of these data files includes the detailed information about the droplet size, velocity, temperature, and the location of each plume face. The mass flow rate through these triangular faces is also noted. As seen in the Figures 9.1, and 9.2, the plume sizes and shapes are highly variable both temporally and spatially. Nonetheless, this approach inherently captures the differences in the spray plume bending and the spray cone angle for different ambient conditions, as shown in Figures 9.1 - 9.4.

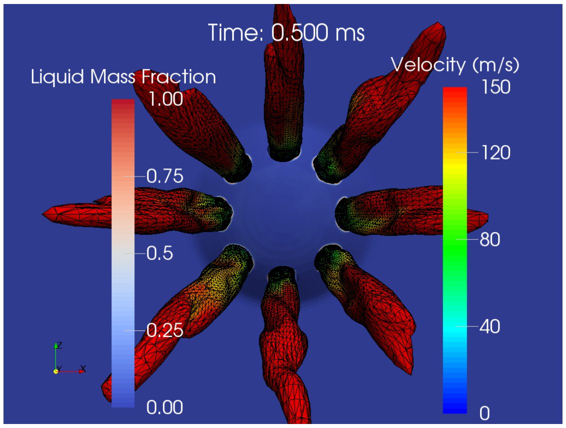

Figure 9.1: Plumes indicated by the iso-surface of LVF=0.04 colored by the velocity magnitude at t = 0.5 ms for the non-flashing condition. The injector tip is colored by the liquid mass fraction.

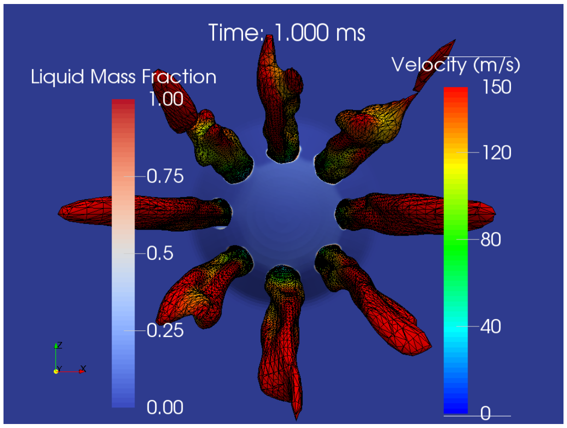

Figure 9.2: Plumes indicated by the iso-surface of LVF=0.04 colored by the velocity magnitude at t = 1.0 ms for the non-flashing condition. The injector tip is colored by the liquid mass fraction.

In the final step of the coupling approach, a C++ application named EnsightToConverge is developed. This application reads the postprocessed plume data and applies subsequent mass flow rate-based filtering to generate a single map to be used for the parcel injection process in CONVERGE-2.4. The filtering process filters out the triangular faces of the plume surface which have the velocity vector directed into the plume. It ensures that the parcels have the initial velocity away from the plume surface. The next challenge of the parcel injection process is to define the parcel injection location at each time step of the simulation. The parcels are created stochastically with probabilities proportional to the mass flow rate. For any given point on a plume surface, the probability of a parcel appearing at that location is

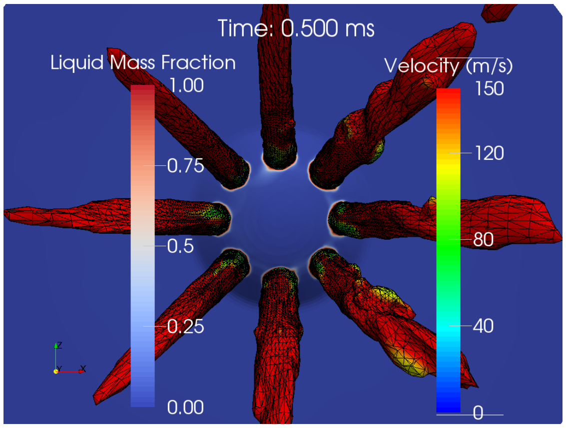

Figure 9.3: Plumes indicated by the iso-surface of LVF=0.04 colored by the velocity magnitude at $t = 0.5$ ms for the flashing condition. The injector tip is colored by the liquid mass fraction.

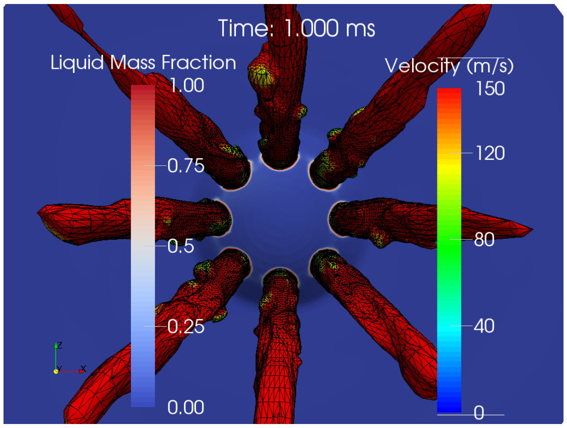

Figure 9.4: Plumes indicated by the iso-surface of LVF=0.04 colored by the velocity magnitude at $t = 1.0$ ms for the flashing condition. The injector tip is colored by the liquid mass fraction.

equal to the mass flow rate through the plume surface at that point divided by the total mass flow rate. Hence, this algorithm creates a representative population of parcels around the plume location. Once the algorithm defines a specific location in the Lagrangian mesh to inject the parcel, it looks for the corresponding tabulated Eulerian mesh data, i.e., the data interpolated to the plume surface. Furthermore, this information is used to initialize each parcel with the corresponding droplet diameter, velocity, temperature, and TKE based on its defined location. Additionally, the droplet diameters are an output of the $\Sigma - Y$ formulation, as explained in the Sec. 4.3. Examples for the plume surface and the plume representation of the injected parcels are shown in Figs. 9.5, and 9.6, respectively.

Mass conservation is ensured by coupling the mass flow rate predicted by the internal flow simulations with the total mass of parcels to be injected at each instance. The current simulation uses the computational ROI curves presented in Fig. 6.2. Additionally, the mass of the individual parcel is kept at a fixed default value of $4.5 \times 10^{-12}\ kg$. This allows the injected parcel count in the Lagrangian calculation to be responsive to the Eulerian ROI predictions. Figure 9.7 represents a detailed work flow of the plume-based one-way coupling approach.

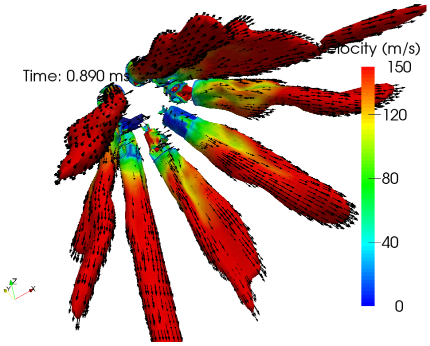

Figure 9.5: Plumes colored by the velocity magnitude with the velocity vectors at $t = 0.89$ ms for the non-flashing condition

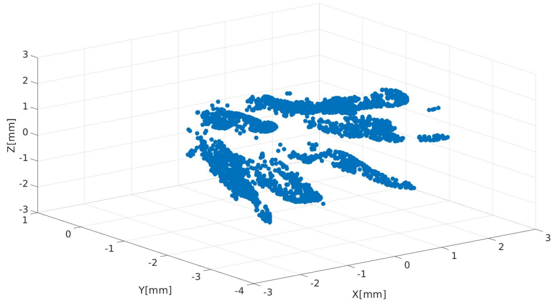

Figure 9.6: The location in x,y,z space of each parcel created at a single time step i.e. 0.55 ms after the start of injection. In this time step, 6327 parcels are created.

9.2 Simulation setup

The plume-based coupling approach assumes that the injector flow is a driver of the in-cylinder flow, but the details of the in-cylinder flow do not alter the injector flow. Consequently, the Lagrangian calculations are performed at a much larger time step with much coarser resolution compared to the internal injector simulations. The simulation setup described in sec. 6.1 is used for the internal flow simulations. Additionally, to account for the primary atomization process, the transport equation for the $\Sigma - Y$ model with two different critical Weber numbers ($We_{cr} = 1 \; and \; 6$) is solved. The details of the $\Sigma - Y$ model with the critical Weber number are described in sec. 4.3.

9.2.1 Lagrangian spray simulations

To avoid interactions between the spray and solid walls, a cylindrical domain with the diameter and height equal to 240 mm is used to simulate the constant volume spray chamber, as seen in Fig. 9.8. The base mesh size is kept at a fixed value of

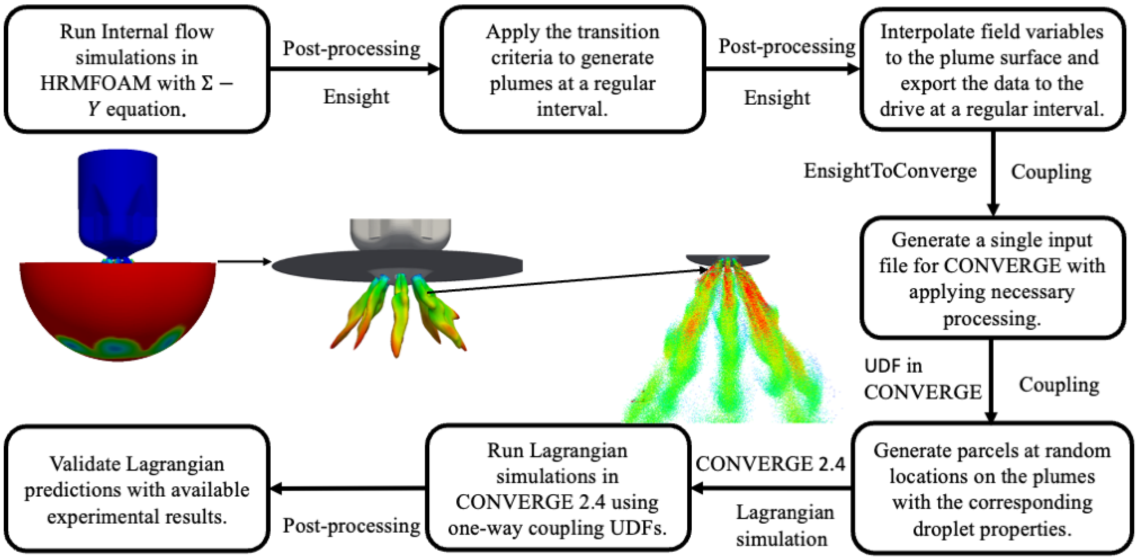

Figure 9.7: Flow chart indicating all the major steps and the software/application used during the each step for the plume based one-way coupling approach.

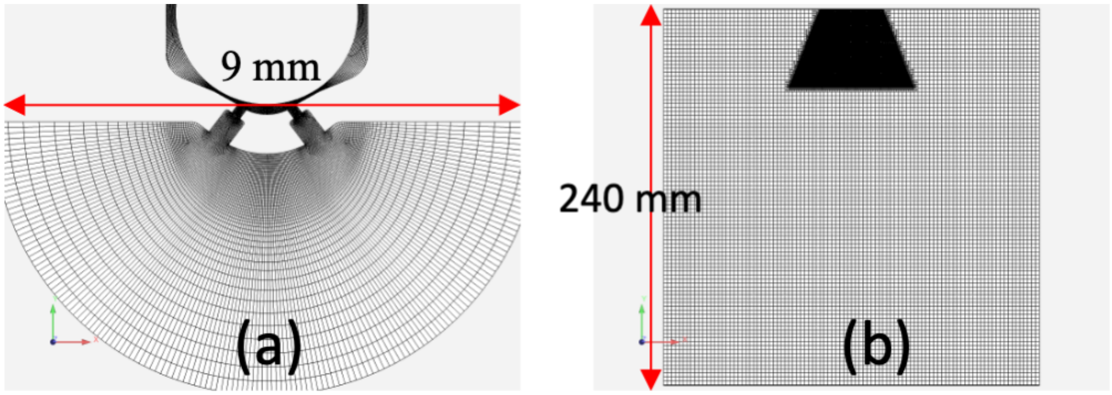

Figure 9.8: (a) Computational domain for the Eulerian internal flow simulation. (b) Computational domain for the Lagrangian external spray simulation.

2.5 mm. Furthermore, a fixed conical embedding region extending 50 mm from the nozzle exit with three levels of refinement is defined. This embedding region accounts for the strong gradient of momentum near the nozzles due to liquid spray injection. Additionally, adaptive mesh refinement (AMR) based on the second derivative of velocity is applied to keep the computational cost minimum while maintaining a fine mesh resolution in the far field of the spray. The Lagrangian simulations do not include the geometry of the injector or nozzles. However, the domain is assumed to be filled with the non-condensible gas, which is consistent with the assumptions for the Eulerian internal flow simulations. In addition, the boundary walls are assumed to have the same temperature as the inlet liquid fuel temperature for both non-flashing and flashing conditions.

9.3 Results and discussion

9.3.1 Qualitative validation

To understand the evolution of spray morphology under different ambient conditions, the CFD predictions from the plume-based coupling approach are first qualitatively compared between the non-flashing and flashing conditions. Furthermore, they are validated against images obtained from the Diffused Back Illumination (DBI) technique. These images have been captured at the University of Melbourne and are made publicly available by the Engine Combustion Network (ECN) data set [1].

In DBI experiments, a light source and detection optical instruments including the high speed camera are placed at either side of the spray. Before injection, the camera records an image to characterize the intensity of the reference light source, i.e., I_0. During the injection event, the light intensity gets attenuated by the spray. The corresponding light intensity (I) is determined by the detection optical instruments. Moreover, the ratio of the attenuated to reference light intensity, i.e., $\frac{I}{I_0}$ is correlated with the measured optical thickness (τ) via Beer-Lambart law, as shown in Eqn. 9.1. Details of this spray diagnostic technique are well explained by Westlye et al. [231].

$$\frac{I}{I_0} = e^{-\tau} \tag{9.1}$$

To compare the Lagrangian parcel simulation results with the experimentally measured optical thickness, Magnotti et al. [118], [119] propose a postprocessing method based on the Mie theory. The proposed correlation is presented in Eqn. 9.2. Before applying the correlation, the 3-D parcel simulation data is projected on to a 2-D interrogation plane with a finite mesh size of $\Delta x \Delta y$ by performing a line-of-sight integral. Then, for each cell, the optical thickness ($\tau_{predicted}$) is determined by considering the extinction coefficient (Q_{ext}), total no. of droplets (N_j) in each parcel in the concerned cell, and the corresponding droplet diameter (d_j). A value of $\tau > 1$ reflects the liquid region. Based on the literature [121], a value of 2.1 is selected for the extinction coefficient, Q_{ext}.

$$\tau_{predicted} = \frac{Q_{ext}\pi}{4\Delta x \Delta y} \sum_{j=1}^{\#parcels} d_j^2 N_j \tag{9.2}$$

Fig. 9.9, and 9.12 include the DBI images quoted from the ECN data set [1] for both non-flashing and flashing conditions, respectively. These figures further capture the time evolution of the spray morphology under different ambient conditions. In the DBI images, the blue and red curves indicate the lower and upper bounds of the liquid spray structure. The transient evolution of the spray morphology predicted by the plume-based coupling approach with two different critical Weber numbers under both non-flashing and flashing conditions are included in Figs. 9.10, 9.11, 9.13, and 9.14. Visual inspections of these figures indicate good agreement between the CFD predictions and the experimental observations for the temporal spray evolution under contrasting thermodynamic states. In the non-flashing condition, the spray morphology is found to be less sensitive to the critical Weber number. In contrast,

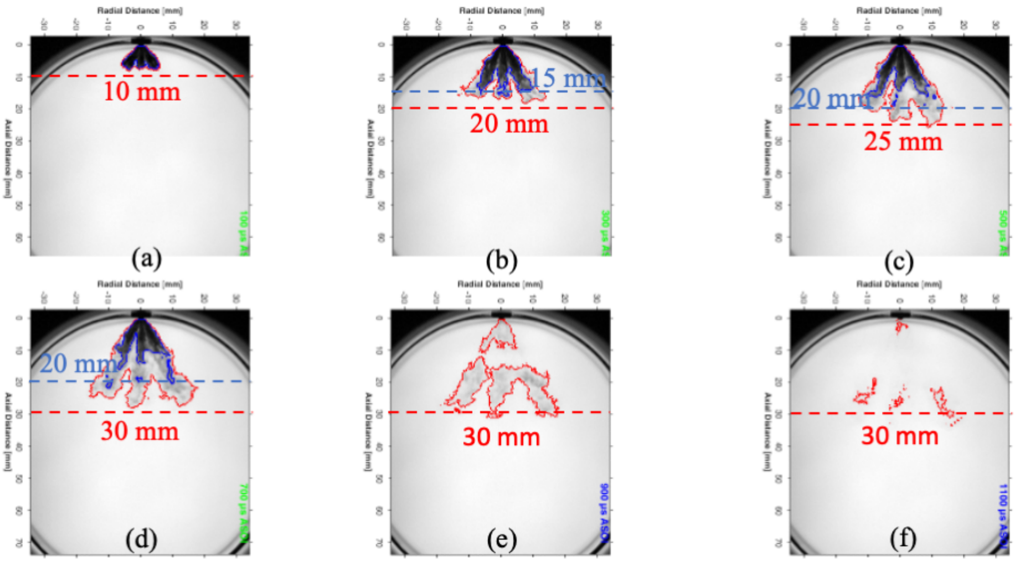

Figure 9.9: DBI images taken from the ECN data set [1] which show the liquid penetration for the non-flashing condition at different time instances, i.e., (a) 0.1 *ms ASOI*, (b) 0.3 *ms ASOI*, (c) 0.5 *ms ASOI*, (d) 0.7 *ms ASOI*, (e) 0.9 *ms ASOI*, and (f) 1.1 *ms ASOI*.

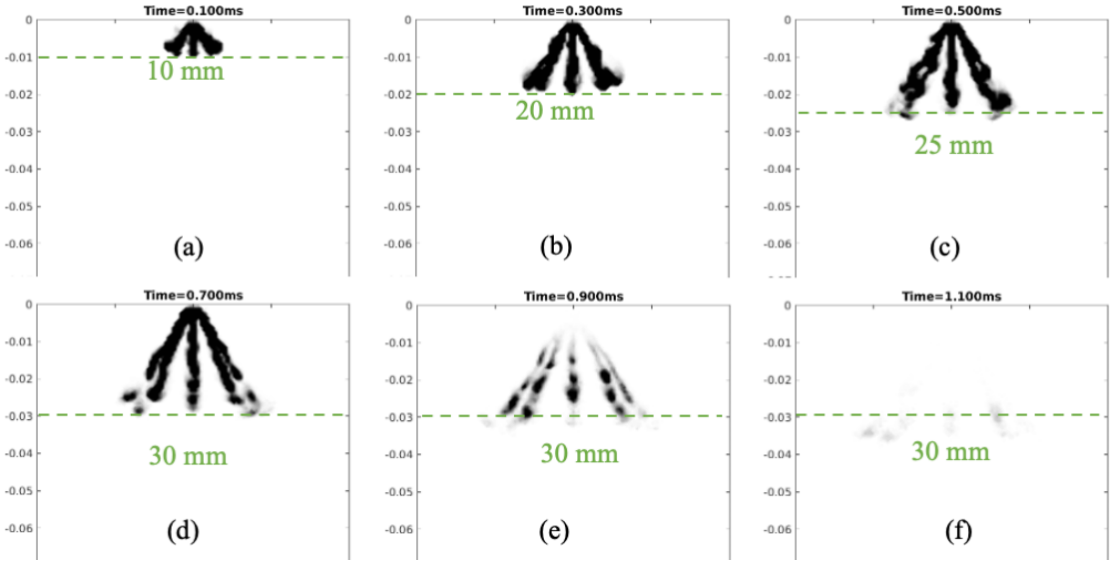

Figure 9.10: Binarized images showing the liquid spray boundary predicted by the plume based coupling approach with $We_{cr} = 1$ for the non-flashing condition at different time instances, i.e., (a) 0.1 *ms ASOI*, (b) 0.3 *ms ASOI*, (c) 0.5 *ms ASOI*, (d) 0.7 *ms ASOI*, (e) 0.9 *ms ASOI*, and (f) 1.1 *ms ASOI*.

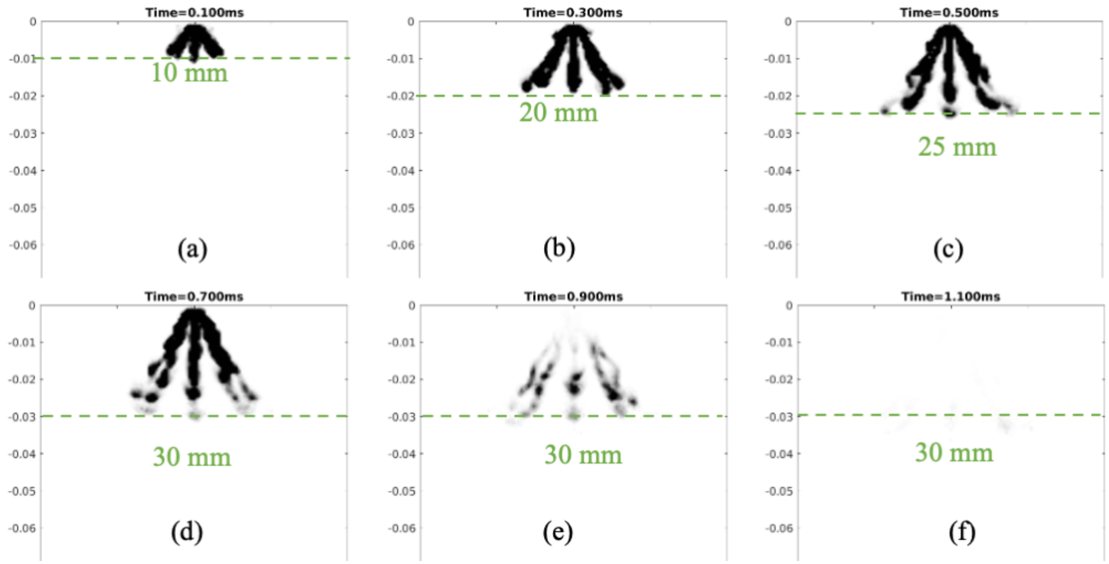

Figure 9.11: Binarized images showing the liquid spray boundary predicted by the plume based coupling approach with $We_{cr} = 6$ for the non-flashing condition at different time instances, i.e., (a) 0.1 ms $ASOI$, (b) 0.3 ms $ASOI$, (c) 0.5 ms $ASOI$, (d) 0.7 ms $ASOI$, (e) 0.9 ms $ASOI$, and (f) 1.1 ms $ASOI$.

in the flashing condition, when the critical Weber number increases, the predicted spray plumes are found to be wider. Consequently, the liquid spray with the lower critical Weber number penetrates the farther distance. As evident from sec. 4.3, a higher critical Weber number leads to a lower equilibrium interfacial surface density (Ω_{eq}) which in turn results in a higher SMD value on the plume surface. The change in penetration distance due to a change in the critical Weber number indicates the sensitivity of the plume-based coupling approach to the initial droplet diameter in the flash-boiling condition. Furthermore, the spray plumes are found to penetrate farther distances in flashing compared to the non-flashing condition, attributing to the fact that the flashing condition has a lower ambient density than the non-flashing. These visual agreements are better than other reported comparisons [140], [141], [150], [184], and [209] for the same operating conditions.

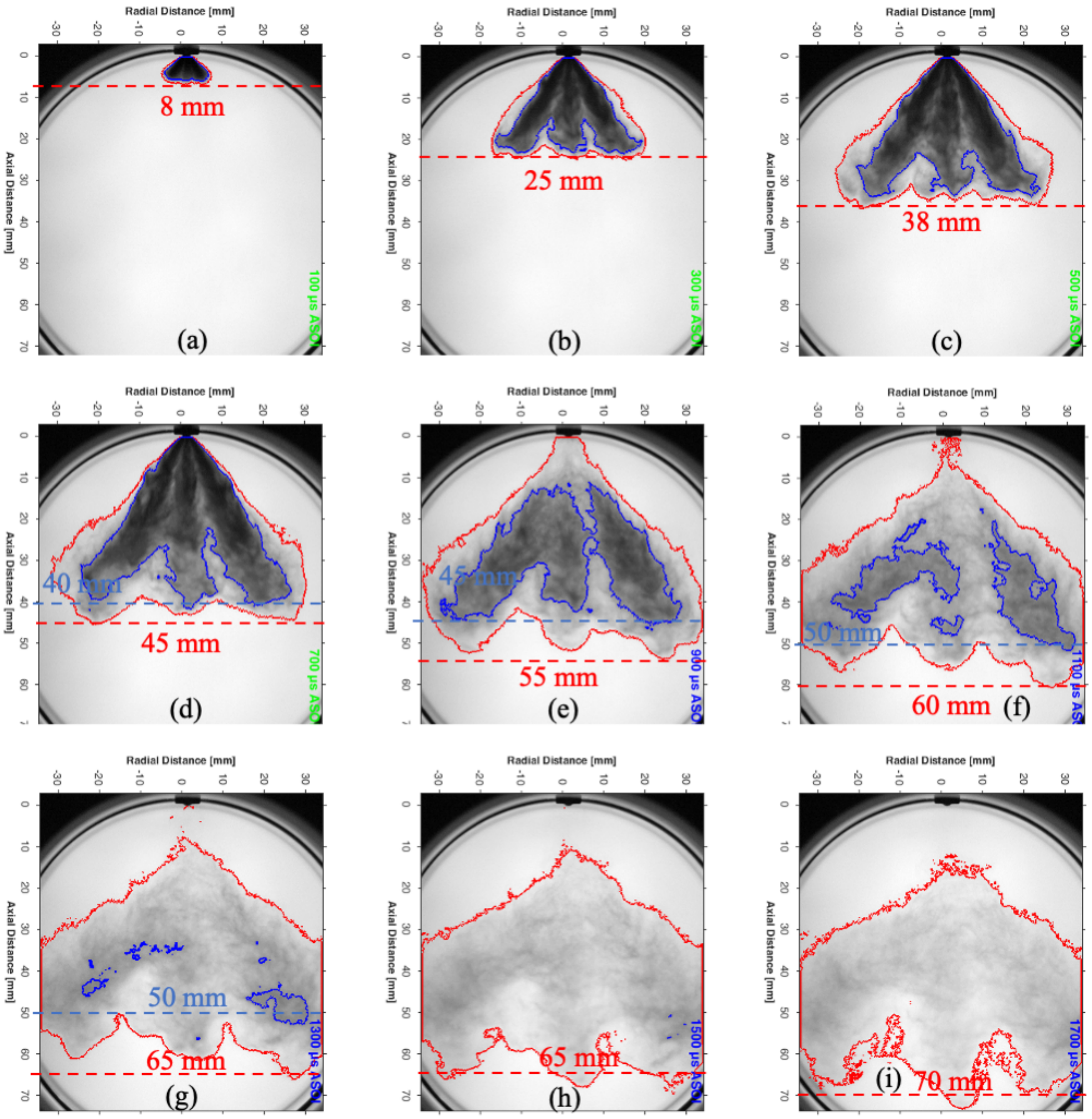

Figure 9.12: DBI images taken from the ECN data set [1] which show the liquid penetration for the flashing condition at different time instances, i.e., (a) 0.1 ms $ASOI$, (b) 0.3 ms $ASOI$, (c) 0.5 ms $ASOI$, (d) 0.7 ms $ASOI$, (e) 0.9 ms $ASOI$, (f) 1.1 ms $ASOI$, (g) 1.3 ms $ASOI$, (h) 1.5 ms $ASOI$, (i) 1.7 ms $ASOI$

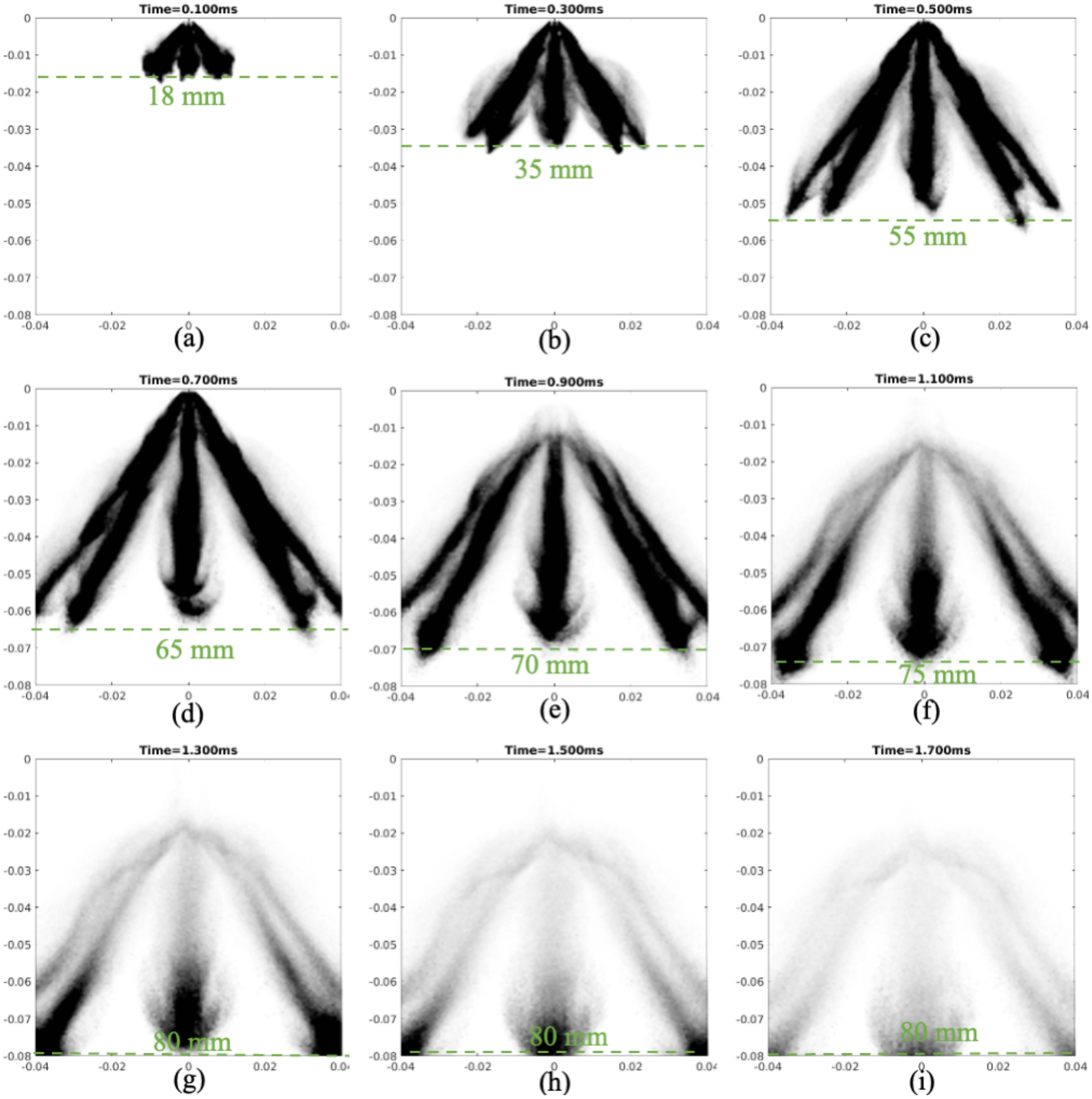

Figure 9.13: Binarized images showing the liquid spray boundary predicted by the plume based coupling approach with $We_{cr} = 1$ for the flashing condition at different time instances, i.e., (a) 0.1 ms $ASOI$, (b) 0.3 ms $ASOI$, (c) 0.5 ms $ASOI$, (d) 0.7 ms $ASOI$, (e) 0.9 ms $ASOI$, and (f) 1.1 ms $ASOI$.

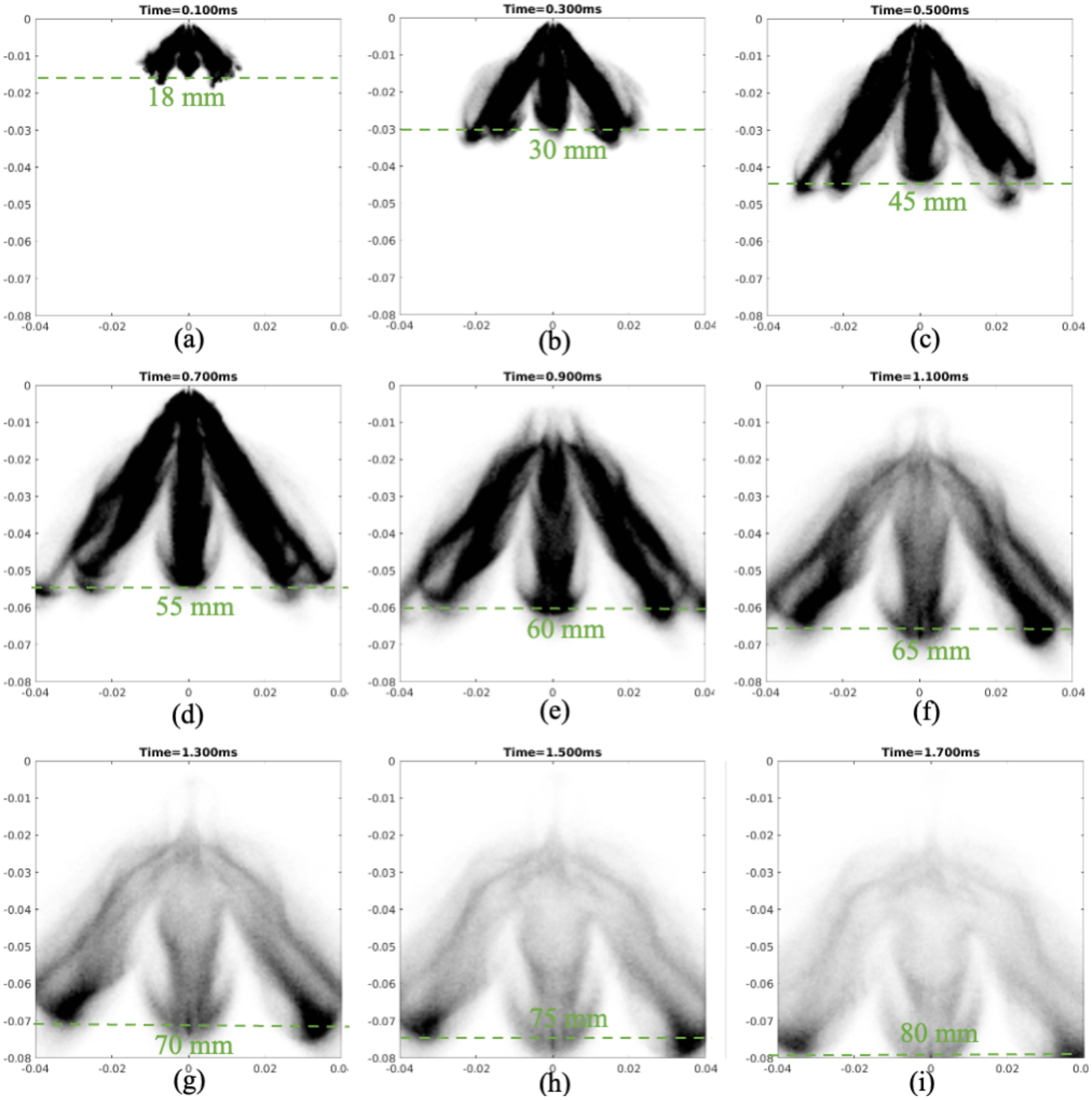

Figure 9.14: Binarized images showing the liquid spray boundary predicted by the plume based coupling approach with $We_{cr} = 6$ for the flashing condition at different time instances, i.e., (a) 0.1 ms $ASOI$, (b) 0.3 ms $ASOI$, (c) 0.5 ms $ASOI$, (d) 0.7 ms $ASOI$, (e) 0.9 ms $ASOI$, and (f) 1.1 ms $ASOI$.

9.3.2 Liquid penetration

In an engine environment, liquid spray penetration influences the wetting of internal components (cylinder and piston). For an effective comparison between the experimental observations and computational predictions, the ECN community [1], [150] has defined an approach based on the the projected liquid volume (PLV) method for the DBI measurements. According to this approach, the measured optical thickness (τ) is correlated with the PLV, which is the integral of the liquid volume fraction (LVF) along the cross-stream direction, y, as shown in Eqn. 9.3. The extinction coefficient (C^*_{ext}) and droplet diameter are defined based on the experimental measurements [81]. In addition, ECN recommends two thresholds for the PLV to define the liquid penetration, i.e., $2 \times 10^{-4}\ mm^3/mm^2$ and $2 \times 10^{-3} mm^3/mm^2$.

$$PLV = \tau \frac{\pi \frac{d^3}{6}}{C^*_{ext}} = \int_{-y_\infty}^{y_\infty} LVF\, dy \tag{9.3}$$

To compare the predictions from the parcel simulations with experimentally predicted liquid penetration, first, an Eulerian LVF field is generated from the Lagrangian parcel simulation. Then, the line-of-sight integrations of the 3-D LVF field along the cross stream direction are performed to project the data onto a 2-D background mesh. Finally, the liquid penetration is defined as the maximum axial position of any plume with the projected value lower than the two experimentally defined thresholds. Comparisons between the computationally predicted liquid penetration and the experimentally measured penetration by two institutions, i.e., Sandia National Lab.(SNL) and University of Melbourne (UoM) for both the LVF thresholds under non-flashing and flashing conditions are included in Figs. 9.15, and 9.16, respectively.

For the non-flashing condition, the discrepancies in the experimental measurements can be attributed to the fact that the UoM results maintain a nozzle temper-

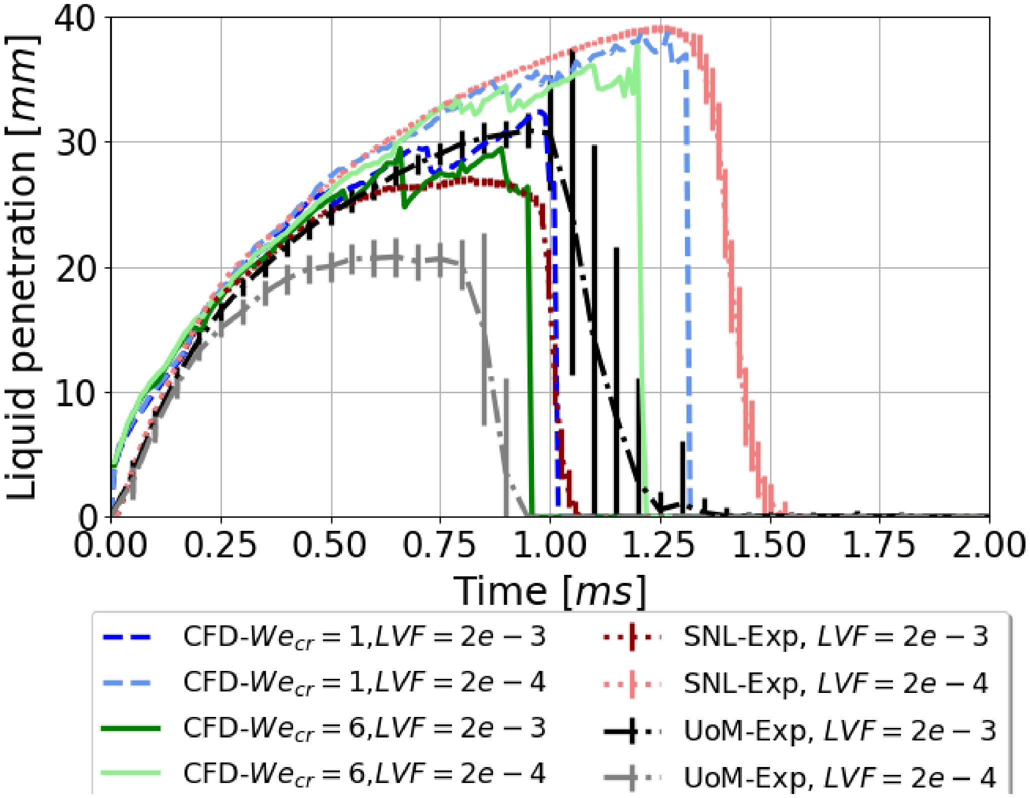

Figure 9.15: The figure includes predictions for the liquid penetration by the plume-based coupling approach for two critical Weber number.(1 and 6) under the non-flashing condition. The predictions are compared with the experimentally measured liquid penetration based on two LVF thresholds for the same condition by the Sandia National Lab (SNL) [81] and University of Melbourne (UoM) [150]. The experimental data are obtained from the ECN data base [1].

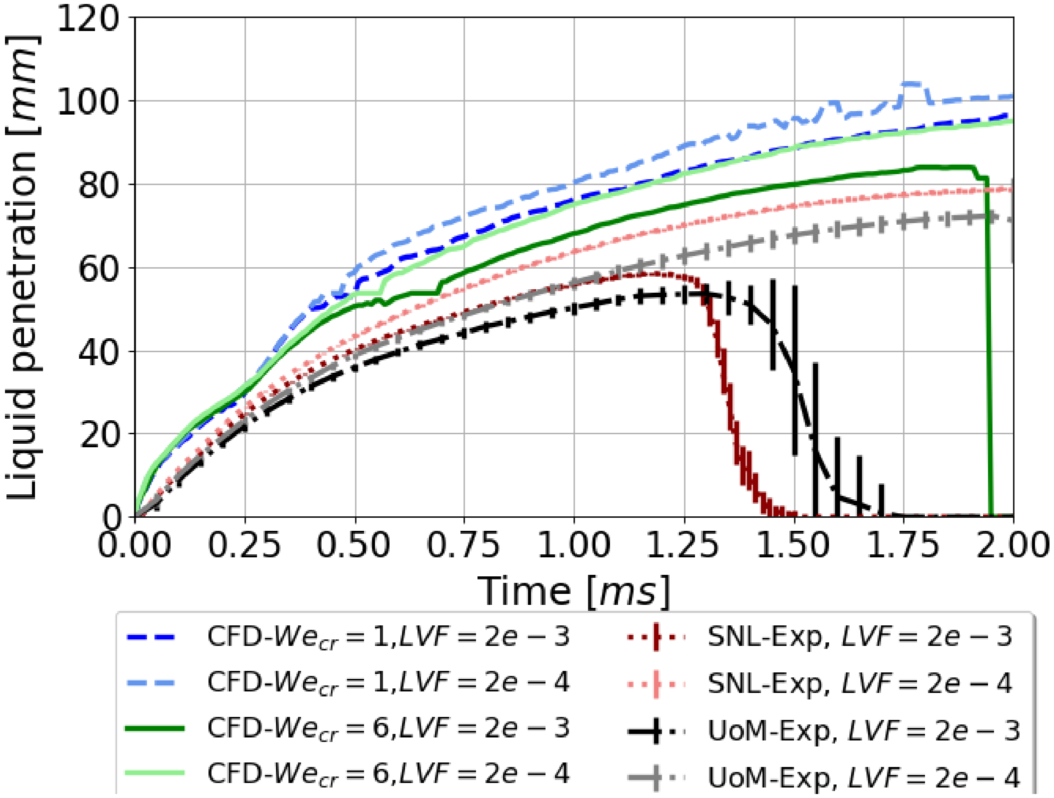

Figure 9.16: The figure includes predictions for the liquid penetration by the plume-based coupling approach for two critical Weber number (1 and 6) under the flashing condition. The predictions are compared with the experimentally measured liquid penetration based on two LVF thresholds for the same condition by the Sandia National Lab (SNL) [81] and University of Melbourne (UoM) [150]. The experimental data are obtained from the ECN data base [1].

ature of 383K, whereas SNL maintains a nozzle temperature of 363K [1], which is the nominal value. Again, the predicted liquid penetration and residence time match well with the SNL's data for the lower LVF threshold (2×10^{-4} mm^3/mm^2). The percentage differences in the maximum predicted liquid penetration and the predicted liquid fuel residence time between the computational predictions for the unity critical Weber number and the SNL measurements for the lower LVF threshold under the non-flashing condition are around one percent. Furthermore, more liquid penetration and liquid fuel residence time are observed in the flashing condition both computationally and experimentally compared to the non-flashing condition, as seen in Fig. 9.16. However, the values predicted by the plume-based coupling approach are higher compared to the experimental measurements. CFD simulation with $We_{cr} = 6$ has the closest penetration value to the SNL experiments for the lower LVF threshold, and the percentage difference in the highest predicted liquid penetration is around twenty percent. Thus, it can be inferred that the computationally predicted spray is less evaporative than the experiment.

9.3.3 Vapor penetration

Vapor penetration is another macroscopic spray characteristic which influences the combustion quality. Experimentally, the vapor penetration is measured by means of a Schlieren technique. The details of the experimental measurements are explained by Hwang et al. [81]. For an effective comparison between the computational predictions and the experimental findings, vapor penetration is defined as the maximum axial distance from the injector tip where a mixture fraction 0.1% is found.

Figs. 9.17, and 9.18 include the vapor penetration comparison between the experimental data [1] and the computational predictions for different ambient conditions. Less difference in the vapor penetration measurements by the different institutions are observed unlike the liquid penetration results. In non-flashing conditions, predictions

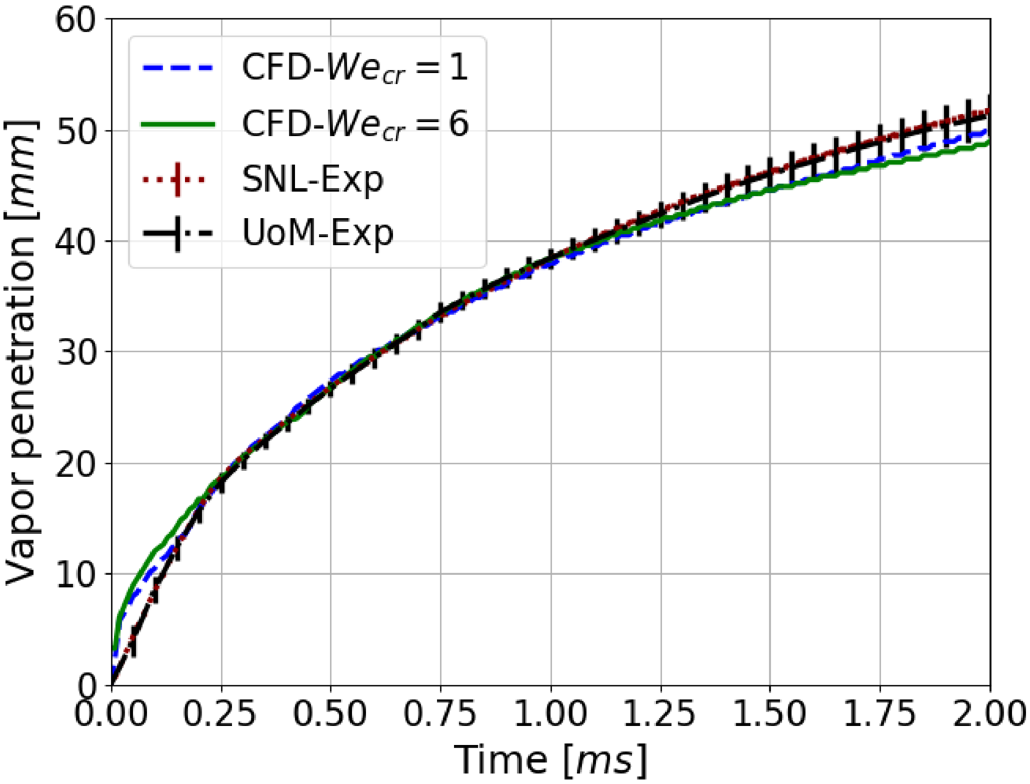

Figure 9.17: The figure includes predictions for the vapor penetration by the plume-based coupling approach for two critical Weber no.(1 and 6) under the non-flashing condition. The predictions are compared with the experimentally measured vapor penetration based for the same condition by the Sandia National Lab (SNL) and University of Melbourne (UoM). The experimental data are obtained from the ECN data base [1].

by the plume-based coupling approach match well with the measured values. However, in flashing conditions, the plume-based coupling approach predicts higher vapor penetration values compared to the experimental observations. The percentage difference between the measured and predicted vapor penetration values are four and six percent in the non-flashing and flashing conditions, respectively. Similar to the liquid penetration predictions, higher vapor penetrations are observed in the flashing condition compared to the non-flashing due to lower ambient density. The non-flashing CFD predictions are found to be insensitive to the initial droplet diameter, however, lower vapor penetration for a higher critical Weber number is observed in flashing.

9.3.4 Axial gas velocity

Sphicas et al. [209], and [210] have performed particle image velocimetry (PIV) measurements and reported the temporal evolution of the gas velocity on the injector axis at 15 mm downstream of the injector tip for the non-flashing condition. For further validation, the gas velocity predictions by the plume-based coupling approach are compared with the experiments, as shown in Fig. 9.19. In Fig. 9.19, the negative axial velocity refers to the condition when the ambient gas has an upward motion, i.e., the gas is moving towards the tip of the injector. As evident from the figure, during the injection phase ($780\mu s\ ASOI$), the predicted axial velocity is within the experimental uncertainties. However, the plume-based simulations predict less positive axial velocities compared to the experiments. Additionally, in the non-flashing condition, the axial velocity predictions are found to be sensitive to the critical Weber number, unlike the penetration predictions. Henceforth, the initial droplet diameter effects the momentum exchange between the ambient gas and the parcels. Similarly, the comparisons between the predictions for the non-flashing and flashing conditions are included in Fig. 9.20. Higher axial gas velocities are observed in the flashing condition compared to the non-flashing. This difference in observations is attributable

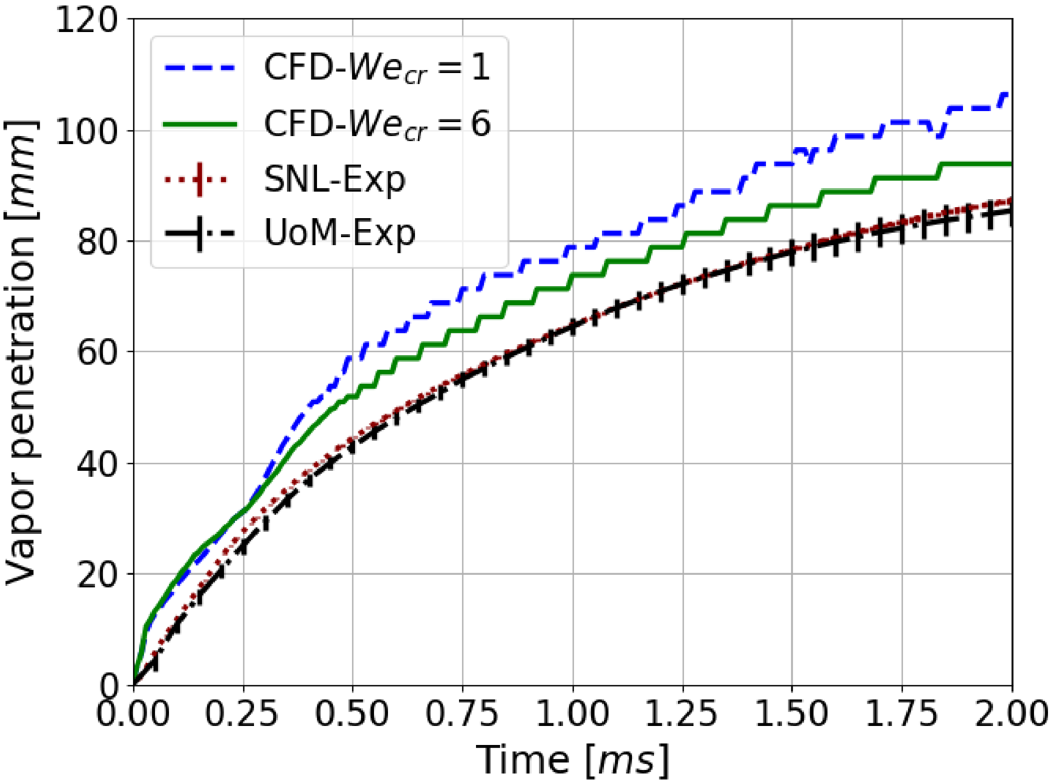

Figure 9.18: The figure includes predictions for the vapor penetration by the plume-based coupling approach for two critical Weber number (1 and 6) under the flashing condition. The predictions are compared with the experimentally measured vapor penetration based for the same condition by the Sandia National Lab (SNL) [81] and University of Melbourne (UoM) [150]. The experimental data are obtained from the ECN data base [1].

to the higher plume velocity due to the lower ambient gas density in flashing. In flashing, the gas velocity is also found to be sensitive to the initial droplet diameter.

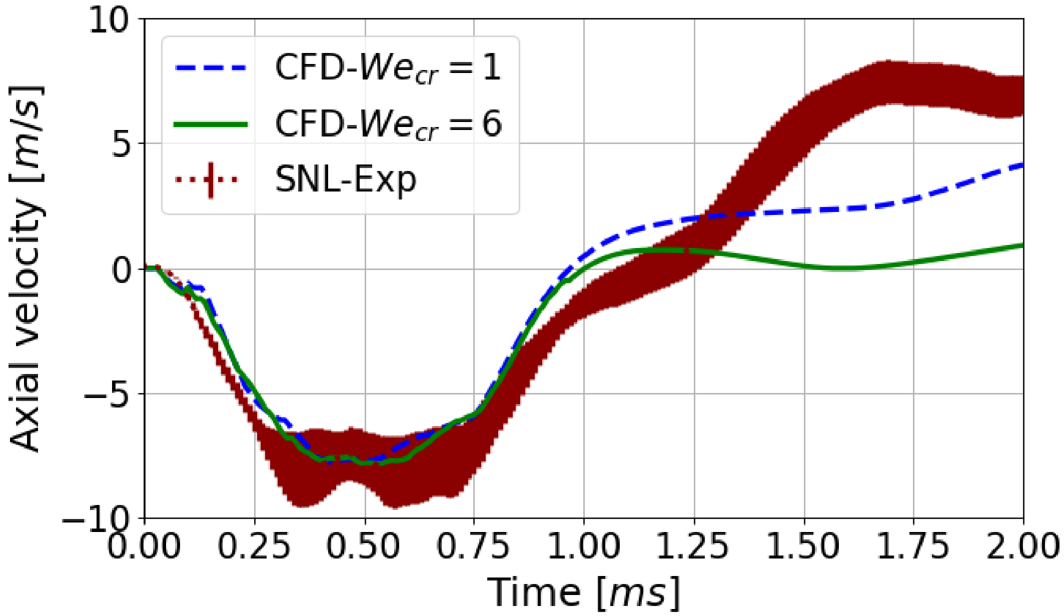

Figure 9.19: The figure includes experimental measurements for the axial velocity at a location 15 mm downstream of the injector tip along the injector axis [209] and the computational predictions by the plume-based coupling approach for the non-flashing condition.

Additionally, Sphicas et al. [210] have subdivided the injection duration into several subphases based on the observed gas velocity to determine the jet-to-jet interactions under different ambient conditions. Similar phenomena are also captured by the plume-based simulations for both flash-boiling and non-flashing conditions as explained below.

- Pre-plume arrival period: This phase is defined as the phase before the heads of the individual plumes reach 15 mm downstream of the injector tip [210]. During

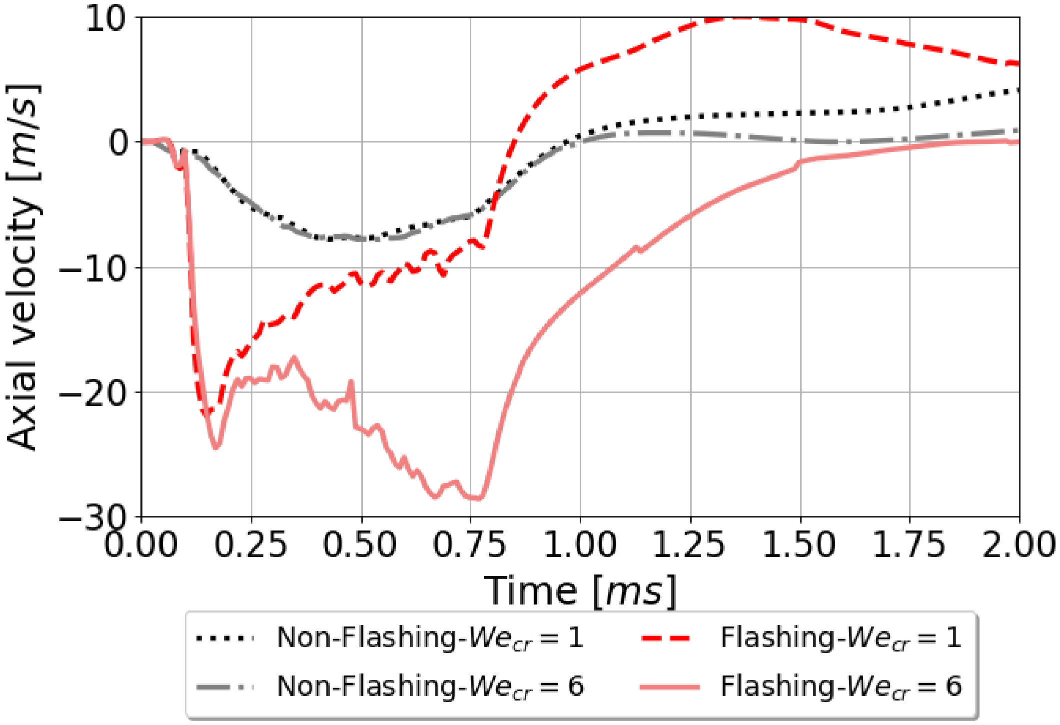

Figure 9.20: The figure includes comparison of the axial velocity predictions by the plume-based coupling approach under flashing and non-flashing conditions.

this phase, although the plumes have not arrived at the predetermined locations, the downstream gas already starts responding to the momentum exchange and the pressure waves created in the upstream locations, as seen in Fig. 9.21. In addition, in the flash-boiling condition, this response is quicker due to higher plume velocities, refer Fig. 9.22. Furthermore, the direction of the gas moment is purely vertical for the non-flashing conditions. This supports the hypothesis proposed by Sphicas et al. [210] that the spray is creating a low pressure regime that pulls the ambient gas up towards the injector tip, establishing a central recirculation zone between the plumes. As time increases, the magnitude of the upstream velocity increases.

- Time of plume arrival at the 15mm location: Similar to the experiments [210] the plumes arrive around $200\mu s$ after the start of injection for the non-flashing condition. As the plumes arrive at the 15mm location, an upward moving ambient gas gets established, as seen in Fig. 9.23.
- Profile relaxation period: As seen in experiments [210], the velocity profile of the upward moving gas becomes homogeneous with respect to the axial position post arrival of the plumes. Moreover, the recirculation velocity plateaus after increasing for certain durations, for the non-flashing condition. Evidence of similar phenomena are captured in Fig. 9.24. In flashing, this state is attained at a much faster rate.
- Uniform upward motion period: During this period, uniform gas velocity profiles are observed on the 15 mm line both experimentally [210] and computationally. Evidence of the same for the non-flashing condition is captured in Fig. 9.25
- Reversing period: Sphicas et al. [210] further defines this period postcompletion of the injection. During this phase, the magnitude of the axial velocity decreases and eventually it changes sign. Hence, the ambient gas no longer

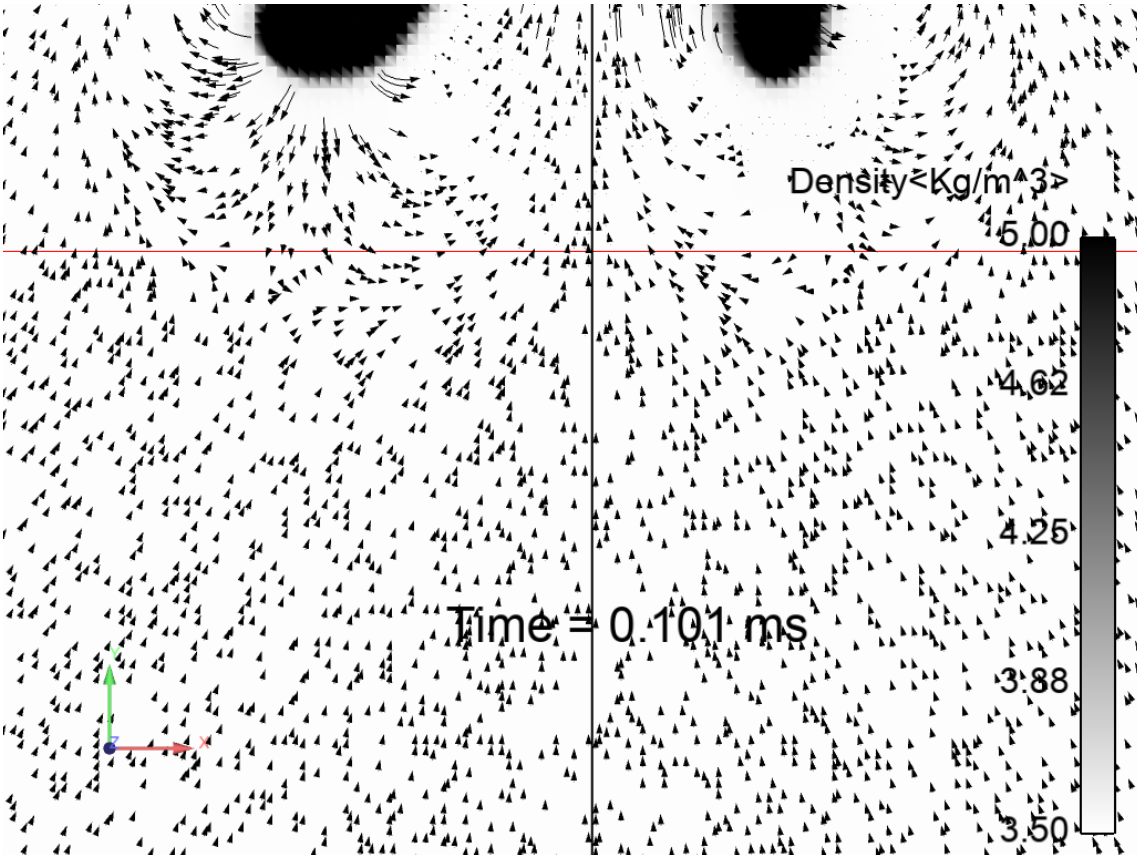

Figure 9.21: Vectors showing the direction of the ambient gas movement for the non-flashing condition and $We_{cr} = 1$ at time = 0.1ms ASOI. The red horizontal line is located at 15 mm downstream of the injector tip. The black vertical line is the injector axis.

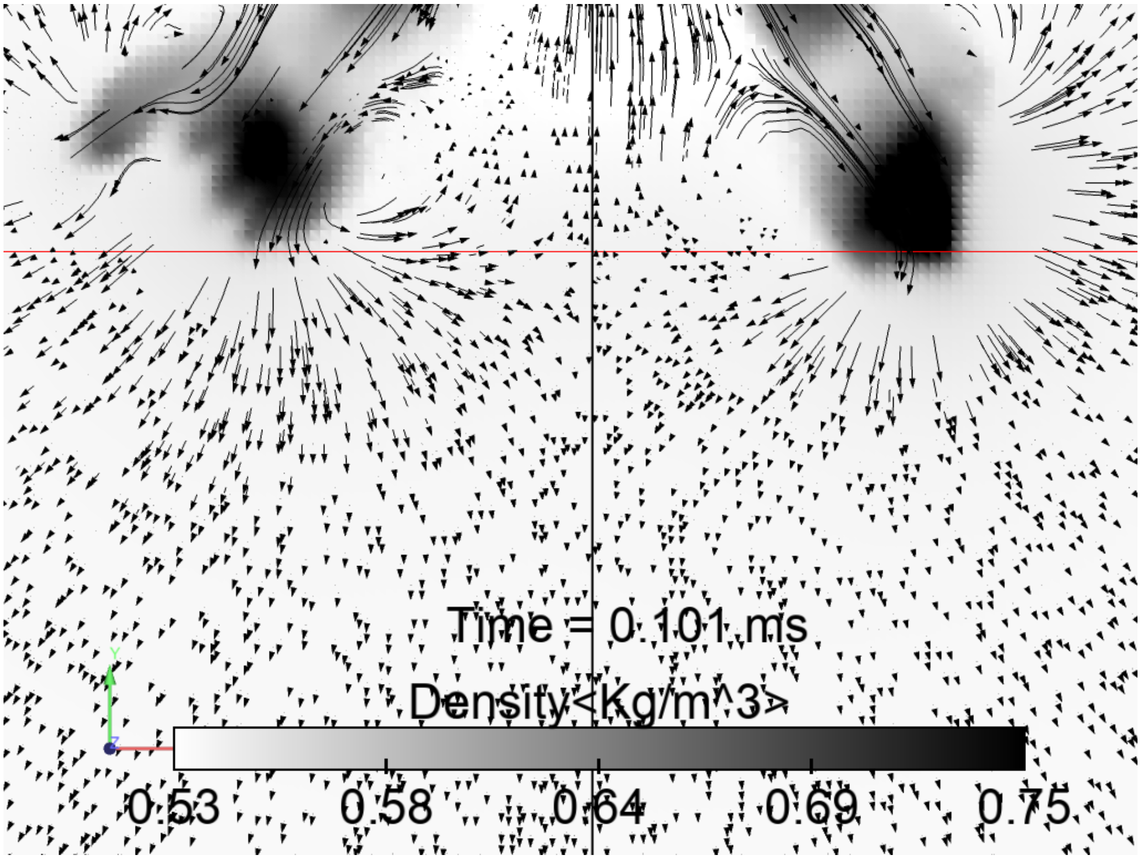

Figure 9.22: Vectors showing the direction of the ambient gas movement for the flashing condition and $We_{cr} = 6$ at time = 0.1ms ASOI. The red horizontal line is located at 15 mm downstream of the injector tip. The black vertical line is the injector axis.

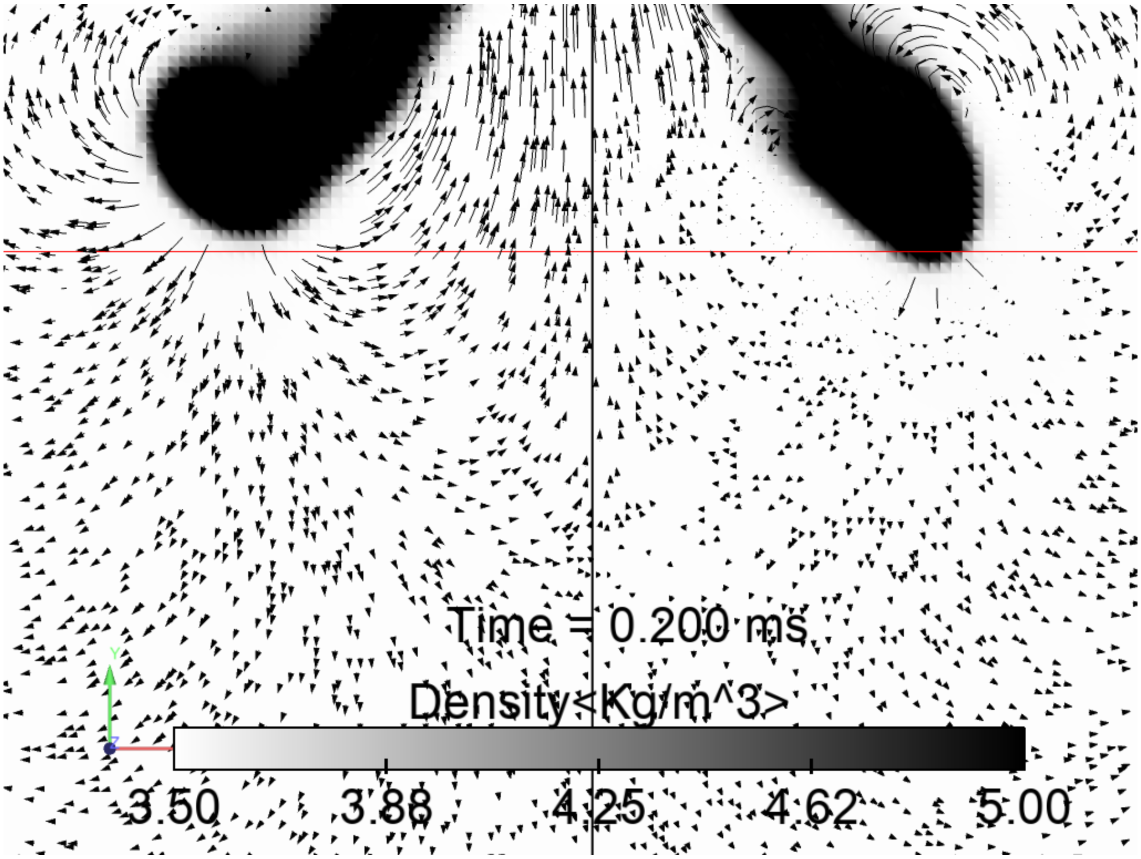

Figure 9.23: Vectors showing the direction of the ambient gas movement for the non-flashing condition and $We_{cr} = 1$ at time = 0.2ms ASOI. The red horizontal line is located at 15 mm downstream of the injector tip. The black vertical line is the injector axis.

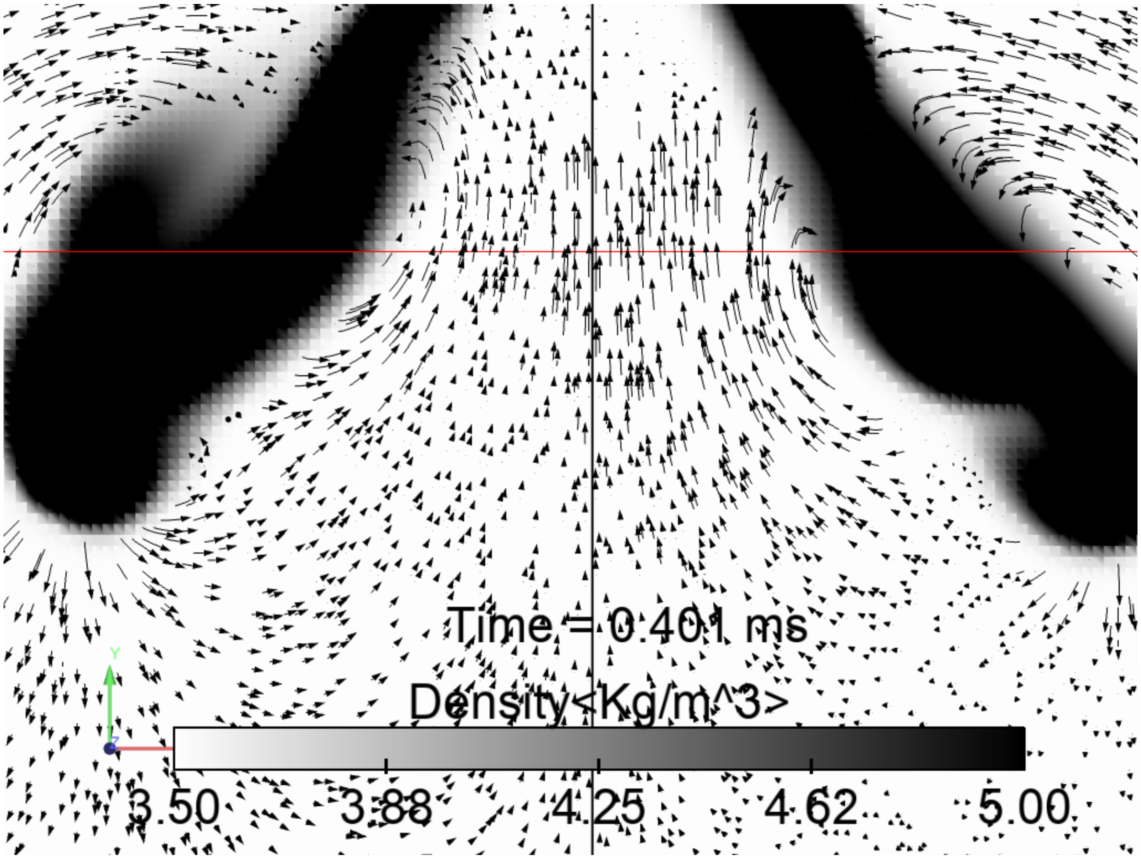

Figure 9.24: Vectors showing the direction of the ambient gas movement for the non-flashing condition and $We_{cr} = 1$ at time = 0.4ms ASOI. The red horizontal line is located at 15 mm downstream of the injector tip. The black vertical line is the injector axis.

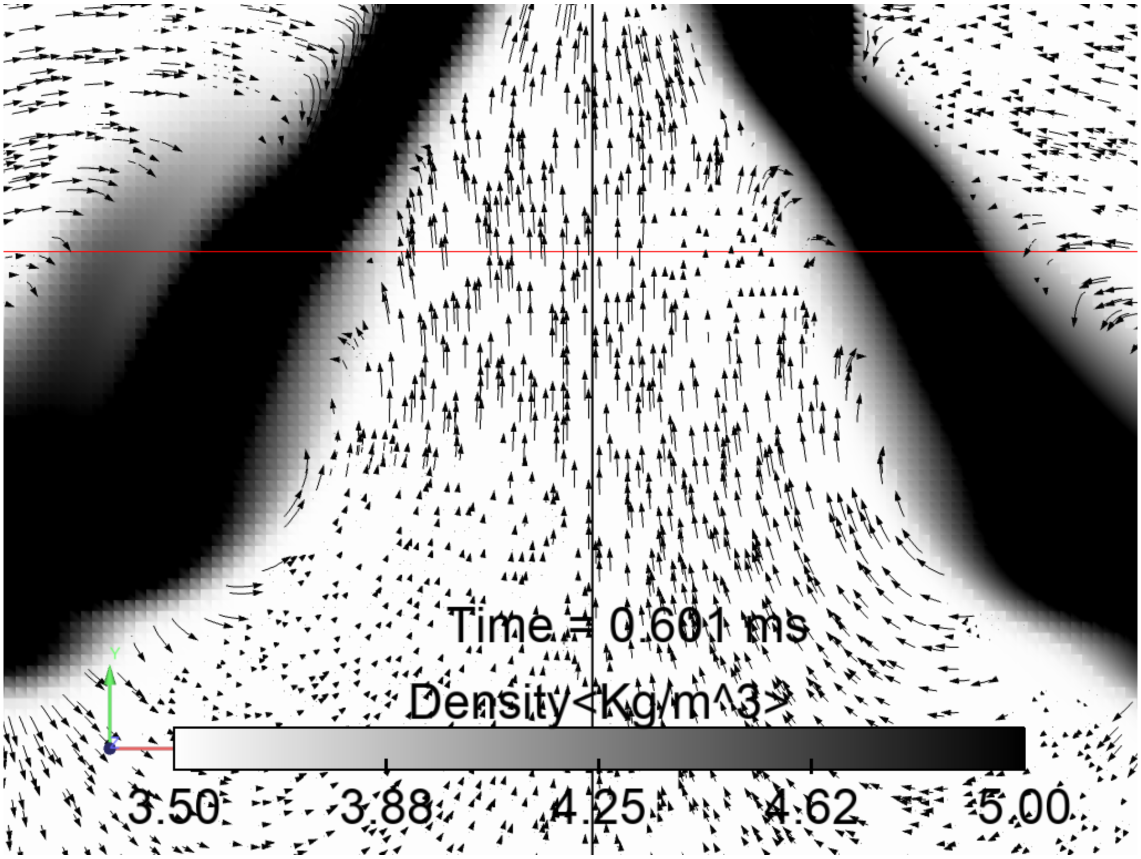

Figure 9.25: Vectors showing the direction of the ambient gas movement for the non-flashing condition and $We_{cr} = 1$ at time = 0.6ms ASOI. The red horizontal line is located at 15 mm downstream of the injector tip. The black vertical line is the injector axis.

moves towards the injector tip, rather it moves in the direction of the plume motion. Merged/connected plumes are accredited for this behavior of the ambient gas [210]. Similar evidences are captured by the plume-based coupling approach for both flashing and non-flashing conditions, Figs. 9.26 and 9.27.

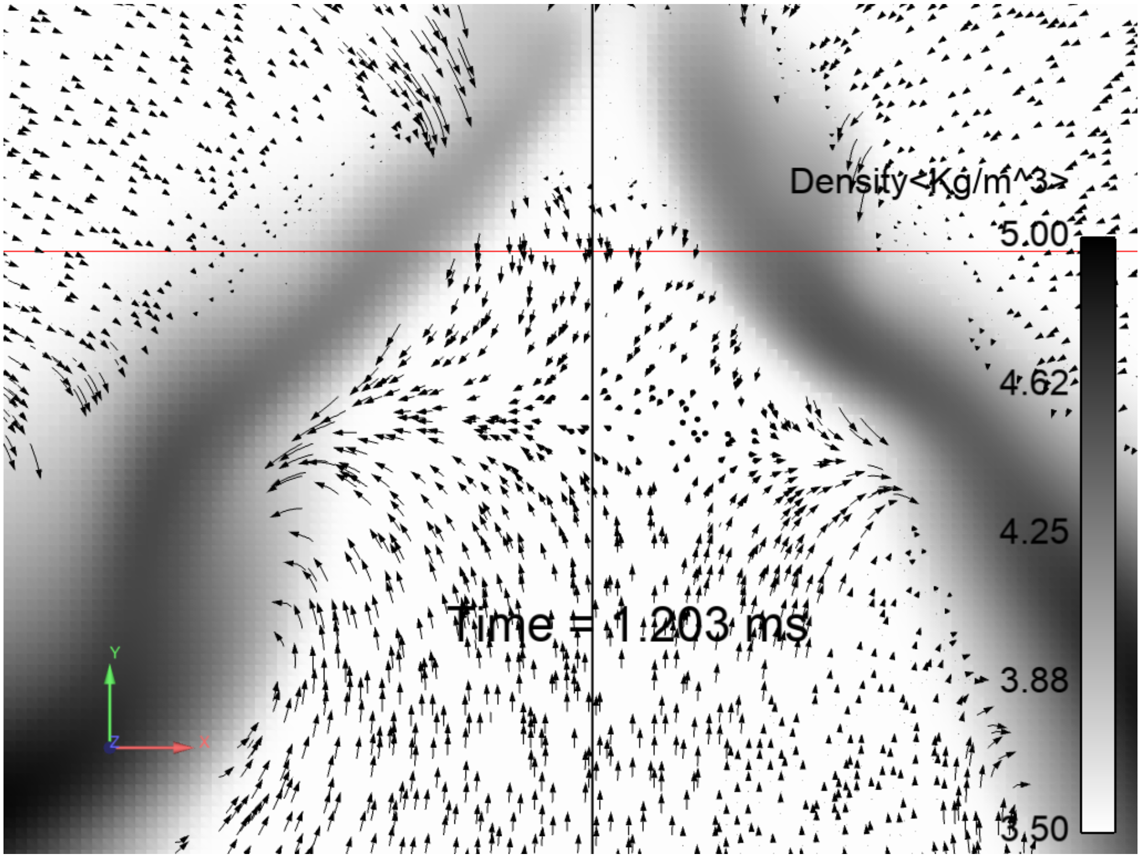

Figure 9.26: Vectors showing the direction of the ambient gas movement for the non-flashing condition and $We_{cr} = 1$ at time = 1.2ms ASOI. The red horizontal line is located at 15 mm downstream of the injector tip. The black vertical line is the injector axis.

9.3.5 Momentum conservation

The plume-based coupling approach inherently accounts for the mass conservation, as the total number of parcels injected into the Lagrangian domain at a specific time is driven by the ROI predictions from the Eulerian simulation. However, the

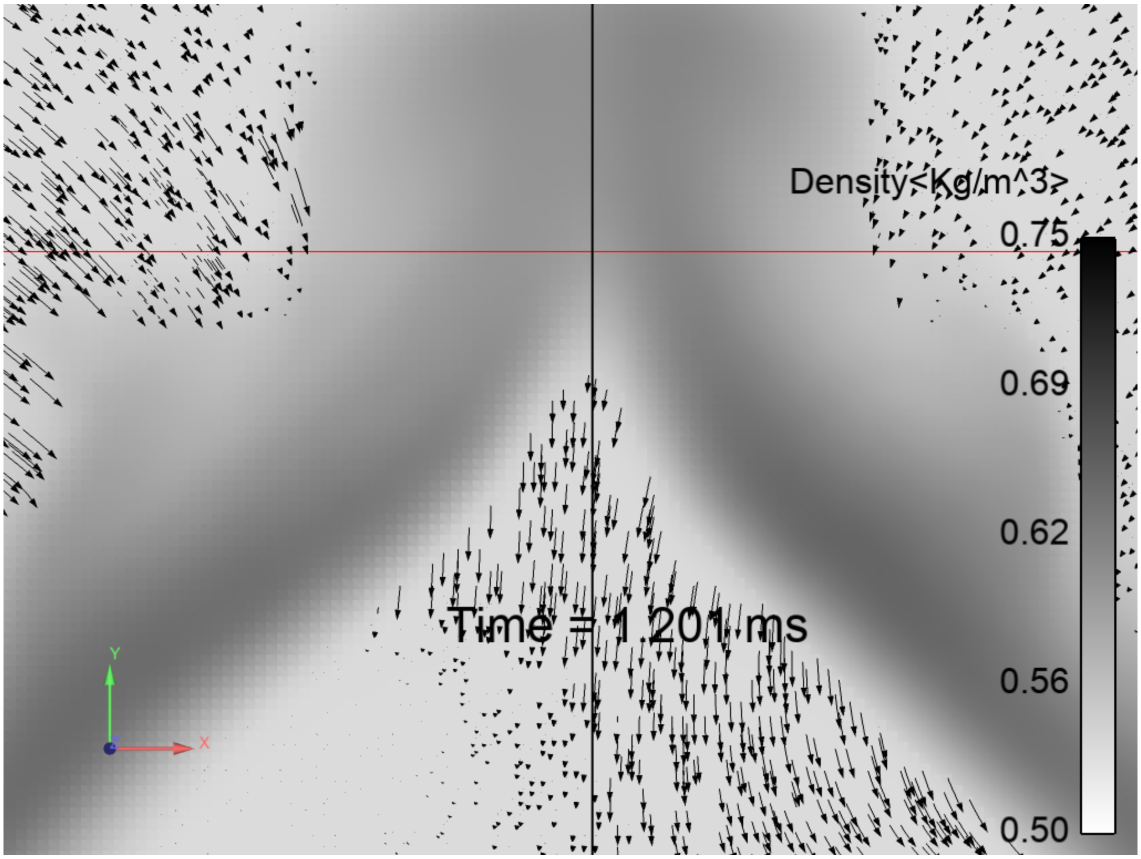

Figure 9.27: Vectors showing the direction of the ambient gas movement for the non-flashing condition and $We_{cr} = 6$ at time = 1.2ms ASOI. The red horizontal line is located at 15 mm downstream of the injector tip. The black vertical line is the injector axis.

same cannot be said for the momentum conservation. The fuel emanating from the nozzle mixes with the ambient gas due to turbulence and results in the momentum exchange between the Non-condensible gas and the spray plumes. The plume-based coupling approach does not account for this Eulerian gas momentum while initializing the parcels in the LE simulations. Hence, there would be a definite difference between the total momentum calculated at the nozzle exit and the total momentum of the parcels. To account for this discrepancy, the total rate of momentum is evaluated at each nozzle's exit. The calculated rate of momentum is further integrated over the whole injection duration to determine the total Eulerian momentum exiting the individual nozzles. Similarly, for the plume-based simulations, the momentum of an individual parcel injected during a specific time step is determined based on its fixed mass and the initialized velocity. Then, the total momentum injected at the specific time step for the individual plume is computed by segregating the total number of injected parcels based on their position vectors for that time instance. Finally, the momentum of the parcels for each plume group are integrated over the injection duration to evaluate the total Lagrangian momentum injected during a single spray event.

Fig. 9.28 includes a comparison of the above described momentum for the non-flashing condition. As expected, the total momentum injected into the Lagrangian domain by the plume-based coupling approach is lesser compared to the Eulerian momentum evaluated at the nozzles' exits. The average percentage of difference is around fourteen percent. In contrast, a similar comparison for the flash-boiling condition reveals a different trend, as shown in Fig. 9.29. For the flashing condition, the momentum of the plumes are found to be higher compared to the respective nozzle's exit. This might be indicative of the vapor acceleration of the downstream plumes due to flashing. In the plume-based Lagrangian simulations, these momentum discrepancies can be accounted for by introducing a source term in the Eulerian N-S

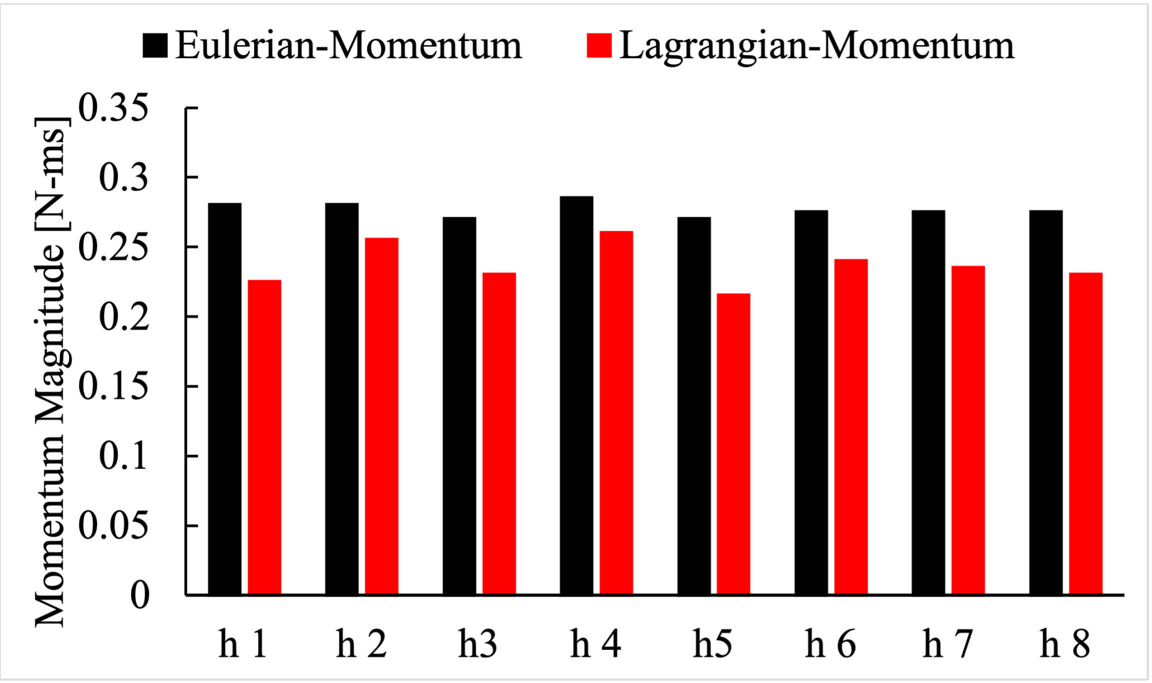

Figure 9.28: Total momentum comparison between the Eulerian HRMFoam and the Lagrangian plume-based simulations for the non-flashing condition. The Eulerian momentum is evaluated at the exit of the nozzle. The Lagrangian momentum is calculated based on the parcel momentum

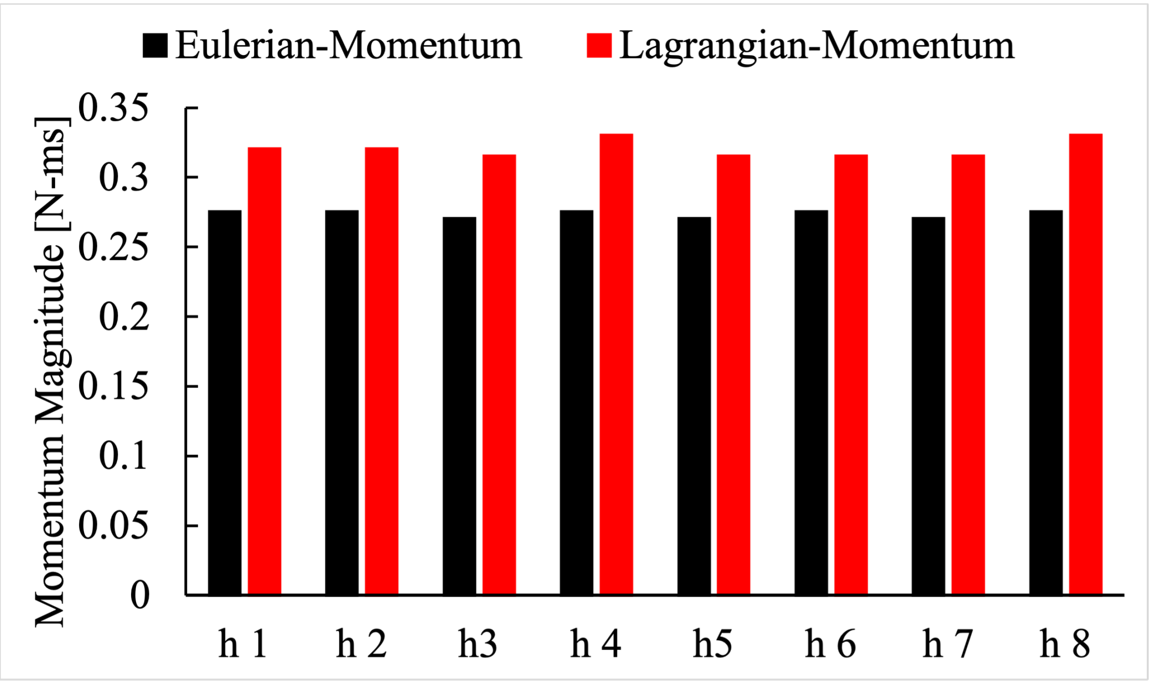

Figure 9.29: Total momentum comparison between the Eulerian HRMFoam and the Lagrangian plume-based simulations for the flashing condition. The Eulerian momentum is evaluated at the exit of the nozzle. The Lagrangian momentum is calculated based on the parcel momentum

equation for the non-condensible gas. However, the source term needs to be modeled based on different ambient conditions.

9.4 Summary and conclusions

A novel plume-based coupling approach is developed in the current chapter. This approach couples the Eulerian spray simulation with the Lagrangian parcel simulation based on the derived plume surfaces as the transition region. This approach is applied to study the flow of a practical GDI injector operating under different ambient conditions. Predictions from the Lagrangian simulations are further validated against the experimental measurements obtained from the publicly available ECN database [1]. Key details of the plume-based coupling approach are summarized below:

- The plume-based coupling approach requires running the Eulerian injector flow simulation with the primary atomization model, i.e., $\Sigma - Y$ model, *a priori*. In the current work, a formulation of the $\Sigma - Y$ model based on the critical Weber number is used. Two different We_{cr}, i.e., one and six are used to predict the SMD value in the near nozzle regions.

- Transition criteria based on the inter-droplet spacing are developed. These transition criteria are used to define the plume boundaries in the Eulerian framework. Subsequent data tabulations on these plume boundaries are accomplished. These tabulated data are used in CONVERGE 2.4 to initialize the parcels in the Lagrangian framework.

- Lagrangian simulations are performed for the ECN [1] prescribed G1(non-flashing) and G2(flashing) conditions. Qualitatively, the spray morphologies predicted by the CFD simulations are compared with DBI measurements obtained from the ECN data set [1] for both non-flashing and flashing conditions, and well agreements are achieved. In flashing, higher axially and radially penetrating liquid spray morphologies are captured compared to the non-flashing condition.

- Predictions for liquid penetration and vapor penetration by the plume-based coupling approach under different ambient conditions are compared with the DBI and Schlieren experiments performed at the Sandia National Lab [81] and the University of Melbourne [150]. In the non-flashing condition, the percentage differences between the CFD predictions and the SNL measurements for the maximum liquid and vapor penetrations are one and four percents, respectively. Whereas, the same differences are twenty and six percent for the flash-boiling condition. Predictions for the flash-boiling predictions can be improved by increasing the size of the embedding region, which extends until 50 mm downstream.

- Lastly, the axial gas velocity predictions from the plume-based approach are compared with the published PIV measurements [210]. CFD simulations are able to capture all subphases described by Sphicas et al. [210] for the non-flashing condition.

- The plume-based coupling approach needs additional source term modeling for different ambient conditions to account for the momentum conservation.

CHAPTER 10

PILOT STUDY AND CONCLUSIONS

The current dissertation is premised on the computational studies of near-nozzle and external spray behaviors of a 8-hole GDI injector under different ambient conditions (non-flash-boiling and flash-boiling conditions). The research includes the development of a needle closure algorithm to study the end of injection phenomena. Subsequently, the primary atomization model of the in-house developed HRMFoam solver is improved. Finally, a novel plume-based coupling approach is developed for external spray simulations.

The next section explores a pilot study to include the surface tension models in the HRMFoam solver. These added features will enable the exploration of the low Weber number flows, i.e., the tip-wetting flow. The following section will include the concluding remarks and based on the major findings of this dissertation.

10.1 Pilot study: Dynamically coupled sharp and diffuse interface approach

As discussed in Ch. 3, gasoline sprays are characterized by high Weber number and Reynolds number. Although a sharp interface exists between the liquid and gaseous phase, when projected on to a finite sized computational mesh, the sharp interface becomes diffused [48], [49]. The in-house HRMFoam solver uses this limitation to its advantage and simulates the hydrodynamics of the spray atomization process using a diffuse interface-based approach. Consequently, it is computationally less expensive for engineering applications such as automotive sprays. Furthermore, the inherent nature of the surface tension force attempts to make all liquid structures spherical in nature due to higher stability. However, in the dense spray region, nonspherical liquid structures like liquid ligaments and distorted large droplets are observed. Hence, the HRMFoam solver has been preferred in the dense spray region. Nonetheless, the flow around the injector tip that drives the wetting phenomenon is associated with low Weber number and Reynolds numbers. The wetting is further influenced by the solid-liquid contact angle. Hence, surface tension models are required to correctly resolve and quantify the fuel film, as indicated in Ch. 7. VOF solvers of OpenFOAM framework, such as interFoam can be applied to simulate such flows. Thus, modifications in HRMFoam solver which are inspired by the interFoam solver will be explored in the subsequent subsections.

10.1.1 Governing equation: interFOAM

A volume of fluid (VOF) method to solve multiphase problems was first postulated by Hirt and Nicholas [78]. The method relies on the definition of an indicator function to resolve the interface. The VOF approach solves a transport equation for the indicator function in conjunction with other conservation equations. The indicator function determines whether the computational cell is occupied by one fluid or the other, or a mixture of both fluids. The VOF solver of OpenFOAM, interFoam, is designed for incompressible flow without phase-change phenomena. Performances of the solver have been evaluated by many publications [55], [222], [113]. The governing equations of the interFoam solver include conservation equations for mass and momentum and a transport equation for the phase fraction (α), as shown below.

$$\nabla \cdot U = 0 \tag{10.1}$$

$$\frac{\partial \rho U}{\partial t} + \nabla \cdot (\rho U U) = -\nabla p^* + g \cdot x \nabla \rho + \nabla \cdot \tau + f_\sigma \tag{10.2}$$

$$\frac{\partial \alpha}{\partial t} + \nabla \cdot (U\alpha) + \nabla \cdot [U_c \alpha (1-\alpha)] = 0 \tag{10.3}$$

In Eqn. 10.2, U is the velocity vector, p^* is the modified pressure formulated by removing the hydrostatic-$(\rho g \cdot x)$ from the total pressure and τ is the shear stress tensor. Furthermore, ρ is the mixture density calculated based on the expression in Eqn. 10.4 by accounting for the density of individual fluids and the volume fraction (α).

$$\rho = \rho_l\,(\alpha) + \rho_g\,(1-\alpha) \tag{10.4}$$

Additionally, In Eqn. 10.2, f_σ is the volumetric surface tension force which is estimated based on the continuum surface force model (CSF) proposed by Brackbill et al. [36]. At first, the model determines the curvature of the interface based on the gradient of the indicator function, α for the interFoam solver. Then, the CSF model calculates f_σ as per the expression presented in Eqn. 10.6.

$$\begin{aligned} \kappa &= \frac{\nabla\alpha}{|\nabla\alpha|} && (10.5) \\ f_\sigma &= \sigma\kappa\nabla\alpha && (10.6) \end{aligned}$$

The transport equation for the volume fraction, Eqn. 10.6, includes an additional convection term involving the compression velocity (U_c), as suggested by Weller et al. [230]. This artificial compression term attempts to compress the free surface towards a sharper interface. However, this term is not included in the original VOF formulation proposed by Hirt and Nicholas [78]. The compression velocity (U_c) is further determined based on the correlation presented in Eqn. 10.7

$$U_c = C_\alpha |U| \frac{\nabla\alpha}{|\nabla\alpha|} \tag{10.7}$$

In Eqn. 10.7, C_α is a user defined constant that determines the effect of the compression term, and $\frac{\nabla\alpha}{|\nabla\alpha|}$ ensures the direction of the compression velocity is normal to the interface. Additionally, to ensure the boundedness of the volume fraction, interFoam uses the multidimensional universal limiter with explicit solver (MULES) [223] [182] which is based on the flux corrected transport (FCT) technique [181].

10.1.2 Governing equations: HRMFoam with additional surface tension models

Inspired by the surface tension modeling approach of the interFoam solver, the liquid volume fraction, $\bar{Y}$, is chosen as the indicator function for HRMFoam. In HRMFoam, $\bar{Y}$ is a derived quantity rather than a transported variable, and can be determined based on other transported mass fraction variables, as shown in Eqn. 10.8. Subsequently, the volumetric surface tension force (f_σ) is modeled based on $\bar{Y}$. Eqn. 10.9 shows the modified momentum conservation equation of HRMFoam.

$$\begin{aligned} \bar{Y} &= (1-x)\,(1-y)\,\frac{\rho}{\rho_l} && (10.8) \\ \frac{\partial \rho \mathbf{u}}{\partial t} + \nabla \cdot (\Phi \mathbf{u}) &= -\nabla p + \nabla \bar{\bar{\tau}} + \bar{f} + \bar{f}_\sigma && (10.9) \\ \bar{f}_\sigma &= \sigma \kappa \nabla \bar{Y} && (10.10) \\ \kappa &= \frac{\bar{Y}}{|\nabla \bar{Y}|} && (10.11) \end{aligned}$$

Unlike interFoam, the transport equation for the NCG mass fraction, i.e., Eqn. 4.5 of HRMFoam is modified to keep the computational cost minimal. An extra anti-diffusion term inspired by the interface compression term is added to Eqn. 4.5, as shown in Eqn. 10.12. Unlike interFoam, U_r is modeled based on the constitutive relation proposed by Desantes et al. [52], as shown in Eq. 10.13. The correlation proposed by Desantes et al. [52] depends upon the gradient of liquid mass fraction. However, in the current formulation, the relative velocity is calculated based on the NCG mass fraction.

$$\frac{\partial \rho y}{\partial t} + \nabla \cdot (\Phi y) + (1-\Psi)\nabla \cdot (\rho U_r y) = -\Psi \nabla \cdot \left(\frac{\mu_t}{Sc_r} \nabla y \right) \quad (10.12)$$

$$\rho U_r = \frac{1}{y(1-y)} \left[\frac{\mu_t}{Sc} \nabla y \right] \quad (10.13)$$

In Eqn. 10.12, Ψ correspond to an indicator function which carries the value of unity in the diffuse interface region, i.e., regions with high Weber number, whereas it is zero in the sharp interface region, i.e., regions with low Weber number. For the current pilot study, a zero value is chosen for the indicator function, Ψ.

10.1.3 Test case: Oscillating drop

For model validation, a 3-D oscillating drop is simulated with the proposed surface-tension based HRMFoam solver. A perturbation of the velocity field $v_x = x$, $v_y = y$, and $v_z = -2z$ is applied to the droplet. According to Lamb [101], the drop oscillation period for this mode $n = 2$ perturbation is given by Eqn. 10.14.

$$T = 2\pi \left[n(n-1)(n+2)\frac{\sigma}{\rho r_0^3} \right]^{-0.5} = 2\pi \left[\frac{8\sigma}{\rho r_0^3} \right]^{-0.5} \quad (10.14)$$

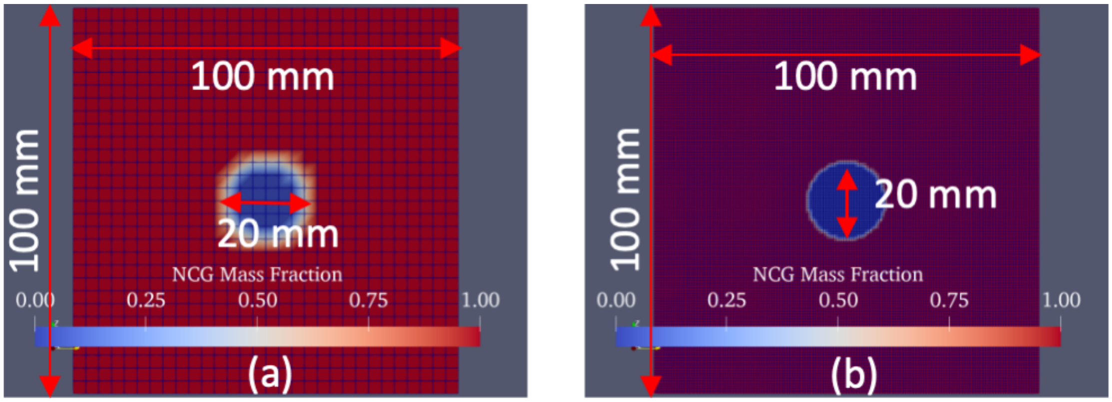

Figure 10.1: Cutplanes colored by the NCG mass fraction showing the initial droplet with different mesh resolutions. (a) coarse (b) Fine

Thus, for a gasoline droplet of 10 mm radius, the period of oscillation is calculated to be 0.4 seconds. The current model is simulated on two meshes of different resolutions, i.e., a coarse mesh with the mesh size of 3.3 mm and a fine mesh of size 0.67 mm, as shown in Fig. 10.1. Dai et al. [192] indicates a CFL criteria for the free surface numerical stability. According to them, the maximum time step for an oscillating drop can be evaluated based on Eqn. 10.15.

$$\Delta t < C\sqrt{\frac{\rho\Delta x^3}{2\pi\sigma}} \tag{10.15}$$

In Eqn. 10.15, C is a constant of order unity and Δx is the cell size. The current simulations use this stability criterion based on the surface tension to decide the time step. The modified HRMFoam solver is able to accurately capture the pressure difference across the interface, as shown in Fig. 10.2. The predicted pressure difference (4.5 *pa*) satisfies the Laplace equation for pressure (4.4 *pa*). However, the predicted period of oscillation does not agree with the exact solution calculated by Eqn. 10.14. Although a finer mesh resolution improves the period prediction, but it is still far from the ground truth, as seen in Fig. 10.3. Due to the inherent diffusive formulation of the HRMFoam solver, the transported mass fractions (x and y) are diffusive in nature. Consequently, the derived field, $\bar{Y}$ is also diffused over multiple cells. Hence, the current formulation for the indicator function, i.e., the use of $\bar{Y}$ to track the interface needs to be reformulated.

Hence, it can be concluded that a sharper interface formulation is required to match the exact solution of the oscillating droplet case. This can be achieved by formulating a new sharp color function inspired by the coupled level set volume of fluid (CLSVOF) [35] method. This function can be built with either the NCG mass fraction or the liquid volume fraction. Furthermore, a separate transport equation for the new color function needs to be included in the in-house solver. The proposed version of HRMFoam does not account for the wettability of the tip wall, which is required to quantify the amount of fuel that sticks to the tip. According to Brackbill [36], this can be accomplished by modifying the surface normal of the cells next to the wall based on the pre-defined static/dynamic contact angle.

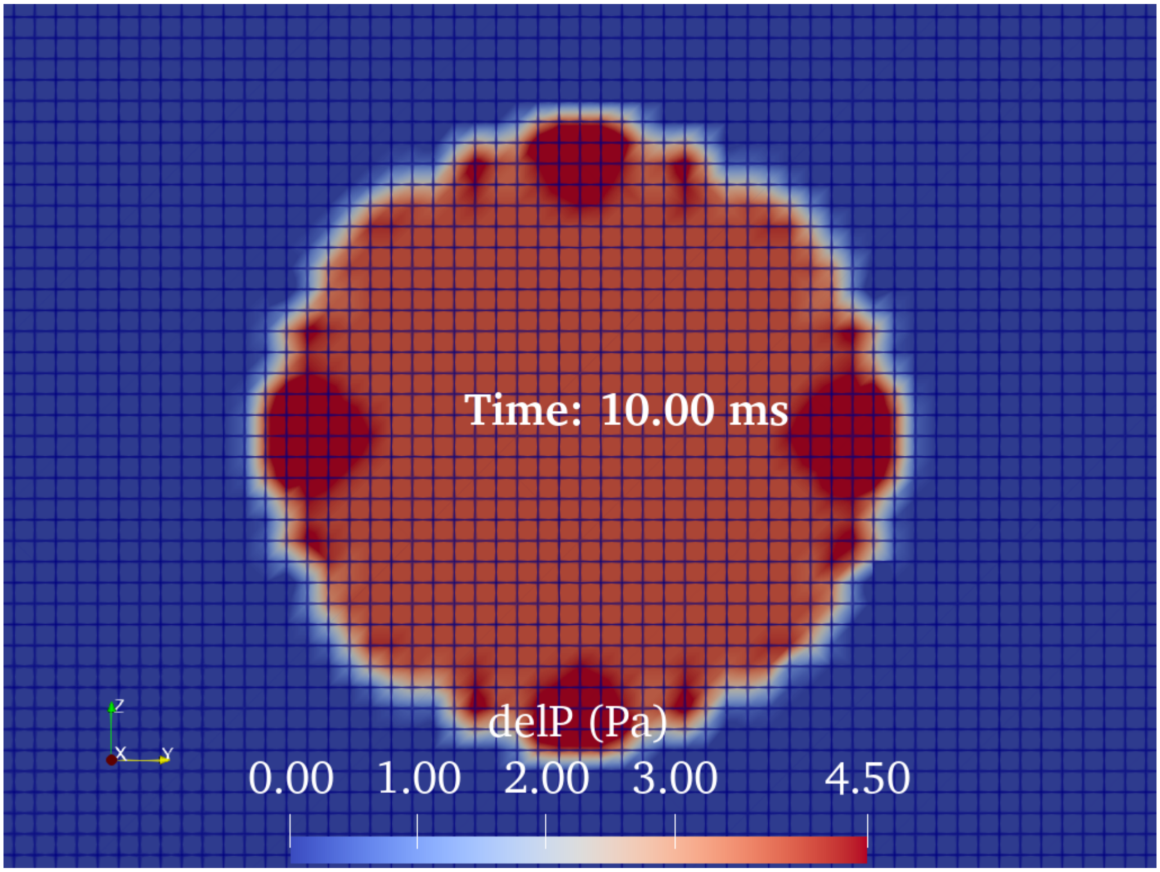

Figure 10.2: Mid-plane clip colored by the pressure difference indicating a higher pressure inside the droplet, i.e. around 4.5 Pa for the fine mesh. The analytical pressure difference in 4.4 Pa for the same droplet.

10.2 Summary and Conclusions

In this dissertation, a novel sealing algorithm is developed. The algorithm is designed to get activated based on a prescribed needle displacement value. Once activated, the algorithm applies a drag force in the sealing region. This force inhibits any flow through the seat area without changing the mesh topology. The algorithm is successfully integrated into the in-house developed HRMFoam solver.

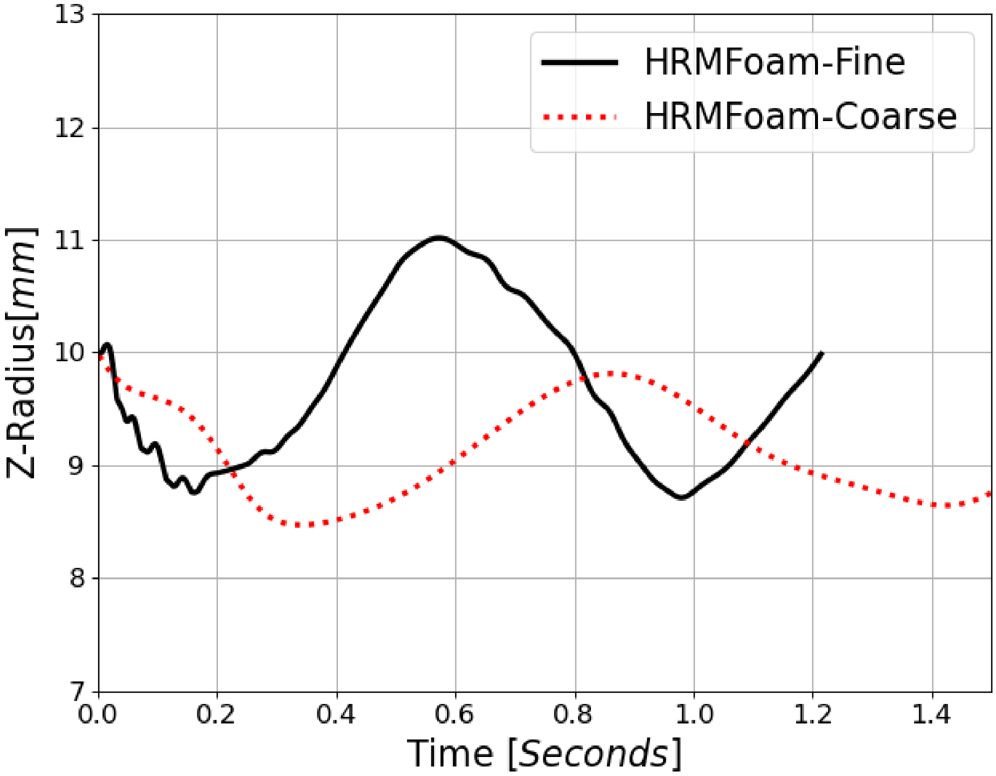

Figure 10.3: Graphs indicating the oscillations of the droplet radius in z-direction for two different meshes as predicted by the surface tension based HRMFoam

Consequently, a multiple injection event is simulated in a single simulation cycle. During this simulation, cavitation is captured at low needle positions. The simulations also capture indications of dribbling fuel after completion of the injection event.

Furthermore, the end-of injection (EOI) phases of a single injection cycle under different ambient conditions are analyzed. During this phase, ambient pressure waves are observed to propagate into the sac region. As a consequence, a mixed sac condition is witnessed for the non-flashing condition, i.e., the sac is filled with both non-condensible gas and liquid fuel. In contrast, a boiling sac condition is captured in the flashing condition, where the residual fuel starts boiling after needle closure. The expanding sac fuel vapors inhibit any flow of ambient gas into the sac region. Eventually, the sac compositions for both non-flashing and flashing conditions are quantified. Post-closure, cavitation is also encountered inside the sac region in addition to the seat regions. A λ_2- criterion analysis confirmed the interactive sac vortices to be the reason behind these sac bubbles.

A qualitative analysis of the tip-wetting phenomena reveals distinct wetting mechanisms for different ambient conditions. During the needle opening phase, the expansion wetting mechanism dominates the wetting process. As a result, more tip wetting is observed in flashing compared to the non-flashing condition. However, during the early needle closing phase, i.e., when the needle starts moving downwards, the indications of fuel mass on the tip around the injector axis are captured in the non-flashing condition. This wetting phenomenon is driven by the upward moving ambient gas carrying traces of fuel due to the the dispersive nature of the non-flashing spray. During the needle closure phase, more wetted tip areas are observed for both simulated ambient conditions. During this phase, the wetting process is dominated by the dribble wetting mechanism. Finally, post-closure tip wetting is influenced by the sac conditions. Hence, more tip wetting is observed for the flash-boiling condition due to the vapor dribbling from the boiling sac.

A quasi-steady state analysis of a single injection event captures hole-to-hole variations in the rate of injection and the rate of momentum for both flashing and non-flashing conditions. Furthermore, the predictions of hydraulic coefficients are compared with the experimental observations. The percentage differences between the computational predictions and the experimental observations are found to be around four percent for the simulated ambient conditions. Furthermore, in-nozzle variations are observed to influence the near-nozzle behaviors for both flash-boiling and non-flashing conditions.

A novel plume-based coupling approach is also developed in this dissertation. This approach involves running Eulerian near nozzle simulations with the primary atomization model beforehand. Transition criteria to couple the Eulerian simulations with the Lagrangian framework are developed based on the inter-droplet spacing.Then, using the transition criteria the plume surfaces with tessellated area are defined at a regular time interval. Data such as droplet diameter, temperature, TKE, density, and velocity in these tessellated cells are tabulated to generate a single input file for the Lagrangian simulations. Finally, in the Lagrangian simulations, the parcels informed by these plume data are generated for the secondary atomization. Predictions from the plume-based approach are validated both qualitatively and quantitatively against the available experimental data, and good agreements are observed for both non-flashing and flash-boiling conditions.

HRMFoam was originally formulated for high Weber number flows where the interface is not sharp when projected on to a finite sized computational mesh. However, to resolve the tip-wetting flow which is associated with low Weber number, surface tension models are required. Hence, a pilot study is performed to include the surface tension-based models in HRMFoam to resolve the interface. The study is able to capture a proper response of the pressure field to the curvature of the interface. However, when validated by an oscillating droplet simulation, the predictions for the oscillation period are found to be in disagreement with the exact solution. Hence, a logical conclusion could not be achieved from the pilot study.

CHAPTER 11

FUTURE WORK

In this dissertation, attempts are made to answer some of the pressing questions of the GDI systems under different ambient conditions. Several models are developed and validated with the available experimental data. Although these models answer some of the pressing concerns of the GDI system, many remain unanswered or unexplored. Hence, there are still a lot of potentials for future exploration of the GDI sprays under both flashing and non-flashing conditions. Based on the findings of the current dissertation, brief descriptions about possible future explorations are included in this section.

Although the current dissertation explores the EOI behaviors of a single injection event under different ambient conditions, it does not answer the effect of these behaviors on subsequent injections. Thus, computational explorations need to be performed while informing the initial sac conditions by the EOI behaviors of a single injection event. Furthermore, EOI analysis of multiple injection events needs to be executed for a better understanding of the post-closure near nozzle behaviors.

The current dissertation also discusses the mechanisms driving the tip-wetting behaviors under different ambient conditions. However, it does not quantify the wetting area due to the current limitations of the in-house solver. The pilot study explores the integration of surface tension-based sharp interface models into the in-house solver without the desired accuracy. Thus, different sharp interface models need to be explored to resolve the fuel film on the tip of the injector under different ambient conditions.

The plume-based coupling approach developed in this dissertation shows promising results in both flashing and non-flashing conditions. However, predictions from this plume-based approach are driven by the Eulerian primary atomization model, i.e., the $\Sigma - Y$ model. This model was initially developed and tuned for diesel injection applications. Hence, no or a little validation of the same model exists in the literature for the GDI applications. GDI systems operate in highly vaporizing conditions, i.e., flash-boiling conditions, which will definitely impact the interface production during the primary atomization process. The current interfacial area density models do not account for such effects, hence need further revisit of the model formulations. Moreover, the modeling constants of these models are heavily tuned for diesel applications. These modeling constants have not been validated for gasoline application due to the lack of experimental data set. Recently, experimentalists at Argonne have performed ultra-small angle X-ray scattering (USAXS) measurements for GDI sprays under different ambient conditions. These experiments measure the path-specific surface area of the spray, a measure of the interfacial area of the liquid-gas boundaries along the X-Ray beam path. These measurements are equivalent to the interfacial surface density predictions of the primary atomization model. Hence, future research can be performed by validating the primary atomization model, $\Sigma - Y$ model, with ultra-small angle X-ray scattering (USAXS) measurements for GDI sprays. The inherent nature of the plume-based coupling approach ensures mass conservation, whereas it does not conserve the momentum while coupling the Eulerian internal flow simulations with the plume-based Lagrangian simulations. Momentum conservation can further be ensured by introducing a source term in the Eulerian gas phase equation of the plume-based Lagrangian simulation. However, this source term can not be an empirical constant , as that would introduce unwanted errors. Future research should be conducted to model this source term for different ambient conditions.

In multihole injectors, for certain operating conditions, individual plumes merge to form a single collapsing spray. The collapsing sprays tend to have a higher penetration compared to other sprays. Hence, wall impingement is also observed for collapsing conditions. Furthermore, when the spray collapses, the emission also deteriorates. The plume-based coupling approach does not discriminate between the Eulerian plumes while creating parcels in the Lagrangian simulations. Thus, the plume-based coupling approach should be employed to study the physics of collapsing sprays, which are often observed in flare flashing conditions.

BIBLIOGRAPHY

[1] Engine Combustion Network. `https://ecn.sandia.gov/`.

[2] Foam-Extend-3.2. `https://github.com/Unofficial-Extend-Project-Mirror/foam-extend-foam-extend-3.2`.

[3] The Outlook for Energy: A View to 2040. `http://cdn.exxonmobil.com/~/media/global/files/outlook-for-energy/2016/2016-outlook-for-energy.pdf`.

[4] Agarwal, A., and Trujillo, M. F. A closer look at linear stability theory in modeling spray atomization. *International Journal of Multiphase Flow 109* (2018), 1–13.

[5] Agarwal, A., and Trujillo, M. F. The effect of nozzle internal flow on spray atomization. *International Journal of Engine Research 21*, 1 (2020), 55–72.

[6] Akoi, I. Water flash evaporation under low pressure conditions. *Heat Transfer Japan Res. 23* (1994), 544–555.

[7] Akoi, I. Analysis of characteristics of water flash evaporation under low-pressure conditions. *Heat Transfer Asian Res. 29* (2000), 22–33.

[8] Aleiferis, P. G., Serras-Pereira, J., Augoye, A., Davies, T. J., Cracknell, R. F., and Richardson, D. Effect of fuel temperature on in-nozzle cavitation and spray formation of liquid hydrocarbons and alcohols from a real-size optical injector for direct-injection spark-ignition engines. *International Journal of Heat and Mass Transfer 53* (2010), 4588–4606.

[9] Allen, J., Hargrave, G. K., and Khoo, Y. C. In-nozzle and spray diagnostic techniques for real sized pressure swirl and plain orifice gasoline direct injectors. Tech. Rep. 2003-01-3151, 2003.

[10] Anez, J, Canu, R, Duret, Benjamin, Reveillon, J, and Demoulin, FX. Turbulent statistical transition from Euler to Lagrange using droplet velocity PDF. In *ICLASS 2018-14th Triennial International Conference on Liquid Atomization and Spray Systems* (2018).

[11] Aori, G., Hung, D. L. S., Zhang, M., Zhang, G. M., and Li, T. Y. Effect of nozzle configuration on macroscopic spray characteristics of multi-hole fuel injectors under superheated conditions. *Atomization and Sprays 26* (2016), 439–462.

[12] Aquino, C., Plensdorf, W., Lavoie, G., and Curtis, E. The occurrence of flash boiling in a port fuel injected gasoline engine. Tech. Rep. 982522, 1998.

[13] Araneo, L., and Donde′, R. Flash boiling in a multihole GDI injector - effects of the fuel distillation curve. *Fuel 191* (2017), 500–510.

[14] Araneo, L., Slima, K. Ben, and Dondé, R. Flash boiling effect on swirled injector spray angle. ILASS-Europe, 2002.

[15] Arcoumanis, C., Badami, M., Flora, H., and Gavaises, M. Cavitation in real-size multi-hole diesel injector nozzles. Tech. Rep. 2000-01-1249, 2000.

[16] Avedisian, CT. Bubble growth in superheated liquid droplets. *Encyclopedia of Fluid Mechanics 3* (1985), 130–190.

[17] Badawy, T., Attar, M. A., Hutchins, P., Xu, H., Venus, J. K., and Cracknell, R. Investigation of injector coking effects on spray characteristic and engine performance in gasoline direct injection engines. *Applied energy 220* (2018), 375–394.

[18] Balachandar, S., Liu, K., and Lakhote, M. Self-induced velocity correction for improved drag estimation in Euler–Lagrange point-particle simulations. *Journal of Computational Physics 376* (2019), 160–185.

[19] Baldwin, E. T., Jr., R. O. Grover, Parrish, S. E., Duke, D. J., Matusik, K. E., Powell, C. F., Kastengren, A. L., and Schmidt, D. P. String flash-boiling in gasoline direct injection simulations with transient needle motion. *Int. J. Multiphase Flow 87* (2016), 90–101.

[20] Bankoff, SG. Entrapment of gas in the spreading of a liquid over a rough surface. *AIChE journal 4*, 1 (1958), 24–26.

[21] Bar-Kohany, T., and Levy, M. State of the art review of flash-boiling atomization. *Atomization and Sprays 26*, 12 (2016).

[22] Battistoni, M., Som, S., and Longman, D. E. Comparison of mixture and multifield models for in-nozzle cavitation prediction. *ASME J. Eng. Gas Turbines Power 136* (2014).

[23] Battistoni, M., Swantek, D. J. Duke A. B., Tilocco, F. Z., Powell, C. F., and Som, S. Effects of noncondensable gas on cavitating nozzles. *Atomization and Sprays 25* (2015), 453–483.

[24] Battistoni, M., Xue, Q., Som, S., and Pomraning, E. Effect of off-axis needle motion on internal nozzle and near exit flow in a multi-hole diesel injector. *SAE Int. J. Fuels Lubr. 7* (2014), 167–182.

[25] Beale, J. C., and Reitz, R. D. Modeling spray atomization with the Kelvin-Helmholtz/Rayleigh-Taylor hybrid model. *Atomization and sprays 9*, 6 (1999).

[26] Beau, P., Me´ nard, T., Lebas, R.and Berlemont, A., Tanguy, S., and Demoulin, F. Numerical jet atomization: part II—modeling information and comparison with DNS results. In *Fluids Engineering Division Summer Meeting* (2006), vol. 47500, pp. 555–563.

[27] Bhattarai, N., Kim, G-H, and Park, S O. Numerical study of the wake flow of a single rectangular low-profile vortex generator by using non-equilibrium eddy viscosity model. In *The 4th Asian Symposium on Computational Heat Transfer and Fluid Flow Hong Kong* (2013).

[28] Bianchi, G. M., Minelli, F., Scardovelli, R., and Zaleski, S. 3D large scale simulation of the high-speed liquid jet atomization. Tech. rep., 2007.

[29] Bianchi, G.M., Pelloni, P., Toninel, S., Scardovelli, R., Leboissetier, A., and Zaleski, S. Improving the knowledge of high-speed liquid-jets atomization by using Quasi-Direct 3D simulation. Tech. Rep. 2005-24-089, SAE, 2005.

[30] Bilicki, Z, and Kestin, J. Physical aspects of the relaxation model in two-phase flow. In *Proceedings of the Royal Society of London A: Mathematical, Physical and Engineering Sciences* (1990), vol. 428, The Royal Society, pp. 379–397.

[31] Bird, GA. Perception of numerical methods in rarefied gasdynamics. *Progress in Astronautics and Aeronautics 117* (1989), 211–226.

[32] Blander, M., and Katz, J. L. Bubble nucleation in liquids. *AIChE Journal 21* (1975), 833–848.

[33] Blinkov, VN, Jones, OC, and Nigmatulin, BI. Nucleation and flashing in nozzles—2. comparison with experiments using a five-equation model for vapor void development. *Int. J. Multiphase Flow 19* (1993), 965–986.

[34] Blokkeel, Gregory, Barbeau, B, and Borghi, R. A 3D Eulerian model to improve the primary breakup of atomizing jet. *SAE transactions* (2003), 45–54.

[35] Bourlioux, A. A coupled level-set volume-of-fluid algorithm for tracking material interfaces. In *proceedings of the 6th international symposium on computational fluid dynamics, Lake Tahoe, CA* (1995), vol. 15.

[36] Brackbill, J. U., Kothe, D. B., and Zemach, C. A continuum method for modeling surface tension. *Journal of computational physics 100*, 2 (1992), 335–354.

[37] Brennen, C. E. *Fundamentals of Multiphase Flows.* Cambridge University Press, 2005.

[38] Brown, R., and York, J. L. Sprays formed by flashing liquid jets. *AIChE Journal 8* (1962), 149–153.

[39] Brusiani, F., Negro, S., Bianchi, G. M., Moulai, M., Neroorkar, K., and Schmidt, D. Comparison of the Homogeneous Relaxation Model and a Rayleigh Plesset cavitation model in predicting the cavitating flow through various injector hole shapes. Tech. Rep. 2013-01-1613, SAE, 2013.

[40] Butcher, A. J., Aleiferis, P. G., and Richardson, D. Development of a real-size optical injector nozzle for studies of cavitation, spray formation and flash-boiling at conditions relevant to direct-injection sprak-ignition engines. *Internation J of Enginer Research 14* (2013), 557–577.

[41] Chen, Y., and Zhang, Z. Mechanism of flash boiling and spray analysis with gasoline, iso-octane, n-pentane and ethanol from a novel heated tip gdi injector. *Applied Thermal Engineering*, 115 (2017), 1109–1117.

[42] Chesnel, J., Reveillon, J., Menard, T., and Demoulin, F. Large eddy simulation of liquid jet atomization. *Atomization and Sprays 21*, 9 (2011).

[43] Cleary, V., Bowen, P., and Witlox, H. Flashing liquid jets and two-phase droplet dispersion I: Experiments for derivation of droplet atomisation correlations. *Journal of Hazardous Materials 142* (2007), 786–796.

[44] Colarossi, M., Trask, N., Schmidt, D. P, and Bergander, M. J. Multidimensional modeling of condensing two-phase ejector flow. *International Journal of Refrigeration 35*, 2 (2012), 290–299.

[45] Cole, Robert. Boiling nucleation. *Advances in heat transfer 10* (1974), 85–166.

[46] Corradini, M. L. Fundamentals of multiphase flow, 1997.

[47] Crua, C., Shoba, T., Heikal, M., Gold, M., and Higham, C. High-speed microscopic imaging of the initial stage of diesel spray formation and primary breakup. In *SAE Technical Paper 2010-01-2247* (10 2010).

[48] Dahms, R. N., Manin, J., Pickett, L. M., and Oefelein, J. C. Understanding high-pressure gas-liquid interface phenomena in diesel engines. *Proceedings of the Combustion Institute 34* (2013), 1667–1675.

[49] Dahms, R. N., and Oefelein, J. C. On the transition between two-phase and single-phase interface dynamics in multicomponent fluids at supercritical pressures. *Physics of Fluids 25* (2013).

[50] De Villiers, E, Gosman, AD, and Weller, HG. Large eddy simulation of primary diesel spray atomization. *SAE transactions* (2004), 193–206.

[51] Demoulin, F., Beau, P., Blokkeel, G., Mura, A., and Borghi, R. A new model for turbulent flows with large density fluctuations: Application to liquid atomization. *Atomization and Sprays 17*, 4 (2007).

[52] Desantes, J. M., Garcia-Oliver, J. M., Pastor, J. M., and Pandal, A. A comparsion of diesel sprays CFD modeling approaches: DDM versus Σ-Y Eulerian atomization model. *Atomization and Sprays 26* (2016), 713–737.

[53] Desantes, JM, García-Oliver, José María, Pastor, JM, Pandal, A, Baldwin, E, and Schmidt, DP. Coupled/decoupled spray simulation comparison of the ecn spray a condition with the Σ-Y Eulerian atomization model. *International Journal of Multiphase Flow 80* (2016), 89–99.

[54] Desderi, U., and Bidni, G. Study of possible optimisation criteria for geothermal power plants. *Energy Convers. Mgmt. 38* (1997), 1681–1691.

[55] Deshpande, S. S, Anumolu, L., and Trujillo, M. F. Evaluating the performance of the two-phase flow solver interFoam. *Computational science & discovery 5*, 1 (2012), 014016.

[56] Dhir, Vijay K. Mechanistic prediction of nucleate boiling heat transfer–achievable or a hopeless task? *Journal of Heat Transfer 128*, 1 (2006), 1–12.

[57] DOE, US. A workshop to identify research needs and impacts in predictive simulation for internal combustion engines (presice). In *Workshop, US Department of Energy* (2011).

[58] Downar-Zapolski, P., Bilicki, Z., Bolle, L., and Franco, J. The non-equilibrium relaxation model for one-dimensional flashing liquid flow. *Int. J. Multiphase Flow 22* (1996), 473–483.

[59] Duke, D J, Kastengren, A L, Matusik, K E, Swantek, A B, Powell, C F, Payri, R, Vaquerizo, D, Itani, L, Bruneaux, G, Grover Jr, R O, Parrish, S, Markle, L, Schmidt, D, Manin, J, Skeen, S. A., and Pickett, L. M. Internal and near nozzle measurements of Engine Combustion Network Spray G gasoline direct injectors. *Experimental Thermal and Fluid Science 88* (2017), 608–621.

[60] Duke, D. J., Swantek, A. B., Tilocco, F. Z, Powell, C. F., Kastengren, A. L., Fezzaa, K., Neroorkar, K., Moulai, M., and Schmidt, D. X-ray imaging of cavitation in diesel injectors. Tech. Rep. 2012-01-1404, SAE, 2014.

[61] Dukowicz, J. K. A particle-fluid numerical model for liquid sprays. *Journal of computational Physics 35*, 2 (1980), 229–253.

[62] Durbin, Paul A, and Reif, BA Pettersson. *Statistical theory and modeling for turbulent flows.* John Wiley & Sons, 2011.

[63] Duret, B, Reveillon, J, Menard, T, and Demoulin, FX. Improving primary atomization modeling through DNS of two-phase flows. *International Journal of Multiphase Flow 55* (2013), 130–137.

[64] Elias, E., and Chambre, P. L. A mechanistic non-equilibrium model for two-phase critical flow. *Int. J. Multiphase Flow 10* (1984), 21–40.

[65] Elias, E., and Chambre, P. L. Bubble transport in flashing flow. *Int. J. Multiphase Flow 26* (2000), 191–206.

[66] Faeth, GM, Hsiang, L-P, and Wu, P-K. Structure and breakup properties of sprays. *International Journal of Multiphase Flow 21* (1995), 99–127.

[67] Fischer, A., and Thelliez, M. Methodology and tools to predict GDI injector tip wetting as predecessor of tip sooting. Tech. rep., SAE Technical Paper, 2018.

[68] Froessling, N. On the evaporation of falling drops. Tech. rep., ARMY BIOLOGICAL LABS FREDERICK MD, 1968.

[69] Garcia-Oliver, J. M., Pastor, J. M., Pandal, A., Trask, N., Baldwin, E., and Schmidt, D. P. Diesel spray CFD simulations based on the Σ-Y Eulerian atomization model. *Atomization and Sprays 23*, 1 (2013).

[70] Gavaises, M, Murali-Girija, M., Rodriguez, C., Koukouvinis, P., Gold, M., and Pearson, R. Numerical simulation of fuel dribbling and nozzle wall wetting. *International Journal of Engine Research* (2021), 1468087420985189.

[71] Gilles-Birth, I., Bernhardt, S., Spicher, U., and Rechs, M. Experimental investigation of the in-nozzle flow of valve covered orifice nozzles for gasoline direct injection. *Proceedings of the Seventh International Symposium on Internal Combustion Diagnostics* (2006), 59–78.

[72] Gopalakrishnan, S, and Schmidt, D P. A computational study of flashing flow in fuel injector nozzles. *SAE International Journal of Engines 1*, 1 (2008), 160–170.

[73] Gorokhovski, M, and Herrmann, M. Modeling primary atomization. *Annu. Rev. Fluid Mech. 40* (2008), 343–366.

[74] Guo, H., Ding, H., Li, Y., Ma, X., Wang, Z., Xu, H., and Wang, J. Comparison of spray collapses at elevated ambient pressure and flash boiling conditions using multi-hole gasoline direct injector. *Fuel 199* (2017), 125–134.

[75] H, Oh. *Improvement of combustion characteristics in a spray-guided direct-injection sprak-ignition engine.* PhD thesis, 2013.

[76] Henry, R. B., and Fauske, H. K. The two-phase critical flow of one-component mixtures in nozzles, orifices and short tubes. *Journal of Heat Transfer 93* (1971), 179–187.

[77] Herrmann, M. Refined Level Set Grid method for tracking interfaces. *Annual Research Briefs* (2005), 3–18.

[78] Hirt, C W, and Nichols, B D. Volume of Fluid (VOF) methods for the dynamics of free boundaries. *J. Comput. Phys. 39* (1981), 201–225.

[79] Hoyas, S, Gil, A, Margot, X, Khuong-Anh, D, and Ravet, F. Evaluation of the Eulerian–Lagrangian Spray Atomization (ELSA) model in spray simulations: 2d cases. *Mathematical and Computer Modelling 57*, 7-8 (2013), 1686–1693.

[80] Huh, KY. A phenomenological model of diesel spray atomization. In *Proc. of The International Conf. on Multiphase Flows' 91-Tsukuba* (1991).

[81] Hwang, J, Weiss, L, Karathanassis, I K, Koukouvinis, P, Pickett, L M, and Skeen, S A. Spatio-temporal identification of plume dynamics by 3D computed tomography using Engine Combustion Network spray G injector and various fuels. *Fuel 280* (2020), 118359.

[82] Hwang, J, Yasutomi, K, Arienti, M, and Pickett, L M. Numerical investigation of near nozzle flash-boiling spray in an axial-hole transparent nozzle. Tech. rep., SAE Technical Paper, 2020.

[83] Ishii, E., Yoshimura, K., Yasukawa, Y., and Ehara, H. Late-fuel simulation near nozzle outlet of fuel injector during closing valve. *Journal of Engineering for Gas Turbines and Power 138*, 10 (2016), 102801.

[84] Ishii, M. One-dimensional drift-flux model and constitutive equations for relative motion between phases in various two-phase flow regimes. Tech. rep., Argonne National Lab., IL.(USA), 1977.

[85] Iyer, V., and Abraham, J. An evaluation of a two-fluid Eulerian-liquid Eulerian-gas model for diesel sprays. *J. Fluids Eng. 125*, 4 (2003), 660–669.

[86] Iyer, V., and Abraham, J. Two-fluid modeling of spray penetration and dispersion under diesel engine conditions. *Atomization and Sprays 15*, 3 (2005).

[87] Janet, J. P., Liao, Y., and Lucas, D. Heterogeneous nucleation in CFD simulation of flashing flows in convering-diverging nozzles. *Int. J. Multiphase Flow 74* (2015), 106–117.

[88] Jeong, J., and Hussain, F. On the identification of a vortex. *Journal of Fluid Mechanics 285* (1995), 69–94.

[89] Kalikmanov, V.I. *Nucleation Theory. [electronic resource].* Lecture Notes in Physics: 860. Dordrecht : Springer Netherlands : Imprint: Springer, 2013., 2013.

[90] Katz, J L, and Wiedersich, H. Nucleation theory without maxwell demons. *Journal of colloid and interface science 61*, 2 (1977), 351–355.

[91] Khan, M M, Hélie, J, Gorokhovski, M, and Sheikh, N A. Experimental and numerical study of flash boiling in gasoline direct injection sprays. *Applied Thermal Engineering* (2017).

[92] Kitamura, Y., Morimitsu, H., and Takahashi, T. Critical superheat for flashing of superheated liquid jets. *Ind. Eng. Chem. Fundam. 25* (1986), 206–211.

[93] Knapp, R. T., Daily, J. W., and Hammitt, F. G. *Cavitation.* McGraw Hill, 1970.

[94] Kocamustafaogullari, G., and Ishii, M. Interfacial area and nucleation site density in boiling systems. *Int. J. Heat Mass Transfer 26* (1983), 1377–1387.

[95] Koci, C P, Fitzgerald, R P, Ikonomou, V, and Sun, K. The effects of fuel–air mixing and injector dribble on diesel unburned hydrocarbon emissions. *International Journal of Engine Research 20*, 1 (2019), 105–127.

[96] Krämer, M., Kull, E., and Wensing, M. Flashboiling-induced targeting changes in gasoline direct injection sprays. *Int. J. Engine Research 17* (2016), 97–107.

[97] Lacey, J, Poursadegh, F, Brear, MJ, Gordon, R, Petersen, P, Lakey, C, Butcher, B, and Ryan, S. Generalizing the behavior of flash-boiling, plume interaction and spray collapse for multi-hole, direct injection. *Fuel 200* (2017), 345–356.

[98] Lacey, J, Poursadegh, F, Brear, MJ, Gordon, R, Petersen, P, Lakey, C, Butcher, B, and Ryan, S. Generalizing the behavior of flash-boiling, plume interaction and spray collapse for multi-hole, direct injection. *Fuel 200* (2017), 345–356.

[99] Lamanna, G. Cryogenic flashing jets:a review. Tech. Rep. AIAA 2016-4787, 2016.

[100] Lamanna, G., Kamoun, H., Weigand, B., and Steelant, J. Towards a unified treatment of fully flashing sprays. *International Journal of Multiphase Flows 58* (2014), 168–184.

[101] Lamb, Horace. *Hydrodynamics.* University Press, 1924.

[102] Leach, F, Stone, R, Richardson, D, Lewis, A, Akehurst, S, Turner, J, Remmert, S, Campbell, S, and Cracknell, R F. Particulate emissions from a highly boosted gasoline direct injection engine. *International Journal of Engine Research 19*, 3 (2018), 347–359.

[103] Lebas, R, Blokkeel, G, Beau, P-A, and Demoulin, F-X. Coupling vaporization model with the Eulerian-Lagrangian Spray Atomization (ELSA) model in diesel engine conditions. Tech. rep., SAE Technical Paper, 2005.

[104] Lebas, R, Menard, T, Beau, P-A, Berlemont, A, and Demoulin, F-X. Numerical simulation of primary break-up and atomization: DNS and modelling study. *International Journal of Multiphase Flow 35*, 3 (2009), 247–260.

[105] Lee, J. M., Fotache, C. R., Gopalakrishnan, S., and Schmidt, D. P. Flashing flow of superheated jet fuel. *Proceedings of the Combustion Institute 32* (2009), 3215–3222.

[106] Leick, P, Bork, B, and Geiler, J N. Experimental characterization of tip wetting in gasoline di injectors. In *Proceedings of the 14th triennial international conference on liquid atomization and spray systems, Chicago, IL* (2018), pp. 22–26.

[107] Leinhard, J. H., and Karimi, A. Homogeneous nucleation and the spinodal line. *ASME Journal of Heat Transfer 103* (1981), 61–64.

[108] Lemmon, EW, Huber, ML, and McLinden, MO. NIST standard reference database23: reference fluid thermodynamic and transport properties-REFPROP, Version 9.1, NIST. *Gaithersburgh. MD* (2013).

[109] Liao, Y., and Lucas, D. 3D CFD simulation of flashing flows in a converging-diverging nozzle. *Nuclear Engineering Design 292* (2015), 149–163.

[110] Liao, Y, and Lucas, D. Computational modelling of flash boiling flows: A literature survey. *International Journal of Heat and Mass Transfer 111* (2017), 246–265.

[111] Lin, S-P. *Breakup of liquid sheets and jets.* Cambridge university press, 2003.

[112] Lindgren, R, Skogsberg, M, Sandquist, H, and Denbratt, I. The influence of injector deposits on mixture formation in a DISC SI engine. *SAE transactions* (2003), 852–861.

[113] Lobosco, RJ, Schulz, HE, and Simões, ALA. Analysis of two phase flows on stepped spillways. *Hydrodynamics-Optimizing Methods and Tools* (2011), 1–25.

[114] Lothe, J, and Pound, G M. Reconsiderations of nucleation theory. *The Journal of Chemical Physics 36*, 8 (1962), 2080–2085.

[115] Luo, H, Nishida, K, Uchitomi, S, Ogata, Y, Zhang, W, and Fujikawa, T. Microscopic behavior of spray droplets under flat-wall impinging condition. *Fuel 219* (2018), 467–476.

[116] Luret, G, Menard, T, Berlemont, A, Reveillon, J, Demoulin, F-X, and Blokkeel, G. Modeling collision outcome in moderately dense sprays. *Atomization and Sprays 20*, 3 (2010).

[117] Mach, Wolfgang, and Bölter, Jens. 13 weniger reibung, aber mehr verschleiß: Auswirkungen von dieselruß im schmieröl. versuchsresultate, interpretationen, ursachenmodelle. *Ölkreislauf von Verbrennungsmotoren III 3* (2009), 174.

[118] Magnotti, G M. *Modeling the influence of nozzle-generated turbulence on diesel sprays.* PhD thesis, Georgia Institute of Technology, 2017.

[119] Magnotti, G. M., and Genzale, C. L. A Novel Spray Model Validation Methodology Using Liquid-Phase Extinction Measurements. *Atomization and Sprays 25* (2015), 397–424.

[120] Maksic, S., and Mewes, D. CFD-calculation of the flashing flow in pipes and nozzles. *Proceedings of ASME Joint US-European Fluids Engineering Division Conference* (2002), 511–516.

[121] Manin, J, Jung, Y, Skeen, S A, Pickett, L M, Parrish, S E, and Markle, L. Experimental characterization of DI gasoline injection processes. Tech. rep., SAE Technical Paper, 2015.

[122] Matusik, K, Duke, D, Sovis, N, Swantek, A, Powell, C, Payri, R, Vaquerizo, D, Giraldo Valderrama, J S, and Kastengren, A. A study on the relationship between internal nozzle geometry and injected mass distribution of eight ECN Spray G nozzles. In *Ilass Europe. 28th european conference on Liquid Atomization and Spray Systems* (2017), Editorial Universitat Politècnica de València, pp. 313–320.

[123] Medina, M, Alzahrani, FM, Fatouraie, M, Wooldridge, MS, and Sick, V. Mechanisms of fuel injector tip wetting and tip drying based on experimental measurements of engine-out particulate emissions from gasoline direct-injection engines. *International Journal of Engine Research* (2020), 1468087420916052.

[124] Menter, F. R. Improved two-equation k-omega turbulence models for aerodynamic flows. *Nasa Sti/recon Technical Report N 93* (1992), 22809.

[125] Mikic, B. B., Rohsenow, W. M., and Griffith, P. On bubble growth rates. *Int. J. Heat Mass Transfer 13* (1970), 657–666.

[126] Miyatake, O., Tanaka, I., and Lior, N. A simple universal equation for bubble growth in pure liquids and binary solutions with a non-volatile solute. *Int. J. Heat Mass Transfer 40* (1997), 1577–1584.

[127] Mohapatra, C K., Jacobsohn, G L., and Schmidt, D P. The end of injection study of a multi-hole gasoline direct injector under flash-boiling conditions. *Atomization and Sprays* (2021).

[128] Mohapatra, C K, Schmidt, D P, Sforzo, B A, Matusik, K E, Yue, Z, Powell, C F, Som, S, Mohan, B, Im, H G, Badra, J, et al. Collaborative investigation of the internal flow and near-nozzle flow of an eight-hole gasoline injector (Engine Combustion Network Spray G). *International Journal of Engine Research*, 1468087420918449.

[129] Mojtabi, M., Wigley, G., and Hélie, J. The effect of flash boiling on the atomization performance of gasoline direct injection multistream injectors. *Atomization and Sprays 24* (2014), 467–493.

[130] Montanaro, A, and Allocca, L. Flash boiling evidences of a multi-hole GDI spray under engine conditions by Mie-Scattering measurements. Tech. rep., SAE Technical Paper, 2015.

[131] Moon, S, Komada, K, Li, Z, Wang, J, Kimijima, T, Arima, T, and Maeda, Y. High-speed X-ray imaging of in-nozzle cavitation and emerging jet flow of multi-hole GDI injector under practical operating conditions. In *13th Triennial International Conference on Liquid Atomization and Spray Systems, Tainan, Taiwan* (2015), vol. 2015.

[132] Moulai, M, Schmidt, D, Grover, R, and Parrish, S. Internal and near-nozzle flow in a multi-hole gasoline injector under flashing and non-flashing conditions. Tech. Rep. 2015-01-0944, SAE, 2015.

[133] Mouvanal, S, Burkhardt, A, Bakshi, S, and Chatterjee, D. Numerical study of purging of a gasoline direct injection nozzle at the end of injection. *International Journal of Engine Research* (2020), 1468087420916658.

[134] Nehmer, D A, and Reitz, R D. Measurement of the effect of injection rate and split injections on diesel engine soot and nox emissions. *SAE transactions* (1994), 1030–1041.

[135] Neroorkar, K., Gopalakrishnan, S., Jr., R. O. Grover, and Schmidt, D. P. Simulation of flash boiling in pressure swirl injectors. *Atomization and Sprays 21* (2011), 179–188.

[136] Neroorkar, K, and Schmidt, D. A computational investigation of flash-boiling multi-hole injectors with gasoline-ethanol blends. In *SAE Technical Paper 2011-01-0384* (2011).

[137] Neroorkar, K, and Schmidt, D. Modeling of vapor-liquid equilibrium of gasoline-ethanol blended fuels for flash boiling simulations. *Fuel 90*, 2 (2011), 665–673.

[138] Neroorkar, K, Shields, B, Grover Jr, R O, Torres, A P, and Schmidt, D. Application of the homogeneous relaxation model to simulating cavitating flow of a diesel fuel. In *SAE Technical Paper 2012-01-1269* (2012).

[139] Nishimura, A. A model for primary diesel fuel atomization based on cavitation bubble collapse energy. In *Proc. 8th ICLASS* (2000), pp. 1249–1256.

[140] Nocivelli, L, Sforzo, B A, Tekawade, A, Yan, J, Powell, C F, Chang, W, Lee, C, and Som, S. Analysis of the spray numerical injection modeling for gasoline applications. Tech. rep., 2020.

[141] Nocivelli, Lorenzo, Yan, Junhao, Saha, Kaushik, Magnotti, Gina M, Lee, Chia-Fon, and Som, Sibendu. Effect of ambient pressure on the behavior of single-component fuels in a gasoline multi-hole injector. In *Internal Combustion Engine Division Fall Technical Conference* (2019), vol. 59346, American Society of Mechanical Engineers, p. V001T02A012.

[142] Noh, and Woods. Simple line interface calculation. vol. 59, 5th Int. Conf. Fluid Dyn.

[143] Olsson, E, and Kreiss, G. A conservative level set method for two phase flow. *Journal of computational physics 210*, 1 (2005), 225–246.

[144] O'Rourke, P J. Statistical properties and numerical implementation of a model for droplet dispersion in a turbulent gas. *Journal of Computational Physics 83*, 2 (1989), 345–360.

[145] O'Rourke, P J, and Amsden, A A. The TAB method for numerical calculation of spray droplet breakup. Tech. rep., SAE Technical Paper, 1987.

[146] Oza, R. D. On the mechanism of flasing injection of initially subcooled fuels. *Journal of Fluids Engineering 106* (1984), 105–109.

[147] Oza, R. D., and Sinnamon, J. F. An experimental and analytical study of flash-boiling fuel injection. Tech. Rep. 830590, 1983.

[148] Pai, M G, and Subramaniam, S. A comprehensive probability density function formalism for multiphase flows. *Journal of Fluid Mechanics 628* (2009), 181–228.

[149] Pakseresht, Pedram, and Apte, Sourabh V. Volumetric displacement effects in euler-lagrange les of particle-laden jet flows. *International Journal of Multiphase Flow 113* (2019), 16–32.

[150] Paredi, D, Lucchini, T, D'Errico, G, Onorati, A, Pickett, L, and Lacey, J. Validation of a comprehensive computational fluid dynamics methodology to predict the direct injection process of gasoline sprays using Spray G experimental data. *International Journal of Engine Research 21*, 1 (2020), 199–216.

[151] Park, B. S., and Lee, S. Y. An experimental investigation of the flash atomizaiton mechanism. *Atomization and Sprays 4* (1994), 159–179.

[152] Park, C, Jung, J, Oh, H, Lee, J, and Bae, C. Injector tip wetting evaluation with different nozzle outlet configurations. In *International Conference on Liquid Atomization & Spray Systems* (2018), UNIVERSITY OF ILLINOIS.

[153] Parker, and Youngs. Two and three dimensional Eulerian simulation of fluid flow with material interfaces. Tech. Rep. 01/92, UK Atomic Weapons Establishment, 1992.

[154] Patterson, M A, and Reitz, R D. Modeling the effects of fuel spray characteristics on diesel engine combustion and emission. *SAE transactions* (1998), 27–43.

[155] Payri, R, Gimeno, J, Martí-Aldaraví, P, and Vaquerizo, D. Internal flow characterization on an ECN GDi injector. *Atomization and Sprays 26*, 9 (2016).

[156] Payri, R, Molina, S, Salvador, FJ, and Gimeno, J. A study of the relation between nozzle geometry, internal flow and sprays characteristics in diesel fuel injection systems. *KSME International Journal 18*, 7 (2004), 1222–1235.

[157] Peter, E. M., Takimoto, A., and Hayashi, Y. Flashing and shattering phenomena of superheated liquid jets. *JSME International Journal 37* (1994), 313–321.

[158] Peterson, K, Grover, R, and Mitcham, C. Application of optical diagnostics and simulation to fuel injector tip wetting and soot production. In *in 11th International Symposium on Combustion Diagnostics, Baden-Baden, Germany* (2014).

[159] Pickett, L M, Manin, J, Payri, R, Bardi, M, and Gimeno, J. Transient rate of injection effects on spray development. In *SAE Technical Paper 2013-24-0001* (9 2013).

[160] Pilch, M, and Erdman, CA. Use of breakup time data and velocity history data to predict the maximum size of stable fragments for acceleration-induced breakup of a liquid drop. *International journal of multiphase flow 13*, 6 (1987), 741–757.

[161] Pinhasi, G. A., Ullmann, A., and Dayan, A. Modeling of flashing two-phase flow. *Reviews in Chemical Engineering 21* (2005), 133–264.

[162] Plesset, M. S., and Prosperetti, A. Bubble dynamics and cavitation. *Annual Reviews of Fluid Mechanics 9* (1977), 145–185.

[163] Pope, SB. An explanation of the turbulent round-jet/plane-jet anomaly. *AIAA journal 16*, 3 (1978), 279–281.

[164] Quan, S, Lou, J, and Stone, H A. Interactions between two deformable droplets in tandem subjected to impulsive acceleration by surrounding flows. *Journal of fluid mechanics 684* (2011), 384.

[165] Rachakonda, S K. *Computational Exploration of Flash-Boiling Internal Flow and Near-Nozzle Spray.* PhD thesis, University of Massachusetts Amherst College of Engineering, University of Massachusetts Amherst, 2018.

[166] Rachakonda, S K, Wang, Y, Grover Jr, R O, Moulai, M, Baldwin, E, Zhang, G, Parrish, S, Diwakar, R, Kuo, T-W, and Schmidt, D P. A computational approach to predict external spray characteristics for flashing and cavitating nozzles. *International Journal of Multiphase Flow 106* (2018), 21–33.

[167] Rahman, MM, K Mohamme, Mohammed, and A Bakar, Rosli. Effects of air-fuel ratio and engine speed on performance of hydrogen fueled port injection engine. *Journal of Applied Sciences 9*, 6 (2009), 1128–1134.

[168] Rayleigh, L. On the pressure developed in a liquid during the collapse of a speherical cavity. *Philos. Mag. 34* (1917), 94–98.

[169] Reiss, HJLER, Katz, JL, and Cohen, ER. Translation–rotation paradox in the theory of nucleation. *The Journal of Chemical Physics 48*, 12 (1968), 5553–5560.

[170] Reitz, R D. Modeling atomization processes in high-pressure vaporizing sprays. *Atomisation Spray Technology 3*, 4 (1987), 309–337.

[171] Reitz, R. D. A photographic study of flash-boiling atomization. *Aerosol Science and Technology 12* (1990), 561–569.

[172] Reitz, R D, and Diwakar, R. Structure of high-pressure fuel sprays. *SAE transactions* (1987), 492–509.

[173] Renardy, and Renardy. PROST:A Parabolic Reconstruction of Surface Tesnsion for the Volume of Fluid Method. *J. Comput. Phys. 183* (2002), 400–421.

[174] Reocreux, M. *Contribution à létude des debits critiques en ecoulement diphasique eau-vapeur.* PhD thesis, Université Scientifique et Médicale, Grenoble, France, 1974.

[175] Richards, K J, Senecal, P K, and Pomraning, E. CONVERGE 2.4 manual, 2017.

[176] Rider, and Kothe. Reconstructing Volume Tracking. *J. Comput. Phys. 141* (1998), 112–152.

[177] Rider, W. A marker particle method for interface tracking. In *Proceedings of 6th International Symposium on Comput. Fluid Dynamics, 1995* (1995).

[178] Ritcher, H. J. Separated two-phase flow model:application to critical two-phase flow. *International Journal of Multiphase Flow 9* (1983), 511–530.

[179] Riznic, J. R., and Ishii, M. Bubble Number Density and Vapor Generation in Flashing Flow. *Int. J. Heat Mass Transfer 32* (1989), 1821–1833.

[180] R.O., Grover Jr, and S.E., Parrish. Characterization of a gasoline multi-hole spray under closely-spaced multiple injection operating conditions. ILASS-America, 2019.

[181] Rudman, M. Volume-tracking methods for interfacial flow calculations. *International journal for numerical methods in fluids 24*, 7 (1997), 671–691.

[182] Rusche, Henrik. *Computational fluid dynamics of dispersed two-phase flows at high phase fractions.* PhD thesis, Imperial College London (University of London), 2003.

[183] Saha, K., Battistoni, M., Li, Y., Pomraning, E., and Senecal, P. K. Numerical investigation of two-phase evolution of in- and near-nozzle regions of gasoline direct injection during needle transients. *SAE Int. J. Engines 9* (2016).

[184] Saha, K, Quan, S, Battistoni, M, Som, S, Senecal, PK, and Pomraning, E. Coupled Eulerian internal nozzle flow and Lagrangian spray simulations for GDI systems. Tech. rep., SAE Technical Paper, 2017.

[185] Saha, K., Som, S., Battistoni, M., Li, Y., Quan, S., and Senecal, P. K. Modeling of internal and near-nozzle flow for GDI fuel injector. ASME Internal Combustion Engine Division Fall Technical Conference.

[186] Santos, E G, Shi, J, Venkatasubramanian, R, Hoffmann, G, Gavaises, M, and Bauer, W. Modelling and prediction of cavitation erosion in GDi injectors operated with E100 fuel. *Fuel 289* (2021), 119923.

[187] Scardovelli, R., and Zaleski, S. Direct numerical simulation of free-surface and interfacial flow. *Annual review of fluid mechanics 31*, 1 (1999), 567–603.

[188] Schmidt, D. P., and Corradini, M. L. The internal flow of diesel fuel injector nozzles:a review. *Int. J. Engine Research 2* (2001), 1–22.

[189] Schmidt, D. P., Gopalakrishnan, S., and Jasak, H. Multi-dimensional simulation of thermal non-equilibrium channel flow. *Int. J. Multiphase Flow 36* (2010), 284–292.

[190] Schmidt, David P, and Bedford, Frederick. An analysis of the convergence of stochastic Lagrangian/Eulerian spray simulations. *International Journal of Multiphase Flow 102* (2018), 95–101.

[191] Schmidt, David P., Corradini, M. L., and Rutland, C. J. Two-Dimensional, Non-Equilibrium Model of Flashing Nozzle Flow. 3rd ASME/JSME Joint Fluids Engineering Conference.

[192] Schmidt, David P, Dai, Meizhong, Wang, Haoshu, and Perot, J Blair. Direct interface tracking of droplet deformation. *Atomization and Sprays 12*, 5&6 (2002).

[193] Schmidt, David P, and Rutland, CJ. A new droplet collision algorithm. *Journal of Computational Physics 164*, 1 (2000), 62–80.

[194] Schmidt, DP, Gopalakrishnan, S, and Jasak, Hrvoje. Multi-dimensional simulation of thermal non-equilibrium channel flow. *International Journal of Multiphase Flow 36*, 4 (2010), 284–292.

[195] Schmitz, I., Ipp, W., and Leipertz, A. Flash boiling effects on the development of gasoline direct-injection engine sprays. Tech. Rep. 2002-01-2661, 2002.

[196] Sebastian, P., and Nadeau, J. Experiments and modelling of falling jet flash evaporators for vintage treatment. *Int. J. Thermal Sci. 41* (2002), 269–280.

[197] Senecal, PK, Pomraning, E, Richards, KJ, and Som, S. Grid-convergent spray models for internal combustion engine computational fluid dynamics simulations. *Journal of Energy Resources Technology 136*, 1 (2014).

[198] Serras-Pereira, J., van Romunde, Z., Aleiferis, P. G., Richardson, D., Wallace, S., and Cracknell, R. F. Cavitation and primary break-up and flash boiling of gasoline, iso-octane, n-pentane with a real-size optical direct-injection nozzle. *Fuel 89* (2010), 2592–2607.

[199] Shahangian, N, Sharifian, L, Miyagawa, J, Bergamini, S, Uehara, K, Noguchi, Y, Marti-Aldaravi, P, Martínez, M, and Payri, R. Nozzle flow and spray development one-way coupling methodology for a multi-hole GDI injector. Tech. rep., SAE Technical Paper, 2019.

[200] Shen, S, Che, Z, Wang, T, Jia, M, and Sun, K. Numerical study on flash boiling spray of multi-hole injector. *SAE International Journal of Fuels and Lubricants 10*, 2017-01-0841 (2017).

[201] Sher, E., Bar-Kohany, T, and Rashkovan, A. Flash-boiling atomization. *Progress in Energy and Combustion Science 34* (2008), 417–439.

[202] Shi, J., Santos, E. G., Hoffmann, G., and Dober, G. Large eddy simulation as an effective tool for GDI nozzle development. *MTZ worldwide 79*, 10 (2018), 58–63.

[203] Shikhmurzaev, Y D. *Capillary flows with forming interfaces.* CRC Press, 2007.

[204] Shin, T. S., and Jones, O. C. Nucleation and flashing in nozzles-1. *Int. J. Multiphase Flow 19* (1993), 943–964.

[205] Shokomand, H., and Atashkadi, P. Performance improvement of single flashing, binary, combined cycle for geothermal powerplant. *Energy 22* (1997), 637–643.

[206] Skripov, V. P. *Metastable liquids.* New York : J. Wiley, 1973.

[207] Som, S, and Aggarwal, S K. Effects of primary breakup modeling on spray and combustion characteristics of compression ignition engines. *Combustion and flame 157*, 6 (2010), 1179–1193.

[208] Song, H, Xiao, J, Chen, Y, and Huang, Z. The effects of deposits on spray behaviors of a gasoline direct injector. *Fuel 180* (2016), 506–513.

[209] Sphicas, P, Pickett, L M, Skeen, S, Frank, J, Lucchini, T, Sinoir, D, D'Errico, G, Saha, K, and Som, S. A comparison of experimental and modeled velocity in gasoline direct-injection sprays with plume interaction and collapse. *SAE International Journal of Fuels and Lubricants 10*, 1 (2017), 184–201.

[210] Sphicas, P, Pickett, L M, Skeen, S A, and Frank, J H. Inter-plume aerodynamics for gasoline spray collapse. *International Journal of Engine Research 19*, 10 (2018), 1048–1067.

[211] Spielger, K., and El-Sayed, Y. The energtics of desalination processes. *Desalination 134* (2001), 109–128.

[212] Steimle, F, Kulzer, A, Richter, H, Schwarzenthal, D, and Romberg, C. Systematic analysis and particle emission reduction of homogeneous direct injection SI engines. Tech. rep., SAE Technical Paper, 2013.

[213] Strek, P., Duke, D., Swantek, A., Kastengren, A., Powell, C. F., and Schmidt, D. P. X-Ray radiography and CFD studies of the Spray G injector. Tech. Rep. 2016-01-0858, SAE, 2016.

[214] Subramaniam, S. Lagrangian–Eulerian methods for multiphase flows. *Progress in Energy and Combustion Science 39*, 2 (2013), 215–245.

[215] Subramaniam, S, and O'rourke, PJ. Numerical convergence of the KIVA-3 code for sprays and its implications for modeling. *Los Alamos Laboratory Report UR-98-5465, Los Alamos, NM* (1998).

[216] Sussman, M. A second order coupled Level Set and Volume of Fluid Method for computing growth and collapse of vapour bubbles. *J. Comput. Phys. 187* (2003), 110–136.

[217] Tanner, F X. Liquid jet atomization and droplet breakup modeling of non-evaporating diesel fuel sprays. *SAE transactions* (1997), 127–140.

[218] Taskinen, P. Effect of fuel spray characteristics on combustion and emission formation in a large medium speed diesel engine. Tech. rep., SAE Technical Paper, 1998.

[219] Taylor, G I. The instability of liquid surfaces when accelerated in a direction perpendicular to their planes. i. *Proceedings of the Royal Society of London. Series A. Mathematical and Physical Sciences 201*, 1065 (1950), 192–196.

[220] Theofanus, T., Biasi, L., Isbin, H. S., and Fauske, H. A theoretical study on bubble growth in constant and time-dependent pressure fields. *Chem. Eng. Sci. 24* (1969), 885–897.

[221] Tow, TC, Pierpont, DA, and Reitz, Rolf D. Reducing particulate and NO_x emissions by using multiple injections in a heavy duty DI diesel engine. *SAE transactions* (1994), 1403–1417.

[222] Trujillo, M F, Hsiao, C-T, Choi, J-K, Paterson, E G, Chahine, G L, and Peltier, L J. Numerical and experimental study of a horizontal jet below a free surface. In *9th International conference on numerical ship hydrodynamics, Ann Arbor, MI* (2007).

[223] Ubbink, O. Numerical prediction of two fluid systems with sharp interfaces.

[224] Überall, A, Otte, R, Eilts, P, and Krahl, J. A literature research about particle emissions from engines with direct gasoline injection and the potential to reduce these emissions. *Fuel 147* (2015), 203–207.

[225] Vallet, A., Burluka, A., and Borghi, R. Development of a Eulerian model for the "atomization" of a liquid jet. *Atomization and Sprays 11* (2001), 619–642.

[226] VanDerWege, B A., and Hochgreb, S. The effect of fuel volatility on sprays from high-pressure swirl injectors. Twenty-Seventh Symposium (International) on Combustion/The Combustion Institute.

[227] Versteeg, HK, Hargrave, GK, and Kirby, M. Internal flow and near-orifice spray visualisations of a model pharmaceutical pressurised metered dose inhaler. In *Journal of Physics: Conference Series* (2006), vol. 45, Iop Publishing, p. 207.

[228] Wallis, G. B. Critical Two-Phase Flow. *Int. J. Multiphase Flow 6* (1980), 97–112.

[229] Wang, C, Xu, H, Herreros, J M, Wang, J, and Cracknell, R. Impact of fuel and injection system on particle emissions from a GDI engine. *Applied Energy 132* (2014), 178–191.

[230] Weller, H G. A new approach to VOF-based interface capturing methods for incompressible and compressible flow. *OpenCFD Ltd., Report TR/HGW 4* (2008), 35.

[231] Westlye, F R., Penney, K, Ivarsson, A, Pickett, L M., Manin, J, and Skeen, S A. Diffuse back-illumination setup for high temporally resolved extinction imaging. *Appl. Opt. 56*, 17 (Jun 2017), 5028–5038.

[232] Wildgen, A., and Straub, J. The boiling mechanism in superheated free jets. *Int. J. Multiphase Flow 15* (1989), 193–207.

[233] Williams, F. A. Spray combustion and atomization. *Phys. Fluids 1* (1958), 541–545.

[234] Woods, A., and Bloom, F. Modelling of flash evaporation I: Formulation of the mathematical model. *Math. Comput. Modelling 32* (2000), 1153–1169.

[235] Wu, S, Xu, M, Hung, D LS, Li, T, and Pan, H. Near-nozzle spray and spray collapse characteristics of spark-ignition direct-injection fuel injectors under subcooled and superheated conditions. *Fuel 183* (2016), 322–334.

[236] Xiao, D, Qiu, S, Zhang, X, Zhang, Y, Li, X, Hung, D, and Xu, M. Dynamic behavior and mechanism analysis of tip wetting process under flash boiling conditions. *Fuel 307* (2022), 121773.

[237] Xu, M., Zhang, Y., Zeng, W., Zhang, G., and Zhang, M. Flash boiling: Easy and better way to generate ideal sprays than the high injection pressure. *SAE Int. J. Fuels Lubr. 6* (2013), 137–148.

[238] Xue, Q., Battistoni, M., Som, S., Quan, S., Senecal, P. K., Pomraning, E., and Schmidt, D. P. Eulerian CFD modeling of coupled nozzle flow and spray with validation against X-Ray radiography data. *SAE Int. J. Engines 7* (2014).

[239] Zalesak, S. T. Fully multidimensional flux-corrected transport algorithms for fluids. *J. Comput. Phys. 31* (1979), 335–362.

[240] Zeng, W., Xu, M., Zhang, G., and Cleary, D. Atomization and vaporization for flash-boiling multi-hole sprays with alcohol fuels. *Fuel 95* (2012), 287–297.

[241] Zeng, W., Xu, M., Zhang, M., Zhang, Y., and Cleary, D. Macroscopic characteristics for direct-injection multi-hole sprays using dimensionless analysis. *Experimental Thermal and Fluid Science 40* (2012), 81–92.

[242] Zhang, G., Hung, D. L., and Xu, M. Experimental study of flash boiling spray vaporization through quantitative vapor concentration and liquid temperature measurements. *Exp. Fluids 55* (2014).

[243] Zhang, Y, Jia, M, Duan, H, Wang, P, Wang, J, Liu, H, and Xie, M. Numerical and experimental study of spray impingement and liquid film separation during the spray/wall interaction at expanding corners. *International Journal of Multiphase Flow 107* (2018), 67–81.

[244] Zhao, F, Harrington, D L, and Lai, M-C D. Automotive gasoline direct-injection engines. *Warrendale, PA: Society of Automotive Engineers, 2002. 372* (2002).

[245] Zhao, H., Quan, S., Dai, M., Pomraning, E., Senecal, P. K., Xue, Q., Battistoni, M., and Som, S. Validation of three dimensional internal nozzle flow model including automatic mesh generation and cavitation effects. *Journal of Engineering for Gas Turbines and Power 136* (2014).